

# **Planar Liquid Crystal Beam-Steering and Beam-Switching Millimeter-Wave Networks with Slow-Wave Structures for Miniaturization and Fast Response**

Vom Fachbereich Elektrotechnik und Informationstechnik  
der Technischen Universität Darmstadt  
zur Erlangung des akademischen Grades eines  
Doktor-Ingenieurs (Dr.-Ing.)  
genehmigte

## **Dissertation**

von

Master of Science

**Dongwei Wang**

geboren am 12.09.1991  
in Shanxi, V.R.China

Referent:	Prof. Dr.-Ing. Rolf Jakoby
Korreferent:	Prof. Philippe Ferrari

Tag der Einreichung:	19. 05. 2023
Tag der mündlichen Prüfung:	07. 09. 2023

D17  
Darmstadt 2023

Wang,Dongwei: Planar Liquid Crystal Beam-Steering and Beam-Switching  
Millimeter-Wave Networks with Slow-Wave Structures for Miniaturization and Fast  
Response  
Darmstadt, Technische Universität Darmstadt  
Year thesis published in TUpriints: 2024  
URN: urn:nbn:de:tuda-tuprints-264222  
Date of the viva voce: 07.09.2023  
Published under CC BY-SA 4.0 International  
<https://creativecommons.org/licenses/>



# Preface

This thesis demonstrates my research achievements during working as a Ph.D candidate in the Institute for Microwave Engineering and Photonics (IMP) at Technische Universität Darmstadt. At this point, I would like to acknowledge all the people who supported me on the long way to my doctorate, especially during the pandemic of COVID-19.

First of all, I would like to thank my supervisor Prof. Dr.-Ing. Rolf Jakoby for his trustful and patient guidance throughout my complete Ph.D time. He provided a flexible working environment and encouraged my research interest in a high degree of freedom. He gave me trust in my first year when I was faced with the hardest time of my work. In the second place, I would like to thank Prof. Dr.-Ing. Holger Maune who taught me how to do scientific research and inspired me to realize my ideas. I learned a lot from him not only about techniques on microwave engineering, but also the way to study and work. In the third place, I want to thank Prof. Dr.-Ing. Gustavo P. Rehder from LME, Laboratório de Microeletrônica, Escola Politécnica da Universidade de São Paulo, São Paulo, Brazil for his professional technical supports and suggestions. Although we never met in person up to now, we had good cooperation and achieved nice results.

Many thanks to my former colleague Matthias Nickel, he is always worth discussing with and helped me a lot in technical issues. Thank Dr.-Ing. Matthias Jost who lead me into my project and patiently answered all my questions on handy even after his graduation. It is impossible to do all the work without the help from Ersin Polat, Henning Tesmer, Dr.-Ing. Alejandro Jiménez-Sáez, Dr.-Ing. Dominik Walk, Dr.-Ing. Christian Schuster, Dr.-Ing. Roland Reese, Prannoy Agrawal, and Stipo Matic, their useful experiences, knowledge, instructions and assistants reduced my workload considerably, kept me always in the right way and reached the goal finally. Many thanks to Peter Kiesslich and Andears Semrad from the work shop and Ion Opera in the clean room, all the samples appear in this thesis are with their help.

Our management staffs are highly acknowledged, Dr.-Ing Martin Schüßler, Maria Kaiser, Nicole Neurohr and Eleonore Titow, they are in charge of general organization, business trip, conference, publication, instrument purchase, software management, etc. Their effort allows us to concentrate more on the research works.

Last but not least, I would like to thank my friends, my parents and parents in law for supporting and motivating me in this challenging and long Ph.D journey. Special thanks go to my darling wife. She supported me in every aspect in life and work, I couldn't finish my Ph.D without her encouragement and inspiration.

Heilbronn, Dec 2022

Dongwei Wang



# Abstract

The upcoming generations of wireless communication hold great promise in providing ultra-fast data rate and very low latency by exploiting the large absolute bandwidths at millimeter-waves (mmW) frequencies. Hardware deployment requires highly directive antenna systems with beam steering capability, which can be provided by microwave liquid crystal (LC) technology at mmW in an analog manner. LC has relatively low dissipation factor above 5 GHz with a decreasing trend as frequency increases up to at least several THz. As a functional material, LC performs continuous tunable permittivity to the propagating signal, depending on the relative orientation between LC molecules and signal polarization. LC-based transmission lines have tunable electrical length and are used as passive analog delay line phase shifters. In terms of planar LC phase shifter, the compromise between fast response and high RF performance arises as the major issue. This work focuses on innovative methods, namely defective ground structure (DGS) and nanowire-filled-membrane (NaM) technologies to realize planar microstrip LC phase shifters with miniaturized size, improved RF performance, and reduced response time. Both technologies show state-of-the-art performance in the realm of planar phase shifters. The one based on defective ground structures filled with 4.6  $\mu\text{m}$  thick GT7-29001 type of LC is suitable for relatively low mmW frequencies, due to the low pass nature of defective ground structures. It achieves a response time of 51 ns and a figure-of-merit (FoM) of 79  $^\circ/\text{dB}$  at 30 GHz. The one based on NaM filled with 4.0  $\mu\text{m}$  thick GT7-29001 is suitable for relatively high frequencies up to at least W-band and achieves 110 ns with 70  $^\circ/\text{dB}$  at 56 GHz. The response time is related to LC layer thickness and surface anchoring condition.

Furthermore, continuously beam steering planar phased antenna arrays are realized by combining the aforementioned LC phase shifters with antennas and feeding networks at around 28 GHz. The first phased array utilizes a  $1 \times 4$  corporate feed network with four full  $360^\circ$  LC phase shifters, and the second utilizes a  $4 \times 4$  Butler Matrix (BM) with four LC phase shifters of reduced length, and hence, losses, since they require only  $135^\circ$  maximum phase shift. For both phased arrays, each individual phase shifter is biased through a high-impedance DC conductive line to prevent RF leakage. DC blocks are integrated on both sides of each phase shifter to ensure DC isolation to other phase shifters and the non-tunable circuitry. While the former realizes a continuous beam scanning range of  $110^\circ$  by tuning phase shifters only, the latter can steer the beam continuously in a small range around the four predefined switchable directions, achieving a total beam scanning range of  $120^\circ$ . Both arrays have decent gain of 4.5 dBi and 5.5 dBi, respectively. The latter has higher gain due to the smaller phase shifters, resulting in lower loss. Both arrays are estimated to be steered within 0.7 s or less for a full scan. Beside phased arrays, an interference-based single-pole double-throw (SPDT) is realized, using two LC phase shifters of  $90^\circ$ . The SPDT achieves not only on/off states, it can continuously adjust the power splitting ratio. When

## *Abstract*

switched-on, the SPDT show 3.4 dB to 4.5 dB insertion loss within 26 GHz to 30 GHz and >10 dB isolation to the switched-off port. When switched-off, the SPDT requires 1.5 s to recover the initial state.

Towards higher mmW band, NaM technology is promising as an interposer. Thus, a second Butler Matrix at W-band is realized on NaM as a proof-of-concept, and is to be integrated with LC NaM phase shifter. Taking the advantage of easy realization of through substrate via on NaM, the crossover as the key component of the Butler Matrix is proposed with compact size, low loss, high isolation and high balance, working from DC to 110 GHz. The final Butler Matrix with integrated patch antennas is measured at 100 GHz to have far field patterns at the desired discrete directions with good symmetry at  $\pm 12^\circ$  and  $\pm 45^\circ$ , with decent maximum gain of 5.4 dBi.

# Kurzfassung

Die kommenden Generationen der drahtlosen Kommunikation versprechen ultraschnelle Datenraten und sehr geringe Latenzzeiten, indem sie die großen absoluten Bandbreiten bei Millimeterwellen (mmW) ausnutzen. Der Hardwareeinsatz erfordert hochgradig richtungsweisende Antennensysteme mit der Fähigkeit zur Strahlschwenkung, die durch Mikrowellen-Flüssigkristalltechnologie (LC) bei mmW auf analoge Weise bereitgestellt werden kann. LC hat einen niedrigen Verlustfaktor oberhalb von 5 GHz mit abnehmender Tendenz bei steigender Frequenz bis mindestens zu mehreren THz. Als funktionales Material hat LC eine kontinuierlich abstimmbare Permittivität für das sich ausbreitende Signal, abhängig von der relativen Orientierung zwischen LC-Molekülen und der Signalpolarisation. LC-basierte Übertragungsleitungen haben eine abstimmbare elektrische Länge und werden als passive analoge Verzögerungsleitungsphasenschieber verwendet. Bei planaren LC-Phasenschiebern stellt der Kompromiss zwischen schnellem Ansprechverhalten und hoher HF-Performance das Hauptproblem dar. Diese Arbeit konzentriert sich auf innovative Methoden, nämlich defekte Bodenstrukturen (DGS) und Nanodraht-gefüllte Membranen (NaM), um planare Mikrostreifen-LC-Phasenschieber mit miniaturisierter Größe, verbesserter HF-Performance und verkürzter Reaktionszeit zu realisieren. Beide Technologien sind auf dem neuesten Stand der Technik im Bereich der planaren Phasenschieber. Die Variante mit defekten Bodenstrukturen, welche mit  $4,6\text{ }\mu\text{m}$  dicken LCs vom Typ GT7-29001 gefüllt ist, eignet sich aufgrund des Tiefpass-Charakters defekter Bodenstrukturen für relativ niedrige mmW-Frequenzen. Es werden Ansprechzeiten von 51 ms und eine Gütezahl (FoM) von  $79\text{ }^\circ/\text{dB}$  bei 30 GHz erreicht. Die Variante mit Nanodraht-gefüllte Membranen, welche mit  $4,0\text{ }\mu\text{m}$  dickem GT7-29001 ist, eignet sich für relativ hohe Frequenzen bis mindestens zum W-Band und erreicht 110 ms mit  $70\text{ }^\circ/\text{dB}$  bei 56 GHz. Die Ansprechzeit hängt hier von der Dicke der LC-Schicht und den Bedingungen der Oberflächenverankerung ab.

Darüber hinaus werden kontinuierlich strahl-schwenkende, phasengesteuerte Antennenarrays durch Kombination der oben genannten LC-Phasenschieber mit Antennen- und Speisungsnetzwerken bei etwa 28 GHz realisiert. Das erste phasengesteuerte Array verwendet ein  $1\times 4$  Corporate-Speisenetzwerk mit vier LC-Phasenschiebern, jeder mit der Fähigkeit zur vollen  $360^\circ$  Phasenabstimmbarkeit. Das zweite verwendet eine  $4\times 4$  Butler-Matrix (BM) mit vier LC-Phasenschiebern mit geringerer Länge und somit geringeren Verlusten, da sie nur eine maximale Phasenabstimmbarkeit von  $135^\circ$  benötigen. Für beide phasengesteuerten Arrays wird jeder einzelne Phasenschieber über eine hochohmige DC-Leitung gespeist, um HF-Leckverluste zu vermeiden. Auf beiden Seiten jedes Phasenschiebers sind Gleichstromblöcke integriert, um die Gleichstromisolierung zu anderen Phasenschiebern und den nicht abstimmbaren Schaltkreisen sicherzustellen. Während der erste Phasenschieber einen kontinuierlichen Strahl-Abtastbereich von  $110^\circ$

## *Abstract*

allein durch die Abstimmung der Phasenschieber realisiert, kann der Letztere den Strahl kontinuierlich in einem kleinen Bereich um die vier vordefinierten schaltbaren Richtungen lenken, wodurch ein Gesamtstrahl-Abtastbereich von  $120^\circ$  erreicht wird. Die Arrays haben eine Verstärkung von 4.5 dBi bzw. 5.5 dBi. Letzteres hat eine höhere Verstärkung aufgrund der kleineren Phasenschieber, was zu geringeren Verlusten führt. Für einen vollständigen Scan können Steuerzeiten von 0.7 s oder weniger für beide Arrays erwartet werden. Neben den Phasen Arrays wird ein interferenzbasierter Single-Pole-Double-Throw (SPDT) realisiert, der zwei LC-Phasenschieber von  $90^\circ$  verwendet. Der SPDT erreicht nicht nur Ein/Aus-Zustände, sondern kann auch das Leistungsverteilungsverhältnis kontinuierlich anpassen. Im eingeschalteten Zustand weist der SPDT eine Einfügungsdämpfung von 3.4 dB bis 4.5 dB innerhalb von 26 GHz bis 30 GHz und eine Isolierung von  $>10$  dB zum ausgeschalteten Anschluss auf. Im ausgeschalteten Zustand benötigt der SPDT 1.5 s, um den Ausgangszustand wiederherzustellen.

In Richtung höherer mmW-Bänder ist die NaM-Technologie als Interposer vielversprechend. Daher wird eine zweite Butler-Matrix für das W-Band als Proof of Concept auf NaM realisiert, die mit einem LC-NaM-Phasenschieber integriert werden soll. Die Kreuzkoppler als Schlüsselkomponente der Butler-Matrix nutzt den Vorteil der einfachen Realisierung von Durchkontaktierungen auf NaM und zeichnet sich durch kompakte Größe, geringe Verluste, hohe Isolation und hohe Ausgewogenheit aus und kann von DC bis 110 GHz betrieben werden. Die endgültige Butler-Matrix mit integrierten Patch-Antennen wurde bei 100 GHz gemessen, um Fernfeldmuster in den gewünschten diskreten Richtungen mit guter Symmetrie bei  $\pm 12^\circ$  und  $\pm 45^\circ$  zu erhalten, mit einem anständigen maximalen Gewinn von 5.4 dBi.

# Contents

<b>Preface</b>	<b>i</b>
<b>Abstract</b>	<b>iii</b>
<b>1 Introduction</b>	<b>1</b>
1.1 Background and Motivation . . . . .	1
1.2 Structure of the Work . . . . .	3
<b>2 Fundamentals of Liquid Crystal (LC)</b>	<b>5</b>
2.1 Nematic Liquid Crystal . . . . .	7
2.2 Magnetic and Electric Properties . . . . .	9
2.3 Alignment and Biasing Schemes . . . . .	10
2.4 Liquid Crystal in Microwave Engineering . . . . .	14
<b>3 Liquid Crystal-based Microstrip Delay Line Phase Shifters</b>	<b>17</b>
3.1 Transmission Line Theory and Slow Wave Effect . . . . .	18
3.2 Inverted Microstrip Line (IMSL) Phase Shifter . . . . .	21
3.3 Stub-Loaded Microstrip Line (LMSL) Phase Shifter . . . . .	28
3.4 Microstrip Line Phase Shifter with Defected Ground Structure (DGS) . . . .	30
3.4.1 Investigations for Different DGS Dimensions and Comparison . . . .	31
3.4.2 Miniaturization and Response Times . . . . .	35
3.5 Nanowire Membrane (NaM)-based Inverted Microstrip Line Phase Shifter .	38
3.5.1 Metallic-Nanowire-Filled-Membrane . . . . .	38
3.5.2 Reference Microstrip Line Filled With Air . . . . .	40
3.5.3 Performance Analysis of NaM-based Phase Shifters with Different LCs . . . . .	43
3.6 Comparison of State-of-the-Art Planar Phase Shifter Technologies . . . . .	47
3.7 Linearity and Power Handling Capability . . . . .	49
3.8 Summary . . . . .	53
<b>4 LC-based Planar Mixed Beam-Steering and Beam-Switching Networks at Ka-Band</b>	<b>55</b>
4.1 Corporate Fed Phased Antenna Array With Integrated Phase Shifters for Beam-Steering . . . . .	56
4.1.1 Integrated LC-Phase Shifter with Defected Ground Structure (DGS)	57
4.1.2 Planar Yagi-Uda Antenna . . . . .	59
4.1.3 Planar $1 \times 4$ Beam-Steering Antenna Array . . . . .	62

## Contents

4.2	Butler Matrix Fed Phased Antenna Array for Beam-Switching and Beam-Steering . . . . .	65
4.2.1	Wideband Branch-Line 3-dB Quadrature Coupler . . . . .	66
4.2.2	Wideband Via-less Crossover . . . . .	68
4.2.3	Planar $1 \times 4$ Mixed Beam-Switching and Beam-Steering Antenna Array . . . . .	70
4.3	Single-Pole Double-Throw . . . . .	79
4.4	Summary . . . . .	84
<b>5</b>	<b>Nanowire Membrane (NaM) Interposer Technology at W-band</b>	<b>87</b>
5.1	Compact DC to 110 GHz Crossover . . . . .	88
5.2	Multi-port On-wafer Measurement Method . . . . .	91
5.3	Proof-of-Concept: Beam-Switching Broadside Antenna Array with Butler Matrix . . . . .	96
5.4	Summary . . . . .	100
<b>6</b>	<b>Conclusion and Outlook</b>	<b>103</b>
<b>A</b>	<b>Appendix</b>	<b>109</b>
A.1	Fabrication Process of LC-Phase Shifter . . . . .	109
A.2	Thru-Reflect-Line Calibration: Mathematics and Practical Considerations . .	112
<b>B</b>	<b>Acronyms</b>	<b>119</b>
	<b>Bibliography</b>	<b>125</b>



# 1 Introduction

## 1.1 Background and Motivation

Recent development of 5G cellular network architecture arises rapidly growing demand for higher data rates to meet the needs for increasing number of subscribers and the capacity for each subscriber [XZS17]. Modern wireless communication are required to keep up with the remarkable speed-up of fiber optic networks. 20, 40 and even 100 Gb/s rates are expected by a large number of use cases [ITU15; XZS17]:

1. Mobile Internet (MI) focuses on people-oriented communication such as Ultra-High Density (UHD) and 3D video, augmented reality (AR), virtual reality (VR), online game, mobile cloud, remote computing, collaborative robots, metaverse, etc.
2. Internet of Things (IoT) which enable communications between things and between things and people, for example, smart grid, critical infrastructure monitoring, industrial automation, eHealth services, smart homes/buildings, smart cities, etc.

To achieve such high data rates, high operating frequency and large absolute bandwidth are required, which are available at millimeter waves (mmW). However, power link budget consideration is dominated by the free-space path loss (FSPL),

$$\text{FSPL} = \left( \frac{4\pi Rf}{c_0} \right)^2 \quad (1.1)$$

where  $R$  is the propagation distance,  $f$  is transmitted signal frequency, and  $c_0$  is the speed of light, as well as atmospheric impairments [ITU16] at these high frequencies, compare Fig. 1.1 [Mau+18].

To overcome the FSPL at mmW range, highly directive antenna arrays are proposed with high gain and corresponding narrow beams to build reliable connections between a user terminal and the desired hub (satellite, relay, or base station). Since the user terminal or hub is moving in most of the practical cases, the beam has to be steered. For this purpose, phased antenna arrays are widely used, which are less space consuming than a parabolic dish of high directivity and more flexible than a mechanically steerable array. Electronically steered passive phased arrays (ESPA), of which the main beam direction can be steered by selectively adjusting the progressive phase shift between the individual antenna element electronically, are of great interest due to their cost-effective fabrication, easily extendable to large arrays and low power consumption in general. Therefore, the scope of this work concentrates on the realization of electronically steered passive phased arrays.

For phased arrays, phase shifters are the key components to modulate the phase of the individual antenna element, and are desired to have high reliability, high performance and

## 1 Introduction

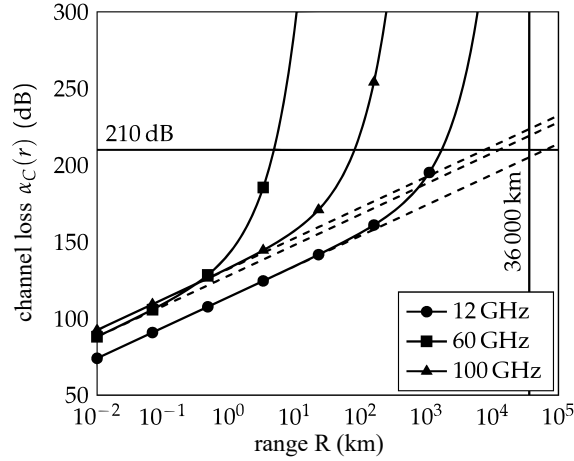


Figure 1.1: Channel loss for different frequencies as sum of free space path loss (dashed lines) and the atmospheric attenuation according to ITU standard atmosphere (solid lines) for homogenous medium between transmitter and receiver. As reference the properties of a geostationary satellite for broadcasting at Ku-band (12 GHz) with 36 000 km transmission range with approximately 210 dB of insertion loss are highlighted [Mau+18].

fast response time at low cost. Therefore, one focus area of this work will be discussing phase shifters. There are several technologies to realize phase shifters in  $K_u$  band (12 GHz to 18 GHz) and above for aforementioned high data rates. Semiconductor technologies, especially silicon based Complementary Metal-Oxide-Semiconductor (CMOS), as well as new semiconductor generations such as InP, GaAs, GaN have been used to realize both analog and digital passive phase shifters [Isk+16; MR07; Han+14; TN09]. However, their high cost, high loss, low power-handling capability are significant in mmW range. Although they can be directly integrated with active power amplifier to increase the gain, the power consumption and fabrication cost are high. RF microelectromechanical systems (RF-MEMS) offer high performance in terms of maximum phase shift, low loss, and low power consumption. However, RF-MEMSs can have wear out failures, dielectric charging, and contact degradation after considerable large number of switching cycles [Pen+09; DD07]. Their encapsulation and high voltage requirement are also problematic. They are difficult to be integrated into antenna arrays due to phase errors induced by their discrete phase change [Kim+02; Che+09; Top+08]. Tunable phase shifters based on ferrites require a high current flow for the generation of high magnetic field strengths for tuning. They have bulky volumes due to the magnets and increased loss in the desired frequency range [GS15; She+10]. Ferroelectrics, mainly Barium Strontium Titanate (BST) in thin or thick film technologies, are already established for the lower GHz range. They require high voltage for bias and suffer from high dielectric loss in mmW range [Saz+11a; Nik+16; Saz+11b; Nik+17].

As ferrites and ferroelectrics, microwave liquid crystal (LC) represents another promising functional tunable dielectric, but generally above 5 GHz, even up to at least 8 THz [Wei+13].

These materials provide continuous tunability, high linearity, and low loss at low cost by using standard technologies. The tunability comes from their anisotropic permittivity, which is more widely known as birefringence in optics used to control the flux of back light in LC display (LCD) technology [TT12]. Specifically synthesized microwave LCs obtained significant development during the past two decades, numerous innovative LC components with high-performance have been implemented. Among state-of-the-art LC components, low profile planar LC one acquired considerable attention, which can be massively and cost-effectively realized with well-established automated LCD manufacturing techniques [Pan+22; Zha+17; Li+22; Ma+18; Hin20; Dol20]. Compared with high-performance volumetric waveguide-based LC devices [Ree+19; Jos+17; Nic+20], they have inherently higher loss, mainly due to ohmic loss from metals. Whereas, they possess the advantages of planar circuits, such as simple fabrication and assembly process, easy expansion, low volume and light weight. Moreover, planar LC components tune much faster than those based on waveguide.

Indeed, response time of LC components is a distinct drawback [JGW20]. While other mentioned phase shifter technologies have  $\mu\text{s}$  level response time, waveguide-based LC components normally have response time up to minutes, which is related to square of LC layer thickness. Only some specially designed planar LC components with extremely thin LC layer of several  $\mu\text{m}$  only are reported to achieve around 100 ms response time [Goe+08; Goe+09; Kar14; Fra+13; Fri+11; Hu+14]. It needs to be further reduced to be less than 10 ms for modern wireless communication. However, high performance and fast response of planar LC device have converse requirements on LC thickness. Besides, LC phase shifters are mostly based on transmission lines, which consume large area due to limited tunability of LC, especially in the low frequency range. Therefore, realizing fast response and compact size while maintaining high performance is a major objective in the realm of planar LC phase shifters and is, therefore, focused on in this work. Further, the LC phase shifters should be validated by integrating into phased arrays.

## 1.2 Structure of the Work

This work consists of the following parts. In chapter 2, the fundamentals of LCs are explained, especially their anisotropic material property and alignment mechanism which are utilized in microwave applications.

In chapter 3, transmission line theory and slow-wave effect are introduced. LC-based inverted microstrip line (MSL) is realized with tunable electrical length, operating as phase shifter. To solve the contrary requirements of high figure-of-merit and fast response, regarding the thickness of LC layer, MSLs are modified with artificial structures to achieve slow wave effect, and thus, increasing FoM, reducing size and reducing response time, simultaneously. The fabrication of the phase shifter demonstrators take advantages of the well-established LCD production line, such that LCs are encapsulated between two glass substrates, serving as the dielectric of the MSL. Three LC-based slow wave phase shifters are proposed, utilizing loaded stubs, defective ground structures (DGS) and metallic-nanowire-filled-membrane (NaM), respectively. They are compared with the

## 1 Introduction

state-of-the-art passive phase shifters.

To further verify the feasibility of the proposed LC phase shifters in microwave devices, DGS-based phase shifter is applied into reconfigurable mmW devices due to its easy fabrication and integration, as demonstrated in chapter 4. Together with other non-tunable passive circuitry, such as feeding and biasing network, as well as antenna elements, three continuously reconfigurable devices are implemented for Ka-band: (1.) steered corporate feed phased array, (2.) switched and steered butler matrix (BM) fed phased array, and (3.) interference-based single-pole double-throw (SPDT) with adjustable power splitting ratio. The two phased arrays are fully planar with similar fabrication effort as LC phase shifters. They are designed with compact size and large beam scanning range, aiming to achieve high gain and fast beam scanning simultaneously by taking the advantages of the LC phase shifter. The SPDT is designed for switching between the different input ports of the butler matrix, while its continuously adjustable power splitting ratio enables multi-input channel selection, which allows multi-beam radiation, apart from a traditional SPDT with only on/off states. The expense is the relatively high insertion loss (IL) on the MSL-based phase shifter.

However, it is noticed from the devices proposed in chapter 4, that the non-tunable circuitry based on LC for easy integration with LC phase shifters leads to unnecessarily high insertion loss. This in turn diminishes the advantages of the high-performance LC phase shifter. Thus, an interposer technology is desired, which allows the integration of components of different substrates. NaM used in chapter 3 allows high-quality MSLs for horizontal components integration and through-substrate vias for vertical integration. Therefore, NaM is considered as a promising interposer technology and is verified in chapter 5 by proposing a Butler matrix fed patch antenna array at 100 GHz. Related components' designs are also discussed in detail.

Finally, the achievements of the work are summarized in chapter 6. Besides, ongoing research on reconfigurable intelligent surface (RIS) are given, as well as further developments based on these research results. Moreover, an outlook about realization of mixed beam-switching and beam-steering networks for millimeter wave applications based on NaM and LC technology is given at the end on component and system level.

## 2 Fundamentals of Liquid Crystal (LC)

Since the discovery of liquid crystalline phase in 1888 by Friedrich Reinitzer and Otto Lehmann [Leh89], researches on liquid crystal (LC) acquired high attention, especially from 1960s on when it was firstly applied into display industry. Subsequently, the manufacturers of liquid crystal displays (LCD) have gradually designed ingenious differences on the technology by taking this display device into an incredible range. LCD is based on the birefringence property of LC, where LC is packed between two polarization grids and is used to adaptively turn the polarization angle of the light transmitted perpendicularly through the LC layer, and thus adjust the grayscale of the colored light. This twisted nematic cell is the fundamental principle for all modern LCD, as depicted in Fig. 2.1. LCD technologies allow displays to be much thinner, less power consuming and lighter compared to a cathode ray tube (CRT) technology.

Since the last two decades, research focuses on the implementation of the LC technology to microwave applications, e.g., as tunable material in phased array antennas for satellite communication applications. As birefringence is a material property in optics, it is known in microwave engineering as anisotropic permittivity, since the rotation of the polarization angle as in LCD is a niche application in microwaves. Therefore, the anisotropy is usually adopted to present a variable effective permittivity  $\epsilon_{\text{eff}}$  to the electromagnetic wave.

The name LC indicates a combination of the material's main properties, i.e., liquid and crystalline solid states. Liquids can flow, while solids cannot, and crystalline solids possess special symmetry properties that liquids lack. The most common liquid crystalline phases depend on the system temperature. Ordinary solids melt into ordinary liquids as the temperature increases, e.g., ice melts into liquid water. Some material actually melts twice or more as temperature rises. Between the crystalline solid at low temperature and the ordinary liquid state at high temperature lies an intermediate state, the LC. LCs share with liquids the ability to flow, but also show symmetries inherited from crystalline solids. Such kind of LCs are defined as thermotropic, whose phase changes with temperature.

Except for thermotropic LC, there are lyotropic and metallotropic LC. Thermotropic and lyotropic LCs consist mostly of organic molecules, although a few minerals are also known. Lyotropic LCs exhibit phase transition as a function of both temperature and concentration of the liquid-crystal molecules in a solvent (typically water). Metallotropic LCs are composed of both organic and inorganic molecules; their liquid-crystal transition depends not only on temperature and concentration, but also on the inorganic-organic composition ratio.

Numerous LC phases have been discovered. Although, different liquid crystals strongly vary in chemical structure, they all have one thing in common: they flow similarly to viscous liquids but show anisotropic physical properties of crystals depending on the molecular structure, temperature, concentration, and the solvent.

## 2 Fundamentals of Liquid Crystal (LC)

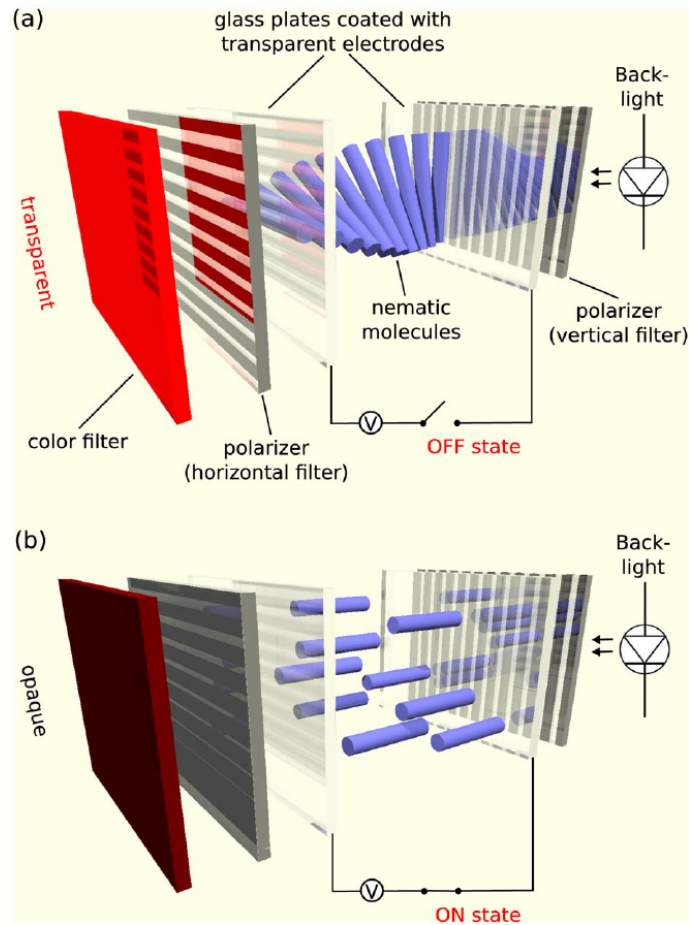


Figure 2.1: Working principle of a twisted nematic cell used in LCD [TT12]. (a) The unbiased LC rotates polarization by  $90^\circ$  such that the back light can pass two twisted polarization grids and the pixel is on. When the LC is biased as (b), the polarization of light is not rotated and cannot pass the second polarization grid, so the pixel is off. LC bias concept is explained later in section 2.2.

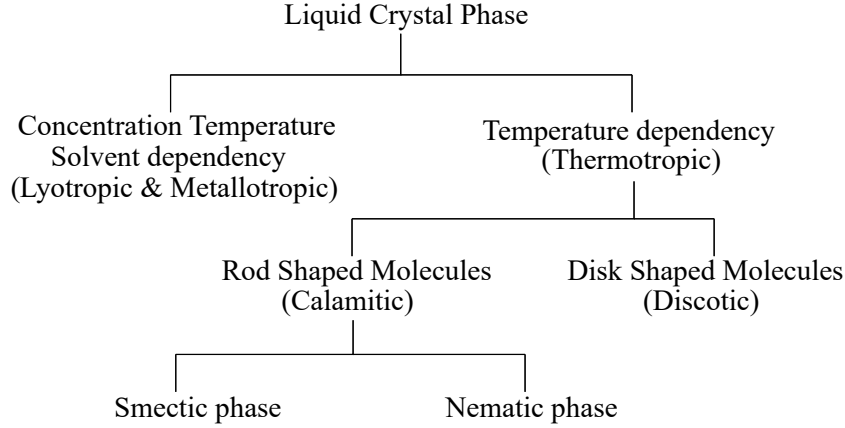


Figure 2.2: Schematic relationship of different types of LC and LC phases.

In this work, all the LC mixtures used for microwave applications are thermotropic calamitic nematic LCs. A schematic which summarizes the different types of LC is provided in Fig. 2.2.

## 2.1 Nematic Liquid Crystal

One of the most common LC phases is the nematic phase, it is discussed in detail in this section. Nematic LCs have been most widely used in both, LCDs and microwave applications. The fundamental properties of nematic LCs as well as their macroscopic characters versus temperature are shown in Fig. 2.3. In nematic phase, the rod-shaped molecules have no positional order, but they self-align to have long-range directional order with their long axes roughly parallel on average [Reg+09]. Thus, the molecules are free to flow and their centers of mass position are randomly distributed as in a liquid, but still maintain their long-range directional order, as shown in Fig. 2.3 C. This means the nematic phase is uniaxial. This axis of uniaxial symmetry has no polarity: although the constituent molecules may be polar, there is no imposed effect on a larger scale. Therefore, it proves convenient to introduce a vector  $\vec{n}$ , called the director, to describe the local direction of the average molecular alignment in LC, as shown in Fig. 2.4.

LC exhibits an anisotropy in the crystalline as well as in the nematic phase, whereas only the nematic phase can be used for electrically tunable RF circuits/devices. The phase transitions occur at certain temperatures, where the liquid crystalline mesophase is defined thermodynamically stable between the melting point of the crystalline phase and the clearing point to the isotropic liquid phase. Both phase transitions at melting and clearing points are of first order, exhibiting a latent heat as well as a discontinuous change in density.

A single LC molecule inside a unit volume with averaged director of  $\vec{n}$  can be represented by a unit vector  $\vec{a}$ , see Fig. 2.4. The orientation order of  $\vec{a}$  follows a distribution function  $f(\theta, \phi)$ , e.g.,  $f(\theta, \phi) = \text{constant}$  in the isotropic phase represents  $\vec{a}$  having equal probability of pointing in any direction. For nematic phase with uniaxial LCs,  $f(\theta, \phi)$  is simplified to

## 2 Fundamentals of Liquid Crystal (LC)

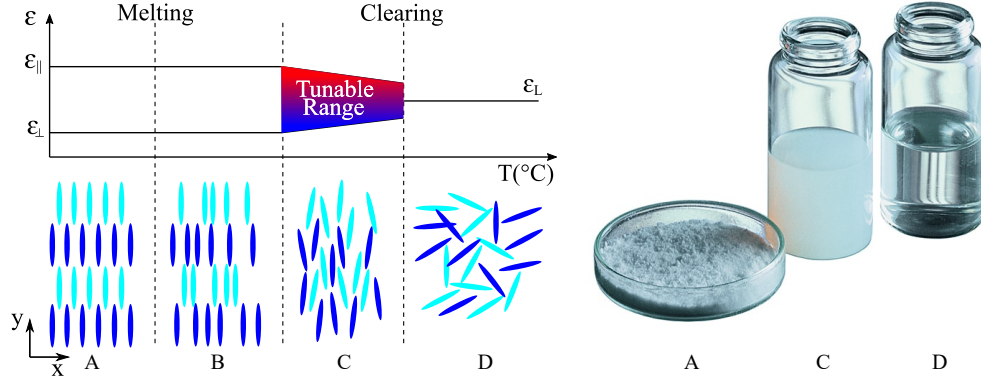


Figure 2.3: Phase variation of thermotropic calamitic LC regarding temperature. A: ordinary crystals. B: anisotropic smectic LC. C: anisotropic nematic LC. D: isotropic liquid.

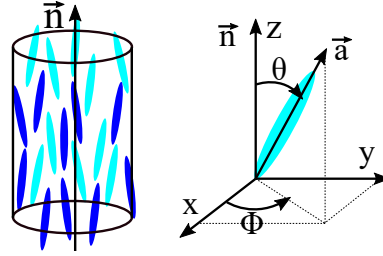


Figure 2.4: Schematic diagram showing the macroscopic (left) and microscopic (right) orientation of calamitic LC with rod-like molecules in nematic phase.

$f(\theta)$ . Thus, the averaged value of projection of  $\vec{a}$  along  $\vec{n}$  is [YW06],

$$\overline{\cos \theta} = \frac{\int_0^\pi \cos \theta f(\theta) \sin \theta d\theta}{\int_0^\pi f(\theta) \sin \theta d\theta}, \quad (2.1)$$

where the overline indicates the average and  $\cos \theta$  is the first-order Legendre polynomial. In the isotropic phase, LC molecules are randomly oriented and  $\overline{\cos \theta} = 0$ . In the nematic phase, the probability of a molecule orienting at angle  $\theta$  and  $\pi - \theta$  is the same, i.e.  $f(\theta) = f(\pi - \theta)$ , since  $\vec{n}$  and  $-\vec{n}$  are equivalent. Therefore,  $\overline{\cos \theta} = 0$ , and so  $\overline{\cos \theta}$  provides no information of the orientational order parameter.

Next, consider the average value of the second-order Legendre polynomial for the orientational order parameter  $S$  [YW06],

$$S = \overline{P_2(\cos \theta)} = \frac{1}{2} \overline{(3 \cos^2 \theta - 1)} = \frac{\int_0^\pi \frac{1}{2} (3 \cos^2 \theta - 1) f(\theta) \sin \theta d\theta}{\int_0^\pi f(\theta) \sin \theta d\theta}. \quad (2.2)$$

In the isotropic phase with  $f(\theta) = \text{constant}$ ,  $S = 0$ . In a perfectly ordered nematic phase where  $\vec{a}$  of every molecule aligns with  $\vec{n}$  as in crystalline phase,  $f(\theta) = \delta(\theta)$ .  $\delta(\theta)$  is the Dirac function and  $\delta(\theta) = \infty$  when  $\theta = 0$ , and  $S$  is calculated to be 1. In the intermediate



nematic phases, the order parameter is in the range of 0 to 1 depending on the temperature. To calculate  $S$  in the nematic phase,  $f(\theta)$  can be described in details by using *Maier-Saupe* or *Landau-de Gennes* theory [YW06]. The first considers the temperature dependency of  $S$  and the distribution function is determined by the Boltzmann distribution. The second accounts additional effects and enables to fit the respective function to a measurement by use of additional parameters [Kar14]. This work focuses on the applications of LC materials in microwave engineering without further discussion on LC from material science aspect.

## 2.2 Magnetic and Electric Properties

The anisotropic property of nematic liquid crystal is reflected in both its magnetic susceptibility and dielectric permittivity. The application of an electric field  $\vec{E}$  to an LC sample produces a dipole moment per unit volume called the polarization, denoted by  $\vec{P}$ . The anisotropy of the LC generally forces  $\vec{E}$  and  $\vec{P}$  to have different directions, which is related by the electric susceptibility tensor  $\chi_e$  via the equation [Ste04]:

$$\vec{P} = \varepsilon_0 \chi_e \vec{E} \quad \chi_e = \begin{pmatrix} \chi_{e\perp} & 0 & 0 \\ 0 & \chi_{e\perp} & 0 \\ 0 & 0 & \chi_{e\parallel} \end{pmatrix}, \quad (2.3)$$

where  $\varepsilon_0$  is the permittivity of free space.  $\chi_{e\perp}$  and  $\chi_{e\parallel}$  denote the electric susceptibilities perpendicular and parallel to the director  $\vec{n}$ , respectively. The electric displacement  $\vec{D}$  induced by  $\vec{E}$  and  $\vec{P}$  is defined by

$$\vec{D} = \varepsilon_0 \vec{E} + \vec{P} = \varepsilon_0 \vec{\varepsilon} \vec{E}, \quad \vec{\varepsilon} = \mathbf{I} + \chi_e, \quad (2.4)$$

where  $\mathbf{I}$  is the identity tensor and  $\vec{\varepsilon}$  is called the dielectric tensor, which can be written as [Ste04]

$$\vec{\varepsilon} = \begin{pmatrix} \varepsilon_{\perp} & 0 & 0 \\ 0 & \varepsilon_{\perp} & 0 \\ 0 & 0 & \varepsilon_{\parallel} \end{pmatrix}, \quad \varepsilon_{\perp} = 1 + \chi_{e\perp}, \quad \varepsilon_{\parallel} = 1 + \chi_{e\parallel}, \quad (2.5)$$

The coefficients  $\varepsilon_{\perp}$  and  $\varepsilon_{\parallel}$  denote the relative dielectric constants of the LC when the field and  $\vec{n}$  are perpendicular and parallel, respectively. With respect to  $\vec{n}$ , Eq. (2.4) is equivalent to

$$\vec{D} = \varepsilon_0 \varepsilon_{\perp} \vec{E} + \varepsilon_0 \Delta\varepsilon (\vec{n}_0 \cdot \vec{E}) \vec{n}_0, \quad \Delta\varepsilon = \varepsilon_{\parallel} - \varepsilon_{\perp}, \quad (2.6)$$

where  $\vec{n}_0$  is the unit vector of the director, and  $\Delta\varepsilon$  is called the dielectric anisotropy of the LC. Values for  $\Delta\varepsilon$  can be negative or positive, depending on the features of each individual LC. When  $\Delta\varepsilon > 0$ , the director is attracted to be parallel to the field and when  $\Delta\varepsilon < 0$ , perpendicular [Ste04].

The total electric energy density  $W_{\text{elec}}$  when a quasi-electrostatic field is applied is given by [Ste04]

$$W_{\text{elec}} = -\frac{1}{2} \vec{D} \cdot \vec{E} = -\frac{1}{2} \varepsilon_0 \varepsilon_{\perp} E^2 - \frac{1}{2} \varepsilon_0 \Delta\varepsilon (\vec{n}_0 \cdot \vec{E})^2. \quad (2.7)$$

## 2 Fundamentals of Liquid Crystal (LC)

Considering the term  $-\frac{1}{2}\epsilon_0\epsilon_{\perp}E^2$  is independent of  $\vec{n}$ , when  $\Delta\epsilon > 0$ , the last term is minimized when  $\vec{n}$  and  $\vec{E}$  are parallel; when  $\Delta\epsilon < 0$ , the last term is minimized when  $\vec{n}$  and  $\vec{E}$  are perpendicular, such that a stable equilibrium of the LC orientation is achieved under the  $\vec{E}$ . Therefore, an external quasi-electrostatic  $\vec{E}$  can be used to manipulate the orientation of LC [Ste04].

Similarly, the application of a magnetic field  $\vec{H}$  across an LC sample induces a magnetisation  $\vec{M}$  in the LC due to the magnetic dipole moments imposed upon the molecular alignment by the magnetic field.

$$\vec{M} = \chi_m \vec{H} = \chi_{m\perp} \vec{H} + (\chi_{m\parallel} - \chi_{m\perp})(\vec{n} \cdot \vec{H})\vec{n} \quad (2.8)$$

The magnetic induction  $\vec{B}$  which plays a similar role as electric displacement  $\vec{D}$  is defined by [Ste04]

$$\vec{B} = \mu_0(\vec{H} + \vec{M}) = \mu_0\mu_{\perp}\vec{H} + \mu_0\Delta\chi(\vec{n} \cdot \vec{H})\vec{n}, \quad (2.9)$$

where  $\mu_0$  is the permeability in vacuum, and

$$\mu_{\perp} = 1 + \chi_{m\perp}, \quad \mu_{\parallel} = 1 + \chi_{m\parallel}, \quad \Delta\chi = \chi_{m\parallel} - \chi_{m\perp} = \mu_{\parallel} - \mu_{\perp} \quad (2.10)$$

The quantity  $\Delta\chi$  is the magnetic anisotropy and is generally positive. The magnetic energy density is given by

$$W_{mag} = -\frac{1}{2}\vec{B} \cdot \vec{H} = -\frac{1}{2}\mu_0\mu_{\perp}H^2 - \frac{1}{2}\mu_0\Delta\chi(\vec{n} \cdot \vec{H})^2, \quad (2.11)$$

and it is clear that the magnetic energy is minimized when  $\vec{n}$  and  $\vec{H}$  are parallel, such that the orientation of LC molecules can also be manipulated by magnetic field [Ste04].

### 2.3 Alignment and Biasing Schemes

To utilize the anisotropic dielectric characteristic of the nematic LCs in an tunable microwave device, the direction of  $\vec{n}$  has to be controlled to exploit the LC material as a tunable dielectric. Possible methods to align the LC molecules are described in this section.

#### Alignment by Surface Anchoring

In most planar LC devices, LCs are sandwiched between two substrates, such as glasses, which are coated with very thin alignment layers. Without external fields, the orientation of the LC molecules is determined by the anchoring forces of the alignment layer [YW06]. Surface anchoring of LC molecules can be already achieved by mechanically rubbing the surface of the substrate, where micro-grooves along the rubbing direction are created to anchor the LC molecules. However, the anchoring force is weak. Therefore, rubbed polyimide is widely used for alignment layer[YW06].

In this work, polyimide films made of Nylon6 are spin coated on the carrier substrate, specially processed and mechanically rubbed in a preferred direction, using a rotating pillar covered by velvet cloth. By this, grooves of only several nanometer wide and thick are

produced on the surface. LC molecules next to this surface will align parallel to these grooves due to the surface anchoring force provided by the grooves. By the elastic force between adjacent LC molecules, LC molecules tend to align parallel to each other, which results in the complete volume aligning parallel to the grooves, as shown in Fig. 2.5. Homeotropic anchoring can be achieved by using monolayer surfactants such as lecithin and silane. The polar head of the surfactant is chemically attached to the substrate and the hydrocarbon tail points out and perpendicular to the surface. The intermolecular interaction between the surfactant and the LC promotes the homeotropic alignment, refer to [YW06]. Whereas, in this work, only the first surface anchoring method is utilized.

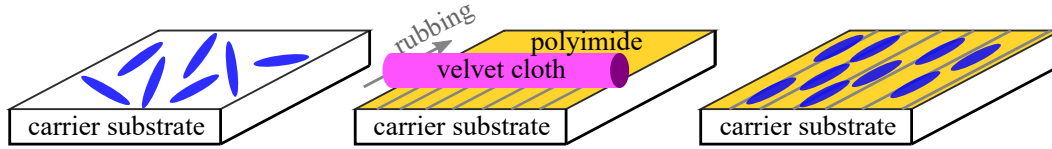


Figure 2.5: Schematic of the alignment layer fabrication process. The polyimide film is spin coated to the substrate and rubbed in a preferred direction using a velvet cloth. By this, nanometer grooves are applied to the polyimide layer, which provides anchoring force to align the LC molecules parallel to these grooves.

#### Alignment by Electric Field

As described in Section 2.2, for LC with positive dielectric anisotropies, the directors tend to align parallel to the electric field lines. For simplicity, assuming an ideal parallel plate capacitor with inner side of both plates covered with alignment layer, and filled with LC as in Fig. 2.6, a bias voltage  $V_B$  is introduced to the capacitor and generates an electric bias field inside which is perpendicular to the alignment grooves' orientation. When  $V_B = 0$ , LC molecules align parallel to the plate due to surface anchoring. When the threshold voltage  $V_{TH}$  is exceeded, LC starts to align along the bias field lines.  $V_{TH}$  is known as the Freedericksz threshold voltage, which defines the voltage where the electric and elastic force of the surface anchoring are in an equilibrium. If the electric force is further increased with higher bias voltage, the electric torques are exceeding the elastic ones and LC starts aligning parallel to the field lines. The dielectric response of LC to DC and AC electric field is theoretically the same, except that the  $\epsilon_{r,LC}$  is frequency dependent [YW06].

#### Alignment by Magnetic Field

Similarly to the electrical bias, as discussed in Section 2.2, LC directors tend to align parallel to the external magnetic field lines to minimize the total free energy. Usually, two rare-earth magnets are placed as parallel plates around the LC cavity. There is evidence indicating that magnetic bias is slightly more efficient than electric bias in terms of utilizing the full range of LC's anisotropy [dJ95]. However, magnetic bias method is up to now only used in the lab for a fast proof-of-concept of particular devices, or characterizing of LC properties. For practical applications it is not feasible, since the reorientation of the magnets would require

## 2 Fundamentals of Liquid Crystal (LC)

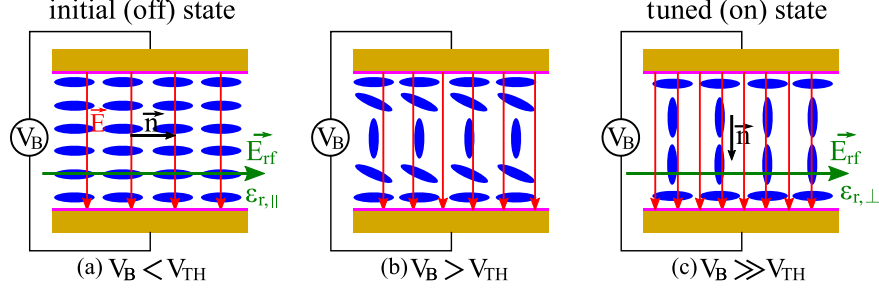


Figure 2.6: Schematic of a simplified electric bias network based on an ideal parallel plate capacitor (the inner sides of the plates covered with alignment layer) filled with LC. The threshold voltage  $V_{TH}$  needs to be exceeded before the LC molecules start aligning parallel to the bias electric field lines.  $\vec{n}$  is the director representing the macroscopic orientation of LC molecules in the volume. In (a), microwave electric field  $\vec{E}_{rf}$  is parallel to  $\vec{n}$ , thus the microwave signal experiences an LC's relative permittivity of  $\epsilon_{r,\parallel}$ . In (c),  $\vec{E}_{rf}$  is perpendicular to  $\vec{n}$ , signal experiences LC's relative permittivity of  $\epsilon_{r,\perp}$ . (b) is the intermediate state where  $\epsilon_{r,\perp} < \epsilon_r < \epsilon_{r,\parallel}$ .

a mechanical adjustment. The magnets bias system is bulky and is not applicable, especially in printed planar devices. Alternatively, electromagnets can be used with the expense of high power consumption.

By properly applying the three alignment mechanisms, LC orientation in microwave components can be tuned accordingly. Thus, the electromagnetic wave propagating through the LC region experiences tunable permittivity, which results in variation of the performance of the component: when the polarization of the electromagnetic wave is parallel to director  $\vec{n}$  as in Fig. 2.6 (a), LC demonstrates a relative dielectric constant of  $\epsilon_{r,\parallel}$  with dissipation factor of  $\tan\delta_{\parallel}$ ; when perpendicular, LC demonstrates  $\epsilon_{r,\perp}$  and  $\tan\delta_{\perp}$ . In practical applications, different orientation mechanisms are combined according to Table 2.7 [Mau+18].

For example, the combination of surface anchoring and electric bias concepts are most widely applied, as in LCD technology. Planar tunable microwave components, such as those based on microstrip line (MSL), co-planar waveguide stripline (CPW) and coupled line topology, utilize the 'Electric-Surface' combination due to their similar structure as LCD, see Fig. 2.6. Without the bias electric field  $\vec{E}$  or when  $\vec{E}$  is small, the director  $\vec{n}$  is aligned to the inner surface of the panel coated with polyimide in initial state. When applying bias field  $\vec{E}$  higher than the threshold  $\vec{E}_{TH}$ , electrical rotating force overcomes the surface anchoring. Thus,  $\vec{n}$  changes its orientation towards tuned state. Once bias field disappears,  $\vec{n}$  recovers initial state gradually under the permanent surface anchoring. This mechanism is preferred in planar devices, since LC layer is usually made to be several  $\mu\text{m}$  thick, such that only one set of bias electrode is required in the LC thickness direction, and a moderate  $V_B$  is required to fully bias the LC. One limitation of the planar devices is that the force of the surface anchoring is weak compared to electrical force. Hence, the tuning time from on-

		Tuned Alignment		
		Magnetic	Electric	Surface
Initial Alignment	Magnetic	Characterization only	Not used	Not used
	Electric	Not used	Waveguide device	Planar device
	Surface	Not used	Planar device	Not tunable

Figure 2.7: Summary of combinations of different alignment mechanisms and their applicability in tunable microwave components. ‘Not tunable’ denotes the static state of LC due to the constant alignment force provided by the surfaces; ‘Not used’ denotes the combinations that can be used in principle but are not used in practice.

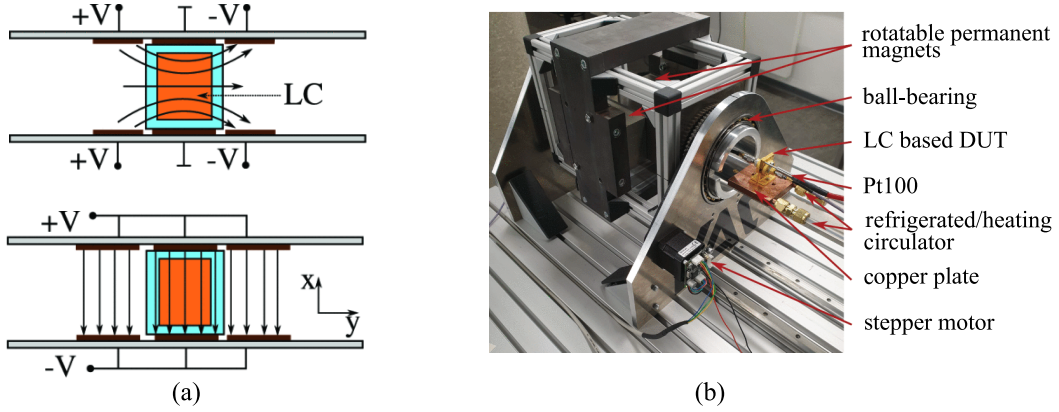


Figure 2.8: (a) Pure electrical bias concept. Electrodes in horizontal direction are arranged on the same layer as vertical electrodes to generate quasi-horizontal bias field on the left side [Pol+19b]. (b) Magnetic bias concept by rotating permanent magnets for LC characterization [Pol+19a].

to off-state, namely  $\tau_{\text{off}}$ , which represents the aforementioned time from releasing the bias to recovering the initial state, is dependent on the sheet thickness, and is much longer than that from off- to on-state, i.e.  $\tau_{\text{on}}$ .  $\tau_{\text{on}}$  and  $\tau_{\text{off}}$  can be calculated as [Ste04]:

$$\tau_{\text{on}} \approx \frac{\gamma_r h_{\text{LC}}^2}{K_{ii} \pi^2 (V_B^2 / V_{\text{Th}}^2 - 1)}, \quad \tau_{\text{off}} \approx \frac{\gamma_r h_{\text{LC}}^2}{K_{ii} \pi^2} \quad (2.12)$$

where  $\gamma_r$  and  $K_{ii}$  represent the rotational viscosity and elastic constant, respectively. According to published works,  $\tau_{\text{off}} > 100 \text{ ms}$  is normally achievable for planar tunable mmW components based on LC. However, it is still regarded as not enough for agile response applications. In this work,  $\tau_{\text{off}} \approx 40 \text{ ms}$  is achieved as a result of both extremely

## 2 Fundamentals of Liquid Crystal (LC)

low  $h_{LC}$  and well-processed alignment layer on both side of the LC cavity. This will be explained in detail in chapter 3.

For volumetric waveguide-based components, surface anchoring mechanism leads to extremely long  $\tau_{off}$  (usually of minute level). Thus, solely electrical bias concept is preferred, e.g., by utilizing multiple electrodes to generate spatially quasi-perpendicular fields, as shown in Fig. 2.8 (a). By switching bias supply between the electrodes, fast LC tuning is realized. It is possible to rotate a pair of magnets around the structure to produce a variable alignment, compare Fig. 2.8 (b). Obviously, both methods require complex bias systems, which are not suitable for modern portable or mobile communication due to space and power consumption. Especially the latter, where bulky permanent magnets and a rotatory platform are required. This work focuses only on planar microwave components combining surface anchoring and electrical bias.

### 2.4 Liquid Crystal in Microwave Engineering

Well-known LC K15(5CB) as a benchmark from display industry was first applied into tunable microwave components in the 90's [Dol+93] and early 2000's [WLJ02]. Other LCs used in optics such as E7 and BL006 [LML93; Kuk+02] have also been widely used in many studies on microwave applications. Experiments in this early development phase were carried out mostly with electrically tunable liquid crystal (LC)-based phase shifters by using the inverted microstrip line (IMSL) topology, achieving, however, only a figure-of-merit (FoM)  $<20^\circ/\text{dB}$  for X- and Ka-band [Dol+93; Kuk+02; WLJ02] with these LCs from optics. A breakthrough in FoM could be achieved with  $110^\circ/\text{dB}$  at 24 GHz for IMSL phase shifter by consciously using for the first time, new, specifically synthesized LC mixtures for microwaves in the framework of a beginning close cooperation of Merck and TU Darmstadt [Wei+03]. These new microwave LCs from Merck KGaA, for example MDA-03-2844, GT3-23001, TUD-566, GT5-26001 and GT7-29001 exhibit a long conjugation body with biphenyl or terphenyl structure, aiming at higher anisotropy, tunability, and FoM of the materials, see [JGW20; Fer+22]. The anisotropy and tunability in relative dielectric constant, as well as the material's FoM, are defined as [JGW20]:

$$\begin{aligned}\Delta\varepsilon &= \varepsilon_{r,\parallel} - \varepsilon_{r,\perp}, \\ \tau_{LC} &= \frac{\Delta\varepsilon}{\varepsilon_{r,\parallel}}, \\ \eta_{LC} &= \frac{\tau_{LC}}{\tan\delta_{\max}}\end{aligned}\tag{2.13}$$

The elastic and dielectric properties of the aforementioned LC mixtures are resumed in Table 2.1. The values of the parameters in Table 2.1 might differ slightly from literature to literature, mainly due to different characterization techniques, accuracy of equipment and fabricated samples, as well as environmental uncertainties such as humidity and temperature. It is clear that microwave LCs, i.e., GT-series and TUD-566, have higher tunability and less power dissipation than optical LCs. Among these microwave LCs, GT5

series and TUD-566 demonstrate the highest  $\eta_{LC}$  values that have ever been reported, however, their response time are much longer than the other LCs mainly due to high viscosity  $\gamma_r$  according to Eq. (2.12). Although numerous microwave LCs have been reported worldwide (a comprehensive summary can be found in [ZFB19]), only GT-series LCs are utilized in this work, particularly GT7-29001 with the highest tunability and lowest response time in the GT-series.

Table 2.1: Material properties of different LC mixtures at room temperature. Elastic constant  $K_{ii}$  in Eq. (2.12) is given here only in terms of splay deformation.  $\Delta\epsilon_{1 \text{ kHz}}$  is the anisotropy at low frequency, typically at 1 kHz. Microwave parameters are measured at 19 GHz [JGW20; Mau+18].

LC	$\epsilon_{r,\perp}$	$\tan \delta_{\perp}$	$\epsilon_{r,\parallel}$	$\tan \delta_{\parallel}$	$\Delta\epsilon$	$\tau_{LC}$ (%)	$\eta_{LC}$	$K_{11}$ (pN)	$\gamma_r$ (pN · S)	$\Delta\epsilon_{1 \text{ kHz}}$
K15(5CB)	2.7	0.0273	3.1	0.0132	0.4	12.9	4.7	7.0	0.126	14.4
E7	2.53	0.022	2.98	0.009	0.45	15.1	6.86	10.8	0.254	14.3
BL006	2.58	0.0191	3.16	0.0069	0.58	18.4	9.6	16.0	0.569	17.1
BL111	2.64	0.0218	3.25	0.0084	0.61	18.8	8.6	/	/	16.5
GT3-23001	2.41	0.0141	3.18	0.0037	0.77	24.2	17.2	24	0.727	4.0
GT5-26001	2.39	0.007	3.27	0.0022	0.88	26.9	38.4	12.0	1.958	1.0
GT5-28004	2.40	0.0043	3.32	0.0014	0.92	27.7	64.4	11.8	5.953	0.8
TUD-566	2.41	0.006	3.34	0.0027	0.93	27.8	46.4	13.0	2.100	1.0
GT7-29001	2.46	0.0116	3.53	0.0064	1.07	30.3	26.1	14.5	0.307	22.1

One of the advantages of LCs compared to other technologies such as semiconductors or Barium Strontium Titanate (BST) is their decreasing dielectric loss with increasing frequency generally from 15 GHz to 1.5 THz. This has been observed using a time domain spectroscopy (TDS) THz measurement system as reported in [Wei+13]. Besides, LC characterization has also been performed using transmission line method in a broadband, such as using MSL [Bul+10b], CPW [Hin05] and coaxial line [Mue+05], since transverse electromagnetic (TEM) mode or quasi-TEM (QTEM) mode can be easily generated in these TL topologies. While the characterized relative dielectric constant  $\epsilon_r$  is relatively accurate, the dissipation factor  $\tan\delta$  has higher uncertainty, mainly due to metallic loss.

Except for the aforementioned broadband characterization methods, narrow-band resonant material characterization methods e.g., the cavity perturbation method (CPM) can be used to obtain very accurate results on  $\epsilon_r$  and  $\tan\delta$  of the material under test (MuT), i.e., LC. A waveguide cavity resonator is reported in characterizing GT3-23001 at 60 GHz in [Pol+19a], and a patch resonator is used to characterize E7 at 38 GHz in [Yaz+10]. With these works, LC is proven to be a well-suitable dielectric material for the realization of continuously tunable devices in the microwave range. Detailed overview over all characterization methods are given in [ZFB19; JGW20; Fer+22]. This work only focuses on realizing such devices with novel design and improved performance than other state-of-the-art works in lower millimeter wave range.





### 3 Liquid Crystal-based Microstrip Delay Line Phase Shifters

Being a part of a reconfigurable microwave device or system, the phase shifter is a key component to provide tunability and to realize reconfigurability. As its name implies, a phase shifter is used to change the transmission phase angle of an input signal. Ideally, phase shifters provide an output signal with an equal amplitude to the input signal. Any loss here will be accounted to as insertion loss (IL) of the component. However, the phase of a single tone is meaningless until it is compared to another one or many. The interference or combination of these correlated signals with adjustable relative phase shifts can be very useful, such as in phased arrays and single-pole double-throw (SPDT) switches in chapter 4. This chapter focuses on the development of phase shifters based on microwave LC technology.

There are three main types of phase shifters: mechanical phase shifters, which control the phase shift manually by changing the physical length of a transmission line; digital phase shifters, which provide discrete phase shift in terms of bit numbers typically controlled by bias voltage; and analog phase shifters, whose phase shifts are also controlled by bias voltage, meaning that continuous tuning of the voltage results in a continuous change of the phase shift.

LC is mostly combined with microwave transmission lines to produce delay line phase shifters, although few reflection type phase shifters based on LC are reported [Fri+12; Fri15; Bul+10a; Deo+13]. The principle of this kind of phase shifter is simple. By utilizing anisotropic LC as the dielectric material, the electrical length of the delay line can be varied by tuning the LC permittivity. In this chapter, LC delay line phase shifters are realized in microstrip line (MSL) topology. In the first section, transmission line theory is briefly introduced with the help of an equivalent circuit, based on which the slow-wave (SW) effect is also studied, which is the premise of high-performance phase shifters. In the second section, the inverted microstrip line (IMSL) topology is introduced as the conventional way to combine with microwave LC technology to form a basic delay line type phase shifter. The major drawbacks of IMSL are then indicated. To overcome these drawbacks, three types of modified LC-based IMSL phase shifters are introduced in the third, fourth and fifth section, respectively. They include special structures such that a significant slow wave effect is generated to achieve enhanced LC tuning efficiency, low insertion loss, high compactness and fast response. The phase shifters in section 3.4 and 3.5 set new benchmarks to planar LC-based phase shifters, and indicate promising prospect of utilizing MSL-based LC phase shifter in reconfigurable mmW applications.

### 3.1 Transmission Line Theory and Slow Wave Effect

As an electromagnetic wave of a particular frequency range, microwaves propagate with the speed of light, which is a constant velocity of  $c_0 = 299\,792\,458$  m/s in vacuum. Before sent into free space by antennas, microwaves are guided by transmission lines in circuits or components for modulation. Their phase velocities  $v_\phi$  are reduced in comparison to  $c_0$  due to the dielectrics and loaded structures used to constitute the transmission lines. Compared to electric circuits where the network dimensions are much smaller than the guided wavelength, microwave transmission lines have the dimensions of a fraction of or several guided wavelengths. Therefore, transmission lines are distributed networks, since the phases and amplitudes of the guided voltage and current vary within the whole length.

#### Transmission Line Theory

As one of the most important concepts of microwave engineering, the transmission line model was developed by Oliver Heaviside together with the telegrapher's equations from 1876 based on a transmission line consisting of two conductors on which a TEM wave propagates. In this model, transmission lines are assumed to be composed of an infinite series of two-port elementary components, which are called the distributed components, each representing an infinitesimally short segment of the transmission line, as shown in Fig. 3.1.

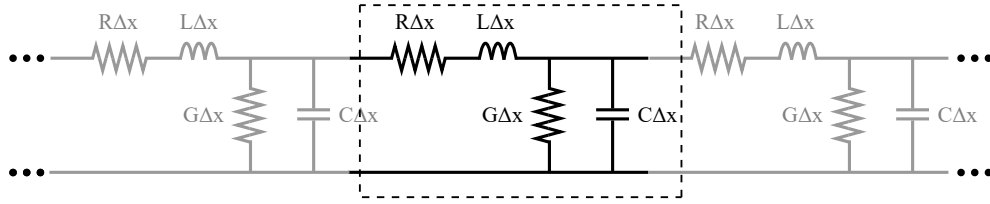


Figure 3.1: Schematic representation of the elementary components of a transmission line.

In the model, the inductance  $L$  is the series inductance of the unit length conductors, and the capacitance  $C$  is the capacitance between the two conductors. The resistance  $R$  represents the ohmic loss generated by the conductors of the line with finite conductivity, while the conductance  $G$  represents the dielectric loss caused by the dielectric materials. The telegrapher's equations are linear partial differential equations that describe the voltage and current on the lossy transmission line in relation to distance and time:

$$\begin{aligned} \frac{\partial V(x, t)}{\partial x} &= -L \frac{\partial I(x, t)}{\partial t} - RI(x, t), \\ \frac{\partial I(x, t)}{\partial x} &= -C \frac{\partial V(x, t)}{\partial t} - GV(x, t). \end{aligned} \quad (3.1)$$

Based on the transmission line model and the telegrapher's equations, the characteristic impedance  $Z_C$  which represents the ratio of the amplitudes of voltage and current of a single wave propagating along the line, the propagation constant  $\gamma$  which measures the change

undergone by the amplitude and phase of the wave as it propagates in a given direction, as well as the  $v_\phi$  which indicates the propagation speed of a wave in a medium, are given in Eq. (3.2):

$$\begin{aligned} Z_C &= \sqrt{\frac{R + j\omega L}{G + j\omega C}} \\ \gamma &= \sqrt{(R + j\omega L)(G + j\omega C)} \\ v_\phi &= 1/\sqrt{(R + j\omega L)(G + j\omega C)} \end{aligned} \quad (3.2)$$

In reality, the ohmic loss on the MSL is minimized by using highly conductive metal such as gold with a thickness much higher than the skin depth of the operating frequency; the dielectric loss is minimized by using low dissipative dielectric material. Thus, we assume an ideal lossless transmission line case where  $R$  and  $G$  are omitted to simplify the analysis. Hence, Eq. (3.2) is simplified to:

$$\begin{aligned} Z_C &= \sqrt{\frac{L}{C}} \\ \gamma &= j\omega\sqrt{L \cdot C} \\ v_\phi &= -j/\omega\sqrt{L \cdot C} \end{aligned} \quad (3.3)$$

These are the most important results derived from the well-known telegrapher's equations, which will be used to explain the circuit design in the following sections and chapters.

#### Slow Wave Effect

In microwave engineering, there are large amounts of applications requiring transmission lines with defined electrical length of a certain number of wavelength ( $\lambda$ ) at the targeted frequency, especially in passive components, such as a  $\lambda/4$  transmission line segment for impedance transformer and in branches of a 3-dB quadrature coupler. The size of such  $\lambda$ -based components might become a serious problem, especially in low microwave range, e.g., sub-6 GHz bands for 5G applications, where  $\lambda_0 > 50$  mm. Such large dimension is not always affordable, especially in mobile and portable devices, thus, highly miniaturized circuit design is desired. Meandering of transmission line consumes less space but maintains the IL, since IL is related to the physical length. Although by utilizing dielectric materials of high relative dielectric constant  $\epsilon_r$ , the length of a MSL, which is correlated to  $1/\sqrt{\epsilon_r}$ , can be reduced. The MSL width is also getting smaller to maintain a constant  $Z_0$  on MSL.

This section focuses on planar slow-wave transmission lines by loading artificially constructed sub-wavelength structures to produce miniaturized MSL with low insertion loss. In the early 20th century, Cunningham et al. constructed an artificial transmission line with very slow  $v_\phi$  through a periodic cascade of lumped cell networks [Cun11], which is regarded as the origin of the slow wave concept. In the 1940s, the helix-based traveling wave tube amplifier was proposed, which marked the introduction of slow-wave structure into

### 3 Liquid Crystal-based Microstrip Delay Line Phase Shifters

microwave engineering [Kom47], where the amplifier reduces the  $v_\phi$  of electromagnetic wave by controlling the pitch of helix. Since then, the planar slow-wave transmission line has been developed rapidly because of its simple processing, low cost, high efficiency and small size employing multi-layer media [KO92], periodically loaded capacitors (inductors or stubs) [GJZ16], cascaded cells [HCY12], and defected ground structure [Lim+02a]. The common feature of these planar slow-wave structures is that they consist of electrically small segments with alternating higher and lower impedance than the terminal load  $Z_L$ , as depicted in Fig. 3.2.



Figure 3.2: Artificial transmission line consisting of electrically small segments with alternantly high ( $Z_{01}$ ) and low ( $Z_{02}$ ) impedance in a  $Z_L$  system.

Derived from the telegrapher's equation Eq. (3.1), the input impedance  $Z_{\text{input}}$  of a lossless transmission line with impedance  $Z_0$  and length  $l$  loaded with impedance  $Z_L$  is:

$$Z_{\text{input}} = Z_0 \frac{Z_L + jZ_0 \tan(2\pi l/\lambda)}{Z_0 + jZ_L \tan(2\pi l/\lambda)}. \quad (3.4)$$

When  $Z_L \ll Z_0$  and  $l \ll \lambda$  for an electrically small segment, Eq. (3.4) can be written as

$$Z_{\text{input}} = Z_L + jZ_0 \tan(2\pi l/\lambda) \approx Z_L + j\omega L_0 l \quad (3.5)$$

Similarly, when  $Z_L \gg Z_0$  and  $l \ll \lambda$ , Eq. (3.4) is simplified to

$$Y_{\text{input}} = \frac{1}{Z_L} + \frac{j}{Z_0} \tan(2\pi l/\lambda) \approx \frac{1}{Z_L} + j\omega C_0 l \quad (3.6)$$

From Eq. (3.5) and (3.6), when  $Z_0 \gg Z_L$ , the high impedance transmission line segment terminated by  $Z_L$  equals to an extra serial inductor  $L_0 l$ . When  $Z_0 \ll Z_L$ , the low impedance transmission line segment terminated by  $Z_L$  equals to an extra shunt capacitor  $C_0 l$ , as shown in Fig. 3.3. According to Eq. (3.3),  $Z_C$  of transmission line with increased  $L$  and  $C$  can be kept unchanged by proper design such that  $L$  and  $C$  increase by the same factor and  $v_\phi$  is reduced.

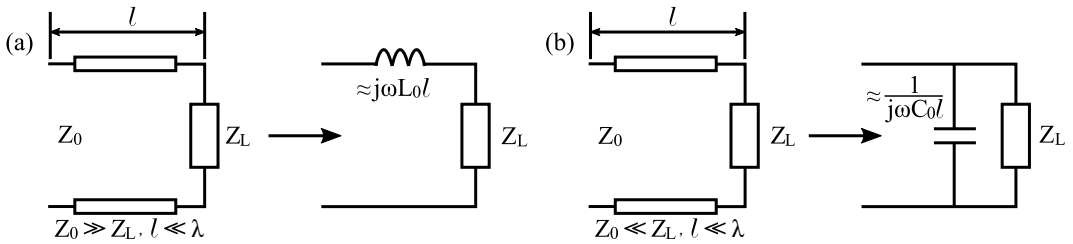


Figure 3.3: Simplified equivalent circuits of electrically small transmission line segments.

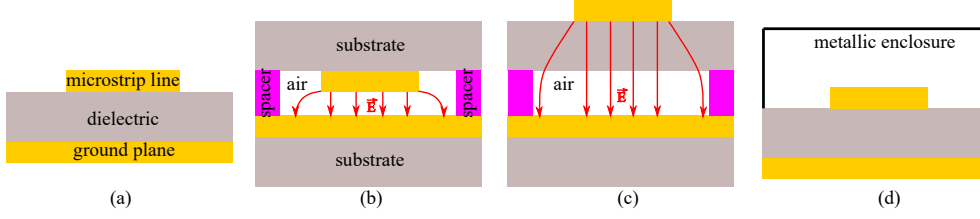


Figure 3.4: MSL and its variants. (a) Basic MSL based on solid dielectric substrate. (b) Inverted microstrip line (IMSL), the ground plane and MSL lie on different substrates facing each other. They are separated by air dielectric and can be filled with gaseous or fluid dielectric with thickness defined by the height of the spacer. (c) Suspended MSL. It is reciprocal to IMSL. MSL and ground plane lie opposite to each other. (d) The shielded MSL is similar to basic MSL except the enclosure. The metallic enclosure covers the entire structure and hence reduce the EMI (electromagnetic interference) due to shielding.

### 3.2 Inverted Microstrip Line (IMSL) Phase Shifter

The MSL is the most popular structure used for RF design and product development due to easy fabrication, planar structure and complete exposure for troubleshooting. The disadvantages compared with waveguides are the lower power-handling capacity, higher loss as well as susceptibility to cross-talk and unintentional radiation. A traditional MSL consists of an electrode, a solid dielectric substrate and a ground plane as demonstrated in Fig. 3.4 (a). Beside the conventional MSL, some important MSL variants are being widely used, e.g. IMSL, suspended MSL and shielded MSL, according to Fig. 3.4 (b)-(d). MSL is compatible and can be integrated with other planar transmission lines, e.g., stripline, CPW, co-planar stripline, substrate integrated waveguide (SIW), etc. Although the MSL evolves from a parallel double line, the inclusion of a dielectric between the two conductors leads to an inhomogeneous medium distribution and brings about hybrid modes of which both  $\vec{E}$  and  $\vec{H}$  fields have longitudinal components. Therefore, the MSL does not support a true TEM wave. However, the longitudinal components are small, so the dominant mode is referred to as quasi-TEM (QTEM). Hence, transmission line model and derivations given in section based on TEM wave assumption are applicable.

Basic MSL and shielded MSL can only be fabricated on solid dielectric, thus, implementing LC is impossible. IMSL and suspended MSL have both air cavities held by solid substrates where metal layers and spacers are attached. LC can be filled into this cavity. While only part of the electric field  $\vec{E}$  of the guided signal of a suspended MSL is in the cavity (other part in top substrate), most of the  $\vec{E}$  of an IMSL lies in the cavity. When filled with LC, it can influence the tunability of the device to a much higher extent, compare Fig. 3.4 (b)(c). In practice, the IMSL has been widely used and is regarded as the standard technology in MSL LC phase shifter worldwide during the past two decades, such as reported in [Dol+93; Kuk+02; Wei+03; Mue+04; KFN02; Kar+12b]. In this section, LC based IMSL phase shifter (LC-IMSL) without any artificial structure is designed, fabricated and measured, serving as reference.

### Fabrication of IMSL

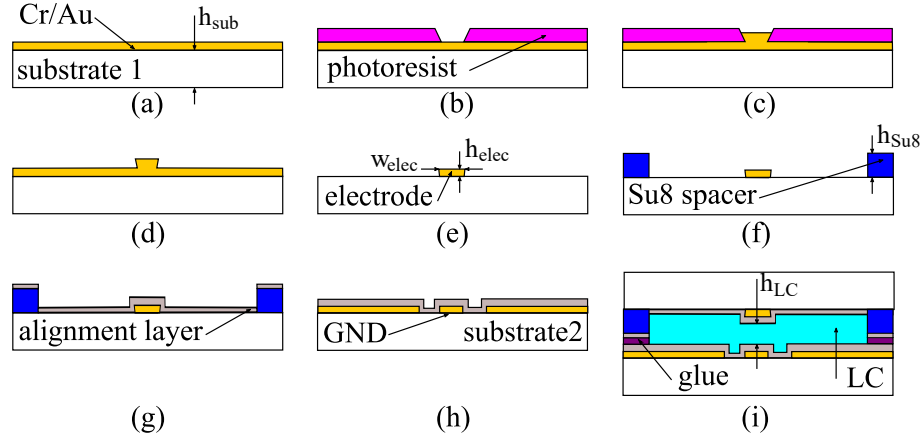


Figure 3.5: Schematic overview of the IMSL fabrication processes. (a) chromium(20 nm)/gold(60 nm) seed layer is evaporated. (b) Positive photoresist is spin-coated, exposed and developed. (c) Gold electrode is electroplated. (d) Photoresist is removed. (e) Seed layer is etched. (f) Su8 spacer is patterned. (g) Polymer layer is spin-coated and rubbed. (h) Step (a)-(e) and (g) are repeated for fabricating the ground plane. If no pattern on ground plane is required, only steps (a)(c)(g) are needed. (i) Finally, two substrates are aligned, bonded and filled with LC.

The fabrication process of the IMSL is illustrated in Fig. 3.5. The substrate in Fig. 3.4 (b) for strip line and ground plane use the glass AF32 from Schott AG with a thickness of  $700 \pm 10 \mu\text{m}$ , suitable for microwaves. It has  $\epsilon_r = 5.1$  and  $\tan\delta = 0.009$  at 24 GHz,  $\epsilon_r = 5.0$  and  $\tan\delta = 0.011$  at 77 GHz [AG22]. The reasons for using glass as substrate are:

1. it is transparent, which eases the manual, alignment between strip line and ground under a microscope
2. it enables the curing of the UV-curable glue used to fix both substrates,
3. it has low dissipation factor,
4. its  $700 \mu\text{m}$  thickness provides good mechanical stability and smooth surface, which are important for forming a precise cavity with a height of several  $\mu\text{m}$  only, and finally, an easy handling during fabrication.

Technical details for fabricating IMSL are given in Appendix A.1. In fact, properties of the glass substrate, i.e., thickness  $h_{\text{sub}}$  and dielectric constant  $\epsilon_r$  affect the performance of the phase shifter by influencing the device tuning efficiency  $\eta_D$ , as shown in Fig. 3.6.  $\eta_D$  is a ratio of effective device tunability  $\tau_{D,\text{eff}}$  to material tunability  $\tau_{LC}$ .  $\eta_D$  shows quantitatively how much of the material tunability is utilized by a proposed device layout. For the LC-based transmission line,  $\tau_{D,\text{eff}}$  and  $\eta_D$  are calculated by

### 3.2 Inverted Microstrip Line (IMSL) Phase Shifter

$$\tau_{D,eff} = \frac{\varepsilon_{r,D,eff,\parallel} - \varepsilon_{r,D,eff,\perp}}{\varepsilon_{r,D,eff,\parallel}}, \quad (3.7)$$

$$\eta_D = \frac{\tau_{D,eff}}{\tau_{LC}}$$

where  $\varepsilon_{r,D,eff,\parallel}$  and  $\varepsilon_{r,D,eff,\perp}$  represent the effective relative dielectric constant of the device when LC is parallel and perpendicular polarized to the guided wave, respectively.

Higher  $h_{sub}$  or  $\varepsilon_r$  leads to increased amount of field propagating inside the non-tunable glass substrate, thus, less influence of LC on device's tunability and decreased  $\tau_{D,eff}$  and  $\eta_D$ . Therefore, utilizing a thin carrier substrate with a low  $\varepsilon_r$  is desired for LC-IMSL. However, making substrate extremely thin i.e.  $h_{sub}$  less than  $500 \mu m$ , is a critical way to increase  $\eta_D$ , because of low mechanical stability. Using glass substrates of less  $\varepsilon_r$  than AF32 ( $\varepsilon_r = 5.1$ ) is a proper way to increase  $\eta_D$ , such as for fused silica ( $\varepsilon_r \approx 3.8$ ).

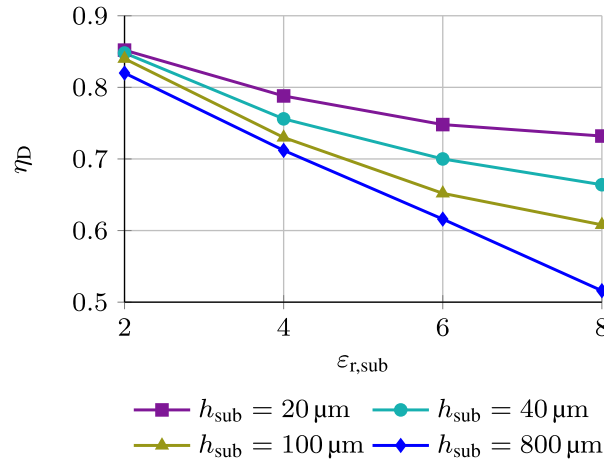


Figure 3.6: Simulated device tuning efficiency  $\eta_D$  of an LC-IMSL for substrates of different  $h_{sub}$  and  $\varepsilon_r$ .  $Z_c$  is kept to be  $50 \Omega$ , and  $h_{LC} = 20 \mu m$  during simulation.

#### Microwave characterization of IMSL

A MSL based on solid substrate at low frequency is normally measured through coaxial RF connectors. However, such connectors cannot be directly fixed to IMSL since IMSL has no solid dielectric. Connectors also introduce parasitics due to soldering or improper contacting, especially at high frequency. Therefore, the microwave characterization are performed on-wafer using 'Ground-Signal-Ground (GSG)' probes. For this purpose, a CPW pad for probe contacting and transition from CPW to IMSL is designed and integrated to the device under test (DuT), i.e., LC-IMSL. Due to the cavity formed between the electrode and ground plane, the CPW to IMSL transition requires to be via-less and is shown in Fig. 3.7 (a). Its equivalent circuit is depicted in Fig. 3.7 (b). The two radial stubs extended from

### 3 Liquid Crystal-based Microstrip Delay Line Phase Shifters

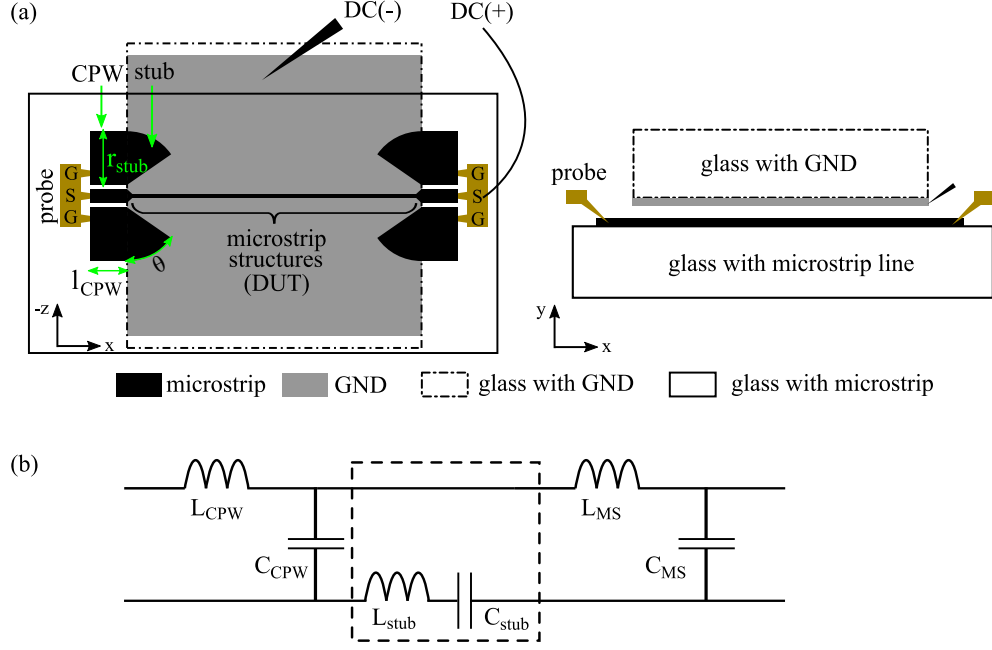


Figure 3.7: (a) Bottom (left) and side (right) view of CPW to IMSL transition with metal layer definition. Dot dashed line gives the boundary of the top glass in x-direction to give enough space for probe contacting. While the size for bottom glass has no restriction. Radial stub dimensions are given as:  $l_{\text{CPW}} = 100 \mu\text{m}$ ,  $r_{\text{stub}} = 700 \mu\text{m}$ ,  $\theta = 70^\circ$ . (b) Equivalent circuit of CPW to IMSL transition. LC-series circuit in dashed block represents the stubs, which couple the GND of the CPW to IMSL.

the ground planes of the CPW pad are open-ended  $\lambda/4$ -impedance transformer. The input impedance when putting  $Z_L = \infty$  and  $l = \lambda_0/4$  into Eq. (3.4) is calculated to be

$$Z_{\text{input}} = \frac{Z_0^2}{Z_L} = 0, \quad (3.8)$$

which is equivalent to short circuit at center frequency. Hence, the radial stub couples the CPW ground to that of IMSL on different metallized layers, instead of using through substrate via (TSV). When  $f < f_0$ ,  $l < \lambda/4$ ,  $Z_{\text{input}}$  has capacitive components; when  $f > f_0$ ,  $l > \lambda/4$ ,  $Z_{\text{input}}$  has inductive components. Therefore, open-ended  $\lambda/4$  stub is equivalent to a lumped L-C (inductor-capacitor) series circuit as in Fig. 3.7 (b). The radial shape of the stub is used to increase the bandwidth of the transition. Within the band, the proposed method can realize a smooth mode transition with low loss.

A demonstrator of IMSL, targeting at K-, Ka- and V-bands is shown in Fig. 3.8 as well as the scattering S-parameter on-wafer measurement setup. Design parameters are summarized in Table 3.1. The IMSL is designed to have an LC layer thickness  $h_{\text{LC}} = 20 \mu\text{m}$ . This is realized by making the  $h_{\text{Su8}} = 22 \mu\text{m}$  and  $h_{\text{elec}} = 2 \mu\text{m}$ , refer to Fig. 3.5, where thickness of glue and alignment layers are neglected. Based on  $h_{\text{LC}}$ , a MS line width  $w_{\text{elec}} = 40 \mu\text{m}$



### 3.2 Inverted Microstrip Line (IMSL) Phase Shifter

Table 3.1: Design parameters of the IMSL structures

	Material	$\epsilon_r$	$\tan\delta$	Frequency	Thickness
Glass substrate	AF32 glass	5.1	0.0049	5 GHz	700 $\mu\text{m}$
LC layer	GT3-23001	2.41-3.18	0.0037-0.0141	19 GHz	20 $\mu\text{m}$

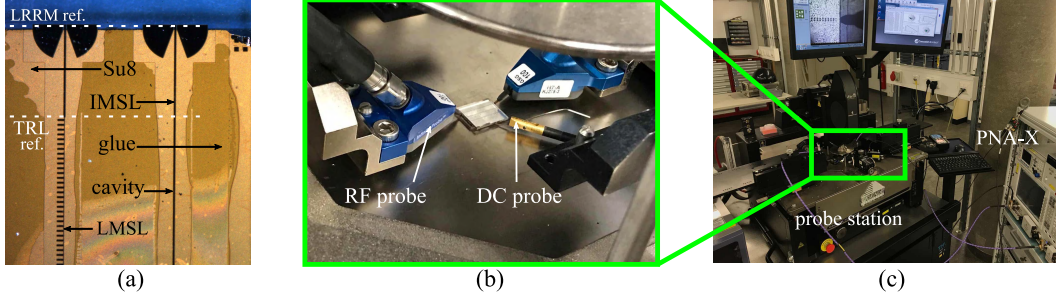


Figure 3.8: (a) Microscopic view of LC-IMSL demonstrator before LC filling. The dashed lines represent the reference planes after LRRM and TRL calibration. (b) On-wafer measurement of IMSL using probes. A DC probe is used to connect the ground plane of IMSL for bias reference. (c) Full setup of the measurement.

is simulated to achieve a characteristic line impedance  $Z_C = 50 \Omega$ . The radial stubs have optimized radius  $r_{\text{stub}} = 700 \mu\text{m}$  and central angle  $\theta = 70^\circ$ . The measurement uses PNA-X from Keysight Technologies and I67-GSG-100 probes from Formfactor, from 100 MHz to 67 GHz, with line-reflect-reflect-match (LRRM) probe tip calibration. 1 kHz square wave voltage is applied as bias, and it is noticed that for  $h_{\text{LC}} = 20 \mu\text{m}$ , the phase shift  $\Delta\phi$  saturates beyond 20 V (40 V peak-to-peak). Therefore, 20 V can fully bias the LC, i.e., the parallel orientation case.

Measurement results with LRRM calibration are shown in Fig. 3.9 as solid lines. The LC-IMSL matches very well to  $50 \Omega$  with reflection coefficient  $|S_{11,\text{LRRM}}| < -15 \text{ dB}$  from 10 GHz to 67 GHz. The transmission coefficient  $|S_{21,\text{LRRM}}|$  below 10 GHz is due to the limited bandwidth of the via-less CPW-IMSL transition, as explained above. It is also noticed that fully biased  $|S_{21,\text{LRRM}}|$  is slightly higher than unbiased due to less dielectric loss of LC when parallel oriented.

The differential phase shift  $\Delta\phi = \angle S_{21,\text{biased}} - \angle S_{21,0\text{V}}$  as a function of bias voltage  $V_B$  is shown in Fig. 3.10. It is not linearly correlated to the bias voltage: when  $V_B$  exceeds  $V_{\text{TH}}$ , even a small increase of  $V_B$  leads to distinct LC molecules reorientation and variation of  $\epsilon_{r,\text{LC}}$ ; when LC's reorientation approaches saturation, a further increment of  $\epsilon_{r,\text{LC}}$  with respect to  $V_B$  becomes insignificant. This figure is helpful in deciding the bias voltages for multiple phase shifters in phased array antennas in chapter 4.

The direct measurement results with LRRM probe tip calibration are embedded, where the CPW to IMSL transitions are included. To de-embed the transitions and get accurate performance of the LC-IMSL only, thru-reflect-line (TRL) calibration is performed based on the LRRM results. Briefly speaking, TRL calibration moves the reference planes of

### 3 Liquid Crystal-based Microstrip Delay Line Phase Shifters

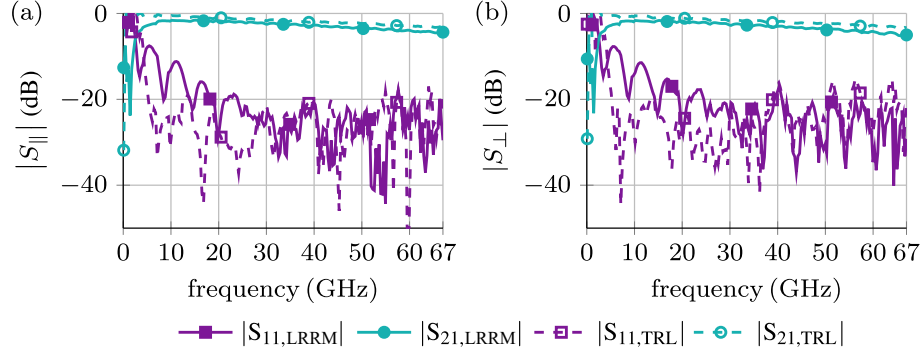


Figure 3.9: LRRM calibrated (solid line) and TRL calibrated (dashed line) results of the LC-IMSL in the (a) fully biased and (b) unbiased cases.

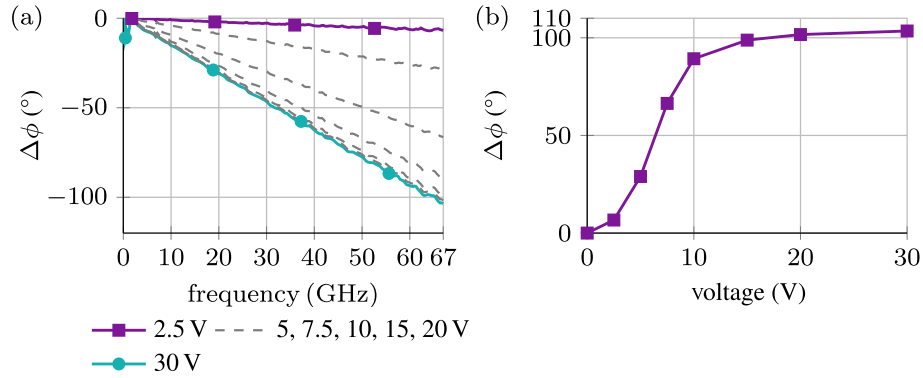


Figure 3.10: (a) Wideband  $\Delta\phi$  of the IMSL with different bias voltages. (b)  $\Delta\phi$  as function of bias voltage at 67 GHz.

the S-parameters from probe tips beyond the transitions to the pre-defined starting and ending point of the DuT to de-embed the transitions' influence. Moreover, the de-embedded S-parameters are automatically normalized to the  $Z_C$  at the reference plane. An introduction to TRL calibration as well as the calibration kits are given in Appendix A.2.

Based on the de-embedded S-parameters, the compactness and FoM of the LC-IMSL can be extracted. Compactness is quantified as the maximum phase shift  $\Delta\phi_{b,\max}$  per unit length. Higher compactness corresponds to the phase shift consuming less space to provide required  $\Delta\phi$ , which is important for the miniaturization of devices. FoM is defined by the ratio of  $\Delta\phi_{b,\max}$  to the highest IL:

$$\text{FoM} = \frac{\Delta\phi_{b,\max}}{\text{IL}_{\max}}. \quad (3.9)$$

Compactness and FoM of the LC-IMSL are given in Fig. 3.11. It can provide up to  $8.5^\circ$  phase shift per millimeter and  $22^\circ$  phase shift per dB loss at 67 GHz. Regarding a full range  $360^\circ$  phase shifter, the proposed LC-IMSL needs approximately a total length of  $9.46\lambda_0$  and IL of 16.4 dB which is unacceptable in most of the application scenarios.

### 3.2 Inverted Microstrip Line (IMSL) Phase Shifter

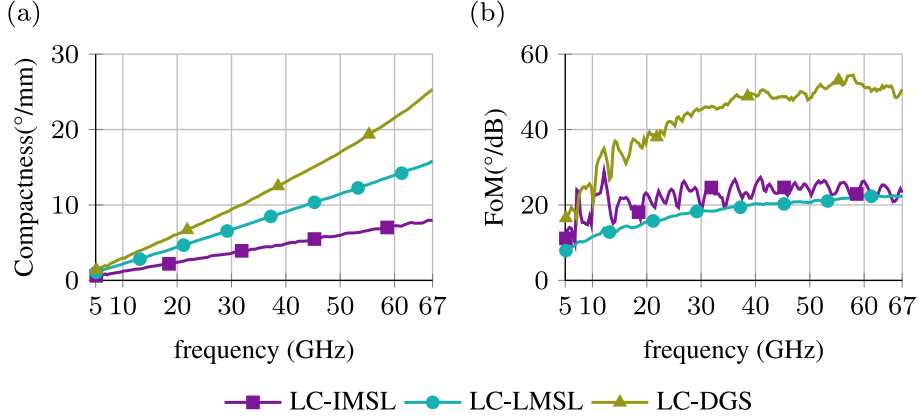


Figure 3.11: Extracted parameters from de-embedded data: (a) compactness and (b) FoM of LC-IMSL, LC-LMSL and LC-DGS with 120  $\mu\text{m}$  DGS. LC-LMSL and LC-DGS are the phase shifters introduced later in section 3.3 and 3.4, respectively.

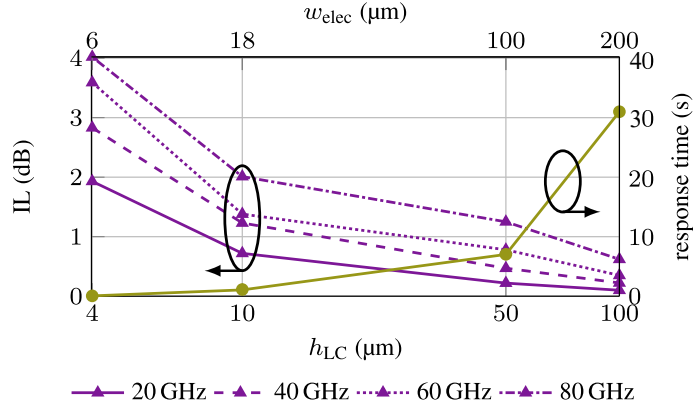


Figure 3.12: Simulated IL and calculated response time of the LC-IMSL phase shifter with respect to  $h_{LC}$  at different frequencies. GT3 LC and AF32 with  $h_{sub} = 700 \mu\text{m}$  are used for simulation. The response time is independent of frequency.  $Z_C$  is kept at  $50 \Omega$  during simulation by using always the proper IMSL width  $w_{elec}$  corresponding to  $h_{LC}$ .

A comparison of the reported LC-IMSL phase shifters during the past decade is listed in Table 3.3 at the end of section 3.5. The one reported in [Kar14] uses LC mixture TUD-566 which is similar to GT3-23001 in this work. It also uses glass substrate with same thickness and only slightly lower  $\epsilon_r$ . However, the FoM is much higher than in this work. The main reason is, a much thicker LC layer with  $h_{LC} = 100 \mu\text{m}$  was applied in [Kar14], and to keep  $Z_C = 50 \Omega$ ,  $w_{elec} = 200 \mu\text{m}$  is used as the IMSL electrode width, which is much wider than  $40 \mu\text{m}$  in this work and leads to less metallic loss. While the FoM is higher, the response

time increases following  $h_{LC}^2$  according to Eq. (2.12). Therefore, low IL and low response time have conflicting requirements regarding  $h_{LC}$  for the IMSL approach. A comparison of the IL performed by CST simulation and the calculated response time with varied  $h_{LC}$  is shown in Fig. 3.12. Values of  $w_{elec}$  and  $h_{LC}$  are one-to-one matched when the cross-section and  $Z_C$  of the IMSL are fixed. To achieve response time of tens of ms to fulfill modern agile communication requirements [Fri+11], LC-IMSL requires  $h_{LC} < 5 \mu m$ . This adds extremely high IL to the modulated signals, such that the signal-to-noise ratio (SNR) drops, and also, cause heating problems. Therefore, the reported LC-IMSLs are generally designed with  $h_{LC} > 100 \mu m$  for good performance [Kar14; Wei+03; Mue+04; BM10]. In the following sections, modified LC-IMSL with artificial structures are introduced to solve the conflict between IL and response time in traditional LC-IMSL. The reason for designing the reference LC-IMSL using  $20 \mu m$  thick LC instead of  $h_{LC} < 5 \mu m$  is considering fabrication tolerances, IL issue and easy comparison. Whereas,  $h_{LC} < 5 \mu m$  is the final goal.

### 3.3 Stub-Loaded Microstrip Line (LMSL) Phase Shifter

As mentioned in Section 3.1, by introducing the slow-wave effect, IMSL can be physically short but electrically long. The feature has the potential to save the power dissipated on the metal electrode and the dielectric materials, which are linearly related to the physical length of the IMSL. The most widely used slow wave MSL structure is the stub-loaded line [GJZ16] as shown in Fig. 3.13 (a) in an IMSL structure.

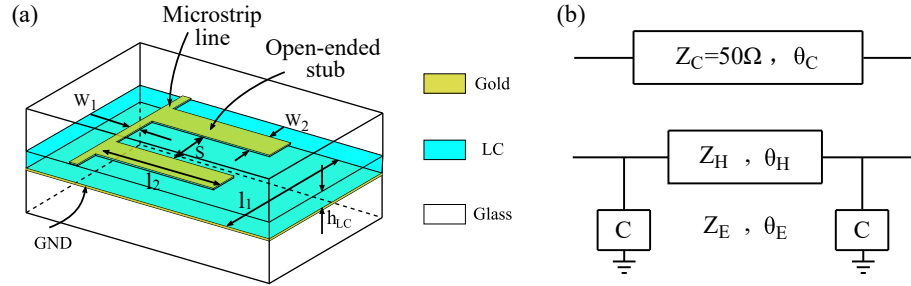


Figure 3.13: (a) 3D view of the LMSL lattices, dimensions are given as:  $w_1 = 10 \mu m$ ,  $w_2 = 40 \mu m$ ,  $l_1 = 220 \mu m$ ,  $l_2 = 150 \mu m$ ,  $S = 70 \mu m$  and  $h_{LC} = 20 \mu m$ . (b) Equivalent circuit of the LMSL lattice.

The stub-loaded IMSL topology (LMSL) is also filled with GT3 LC with  $h_{LC} = 20 \mu m$  as the reference LC-IMSL. Its center MSL has a width  $w_1 < 40 \mu m$  such that it has higher line impedance than  $50 \Omega$ . The open-ended stub shorter than  $\lambda/4$  act as shunt capacitor as discussed in Section 3.1. The equivalent circuit of LMSL is shown in Fig. 3.13 (b).  $Z_C$  and  $\theta_C$  represent the characteristic line impedance and electrical length of a conventional IMSL without artificial structures as reference, where  $Z_C = 50 \Omega$ . Similarly,  $Z_H$  and  $\theta_H$  represent the high impedance line between two capacitive stubs of LMSL.  $C$  is the equivalent capacitance of the open ended stub. The equivalent characteristic impedance  $Z_E$

### 3.3 Stub-Loaded Microstrip Line (LMSL) Phase Shifter

and electrical length  $\theta_E$  of LMSL can be derived using ABCD-matrix:

$$\mathbf{A}_E = \mathbf{A}_{\text{stub}} \cdot \mathbf{A}_H \cdot \mathbf{A}_{\text{stub}}. \quad (3.10)$$

where

$$\mathbf{A}_E = \begin{bmatrix} \cos\theta_E & Z_E \sin\theta_E \\ \frac{1}{Z_E} \sin\theta_E & \cos\theta_E \end{bmatrix}, \quad (3.11)$$

$$\mathbf{A}_H = \begin{bmatrix} \cos\theta_H & Z_H \sin\theta_H \\ \frac{1}{Z_H} \sin\theta_H & \cos\theta_H \end{bmatrix}, \quad (3.12)$$

$$\mathbf{A}_{\text{stub}} = \begin{bmatrix} 1 & 0 \\ \omega C & 1 \end{bmatrix}. \quad (3.13)$$

When  $\mathbf{A}_E$  is equivalent to a transmission line segment of  $Z_C$  and  $\theta_C$ , i.e.

$$\mathbf{A}_E = \mathbf{A}_C \quad (3.14)$$

this gives:

$$Z_C \sin\theta_C = Z_H \sin\theta_H \quad (3.15)$$

$$\cos\theta_C = \cos\theta_H - \omega C Z_H \sin\theta_H, \quad (3.16)$$

The slow-wave factor  $K$  is defined as:

$$K = \frac{\theta_C}{\theta_H}, \quad (3.17)$$

According to Eq. (3.15), with  $Z_C = 50 \Omega$  and  $Z_H > 50 \Omega$ ,  $\theta_H < \theta_C$  is valid, which indicates a shorter line. The achievable slow-wave factor  $K$  depends on the highest possible  $Z_H$  that can be realized by a MSL. Nevertheless, the highest achievable  $Z_H$  by utilizing a narrow MSL is generally less than  $100 \Omega$  due to fabrication limitation and insertion loss consideration, which largely limit the slow-wave effect. Moreover, narrow MSL causes high metallic loss and low power-handling capability.

A demonstrator of an LC-LMSL as Fig. 3.13 (a) is shown in Fig. 3.8 (a) together with LC-IMSL. They are fabricated and measured simultaneously such that fabrication and measurement tolerances are removed. The LC-LMSL demonstrator starts with a section of  $50 \Omega$  IMSL for smooth CPW to LMSL transition. This section is de-embedded using TRL method. Raw LRRM and de-embedded S-parameter are shown in Fig. 3.14. Its maximum phase shift  $\Delta\phi_{\text{max}}$  is presented in Fig. 3.15.

With the same de-embedded physical length of 10 mm, LC-LMSL provides  $\Delta\phi_{\text{max}} = 177^\circ$  at 67 GHz, whereas LC-IMSL has  $\Delta\phi_{\text{max}} = 103^\circ$  only. This result validates the slow-wave effect of LMSL structure. However, from Fig. 3.14,  $|S_{21}|$  of LC-LMSL is clearly less than that of LC-IMSL from Fig. 3.9, mainly due to the inhomogeneous configuration of LMSL with artificial structures and high impedance line segments with high loss. Compactness and FoM of the LC-LMSL are calculated and plotted in Fig. 3.11. From Eq. (3.15), the higher the  $Z_H$ , the more compact the LMSL. IMSL line of  $w_1 = 10 \mu\text{m}$  wide is implemented, which is nearly the fabrication limit using a film photo-lithography mask in

### 3 Liquid Crystal-based Microstrip Delay Line Phase Shifters

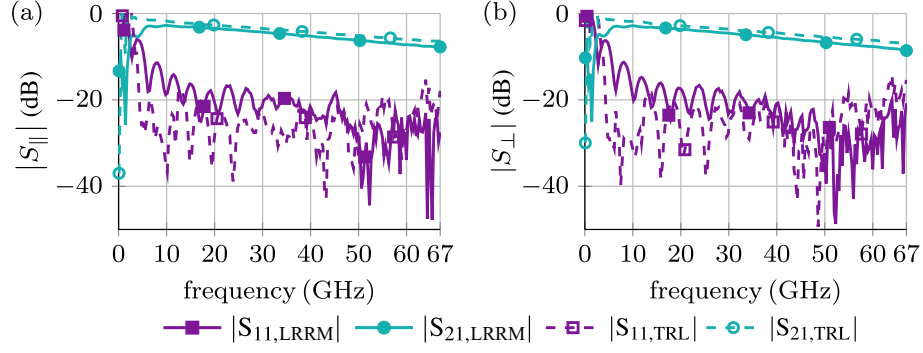


Figure 3.14: LRRM calibrated (solid line) and TRL calibrated (dashed line) results of the LC-LMSL under (a) fully biased and (b) unbiased cases.

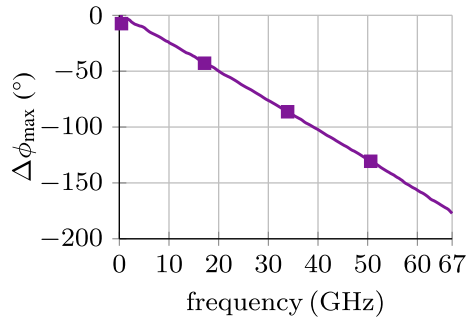


Figure 3.15: Wideband de-embedded  $\Delta\phi_{\max}$  of the LC-LMSL.

our lab. However, its  $Z_H$  is only simulated to be  $80\ \Omega$ . As expected, LC-LMSL is only 1.7 times as compact as (0.58 times the size) an LC-IMSL, with slightly smaller FoM due to the high insertion loss. It is concluded that, the widely used LMSL topology is not an efficient way to realize slow-wave effect in MSL, especially in thin dielectric and high-frequency cases.

### 3.4 Microstrip Line Phase Shifter with Defected Ground Structure (DGS)

Defected ground structures (DGS) are originally invented for planar low pass (LP) filters [Lim+02a; Chu+00; Ahn+01], since they can provide excellent cutoff and stopband characteristic due to the improved effective serial inductance by disturbing the returning current on the ground plane of the MSL. Moreover, DGS has been exploited widely in the miniaturization of transmission line based passive circuits [Ahn+01; Lim+02b; Dau+22] due to the slow-wave effect in its passband. The application of DGS in LC-based delay line phase shifter is proposed in this work for the first time.

### 3.4.1 Investigations for Different DGS Dimensions and Comparison

The most popular configuration of DGSs is the dumbbell shaped as in Fig. 3.16 (a) in an IMSL structure filled with LC (LC-DGS). The equivalent circuit of a DGS-loaded MSL cell is shown in Fig. 3.16 (b).

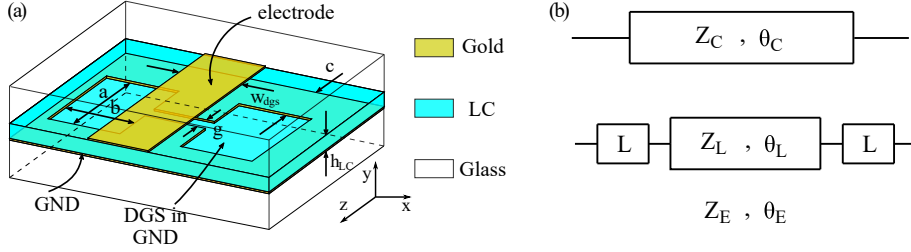


Figure 3.16: (a) 3D view of a unit cell of LC-DGS IMSL phase shifter based on  $20\mu\text{m}$  thick GT3 LC layer. Dimensions are given as  $w_{dgs} = 100\mu\text{m}$ ,  $a = b = 120\mu\text{m}$ ,  $c = a/2 = 60\mu\text{m}$ , and  $g = 20\mu\text{m}$ . (b) Schematic equivalent circuit of LC-DGS.

$L$  represents the serial inductance introduced by one DGS lattice.  $Z_L$  and  $\theta_L$  represent the line impedance and electric length of the MSL between two DGSs.  $Z_C$  and  $\theta_C$  represent the line impedance and electric length of standard  $50\Omega$  IMSL. Considering

$$\mathbf{A}_{\text{DGS}} = \begin{bmatrix} 1 & \omega L \\ 0 & 1 \end{bmatrix}, \quad (3.18)$$

the slow-wave effect equation

$$Z_L \sin \theta_C = Z_C \sin \theta_L \quad (3.19)$$

can be derived similarly to Eq. (3.15). Different from LMSL, to achieve the a slow-wave effect  $\theta_L < \theta_C$ , a low impedance line with  $Z_L < Z_C = 50\Omega$  is required, such that the line is made wider which leads to less metallic loss than IMSL or LMSL. This is an advantage, especially in high-frequency applications as well as in applications where thin dielectrics of  $\mu\text{m}$  level are used.

LC-DGS demonstrators based on the same cross-section as the previous LC-IMSL and LC-LMSL, i.e.  $h_{\text{LC}} = 20\mu\text{m}$  GT3-23001 and  $h_{\text{sub}} = 700\mu\text{m}$  AF32 glass are shown in Fig. 3.17. As LMSL, a short segment of IMSL is for transition usage, and is de-embedded. The dashed line in Fig. 3.17 gives the reference plane after de-embedding.

Measured S-parameters and phase shift  $\Delta\phi_{\text{max}}$  of the three demonstrators are plotted in Fig. 3.18 and Fig. 3.19 (a), respectively. It can be observed, as the DGS size increases,  $\Delta\phi_{\text{max}}$  increases, representing an increase in slow-wave effect; The slow-wave effect gets increasingly high towards the cut-off frequency  $f_{\text{cutoff}}$ . Meanwhile, the  $f_{\text{cutoff}}$  decreases and falls into the measurement range. This is due to the low-pass feature introduced by the DGSs. The  $f_{\text{cutoff}}$  of the low-pass filter is referred to as Bragg frequency  $f_{\text{Bragg}}$  in other literature on artificial transmission line, above which transmission ceases. In this work,



### 3 Liquid Crystal-based Microstrip Delay Line Phase Shifters

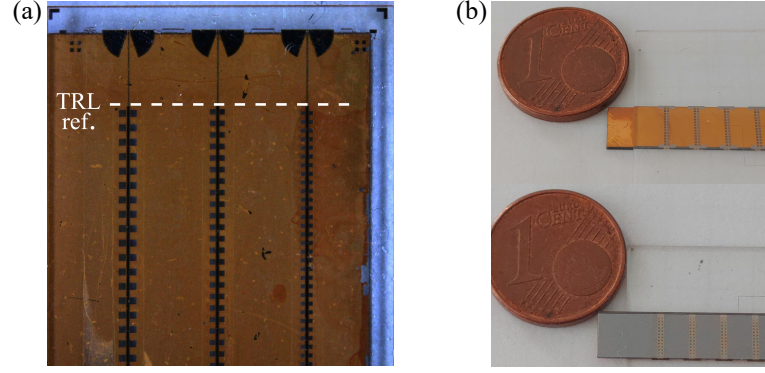


Figure 3.17: (a) LC-DGSs based on 20  $\mu\text{m}$  GT3, with 3 different sizes of DGS, i.e.  $a = b = 120, 160, 200 \mu\text{m}$ . The dashed line shows the reference plane after TRL de-embedding. The LC-DGSs have de-embedded length of 16 mm. (b) Top and bottom view of LC-DGSs based on 4.6  $\mu\text{m}$  GT7.

$f_{\text{cutoff}}$  is used. From DGS of  $a = 200 \mu\text{m}$ , the slow-wave effect gets increasingly high towards  $f_{\text{cutoff}}$  and  $\Delta\phi$  becomes more nonlinear with respect to frequency. While  $f_{\text{cutoff}}$  of LC-DGS is observed during measurement, that of LC-LMSL is not. The reason is the slow-wave effect of LC-LMSL is less than that of LC-DGS, such that the  $f_{\text{cutoff}}$  of the former is higher than the latter and lies beyond 67 GHz.  $f_{\text{cutoff}}$  of the proposed LC-LMSL appears at around 120 GHz according to simulation.

When  $a = 120 \mu\text{m}$ , the bandwidth of LC-DGS is up to 65 GHz. When DGS width increases to 160  $\mu\text{m}$  and 200  $\mu\text{m}$ , LC-DGSs only work up to 60 GHz and 50 GHz, respectively. The de-embedded S-parameters are only shown for the DGS width of  $a = 120 \mu\text{m}$ . Different from a true delay line, nonlinear  $\Delta\phi_{\text{max}}$ -frequency relationship near  $f_{\text{cutoff}}$  is observed in Fig. 3.19 (a) due to the LP feature of LC-DGSs. This will be problematic in wide-band phased array applications resulting in beam squinting. Whereas, LC-DGS can be designed to have higher  $f_{\text{cutoff}}$  and result in  $\Delta\phi_{\text{max}}$ -frequency response with higher linearity at the expense of less slow-wave effect. For narrow-band use cases such as phased array patch antennas, the nonlinearity has less impact.

The FoMs of the three LC-DGSs are extracted in Fig. 3.19 (b). Their FoMs maximize at 55 °/dB at around 55 GHz. A larger DGS size leads to slightly higher FoM in its passband in average. Roughly 2 °/dB to 3 °/dB higher FoM is observed between 160  $\mu\text{m}$  and 200  $\mu\text{m}$  DGSs as well as between 120  $\mu\text{m}$  and 160  $\mu\text{m}$  DGS. It is concluded that a trade-off among FoM, compactness and bandwidth of the LC-DGS phase shifter has to be considered.

As the only one that covers 5 GHz to 67 GHz band, compactness and FoM of the  $a = 120 \mu\text{m}$  DGS demonstrator are plotted in Fig. 3.11 for comparison with LC-IMSL and LC-LMSL. LC-DGS is nearly three times as compact as LC-IMSL, meanwhile, performs more than twice the FoM. This is because IMSL with DGS can easily result a line impedance higher than 200  $\Omega$ , without narrowing the MSL electrode's width. Thus, the DGS technology can bring extremely high slow-wave effect to MSL without increasing the loss too much.



### 3.4 Microstrip Line Phase Shifter with Defected Ground Structure (DGS)

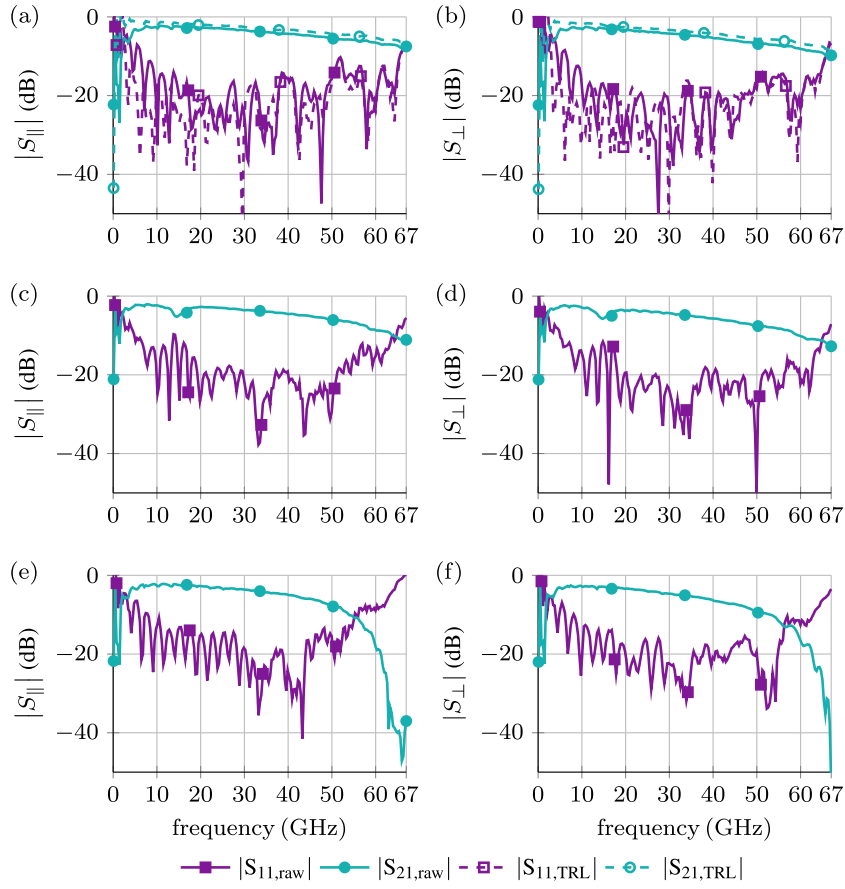


Figure 3.18: (a)(b) Raw and de-embedded S-parameters for LC-DGS with 120  $\mu\text{m}$  DGS. (c)(d) Raw S-parameters for 160  $\mu\text{m}$  DGS, and (e)(f) raw S-parameters for 200  $\mu\text{m}$  DGS.

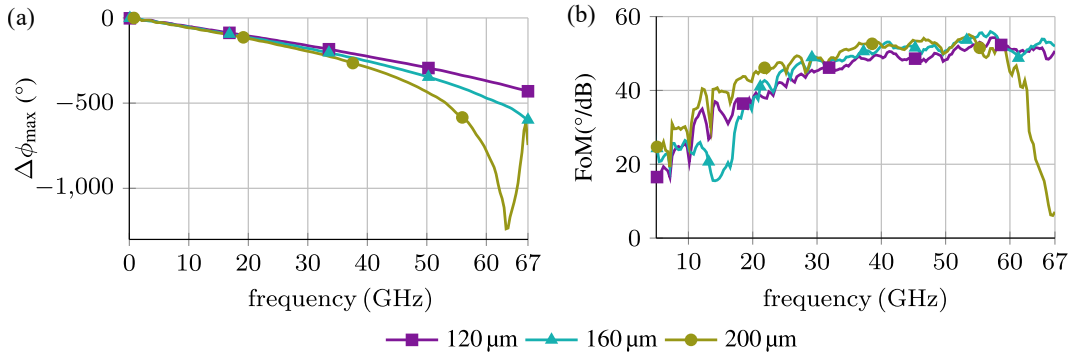


Figure 3.19: (a) Maximum phase shift  $\Delta\phi_{max}$  and (b) FoM of the three LC-DGS phase shifters as a function of operating frequency.

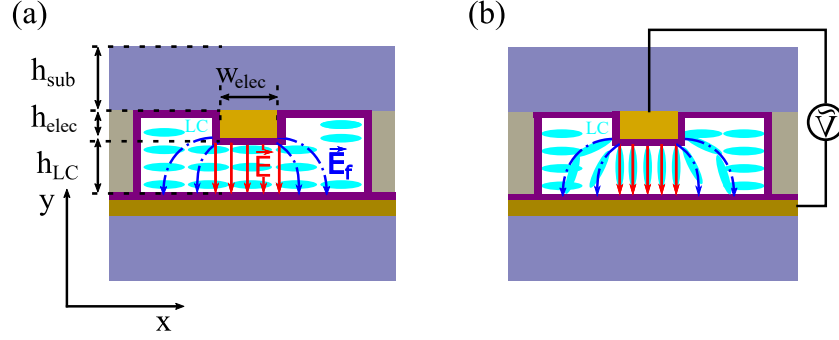


Figure 3.20: Cross-section and field distribution of LC-IMSL: (a) unbiased case and (b) fully biased case.

Except for the high slow-wave effect and relatively low loss, another crucial fact of performing high FoM of LC-DGS is the enhanced LC tuning efficiency. In Eq. (2.13), LC tunability  $\tau_{LC}$  is defined as its maximum anisotropy  $\Delta\epsilon$  over the maximum dielectric constant which is  $\epsilon_{r,\parallel}$ . However, the maximum anisotropy as stated in Table 2.1 is barely achievable in practice, especially for IMSL. Considering the cross section of LC-IMSL in Fig. 3.20, bias voltage is applied directly between strip line and ground plane without using external bias network for simplicity. Therefore, the bias field has identical distribution as the RF field. For this reason,  $\epsilon_{r,\parallel}$  of LC is achievable when bias voltage is strong enough, as in Fig. 3.20 (b). When not biased, LC molecules tend to align parallel to the surface of the top and bottom substrate due to anchoring force, and the fringing field  $\vec{E}_f$  around the edge of the MSL is not strictly perpendicular to LC molecules, which leads to higher effective relative permittivity  $\epsilon_{r,\text{eff},\perp}$  of LC at unbiased cases than  $\epsilon_{r,\perp}$ . LC tuning efficiency  $\eta_\tau$  quantifies how much of LC's tunability is actually utilized and is defined as the ratio of effective LC tunability to the material tunability  $\Delta\epsilon$ :

$$\eta_\tau = \frac{\epsilon_{r,\text{eff},\parallel} - \epsilon_{r,\text{eff},\perp}}{\epsilon_{r,\parallel} - \epsilon_{r,\perp}} \quad (3.20)$$

where  $\epsilon_{r,\text{eff},\parallel}$  and  $\epsilon_{r,\text{eff},\perp}$  are the effective relative permittivities of LC when the LC-IMSL is fully biased and unbiased, respectively. It is worth mentioning, the device tuning efficiency  $\eta_D$  of Eq. (3.7) should be distinguished from  $\eta_\tau$ . Briefly speaking,  $\eta_D$  depicts how much the LC's tunability influences the tunability of the whole device. Even the LC inside the device has a high  $\eta_\tau$ , if most RF field is simply not propagating through LC, its influence to device tunability is limited and  $\eta_D$  is low. Whereas, obviously, a high  $\eta_\tau$  is the premise of high  $\eta_D$  and high FoM.

Intuitively, the wider the strip line  $w_{\text{elec}}$ , the less percentage of the  $\vec{E}_f$ , the less difference between  $\epsilon_{r,\text{eff},\perp}$  and  $\epsilon_{r,\perp}$ . This has also been mathematically proven in [Goe10] using conformal mapping. Based on the given de-embedded S-parameters of the three phase shifters, i.e., LC-IMSL, LC-LMSL and LC-DGS, their  $\epsilon_{r,\text{eff},\parallel}$  and  $\epsilon_{r,\text{eff},\perp}$  can be extracted by comparing to simulation, i.e., sweeping the  $\epsilon_r$  of the LC material and match the measured  $\angle S_{21}$  to the simulation results. The extracted  $\epsilon_{r,\text{eff},\parallel}$ ,  $\epsilon_{r,\text{eff},\perp}$ , calculated  $\eta_\tau$  as well

### 3.4 Microstrip Line Phase Shifter with Defected Ground Structure (DGS)

as compactness, unit length loss and FoM of the phase shifters are listed in Table. 3.2. As expected, LC-DGS with the widest line width of  $100\mu\text{m}$  achieves the highest  $\eta_\tau$ , which is much higher than that of LC-IMSL and LC-LMSL. Due to the strongest slow-wave effect, LC-DGS also shows much higher compactness than the others. The unit length insertion loss of LC-DGS is only slightly higher than LC-IMSL mainly due to the disturbed returning current on the defected ground plane. All these facts together lead to the highest FoM of LC-DGS.

Table 3.2: Comparison of LC-IMSL, LC-LMSL and LC-DGS filled with  $20\mu\text{m}$  thick GT3 at 60 GHz.

Technology	$\varepsilon_{r,\text{eff},\perp}$	$\varepsilon_{r,\text{eff},\parallel}$	$\eta_\tau$	$\Delta\phi_{b,\text{max}}/\lambda_0$ ( $^\circ/\lambda_0$ )	IL/mm (dB/mm)	FoM $^\circ/\text{dB}$
LC	2.43	3.16	100 %	/	/	/
LC-IMSL	2.68	3.15	64.6 %	36.15	0.306	24.7
LC-LMSL	2.72	3.15	59.1 %	69.69	0.623	22.4
LC-DGS	2.53	3.16	86.3 %	107.65	0.411	51.3

#### 3.4.2 Miniaturization and Response Times

A critical performance parameter for phase shifters is the response time, which quantifies how fast the desired phase shift is achieved (switch-on response time  $\tau_{\text{on}}$ ) or the initial state is recovered (switch-off response time  $\tau_{\text{off}}$ ) after triggering. According to Eq. (2.12), response time of LC based IMSL is proportional to the square of LC layer thickness  $h_{\text{LC}}^2$ . While  $\tau_{\text{on}}$  driven by  $V_B$  is short,  $\tau_{\text{off}}$  is much longer due to the weak surface anchoring. Therefore, response time normally refers to  $\tau_{\text{off}}$ . To measure the response time of the LC-DGS, sweep type of the PNA-X is set to be CW time mode (continuous wave), where the data of a single frequency versus time is measured.  $\angle S_{21}$  is measured and shown in Fig. 3.21. Under 20 V bias, LC-DGS spends  $\tau_{\text{on}} = 1.13\text{ s}$  to switch on, and  $\tau_{\text{off}} = 1.98\text{ s}$  to switch off when bias is released. The  $\tau_{\text{on}}$  can be easily decreased by using  $V_B \gg 20\text{ V}$ . Modern agile

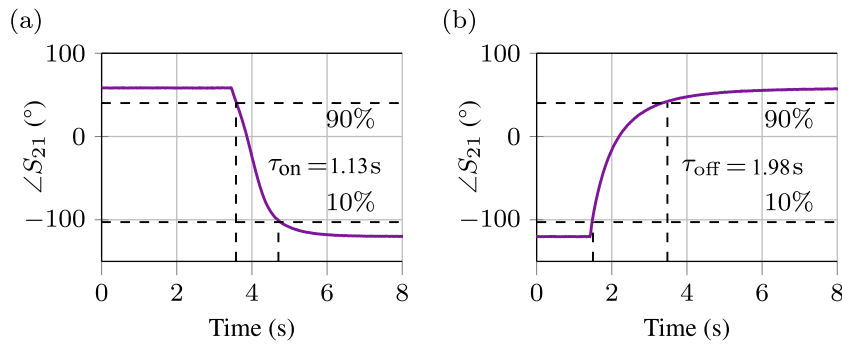


Figure 3.21: Response times of LC-DGS filled with GT3 of  $h_{\text{LC}} = 20\mu\text{m}$ .

### 3 Liquid Crystal-based Microstrip Delay Line Phase Shifters

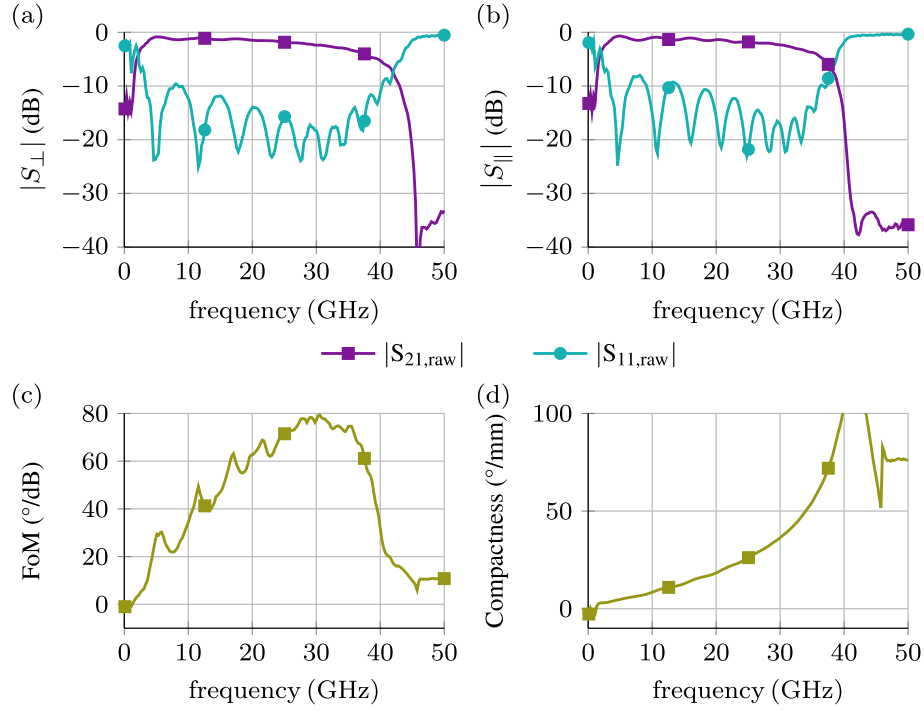


Figure 3.22: S-parameter of GT7-DGS (a) without bias, and (b) with 5 V bias. (c) FoM and (d) compactness of GT7-DGS.

communication requires  $h_{LC}$  of  $\mu\text{m}$  level for fast response. This is difficult for LC-IMSL or LC-LMSL, since small  $h_{LC}$  leads to narrow line, which results in extremely high insertion loss and low FoM, as explained in section 3.2. Whereas, small  $h_{LC}$  is achievable by LC-DGS technology.

A second version of LC-DGS with thinner LC layer  $h_{LC} = 4.6 \mu\text{m}$  is designed and filled with more advanced GT7-29001 LC with higher anisotropy, as shown in Fig. 3.17 (b) with the name GT7-DGS to distinguish from the previous LC-DGS. The design parameters use the same definition as in Fig. 3.16, and are given as:  $a = b = 2c = 80 \mu\text{m}$ ,  $g = 20 \mu\text{m}$  and  $w_{dgs} = 40 \mu\text{m}$ . GT7-DGS is designed targeting 25 GHz to 29 GHz for 5G applications. Performing TRL calibration is rather difficult and inaccurate mainly due to the non-negligible uncertainty of dielectric thickness. Thus, CPW-to-IMSL transitions are made to be extremely short and DGSs start directly from the edge of the ground plane, such that the transitions barely influence. The LRRM calibrated raw measured S-parameters are shown in Fig. 3.22 (a)(b). Under both unbiased and fully biased cases,  $|S_{11}| < -10 \text{ dB}$  is achieved between 20 GHz to 35 GHz which indicates a good matching to  $50 \Omega$ . To achieve the matching, fabrication is repeated four times, each time with slightly varied height of the SU8 spacers. This is because  $h_{LC} = 4.6 \mu\text{m}$  cannot be precisely obtained due to multiple reasons, which brings uncertain extra height, such as uneven surface of SU8 spacer (due to air bubble or O<sub>2</sub> etching), undefined glue thickness on SU8, and possible glass substrate bending due to the tension during the curing of the glue, see Appendix A.1. By fitting

### 3.4 Microstrip Line Phase Shifter with Defected Ground Structure (DGS)

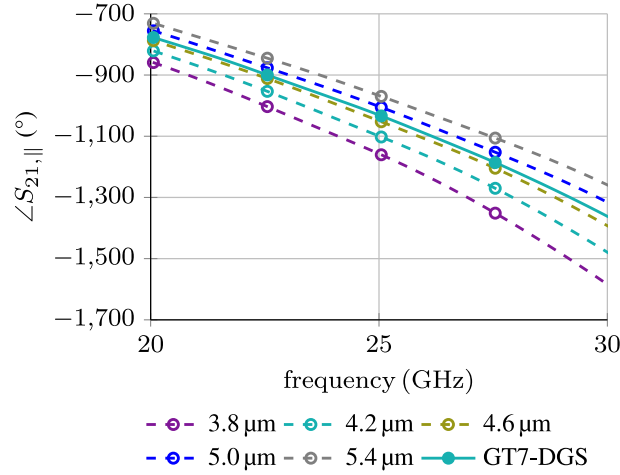


Figure 3.23: Determination  $h_{LC}$  by fitting measured  $\angle S_{21,\parallel}$  to simulations.

measured  $\angle S_{21,\parallel}$  to simulation, as shown in Fig. 3.23, one of the four GT7-DGS batch almost has  $h_{LC} = 4.6 \mu\text{m}$  as required. This batch was made to have  $h_{SU8} - h_{elec} = 4.0 \mu\text{m}$  with a  $h_{LC}$  deviation of  $0.6 \mu\text{m}$ . Comparing the results from the other three batches with simulation, it can be concluded that  $h_{LC}$  is generally  $0.5 \mu\text{m}$  to  $1 \mu\text{m}$  higher than  $h_{SU8} - h_{elec}$  due to the aforementioned reasons. Such deviation barely influences the previous LC-DGS designed with  $h_{LC} = 20 \mu\text{m}$ , but has significant impact on current GT7-DGSs. With the help of modern industrial manufacturing, the cavity height can be accurately controlled. Actually, commercial LC based mmW panel devices, e.g., LC-based phased array antennas from ALCAN Systems GmbH [JGW20], have been using the well-established LC display production line for years to realize  $\mu\text{m}$  level thin LC layer with high accuracy.

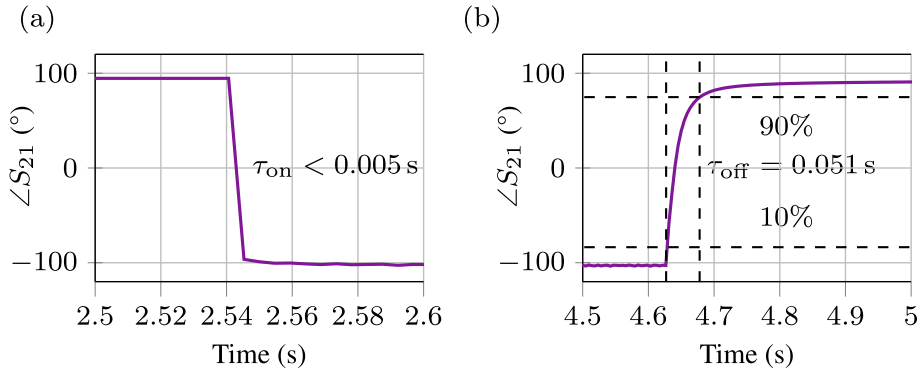


Figure 3.24: Response time of GT7-DGS.

FoM of the GT7-DGS phase shifter in Fig. 3.22 (c) peaks with  $80^\circ/\text{dB}$  at 30 GHz, and maintains higher than  $70^\circ/\text{dB}$  from 25 GHz to 35 GHz. At 30 GHz, the IMSL phase shifter with DGS and  $4.6 \mu\text{m}$  GT7 layer has a compactness of  $38^\circ/\text{mm}$ , while the previous design  $20 \mu\text{m}$  GT3 layer has only  $10.7^\circ/\text{mm}$ . This is the result of using GT7 with higher anisotropy

and DGS with lower  $f_{\text{cutoff}}$  and stronger slow-wave effect.

$\tau_{\text{off}}$  of GT7-DGS is measured to be 51 ms as given in Fig. 3.24. The laboratory alignment layer processing is suboptimal, which might negatively influence the  $\tau_{\text{off}}$ . It is reported in [JGW20] that by using proper parameters and standard manufacturing process, ALCAN achieves  $\tau_{\text{off}} = 30$  ms utilizing a similar LC mixture as GT7-29001 with the same  $h_{\text{LC}} = 4.6 \mu\text{m}$ . It is reasonable to believe that based on LC-DGS technology, smaller  $h_{\text{LC}}$  for faster response is realistic, i.e.,  $h_{\text{LC}} < 2 \mu\text{m}$  for  $\tau_{\text{off}} < 10$  ms. Although not as fast as semiconductor or MEMS phase shifters with  $\mu\text{s}$ -level response time, it is capable to be used in wide range of the modern reconfigurable mmW applications [Fri+11]. A comparison of the proposed LC phase shifters to the state-of-the-art phase shifter technologies is given in chapter 3.6.

## 3.5 Nanowire Membrane (NaM)-based Inverted Microstrip Line Phase Shifter

In Section 3.3 and 3.4, slow-wave IMSL is realized by modifying the MSL and ground plane with lumped artificial structures, respectively. In this section, a special dielectric material named metallic-nanowire-filled aluminum oxide membrane (NaM) is implemented into the IMSL structure as the substitution of the ground plane to realize slow-wave IMSL.

### 3.5.1 Metallic-Nanowire-Filled-Membrane

NaM is fabricated based on a commercial porous Anodic Aluminum Oxide (AAO) membrane from Inredox, with  $\epsilon_r = 6.7$  and  $\tan\delta = 0.015$  at 110 GHz. These nanopores are periodically and regularly distributed with a pore diameter and an inter-pore pitch of approximately 40 nm and 107 nm, respectively. Copper is first sputtered on the bottom side of the membrane as the seed layer, then, copper nanowires are grown into these nanopores by electrodeposition until they reach the front side. Finally, the top side is polished down to the desired thickness 50  $\mu\text{m}$ , and it is ensured that the nanowires are isolated from each other on the front side [Ser+14b; Ser+14a]. A NaM sample under electron microscope is shown in Fig. 3.25.

The growing of nanowires by electrodeposition is accurately selective. Thanks to a photo-lithography mask, nanowires will grow only in the nanopores which are not covered by photoresist. A valid nanowire area as small as  $20 \mu\text{m} \times 30 \mu\text{m}$  is reported in [Pin+18]. An even smaller nanowire area of  $10 \mu\text{m} \times 10 \mu\text{m}$  is tested to be realizable in the lab.

The NaM needs to be cut into required shapes. Due to the thin thickness, it can be easily broken during saw dicing. Besides, sputtered copper can be easily delaminated from the AAO membrane due to the shear force during dicing. Laser cutting is used in [Jos+18b], however, the generated high temperature melts copper and AAO and forms a ridge with around 5  $\mu\text{m}$  height after cooling down, as shown in Fig. 3.26 (a). This causes undefined increment of LC cavity height  $h_{\text{LC}}$ . Therefore, NaM cutting is done by etching in this section. An extra mask with desired NaM shapes is used to pattern the photoresist coated on NaM. Afterwards, the sample is immersed into sodium hydroxide (NaOH) solution. The uncovered part of the NaM wafer is etched away, and NaM pieces with desired shapes

### 3.5 Nanowire Membrane (NaM)-based Inverted Microstrip Line Phase Shifter

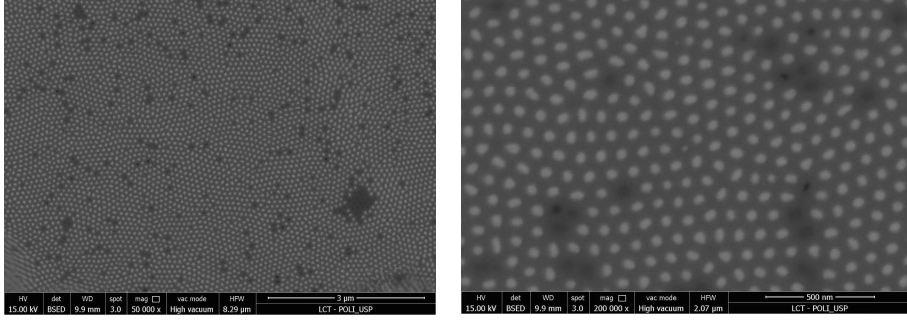


Figure 3.25: Front side of the NaM under electron microscope provided by LME, Escola Politécnica da Universidade de São Paulo. The bright dots are pores filled with copper. Dark dots are non-filled pores.

are left. Hence, the NaM pieces have flat surfaces, but relatively rough edges compared to cutting, see Fig. 3.26 (b).

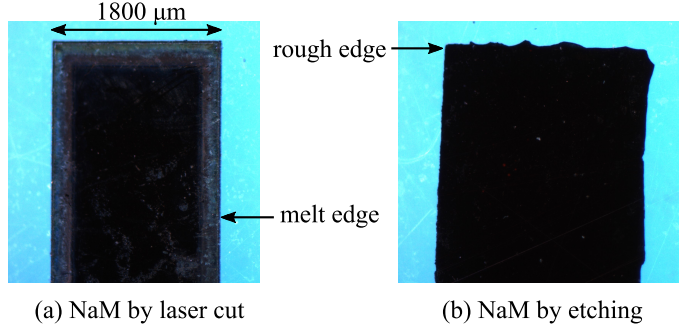


Figure 3.26: NaM pieces under microscope: (a) laser cut, and (b) NaOH solution etching.

The configuration of integrating NaM into IMSL is shown in Fig. 3.27. While the glass substrate with strip line electrode and SU8 spacers is the same AF32 as in previous LC-IMSLs, only the substrate with ground plane is substituted by the NaM. Fabrication procedure follows that of LC-IMSL as in Appendix A.1. After LC is filled in, it can perform as a phase shifter, namely LC-NaM. The principle of using NaM to generate slow-wave effect in LC-NaM is demonstrated in Fig. 3.27.

Due to the dense distribution of the copper nanowires, the RF  $\vec{E}$  field is mostly captured on the top surface of the NaM and being concentrated fully in the LC. In contrast, the magnetic field is almost unperturbed by the nanowires because they are much thinner than the skin depth at least up to 110 GHz, compare Fig. 3.27. Due to the larger  $\vec{H}$  distribution area than  $\vec{E}$ , distributed inductance  $L$  is relatively large, such that the distributed capacitance  $C$  must be increased as a compensation to maintain  $Z_C = 50 \Omega$  according to Eq. (3.3). This is done by increasing the line width  $w_{elec}$  as in LC-DGS. As a result,  $Z_C$  remains to be  $50 \Omega$ , while the phase velocity  $v_\phi$  and the wavelength  $\lambda$  decreases.

Considering the special structure combining metal and dielectric, NaM has anisotropic



### 3 Liquid Crystal-based Microstrip Delay Line Phase Shifters

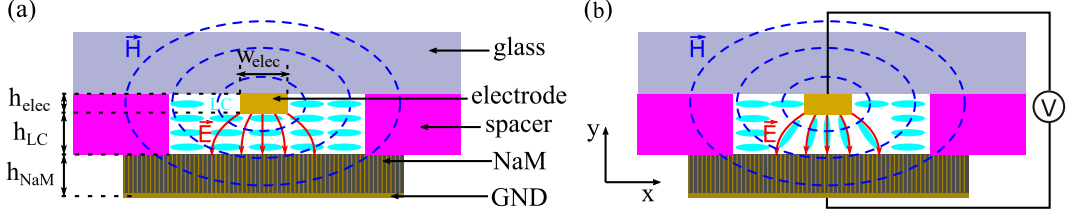


Figure 3.27: Cross-section of the LC-NaM phase shifter and its working principle. (a) Unbiased: LC molecules are parallel to the  $xz$ -plane and quasi-perpendicular to the RF  $\vec{E}$  field. (b) Fully biased: parallel orientation.  $h_{\text{elec}} = 2 \mu\text{m}$ ,  $h_{\text{LC}} = 4 \mu\text{m}$ ,  $w_{\text{elec}} = 25 \mu\text{m}$ ,  $h_{\text{NaM}} = 50 \mu\text{m}$  are designed for  $50 \Omega$  matching.

$\epsilon_r$  and conductivity  $\sigma$ . Since the dense nanowires are growing along  $y$ -direction, and the porosity of the membrane is around 12 %, NaM has 12 % conductivity of copper in  $y$ -direction only and is electrically insulative in  $x, z$ -directions. Therefore, an anisotropic conductivity value of  $(\sigma_x, \sigma_y, \sigma_z) = (0, 7.15e6, 0)$  is defined for NaM in CST. Meanwhile, NaM should have the  $\epsilon_r$  of AAO in  $x, z$ -direction, and  $\epsilon_r$  of copper in  $y$ -direction. Hence, an anisotropic  $(\epsilon_{r,x}, \epsilon_{r,y}, \epsilon_{r,z}) = (6.7, 2e5, 6.7)$  of NaM is also applied in CST. Due to lacking of  $\epsilon_r$  of copper,  $\epsilon_{r,y} = 2e5$  is a random large number chosen to represent conductor, which doesn't have impact on the simulation results as long as  $\sigma_y = 7.15e6$  is defined in CST.

#### 3.5.2 Reference Microstrip Line Filled With Air

To verify the principle of introducing slow-wave effect using NaM in MSL, and to validate the simulation model of NaM as well as the fabrication process in a simplified situation, NaM based IMSLs of different lengths ( $1200 \mu\text{m}$ ,  $2400 \mu\text{m}$  and  $3600 \mu\text{m}$ ) filled with  $6 \mu\text{m}$  thick air instead of  $4 \mu\text{m}$  LC are realized and measured. Fig. 3.28 shows the sample with length  $l_{\text{PS}} = 1200 \mu\text{m}$  under a microscope. The measurement results of the three NaM based IMSLs with air of different lengths are shown in Fig. 3.29.

Electrode's dimensions given in Fig. 3.28 are designed for LC-NaM with  $4 \mu\text{m}$  thick LC. However, by simply increasing the height of SU8 spacers by  $2 \mu\text{m}$ ,  $50 \Omega$  matching with  $6 \mu\text{m}$

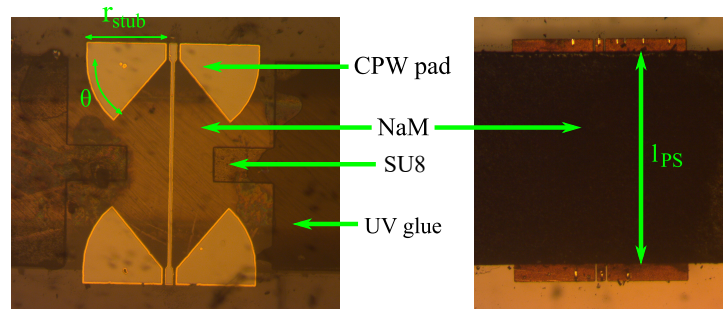


Figure 3.28: NaM based IMSL under a microscope. Left is top view, right is bottom view.  $r_{\text{stub}} = 470 \mu\text{m}$ ,  $\theta = 50^\circ$  and  $l_{\text{PS}} = 1200 \mu\text{m}$ .



### 3.5 Nanowire Membrane (NaM)-based Inverted Microstrip Line Phase Shifter

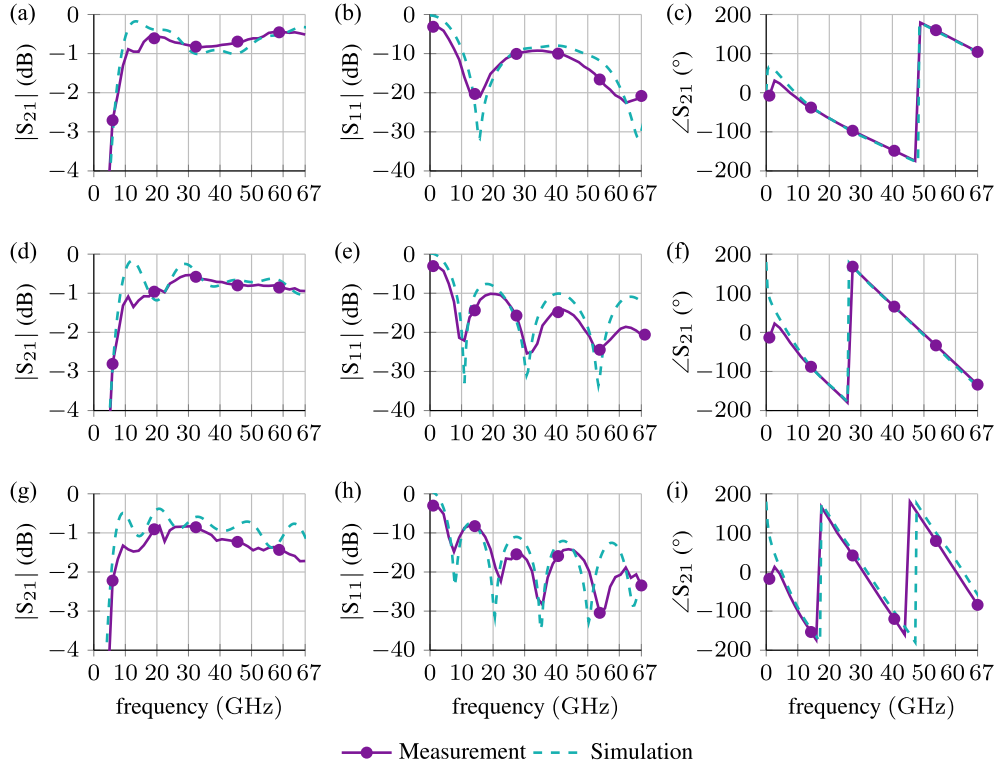


Figure 3.29: Measured (in solid lines) and simulated (in dashed line) S-parameters of the NaM based IMSLs filled with air with length (a)(b)(c)  $l_{PS} = 1200 \mu\text{m}$ , (d)(e)(f)  $2400 \mu\text{m}$  and (g)(h)(i)  $3600 \mu\text{m}$ .

thick air can be achieved according to simulation, as shown in Fig. 3.29 in dashed line. As expected, decent wideband impedance matching with  $|S_{11}| < -10 \text{ dB}$  as well as good agreement between measurement and simulation is observed for all three NaM based IMSLs demonstrators. The transmission starts from around 15 GHz due to the via-less CPW-IMSL transition.

Next, the effective relative dielectric constant  $\epsilon_{r,\text{eff}}$  and quality Q-factor of the three demonstrators are calculated from the measured S-parameters, as shown in Fig. 3.30.  $\epsilon_{r,\text{eff}}$  and Q-factor of a MSL are defined as

$$\epsilon_{r,\text{eff}} = \left( \frac{\lambda_0}{\lambda} \right)^2 \quad (3.21)$$

$$Q = \frac{\beta}{2\alpha}$$

respectively, where  $\lambda$  and  $\alpha$  represents the guided wavelength and unit length loss, respectively.  $\lambda$  is calculated by

$$\lambda = l_{PS} \cdot \frac{360^\circ}{|\angle S_{21,\text{unwrap}}|}. \quad (3.22)$$

### 3 Liquid Crystal-based Microstrip Delay Line Phase Shifters

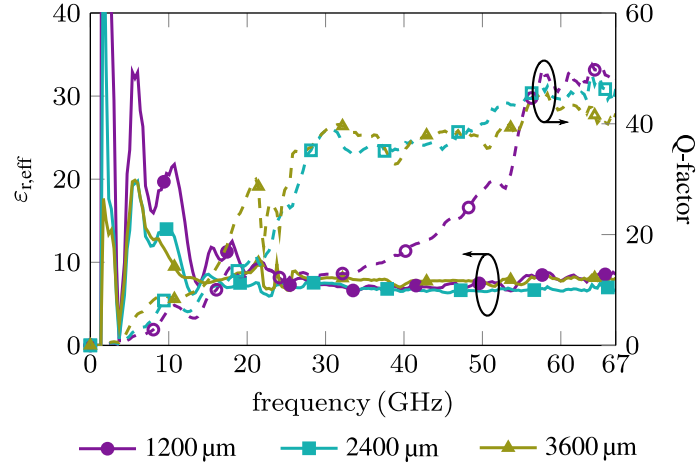


Figure 3.30: Extracted value of  $\epsilon_{r,\text{eff}}$  and Q-factor of the three NaM based IMSLs with air.

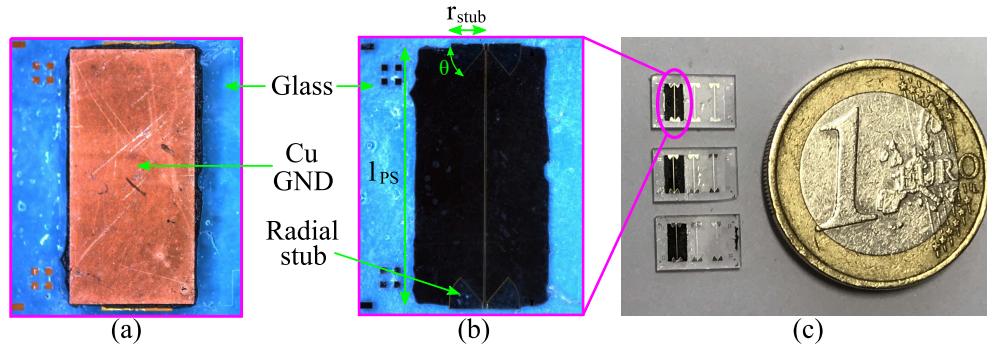


Figure 3.31: (a) Bottom side of LC-NaM with the sputtered copper as the ground plane. (b) Top side of LC-NaM. (c) Macroscopic view of three LC-NaM demonstrators. Dimensions are given as:  $r_{\text{stub}} = 470 \mu\text{m}$ ,  $\theta = 50^\circ$ ,  $l_{\text{PS}} = 3600 \mu\text{m}$ .

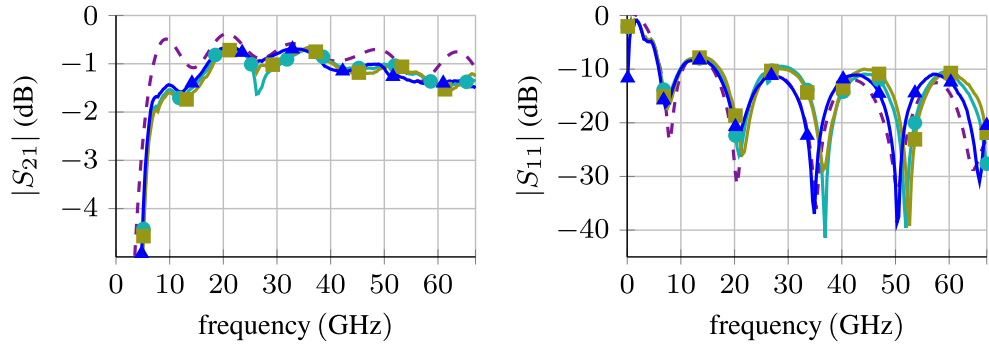


Figure 3.32: Measured (in solid lines) and simulated (in dashed line) S-parameters of the three LC-NaMs before LC filling (filled with air).

with air with  $\epsilon_r = 1$ , the demonstrators'  $\epsilon_{r,\text{eff}} > 8$  beyond 20 GHz. This indicates a strong

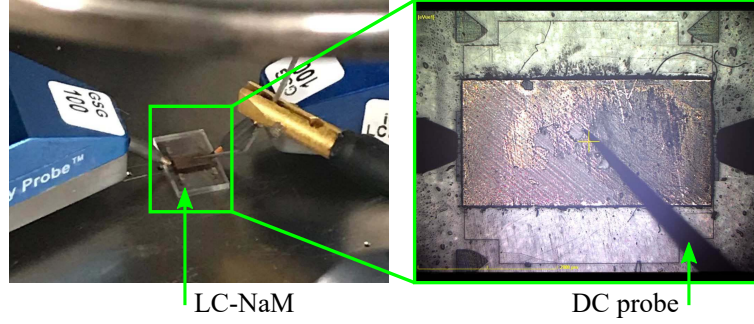


Figure 3.33: On-wafer measurement setup for characterizing LC-NaM.

slow-wave effect is generated by NaM, and the MSL is largely shortened. High Q-factor represents large number of wavelengths are guided by the MSL at the expense of low insertion loss, which is the premise of high FoM delay line phase shifter. The demonstrators have excellent Q-factors higher than 40 above 58 GHz. Therefore, with the analysis above, the anisotropic NaM model used in the simulation, the fabrication process, as well as the slow-wave principle with high Q-factor based on NaM are validated. These works are the premises for realizing the LC-NaM.

#### 3.5.3 Performance Analysis of NaM-based Phase Shifters with Different LCs

LC-NaM demonstrators are shown in Fig. 3.31. They have the same CPW pad and radial stub design as in Fig. 3.28, but different dielectric thickness of  $h_{LC} = 4\mu\text{m}$ . Besides, in order to provide distinct phase shift, LC-NaMs are made to have length of  $l_{PS} = 3600\mu\text{m}$  only.

Three LC-NaMs of  $l_{PS} = 3600\mu\text{m}$  are identically fabricated in the same batch. Measurements are carried out already before LC is filled to validate the fabrication repeatability, i.e., the similarity among the three demonstrators. Their measured S-parameters are shown in Fig. 3.32, together with the simulation results for comparison.

Measured S-parameters of the demonstrators show good agreement with each other and with simulation from 0 GHz to 67 GHz. Therefore, the cavity heights of the demonstrators are considered as identical and equal to  $4\mu\text{m}$  as designed. This allows the comparison between LCs by filling each demonstrator with different LCs. From Fig. 3.32,  $|S_{11}|$  has strong resonance behavior because the demonstrators are designed to work with LCs with  $\epsilon_r \approx 2.4$  to 3.5, which leads to a distinct impedance mismatch when filled with air ( $\epsilon_r = 1$ ).

The three demonstrators are filled with GT3-23001, GT5-26001 and GT7-29001, respectively, refer to Table 2.1. The measurement setup is shown in Fig. 3.33. Different from LC-IMSL phase shifters in previous sections, where DC probe contacts their flipped ground plane underneath, see Fig. 3.7 and 3.8, the ground plane of LC-NaM is on the top side and easy to be contacted with DC probes. During the measurement, a square wave of 1 kHz is applied between the electrode and NaM in the range of 0 V to 10 V, i.e., 20 V peak-to-peak, in steps of 1 V. The reason for using 1 kHz square wave instead of DC bias is explained later. When bias voltage exceeds 5 V, the phase shift  $\Delta\phi$  barely increases.

### 3 Liquid Crystal-based Microstrip Delay Line Phase Shifters

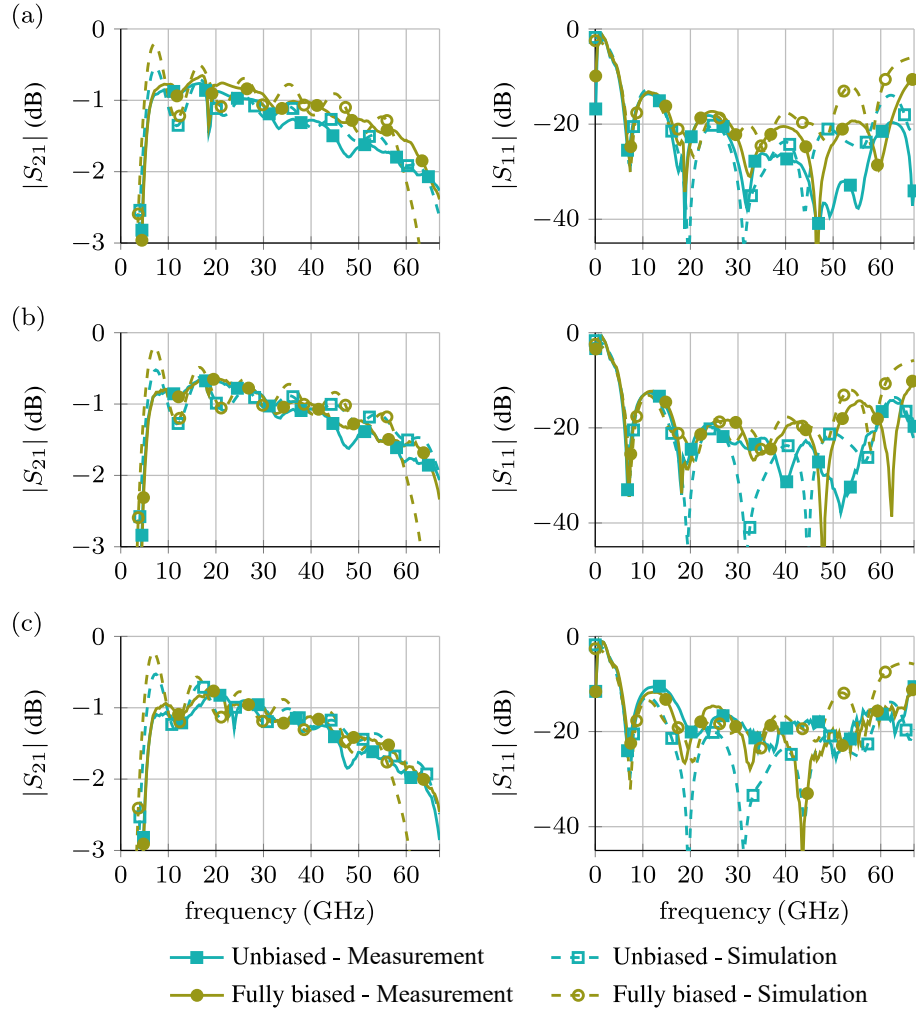


Figure 3.34: Measured and simulated S-parameters of the three identically fabricated LC-NaMs filled with (a) GT3-23001, (b) GT5-26001 and (c) GT7-29001.

Therefore, 5 V can fully bias the LC-NaMs.

Fig. 3.34 presents the measured and simulated S-parameters of the three LC-NaMs in both, unbiased and fully biased cases. Broad pass band with  $|S_{11}| < -15$  dB is generally achieved from 10 GHz to 60 GHz for all LC-NaMs. The bandwidth is defined by the via-less CPW to IMSL transition, not the cut-off mechanism as in LC-DGS. Based on the S-parameters, maximum phase shift  $\Delta\phi_{b,max}$  and FoM of the LC-NaMs are extracted in Fig. 3.35.

The LC-NaMs have the peak FoM of 41 °/dB at 52 GHz, 48 °/dB at 52 GHz and 70 °/dB at 56 GHz, for GT3-23001, GT5-26001, and GT7-29001, respectively. While the differences between the measured and simulated results for GT3 and GT5 LC-NaMs are quite obvious, GT7 shows less difference. The possible reason is, although the inner surfaces of LC cavities are processed identically, they provide various anchoring forces to different LCs. Besides,

### 3.5 Nanowire Membrane (NaM)-based Inverted Microstrip Line Phase Shifter

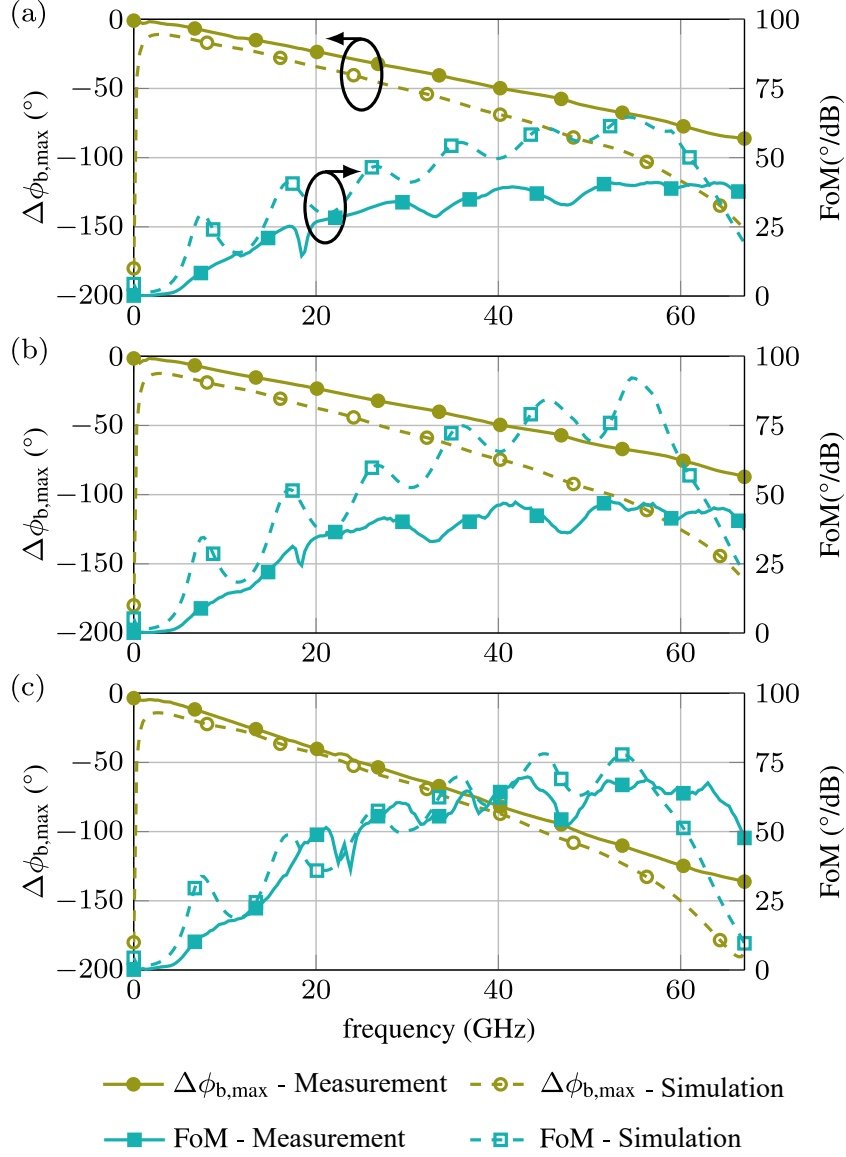


Figure 3.35: Measured and simulated FoM and  $\Delta\phi_{b,max}$  of LC-NaM demonstrators filled with (a) GT3-23001, (b) GT5-26001 and (c) GT7-29001.

### 3 Liquid Crystal-based Microstrip Delay Line Phase Shifters

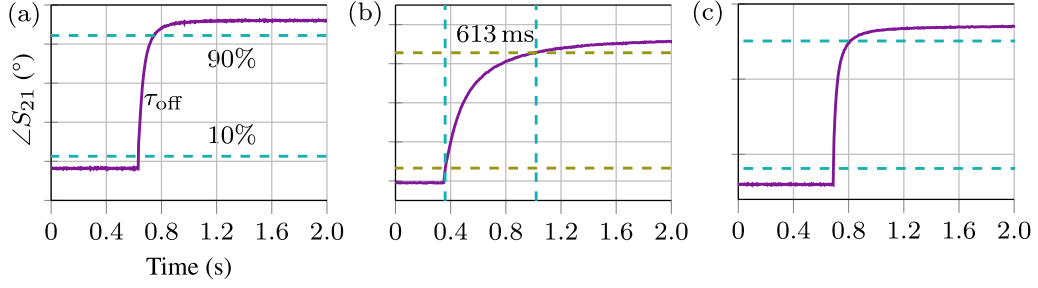


Figure 3.36: Measured switch-off response time  $\tau_{\text{off}}$  of LC-NaM filled with (a) GT3-23001, (b) GT5-26001 and (c) GT7-29001 under 5 V bias of 1 kHz.

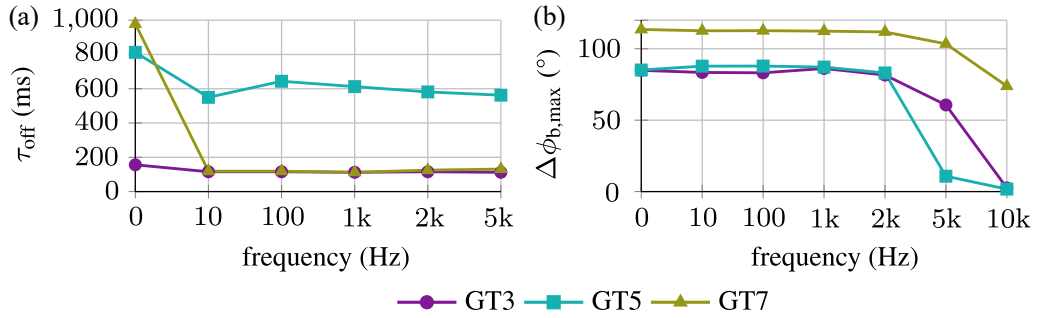


Figure 3.37: Influence of bias voltage frequency on (a)  $\tau_{\text{off}}$  and (b)  $\Delta\phi_{\text{b,max}}$  of LC-NaM with GT3-23001, GT5-26001 and GT7-29001. Measurements are performed at 60 GHz.

the MSL topology has fringing fields, such that tuning efficiency  $\eta_{\tau}$  of the LC is hard to evaluate. The LC parameters given in Table 2.1 cannot be fully achieved in practice.

The switch-off response time  $\tau_{\text{off}}$  of the LC-NaMs are shown in Fig. 3.36. While LC-NaM with GT3 and GT7 has  $\tau_{\text{off}}$  of 110 ms and 120 ms, respectively, the one with GT5 is 613 ms due to the extremely high viscosity  $\gamma_r$  of GT5. It is noticed that LC-NaM with 4  $\mu\text{m}$  thick GT7 has longer response time than previous GT7-DGS with 4.6  $\mu\text{m}$  thick GT7. This is because the top surface of NaM is not processed with alignment layer, since the handling of NaM for alignment layer processing is difficult, such that the total anchoring force for realignment of LC in LC-NaM is weaker than in GT7-DGS.

The influence of the bias frequency on  $\tau_{\text{off}}$  of the three LC-NaMs is tested from DC to 5 kHz with the same amplitude, as given in Fig.3.37 (a). It is concluded that the LCs biased by DC voltage generally takes a longer time to realign.

Fig. 3.37 (b) shows phase shift  $\Delta\phi_{\text{b,max}}$  versus the bias frequency.  $\Delta\phi_{\text{b,max}}$  for all LC-NaMs remain almost unchanged when the bias frequency is below 2 kHz. Above 2 kHz, GT5 shows a severe degradation of tunability  $\tau_{\text{LC}}$ , and becomes almost non-tunable above 5 kHz. GT3 and GT7 also suffer a significant decrease in  $\tau_{\text{LC}}$  from 2 kHz to 5 kHz. At 10 kHz, GT3 becomes non-tunable, while GT7 still remains around 60% of tunability. Hence, the optimum bias voltage frequency is approximately 1 kHz. It is worth mentioning

that each switch-on and switch-off case has been repeated more than 10 cycles with stable results. Since LC-NaM with GT3 and GT5 perform no phase shift under 10 kHz bias,  $\tau_{\text{off}}$  under 10 kHz bias is not measurable. Therefore, Fig. 3.37 (a) only show up to 5 kHz.

### 3.6 Comparison of State-of-the-Art Planar Phase Shifter Technologies

A comparison to the state-of-the-art phase shifter technologies is given in Table 3.3. The table concentrates on the state-of-the-art planar passive phase shifters in various technologies. It includes the reference LC-IMSL phase shifter and the two major LC phase shifters proposed in this chapter with fast response, i.e., LC-DGS and LC-NaM phase shifters filled with GT7.

The phase shifter technologies can be summarized into three categories:

1. semiconductor technologies in particular silicon technologies (CMOS and Bipolar CMOS) that offer much lower cost comparing with InP or GaAs technologies,
2. RF-MEMS,

Table 3.3: Performance comparison to the state-of-the-art planar passive phase shifter technologies.

Technology	f (GHz)	$\Delta\phi_{b,\text{max}}$ (°)	IL (dB)	FoM (°/dB)	LC	$\tau_{\text{off}}$ (s)	$\Delta\phi_{b,\text{max}}/\lambda_0$ (°/ $\lambda_0$ )	Bias Voltage (V)	Ref.
Si	60	360	17	21	/	/	/	/	[LW16]
SiGe	60	180	7.5	24	/	/	/	1	[TN09]
GaAs	60	360	10.7	33.6	/	/	/	1	[Han+14]
BiCMOS	40	60	5.0	12	/	/	/	2.5	[Isk+16]
Ferrites	13.1	83.2	1.5	55	/	/	381	/	[GS15]
BST	10	342	6.6	52	/	< 0.01	1500	150	[Saz+11a]
BST	3	274	7.3	37.3	/	< 0.01	1440	200	[Nik+16]
MEMS	65	337	2.8	120	/	/	197	35	[Kim+02]
LC-IMSL	17.5	250	4	62.5	TUD-566	> 30	63	30	[Kar14]
LC-IMSL	24	320	2.9	110	/	> 200	81	30	[Mue+04]
LC-IMSL	24	/	/	110	/	/	/	35	[Wei+03]
LC-IMSL	37	168	8	21	E7	> 30	178	8	[BM10]
LC-VCPW	20	90	1.5	60	TUD-566	0.34	106	40	[Goe+09]
LC-VMS	20	60	2	30	TUD-566	3	46	40	[Hu+14]
LC-CMOS	45	275	5.4	51	GT3	/	870	20	[Fra+13]
LC-MEMS	40	135	2.05	66	GT3	/	430	50	[Gom+22]
LC-NaM	60	89	2.9	31	GT3	1.3	74	40	[Jos+18b]
LC-IMSL	67	103	4.6	22	GT3	/	38	5	section 3.2
LC-DGS	30	190	2.4	79	GT7	0.05	380	5	section 3.4
LC-NaM	56	116	1.7	70	GT7	0.12	173	5	section 3.5

\* VCPW: varactor loaded CPW, VMS: varactor loaded microstrip line,

### 3 Liquid Crystal-based Microstrip Delay Line Phase Shifters

3. functional materials such as BST in thin or thick-film technology and the Microwave LC technology.

As another functional material, ferroelectrics, mainly BST phase shifter shows good compactness, fast response, and comparable FoM, but a limited frequency range, and requires extremely high bias voltage for tuning. RF-MEMS show higher FoM but with critical application drawbacks such as discrete phase shift with limited resolution, fragility against wear out failures, dielectric charging, contact degradation, encapsulation and high driven voltage requirement.

Since LC phase shifters are all passive, the listed phase shifters based on semi-conductor technologies are also passive without gain amplifier for easy comparison. They are mostly switch type phase shifter (STPS) where the MOSFETs are used to switch signal path to realize digital discrete phase shift [LW16]; or reflection type phase shifter (RTPS) where MOS varactors are used as the reflective loads of a coupler to achieve continuous phase shift [TN09; Isk+16]; or combination of both STPS and RTPS to produce large range continuous phase shift with relatively low IL [Han+14]. However, they are not competitive to proposed LC-DGS or LC-NaM phase shifters in terms of FoM due to the highly lossy passive circuits realized on the semiconductor wafer with high  $\epsilon_r$ . Besides the cost of integration, large passive circuits in advanced semiconductor technologies for mmW applications can be prohibitive for consumers [Lé+22].

As has been explained in Fig. 3.12, although traditional LC-IMSL phase shifters in [Wei+03; Mue+04] can achieve FoM as high as 110 °/dB, it is at the expense of extremely slow response time due to using LC layer thicker than 200  $\mu\text{m}$ .

As concluded in section 3.2, using thin substrates with low  $\epsilon_r$  in IMSL helps in increasing the device tuning efficiency  $\eta_D$  and thus, increasing FoM. However, considering the availability and cost of the materials, as well as the practical situations, the flexibility of choosing thickness and  $\epsilon_r$  of the substrate is limited. Therefore, to improve FoM of LC phase shifters, effort is devoted to enhance LC's material tunability  $\tau_{LC}$  and to decrease the power dissipation by implementing artificial structures to the IMSL. All the reported planar LC phase shifters with high performance, i.e., high FoM, high compactness and fast response, use loaded line structures of multiple variants, since they generate slow-wave effect in a manner similar to the proposed phase shifters in this work. In [Hu+14], the authors periodically load a non-tunable MSL with tunable LC varactors (LC-VMS) connected in series to the line. Although LC is not the substrate for the IMSL in this topology such that  $h_{LC}$  of the varactor can be lowered independently of the line's impedance, the limited tunability of LC-based varactors, complex biasing network and high discontinuity degrade its behaviour. In [Goe+09], a CPW is periodically loaded with shunt LC varactors (LC-VCPW), achieving a good FoM, high compactness and fast response. However, VCPW configuration has higher fabrication effort, higher inhomogeneity and requires a complex bias network and suffers from a distorted wave front when meandered. In [Fra+13], a complex phase shifter combining MEMS and LC (CPW with suspended deflected signal strip filled with LC) is realized based on the 0.35  $\mu\text{m}$  CMOS technology. It shows the highest compactness due to the slow-wave effect and the deflective MEMS structures, which brings extra phase shift in addition to LC. It allows precise fabrication of extremely thin LC



layers of 1  $\mu\text{m}$  with estimated  $\tau_{\text{off}} < 10$  ms. Although FoM is comparable, its fabrication is extremely complex and costly. Its compatibility to LCD manufacturing is questionable. A similar idea, combining LC and MEMS has been reported in [Gom+22] by utilizing NaM technology. Excellent FoM and compactness are achieved. Nevertheless, relatively high bias voltage is required to activate the MEMS and the phase shift becomes discrete.

While both, LC-NaM and LC-DGS phase shifters are well performing with high FoM and fast response time among LC-based phase shifters, LC-DGS shows clearly a low-pass feature with cut-off frequency  $f_{\text{cutoff}}$ . Generally speaking, the lower the  $f_{\text{cutoff}}$  of LC-DGS, the higher the slow-wave effect and FoM. That is why LC-DGS performs higher FoM and compactness than LC-NaM at 30 GHz. However, when talking about mmW applications higher than Ka-band, even up to W-band, LC-NaM will maintain the high performance with no  $f_{\text{cutoff}}$ , since the nanowires are thin enough (nearly four times smaller than the skin depth at 100 GHz) to allow operation with good performance at W-band or higher with very moderate eddy current loss and low conductive loss.

LC phase shifters are entirely passive. The biasing requires low power and takes advantage of existing LCD driver technology. Controlling up to 512 radiating elements consumes a power of less than 1/2 Watt, which represents a 30 times improvement over a standard semiconductor-based phase shifter [ALC]. Moreover, by leveraging the existing mass production capability of LCD production lines, as well as the low marginal cost of producing additional types of LC panels, ALCAN claims to be able to reduce the LC phase shifter costs by 100 times to around 300  $\$/\text{m}^2$  compared to semiconductor-based phase shifter costs, which are estimated to be around 30.000  $\$/\text{m}^2$  when using 30 cm diameter wafers [Dol20].

## 3.7 Linearity and Power Handling Capability

The on-wafer measurement so far is performed by using RF signal with low power, i.e.,  $< -10$  dBm, such that the nonlinearity of the LC phase shifter is not observable from the measurement. However, when a large signal propagates through a nonlinear device, unwanted higher-order harmonics appear at frequencies close to the basic tones which are hard to be filtered out. They might also lead to interference with actual signals on these channels. Except for linearity, the high power S-parameters, which straightforwardly depict the variation of DuT's performance with increased RF power, is of great interest.

### Definition of the Third-Order Intercept Point (IP3)

The third-order intercept point (IP3) is used to evaluate nonlinear systems and devices. It is based on the idea that the weakly nonlinear transfer function between the input and output signal of the device can be modeled using a low-order polynomial, derived by means of Taylor series expansion. The amplitude of harmonics usually decreases as the harmonics order increases. Harmonics higher than third-order have very low amplitudes and thus can usually be ignored and most of these higher-order products often fall outside of amplifier bandwidth, filter passbands, etc. When the device is fed with two tones at  $f_1$  and  $f_2$ , third

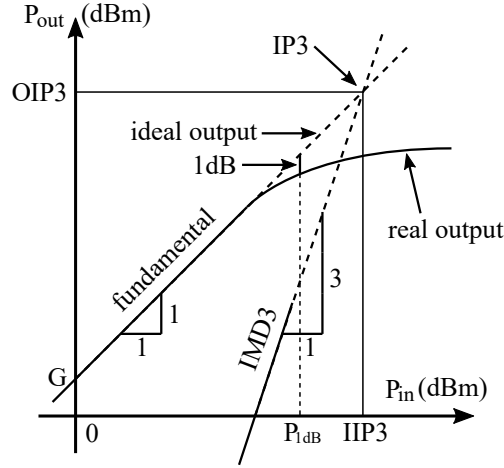


Figure 3.38: Schematic definition of IP3 and related concepts.

order intermodulation (IMD3) products will occur at various frequencies including  $2f_1 - f_2$  and  $2f_2 - f_1$ . If  $f_1$  and  $f_2$  are close,  $2f_1 - f_2$  and  $2f_2 - f_1$  will be very close to  $f_1$  and  $f_2$ . These two IMD3s distort and decrease the power of wanted signal at  $f_1$  and  $f_2$ , and degrade the system's selectivity as well. By plotting the output power versus the input power both on logarithmic scales, the IMD3 product triples the slope of the linearly amplified signal (wanted) at the input tone frequency, as shown in Fig. 3.38 in solid lines. Both curves are extended in dashed lines and intersect at IP3. It can be read off from the input or output power axis, leading to input (IIP3) or output (OIP3) intercept point, respectively. It is worth mentioning, IP3 is a purely mathematical concept and does not correspond to a practically occurring physical power level. In many cases, IP3 lies far beyond the maximum operating power level and damage threshold of the device. For real applications, 1-dB compression point is usually used to define the linear operating range, as  $P_{1dB}$  in Fig. 3.38. It is the input power that causes the gain to decrease 1 dB from the expected linear gain trace. It is the point where the component goes into compression and becomes non-linear. Normal operation should occur below this point in the linear region. The IIP3 point is typically about 10 dB above the 1-dB compression point as a rule of thumb for most linear devices.

According to Fig. 3.38, IP3 is calculated by

$$\begin{aligned} \text{IIP3} &= P_{\text{in}} + \frac{1}{2}(P_{\text{out}} - \text{IMD3}) \\ \text{OIP3} &= P_{\text{out}} + \frac{1}{2}(P_{\text{out}} - \text{IMD3}) = \text{IIP3} + G \end{aligned} \quad (3.23)$$

where  $P_{\text{in}}$  is the power of the input signal at  $f_1$  and  $f_2$ ,  $P_{\text{out}}$  is the power of the fundamental output signal at  $f_1$  and  $f_2$  and  $G$  is the gain.

### Measurements of IP3

Reported LC based tunable devices barely consider their non-linearity, except for [Goe10]. In this work, IP3 measurements are performed in a more accurate manner in which the

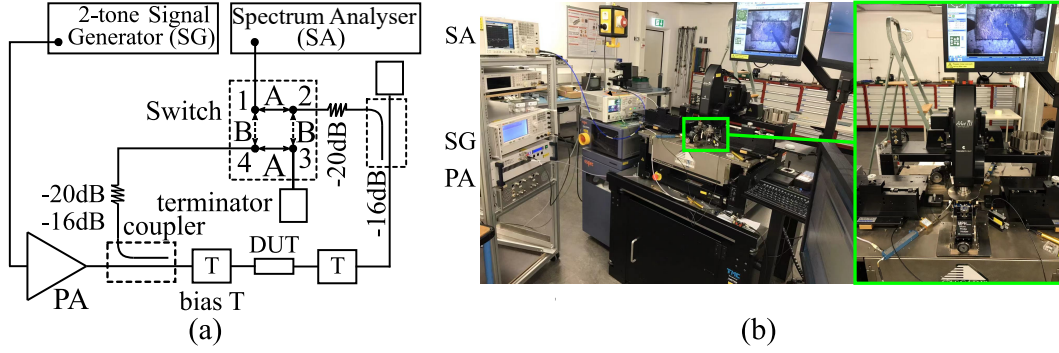


Figure 3.39: Block diagram and photograph of the on wafer IP3 measurement setup.

nonlinearities from the measurement devices are excluded, especially the power amplifier (PA). A combined two-tone signal centered at 6 GHz with  $\Delta f = 1$  MHz tone spacing, i.e.,  $f_1 = 5.9995$  GHz and  $f_2 = 6.0005$  GHz is generated by Keysight E8267D Vector Signal Generator (SG), and is amplified from  $-10$  dBm up to 30 dBm by a BONN power amplifier and fed to the phase shifter under test. The output signal from the phase shifter is monitored by Agilent N9020A MXA Spectrum Analyzer (SA). Spectrum analyzer is set to monitor slightly larger band than  $2f_1 - f_2$  to  $2f_2 - f_1$  so as to show the IMD3 products.

The measurement setup is shown in Fig. 3.39, in which LC-NaM is being measured for example. The Agilent 87222C switch is used to linearize the power amplifier as following.

1. At each power level, it first switches to path B (calibration path). The signal from the signal generator is pre-distorted by using the Keysight Multitone software to counteract the non-linearity of the devices in the loop, especially the power amplifier. These harmonics are suppressed to be 100 dB lower than the fundamental two tones, such that they are barely detected in spectrum analyzer.
2. Next, it switches to path A (DuT path), where the detected IMD3 by spectrum analyzer is generated by the DuT only. Before IP3 measurement, the gain from signal generator until DuT (including the power amplifier, coupler, bias T and wafer probe) and the gain from DuT until spectrum analyzer (including the wafer probe, bias T, coupler, attenuator, and switch) are measured respectively, such that the desired RF power can be accurately applied to DuT at desired frequency.

Measured power of fundamental output tones and IMD3 products based on  $\Delta f = 1$  MHz tone spacing, as well as the spectrum at a certain power level are given in Fig. 3.40 for all three LC-NaMs. Since LC-NaMs are all passive components with very low loss ( $G < 0$ ), the fundamental output trace almost passes the original point, which leads to  $\text{OIP3} \approx \text{IIP3}$ . The spectrum analyzer has a very high dynamic range for high IP3 measurement as shown in the spectrum, tones with higher than  $-130$  dBm power are observable on spectrum analyzer, while in IP3 plot, noise level is around  $-80$  dBm. This is because around 50 dB loss occurs from the probe to spectrum analyzer, among which 16 dB loss is introduced by directional coupler and 20 dB loss is introduced by attenuator. They are applied to protect the switch

### 3 Liquid Crystal-based Microstrip Delay Line Phase Shifters

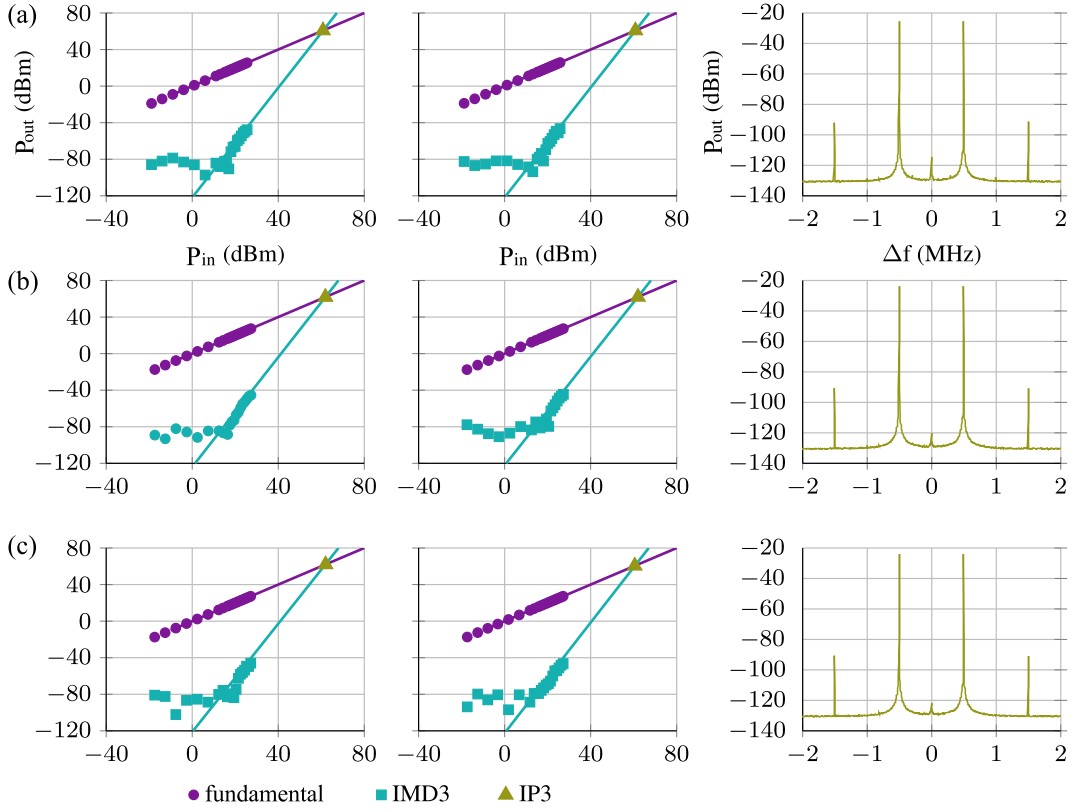


Figure 3.40: IP3 measurement of the three LC-NaM demonstrators. (a) GT3-23001, (b) GT5-26001 and (c) GT7-29001. From left to right, unbiased case, fully biased case and the spectrum of the output signal at  $P_{\text{out}} = 24$  dBm.

and spectrum analyzer from high RF power at the expense of decreased dynamic range of spectrum analyzer.

When  $P_{\text{in}} > 18$  dBm, IMD3 products arise above noise level, and strictly follow the slope of 3, which validates the measurement.

All three LC-NaMs have  $\text{OIP3} \approx 60$  dBm, which indicates very high linearity of the proposed LC shifters and LC materials of GT-series. This result corresponds well with that reported in [Goe10], the improvement is mainly due to the introduction of pre-distortion of the calibration path. The setup is also used to measure the IP3 of LC-DGS with 20  $\mu\text{m}$  thick GT3 layer and a similar IP3 is observed.

#### Power Handling Capability

IP3 is an imaginary point that is never reached in reality. It indicates how linear the device is when working with low input power, i.e., linear region below 1-dB compression point. The performance of the phase shifter at high RF power, especially the S-parameter is measured, as shown in Fig. 3.41 (a). Due to power amplifier, only forward transmission  $S_{21}$  is measured, and a simple response calibration [ZSW93] is performed instead of the LRRM

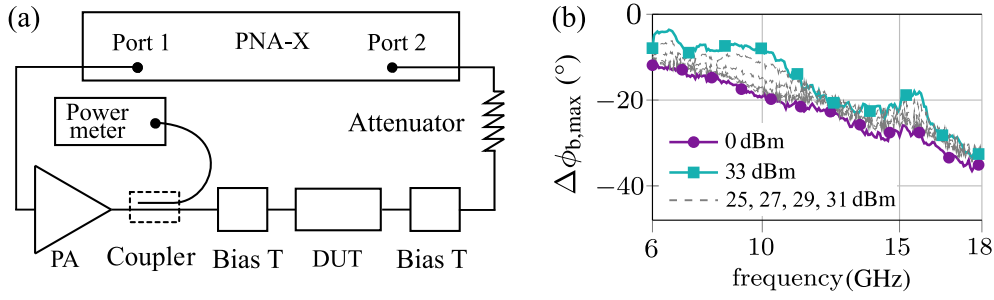


Figure 3.41: (a) Block diagram of the non-reciprocal high power S-parameter measurement setup. (b)  $\Delta\phi_{b,max}$  of LC-NaM with GT7 under different RF power.

method. Measured normalized  $\Delta\phi_{b,max}$  of LC-NaM with GT7 at various power levels is given in Fig. 3.41 (b).  $\Delta\phi_{b,max}$  starts varying above 27 dBm, but the phase shifter is able to handle at least 33 dBm power with only slightly degraded behavior without destruction or irreversible issues. The reason might be, that high RF power leads to increased temperature of LC, and thus, decreased LC tunability [Tes+21]. Thus, a high power phased array is realizable consisting of large amount of LC phase shifters.

### 3.8 Summary

In this chapter, LC based MSL phase shifters are studied. Starting with the fundamental microwave transmission line theory, equivalent circuit of MSL and telegrapher's equations, slow-wave effect of MSL is explained, based on which MSL with reduced physical length and less insertion loss can be realized by introducing periodic lumped artificial structures. To suit LC technology, IMSL is widely used instead of conventional MSL due to its good encapsulation of LC and high LC tuning efficiency. The details of fabrication and on-wafer measurement of LC-IMSL are discussed.

Three variations of LC-IMSL combining slow-wave effect are demonstrated, namely LC-LMSL, LC-DGS and LC-NaM. They are realized by artificially modifying the electrode, the ground plane and the dielectric substrate, respectively. The slow-wave effect is achieved with all demonstrators, while the LC-DGS and LC-NaM achieve much higher slow-wave and less loss than LC-LMSL. As the main contributions, LC-DGS with 4.6  $\mu\text{m}$  thick GT7 achieves peak FoM of 79  $^\circ/\text{dB}$  at 30 GHz, very high compactness of  $380^\circ/\lambda_0$  and fast switch-off response time of 51 ms. While LC-NaM with 4  $\mu\text{m}$  thick GT7 achieves peak FoM of 70  $^\circ/\text{dB}$  at 56 GHz, high compactness of  $173^\circ/\lambda_0$  and fast switch-off response time of 120 ms.

The longer  $\tau_{\text{off}}$  of LC-NaM compared to GT7-DGS is due to the LC-NaM lacking one alignment layer on the NaM surface. The fabrication of LC-DGS is more cost-effective and time-saving than LC-NaM. However, LC-DGS is limited in bandwidth due to its low-pass nature, i.e. its slow-wave effect and bandwidth are mutually contrary. While LC-NaM has theoretically no cut-off mechanisms at least up to W-band. Both of them advance the modern LC-based phase shifter researches and are promising in reconfigurable mmW applications.

### *3 Liquid Crystal-based Microstrip Delay Line Phase Shifters*

Besides, linearity and high-power performance of LC phase shifters are studied. The IP3 is higher than 60 dBm, indicating that the phase shifters introduce almost no distortion to the systems in general operation cases. The high-power S-parameters show the phase shifter can work with at least 27 dBm power.

## 4 LC-based Planar Mixed Beam-Steering and Beam-Switching Networks at Ka-Band

This chapter demonstrates how the proposed LC-DGS phase shifter in chapter 3 is implemented in reconfigurable mmW systems, e.g., phased array antennas with tunable beam forming networks.

Ideally, the tunable part of the antenna system, i.e., phase shifters should use a thin LC layer height, i.e.  $h_{LC} = 4.6\mu\text{m}$ , for fast response, while the non-tunable part should be based on thick and low dissipative dielectrics apart from LC for low-loss purpose. Although LC-DGS phase shifter with  $4.6\mu\text{m}$ -thick GT7 LC has the overall best performance in Ka-band in this work, however, when integrated into an antenna, the LC layer height of  $h_{LC} = 4.6\mu\text{m}$  is hard to be maintained, because of limitations in the fabrication techniques of our laboratory. So far, LC phase shifters and feeding network have to be

1. made in the same layer on the same substrate, because vertical coupling through thick glass is difficult;
2. based on the same dielectric, i.e., LC, because the integration of LC with other dielectrics is practically problematic within LCD fabrication process.

As a result, to fit in  $50\Omega$  system, the feeding network consisting of MSLs based on the thin LC layer will be extremely narrow and lossy. Implementing DGSs to all transmission line-based structures is a possible solution to widen the transmission lines. However, the design effort increases significantly, particularly for feeding networks of high complexity. Besides, the inevitable misalignment between transmission lines' electrodes and DGSs, as well as the undefined sub- $\mu\text{m}$  level deviation of  $h_{LC}$  leads to distinct impedance mismatch over the whole system. This will result in severely degraded performance and difficult trouble-shooting.

Therefore, for easy fabrication and characterization, IMSL structure with homogeneous  $h_{LC} = 20\mu\text{m}$  is applied in this chapter, following the same fabrication procedure as in Fig. 3.5. As a result, a MSL with impedance  $Z_C = 50\Omega$  has line width of  $w_{elec} = 40\mu\text{m}$ .

Two phased array antenna prototypes integrated with LC-DGSs are demonstrated in this chapter with continuously steerable beam. MSL end-fire Yagi-Uda antenna is designed as the radiating element. Both phased arrays are  $1 \times 4$  and work at around 30 GHz, aiming at 5G mmW applications fed by different beam-forming networks. Besides phased arrays, an interference based single-pole double-throw (SPDT) is proposed based on LC-DGS phase shifter. SPDT is designed for switching among input ports of multi-input networks such as

Butler matrices (BM). The SPDT can continuously adjust the power splitting ratio between the output ports, which allows the SPDT to be used not only as a switch, but also as beam-forming network in polarization reconfigurable antennas. These devices are capable to demonstrate the feasibility of applying the proposed LC phase shifters into tunable mmW use cases. Each component used in the aforementioned devices is introduced individually with measurement results.

The components and devices mentioned in this chapter follow the cross-section and fabrication procedures of LC-IMSL as in Fig. 3.5 as long as not otherwise stated. The circuit designs are mostly given in planar 2D layer view which better shows the dimensions.

## 4.1 Corporate Fed Phased Antenna Array With Integrated Phase Shifters for Beam-Steering

Beam-forming networks are used to combine signals from each individual antenna into a pattern that is more directional than each antenna element by itself, because of the array factor. The most widely known and used beam-forming network is the corporate feed network, which is also known as parallel feed. It is realized by concatenate several power splitters to obtain a specified magnitude and phase distribution for the output signals. As a result, the radiated beam by the array antennas can have a specified polarization, orientation, beamwidth, side lobes, etc.

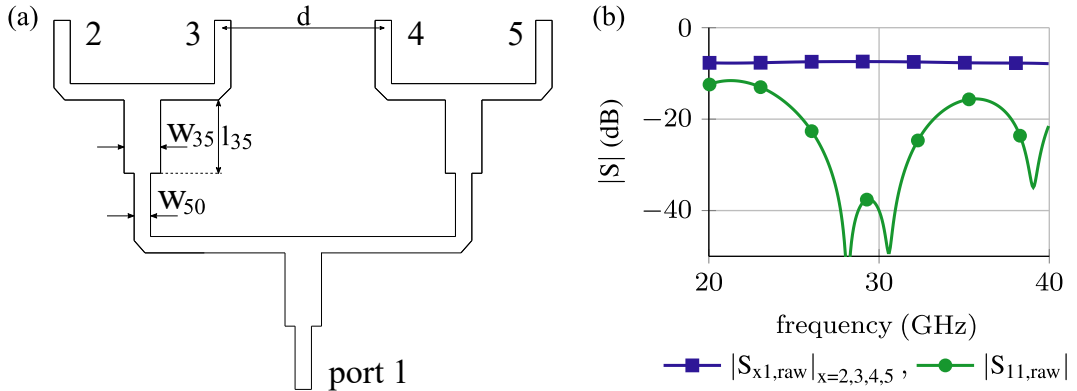


Figure 4.1: (a) Schematic diagram of the electrode of  $1 \times 4$  corporate feed network, with dimensions given as  $w_{35} = 80 \mu\text{m}$  and  $l_{35} = 1400 \mu\text{m}$  for  $\lambda/4$ -transformer with  $35.35 \Omega$  impedance,  $w_{50} = 40 \mu\text{m}$  for  $50 \Omega$ , as well as radiating element spacing  $d = 5000 \mu\text{m}$  at 30 GHz to prevent grating lobes. (b) Simulated S-parameters of the corporate feed network. Port 2,3,4,5 are equivalent due to symmetry.

In this section, to concentrate on validating the applicability of LC-DGS topology in phased array antennas, the corporate feed network is designed to be in its simplest form, which equally power splits and distributes the incident power evenly to the individual antenna element.

The schematic diagram and design parameters of a  $1 \times 4$  corporate network with equal



#### 4.1 Corporate Fed Phased Antenna Array With Integrated Phase Shifters for Beam-Steering

power and equal phase splitting are shown in Fig. 4.1 (a). To maintain  $50\Omega$  at both input and output ports,  $\lambda/4$ -transformer with line impedance  $Z_C = \sqrt{50 \cdot (50/2)} = 35.35\Omega$  realizes a smooth power division with low reflection. Simulation results are shown in Fig. 4.1 (b). From 24 GHz to 40 GHz,  $S_{11} < -15\text{ dB}$  is achieved representing good impedance matching. Considering metallic and dielectric loss, simulation indicates the network introduces additional 1.2 dB to each output port beside the intrinsic 6 dB power split.

##### 4.1.1 Integrated LC-Phase Shifter with Defected Ground Structure (DGS)

###### Resistive Chromium Bias Line

In chapter 3, biasing of the LC phase shifters is realized by directly applying bias voltage between electrode and ground through the RF probe for fast proof-of-concept. However, this is not possible when multiple phase shifters are integrated in one device, e.g., phased arrays. In order to manipulate  $\Delta\phi$  of each phase shifter independently, individual bias voltages are needed for each phase shifter. Highly resistive lines are used for conducting bias voltage to MSL. It is conductive for DC or low frequency AC bias voltage, with negligible influence on the RF circuitry due to the extremely high resistance. It can be realized from the seed layer as explained in Appendix A.1. For example, Chromium (Cr) lines in [Saz+11b] and indium tin oxide (ITO) lines of higher resistivity in [Al+08]. In the proposed antenna array, Cr lines have thickness, width, length of 20 nm, 40  $\mu\text{m}$  and 30 mm, respectively, with measured DC resistivity of around 120 k $\Omega$ .

###### DC Block

Individual biasing of phase shifters requires them to be DC isolated from each other and from other non-tunable parts of the circuit, while the RF transmission is not interrupted. This can be realized with the help of a DC block, as shown in Fig. 4.2. The DC block consists of back-to-back cascaded via-less MSL-to-CPW transition as shown in Fig. 4.2 (a)(b). The broadside overlapping area of the MSL and CPW on ground plane forms a capacitor and couples the RF power via-lessly in a certain frequency range [LM04], while DC transmission is blocked. Refer to Fig. 3.7, the radial stubs and CPW contact pads are designed for on-wafer measurement.

The LRRM calibrated raw S-parameters of the DC blocks with different gap length and the TRL de-embedded S-parameters of DC block A are shown in Fig. 4.3. All DC blocks show good matching with  $|S_{11}| < -15\text{ dB}$  from 22 GHz to 40 GHz. TRL kits were only designed to de-embed DC block A, which shows a de-embedded IL of 0.9 dB at 28 GHz. Based on this, the de-embedded IL of DC block C is estimated to be  $\approx 0.5\text{ dB}$  according to simulation.

###### Meandered LC-DGS phase shifters with Cr Lines and DC Blocks

LC-DGS phase shifters in this section are meandered as in Fig. 4.2 (c) to keep it within the array size of  $\lambda/2 \times \lambda/2$ . DC block A and C are on both ends of the LC-DGS phase shifter

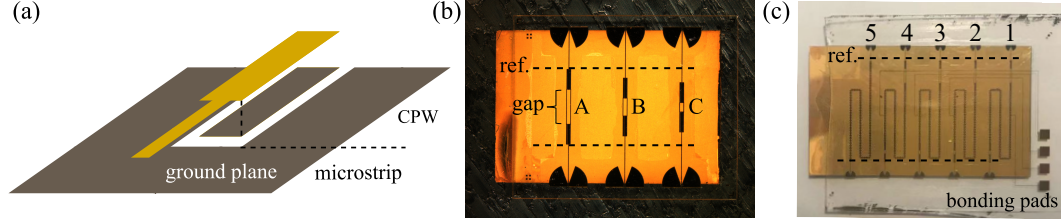


Figure 4.2: (a) 3D schematic diagram of the broadside coupled MSL-to-CPW transition. (b) DC blocks filled with LC with different gap lengths of 2000, 1000 and 500  $\mu\text{m}$  for DC block A, B, C, respectively. (c) Meandered LC phase shifters with DC blocks on both ends and Cr bias lines. Dashed lines represent the reference plane after TRL de-embedding.

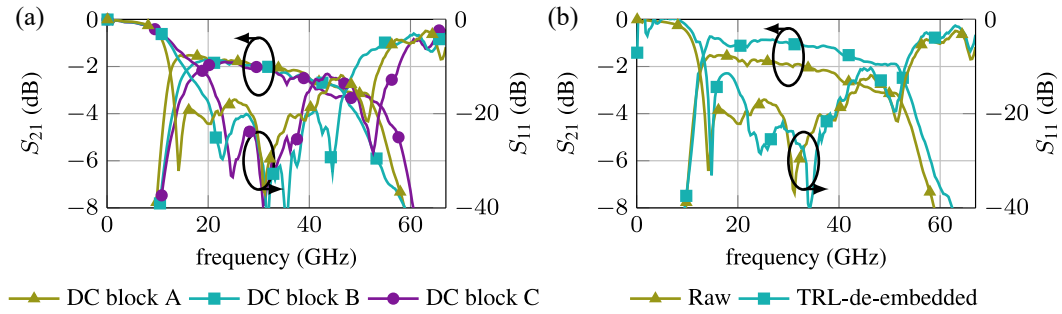


Figure 4.3: (a) Raw S-parameters of DC blocks with different CPW gap length. (b) Raw and TRL de-embedded S-parameter of DC block A.

for individual biasing requirement. DC block A are used to permit all Cr bias lines to cross, thus, with a larger gap than C. Besides, LC-DGSs are biased by using Cr bias lines, which are routed to the bonding pads cross the gaps of the DC block A, which helps arranging the layout. GT7-29001 LC is filled into the 20  $\mu\text{m}$  high cavity for high FoM. The 5<sup>th</sup> LC-DGS on the very left side is without DC blocks or Cr bias line serving as reference.

The measured raw S-parameters of the meandered LC-DGSs are shown in Fig. 4.4. With or without DC blocks,  $|S_{11}| < -15$  dB is almost valid from 15 GHz to 40 GHz, except that at 26 GHz,  $|S_{11}|$  of LC-DGS with DC blocks rises to  $-13$  dB. This indicates that meandering of the LC-DGS barely introduces reflection. The insignificantly degraded matching condition is mainly due to Cr bias lines as well as a slight mismatch between LC-DGS and DC block. Fig. 4.4 (a) shows a passband starting from 5 GHz because of the via-less CPW-IMSL transition for on-wafer measurement, while passband of Fig. 4.4 (b) starting from 17 GHz is due to the integrated DC blocks, compare Fig. 4.3.

The calculated FoM and  $\Delta\phi_{b,\max}$  of the LC-DGSs from Fig. 4.2 (c) after TRL de-embedding are shown in Fig. 4.5 (a). The maximum differential phase shift  $\Delta\phi_{b,\max}$  of LC-DGS with DC blocks is measured to be  $400^\circ$  at 28 GHz at 20 V DC bias. The FoM is calculated to be 45  $^\circ/\text{dB}$ , including DC blocks. For LC-DGS without DC block, a  $\Delta\phi_{b,\max}$  and FoM equal to  $475^\circ$  and 54  $^\circ/\text{dB}$  can be achieved, respectively.

#### 4.1 Corporate Fed Phased Antenna Array With Integrated Phase Shifters for Beam-Steering

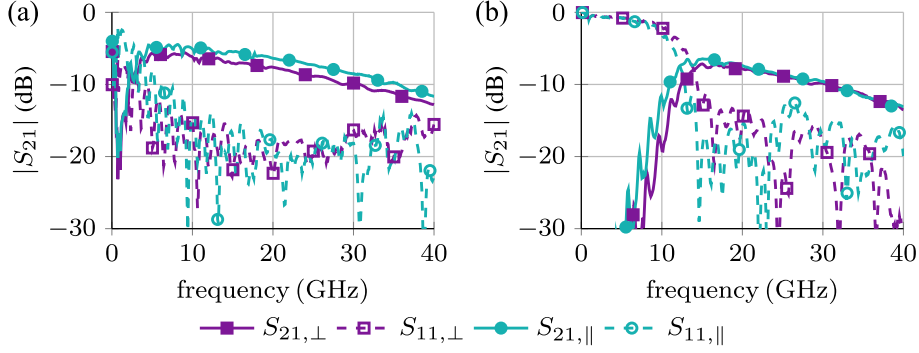


Figure 4.4: Raw S-parameters of (a) the reference LC-DGS phase shifter without DC blocks or Cr bias line at the very left side, (b) LC-DGS phase shifter with two DC blocks and Cr bias line connecting bonding pad.

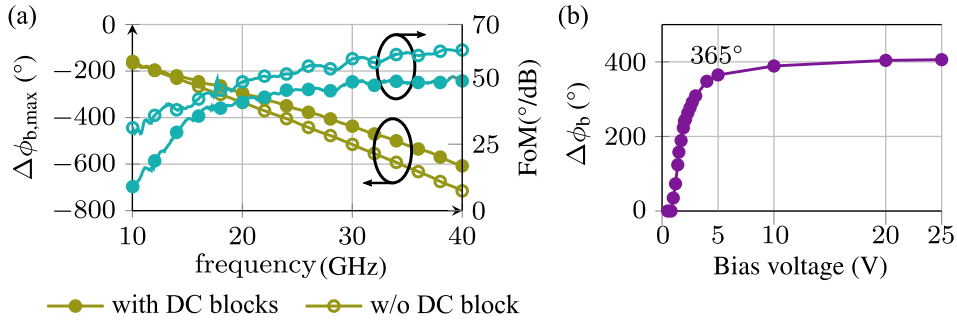


Figure 4.5: (a) Extracted FoM and  $\Delta\phi_{b,\max}$  based on de-embedded S-parameters of LC-DGS. (b) Phase response of LC-DGS phase shifter with DC blocks regarding DC bias voltage at 28 GHz.

The phase shift  $\Delta\phi_b$  versus bias voltage is shown in Fig. 4.5 (b). The phase shifters are designed to provide  $\Delta\phi_{b,\max} > 360^\circ$  for full scanning range, and it is found that a DC bias voltage of 5 V already fulfills the requirement with  $\Delta\phi_b = 365^\circ$ .

It is worth mentioning, that the bias voltage used in this chapter is DC instead of 1 kHz square wave in chapter 3. This is because our anechoic chamber are not equipped with multi-channel square wave generator. For later measurement of phased arrays systems, integrated LC-DGSs are much easier to be biased simultaneously, using a multi-channel DC voltage supplier for practical considerations.

##### 4.1.2 Planar Yagi-Uda Antenna

Reported LC based planar reconfigurable antenna arrays generally uses patches as the radiating elements [Kar+12b; Pan+22; Zha+17], since patches are easy to be expanded into a 2D M×N array without increasing fabrication effort significantly. The patches alone constitute the third metal layer of the array, which is on the same substrate as the ground plane of the phase shifters but the opposite side. The signal modulated by LC phase shifters

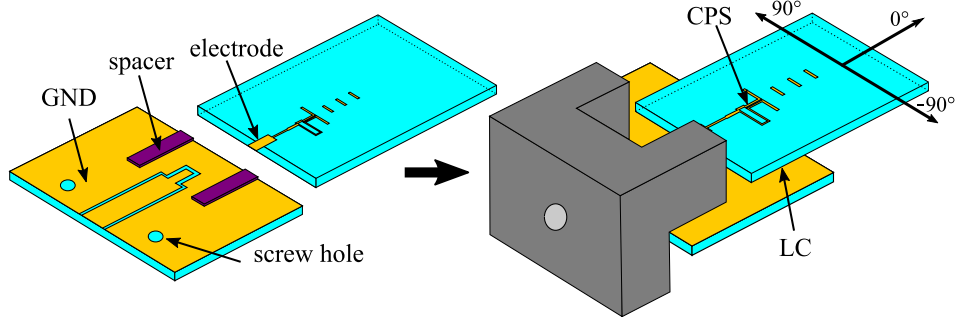


Figure 4.6: 3D schematic view of the proposed Yagi-Uda antenna with integrated coaxial-CPW-IMSL transition for measurement purpose. Coordinates are given for far field measurement.

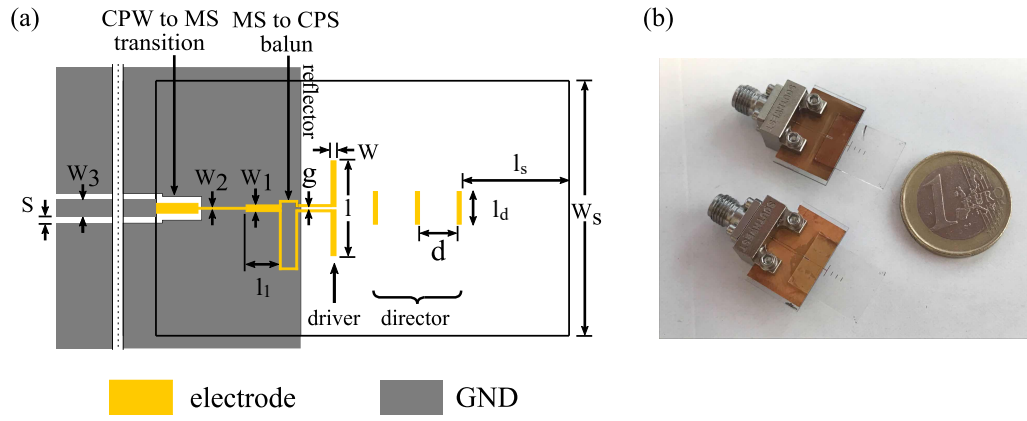


Figure 4.7: (a) Dimensions of the planar Yagi-Uda antenna:  $w_s = 10$  mm,  $l_s = 6.9$  mm,  $l_d = 900$   $\mu$ m,  $d = 1025$   $\mu$ m,  $w = 120$   $\mu$ m,  $l = 2630$   $\mu$ m,  $g = 15$   $\mu$ m,  $w_1 = 70$   $\mu$ m,  $w_2 = 40$   $\mu$ m,  $w_3 = 500$   $\mu$ m,  $l_1 = 900$   $\mu$ m,  $s = 40$   $\mu$ m. (b) Two identically fabricated antenna demonstrators.

is aperture coupled to the patch through a slot in the ground plane.

A planar Yagi-Uda antenna is designed as a substitution to a broadside patch array and enrich the component library of the planar LC phased array to radiate to endfire. It provides the advantage of high gain, low cross-polarization level and high front-to-back ratio. Besides, the proposed antenna requires low fabrication effort because no third metal layer is needed.

The Yagi-Uda antenna design is adopted from [Kan+02], with the change from MSL to IMSL. The design is shown in Fig. 4.6. The layer view and dimensions are given in Fig. 4.7 (a).

A coaxial-to-CPW transition is designed for K-connectors from SouthWest Microwave for measuring with coaxial cable, followed by a broadside coupled CPW-to-MSL transition and the Yagi-Uda antenna, which consists of IMSL-to-coplanar stripline (CPS) balun, dipole driver, truncated ground as reflector, and three parasitic directors for increasing the radiation

#### 4.1 Corporate Fed Phased Antenna Array With Integrated Phase Shifters for Beam-Steering

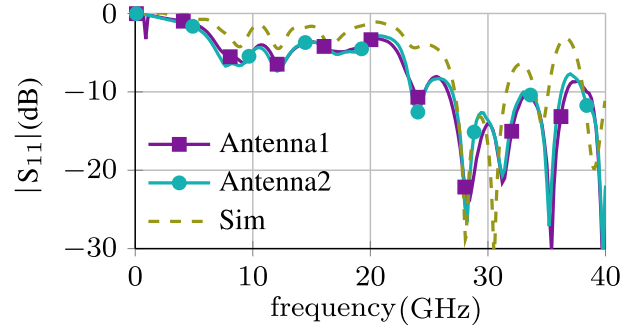


Figure 4.8: Measured and simulated  $S_{11}$  of both antenna demonstrators.

directivity. Two identically fabricated demonstrators are shown in Fig. 4.7 (b), defined as Antenna 1 and Antenna 2.

Measurements of the demonstrators start with reflection coefficient  $S_{11}$  by using PNA-X from Keysight Technologies. Results are shown in Fig. 4.8, as well as the simulated  $|S_{11}|$ . Good agreement between both demonstrators as well as between measurements and simulations are observed, which indicates decent fabrication repeatability and accuracy of simulation. 10 dB-bandwidth of the antennas are from 26 GHz to 34 GHz.

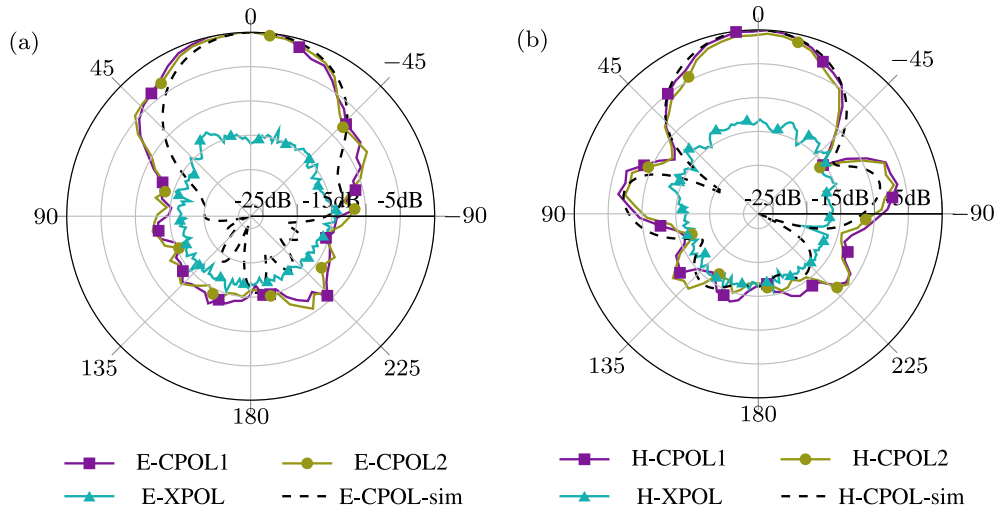


Figure 4.9: Normalized measured (in solid lines) and simulated (in dashed line) (a) E- and (b) H-planes co- and cross-polarization radiation patterns of the two planar Yagi-Uda antennas at 28 GHz. CPOL: co-polarization, XPOL: cross-polarization.

Knowing the operational bandwidth, the far field radiation patterns of both antennas are measured in the receiving mode in an anechoic chamber at 28 GHz. Results are shown in Fig. 4.9. Both antennas have almost identical far field patterns in both, E- and H-plane, and they agree well with simulations. A front-to-back ratio better than 15 dB, cross-polarization

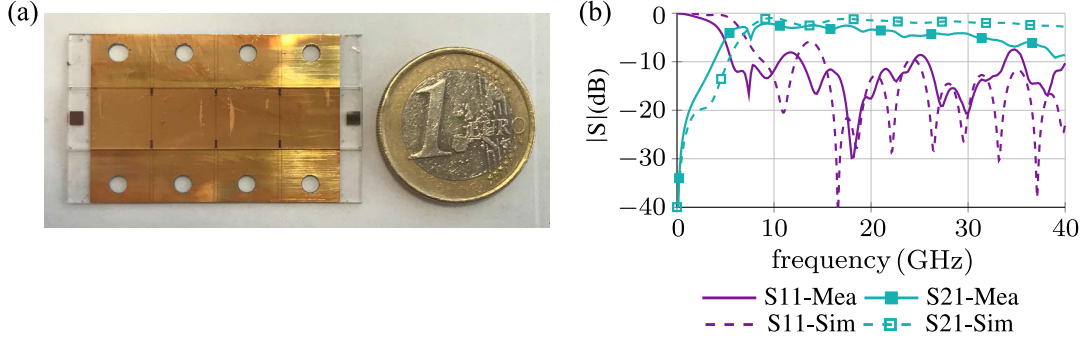


Figure 4.10: (a) Back-to-back cascaded coaxial-CPW-IMSL transitions (K-connectors are not attached). Screw holes are shared with adjacent samples. (b) Measured and simulated S-parameters of the back-to-back cascaded transitions.

less than  $-13$  dB at both E-, H-plane are observed. The patterns are of good symmetry with half power beamwidth (HPBW) of  $61^\circ$  and  $46^\circ$  on E- and H-plane, respectively.

The gain of the antennas are estimated by comparing to a standard horn antenna with known gain. While the immobile transmitter is replaced by the proposed antenna 1, horn antenna and antenna 2 serve as the receiver on the rotary platform, respectively. The difference in received power is the difference of gain, which equals to 8.6 dBi. The gain of the reference horn antenna at 28 GHz is 15.6 dBi from its datasheet, so the gain of the proposed Yagi-Uda antenna is estimated to be 7.0 dBi.

The result includes the IL of the coaxial-CPW-IMSL transition. To de-embed, a back-to-back cascaded transitions is fabricated, as shown in Fig. 4.10 (a). The measured and simulated S-parameters are given in Fig. 4.10 (b).  $|S_{11}|$  maintains lower than  $-10$  dB from 26 GHz to 34 GHz, indicating a decent matching property within the antenna bandwidth, such that the  $|S_{21}|$  is regarded as twice the IL of a single transition:  $|S_{21}| = -4.0$  dB at 28 GHz, which provides the IL of a single transition as 2.0 dB. Hence, the gain of de-embedded Yagi-Uda antenna is estimated to about 9.0 dBi.

### 4.1.3 Planar $1 \times 4$ Beam-Steering Antenna Array

A  $1 \times 4$  phased array consisting of the aforementioned components is designed. Its two-layer view is shown in Fig. 4.11 (a), where the layout of LC-DGSs, antennas, DC blocks, spacers, Cr bias lines, bias pad and corporate network are clearly seen. Fig. 4.11 (b) shows the tunable demonstrator for beam-steering screwed with K-connector, filled with GT7-29001, and soldered with pins for bias conducting. A non-tunable array without phase shifters or DC blocks, i.e. for a fixed beam, is also fabricated as reference.

As single Yagi-Uda antenna,  $|S_{11}|$  is measured to show the operational bandwidth of the array, as shown in Fig. 4.12. Both arrays are designed to operate at 30 GHz. An element spacing  $d = 0.5\lambda_0 = 5$  mm is chosen to prevent grating lobes during beam steering. While the non-tunable array almost works at 30 GHz as expected, the operating frequency of the tunable array without bias shifts down to 28.4 GHz, mainly due to fabrication tolerances,

#### 4.1 Corporate Fed Phased Antenna Array With Integrated Phase Shifters for Beam-Steering

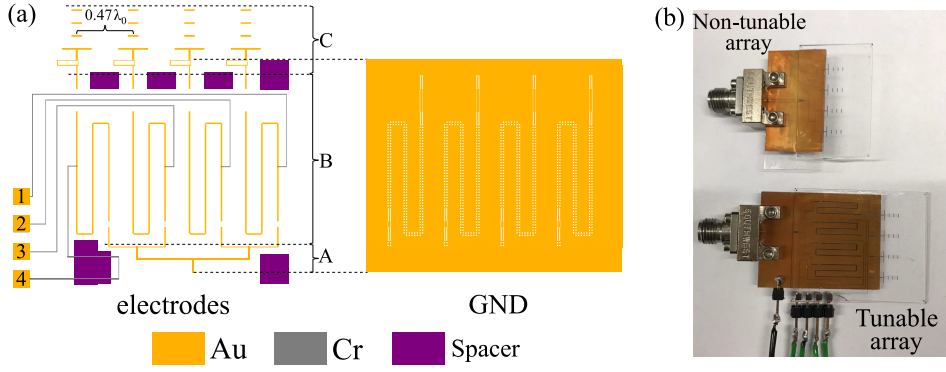


Figure 4.11: (a) Layer view of the  $1 \times 4$  tunable array. (b) Photograph of the proposed  $1 \times 4$  tunable and non-tunable array without LC-DGS phase shifters as reference.

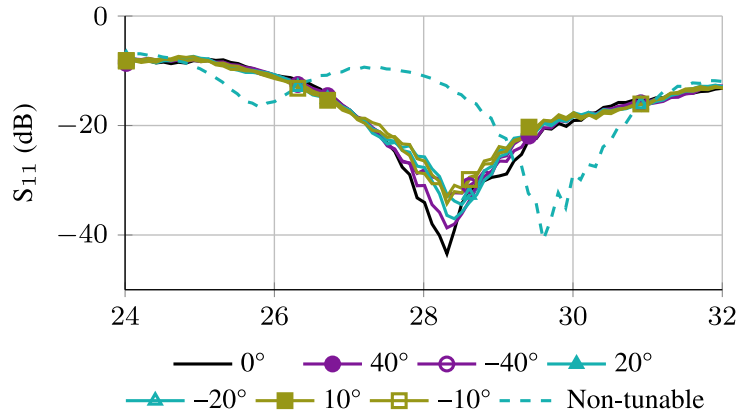


Figure 4.12: Measured  $S_{11}$  of both array antennas:  $S_{11}$  of the tunable array at different beam directions is indicated by solid lines and non-tunable array is given by dashed line. Coordinate definition refers to Fig. 4.6.

especially the deviation of LC layer height  $h_{LC}$ . It affects the resonance frequencies of the relatively narrow-band components, such as  $\lambda/4$ -transformer, broadside coupled CPW-IMSL transitions, as well as the Yagi-Uda antennas, etc. This results in element spacing of  $0.47\lambda_0$ .

The far field patterns of the tunable array are measured in anechoic chamber at 28.4 GHz. A 4-channel DC source is used to supply the bias voltages. The voltage values are adjusted manually around the values read from the  $\Delta\phi_b$ -V curve in Fig. 4.5 (b). The optimal voltages found for different beam directions are listed in Table. 4.1.

$|S_{11}|$  as well as the far field radiation pattern at different beam directions are plotted in Fig. 4.12 and Fig. 4.13, respectively. Coordinate definition refers to Fig. 4.6.  $|S_{11}|$  changes only slightly with bias settings and always stays below  $-30$  dB around 28.4 GHz.  $|S_{11}| < -10$  dB ranges from 26 GHz to 32 GHz, indicating a bandwidth of about 21 % which is much larger than the one for patch antenna arrays, which are usually less than 10 %. The side lobe level



Table 4.1: Bias voltage for variable beam directions.

Direction ( $^{\circ}$ )	Stepped $\Delta\phi_b(^{\circ})$	Ch 1-4 Voltage (V)
0	0	0.0, 0.0, 0.0, 0.0
10	30	5.0, 3.3, 2.7, 2.1
20	60	5.0, 2.7, 1.9, 1.4
40	110	5.0, 2.0, 1.3, 0.0
60	150	5.0, 1.7, 0.0, 1.9

\* Reversed voltage values are used for beam steering in symmetrical directions about  $0^{\circ}$ . Voltage values refer to Fig. 4.5 (b), with slight adjustment.

from  $-20^{\circ}$  to  $20^{\circ}$  are lower than  $-5$  dB. A narrow side lobe with  $-2$  dB level occurs when steering to  $-40^{\circ}$ . More and stronger side lobes occur when the array is steered towards  $\pm 50^{\circ}$  and  $\pm 60^{\circ}$ , where the main lobe level drops accordingly.

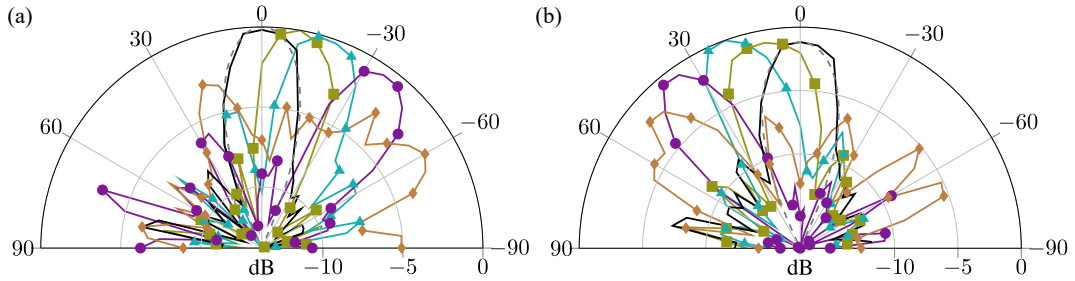


Figure 4.13: Far-field patterns of the tunable array in the E-plane for (a) positive beam angles and (b) negative beam angles. The dashed pattern at  $0^{\circ}$  is simulated.

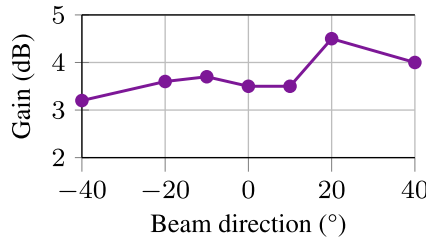


Figure 4.14: Measured gain of tunable array on different beam directions at 28.4 GHz.

The gain of both arrays are measured by comparison as for the single antenna. At 28.4 GHz, the tunable array has 3.5 dBi gain at  $0^{\circ}$ , which is 9.5 dBi less than the gain of the non-tunable array due to the integration of phase shifters and DC blocks. This corresponds well with the  $|S_{21}|$  of the LC-DGS with DC blocks in Fig. 4.4 (b).

Since the simulated pattern matches the measurement at  $0^{\circ}$ , the directivity can be directly read from simulation as 14.13 dBi. Therefore, the array efficiency of  $-10.6$  dB or 8.6 % can



be estimated at  $0^\circ$ . The gain on other beam directions are measured similarly as shown in Fig. 4.14. They are generally slightly higher than that at  $0^\circ$ , having a maximum of 4.5 dBi at  $20^\circ$ . This is because LC phase shifters are less lossy when biased, as it has been observed in previous sections.

## 4.2 Butler Matrix Fed Phased Antenna Array for Beam-Switching and Beam-Steering

The corporate feed network in section 4.1 can be regarded as the simplest beam-forming network where only signals of equal phase and amplitude are fed into antennas, i.e., a constant array factor. Although a wide scanning range can be achieved with the integration of full  $360^\circ$  LC-based phase shifters, it is at the expense of an additional 10 dB insertion loss.

The Butler matrix is a type of beam-forming network, which was first described by Jesse Butler and Ralph Lowe in [But61]. It has primarily  $N$  input and  $N$  output ports, where  $N$  usually equals to 4, 8 or 16. Depending on which input is accessed, the antenna beam is switched in a specific direction in one plane. Butler matrices can also be combined in two layers to facilitate 3D scanning [Wan+19b].

A typical  $4 \times 4$  Butler matrix is shown schematically as a part of Fig. 4.15. It consists of four quadrature hybrid couplers, two crossovers and two  $45^\circ$  fixed phase shifters. Input from one of the four input ports, the progressive phase steps among the output ports are  $\pm 45^\circ$  and  $\pm 135^\circ$ . Therefore, four discrete beam directions are obtained. Butler matrix fed beam-switchable phased arrays realized in MSL topology have been frequently reported, such as in [Ren+16; TSF19; Liu+11].

Nevertheless, beam-switchable arrays provide too low spatial resolution to fulfill requirements set by modern communication systems. To increase resolution,  $8 \times 8$  Butler matrices with eight pre-defined beam directions have been reported in [CLS10; TVL08]. However, they are not based on MSL but stripline topology, where multi-layer technologies with through substrate via (TSV) are utilized to ease the layout, namely PCB and low temperature co-fired ceramics (LTCC) with inevitably high fabrication effort and insertion loss. Besides, multi-layer stripline with through substrate via is not supported by standard panel LCD manufacturing.

Integrating tunable phase shifters to a Butler matrix enables continuous beam steering around each of the switched, i.e. discrete directions, as shown in Fig. 4.15, which has been in the focus of [Jos18]. The principle is, for a typical Butler matrix of order  $N$ , the difference among the  $N$  discrete progressive phase steps at outputs are  $360^\circ/N$ . An extra progressive phase step of  $\pm 360^\circ/2N$  is required at each output port to provide continuously tunable progressive phases. There are  $N - 1$  steps between  $N$  output ports, hence, phase shifters of  $\Delta\phi_{b,\max} = 360^\circ(N - 1)/2N$  are required to realize  $\pm 360^\circ/2N$  progressive phase steps. As a result, a Butler matrix combined with such phase shifters is equivalent to full  $360^\circ$  phase shifters, for  $N = 4$  as in our case,  $\Delta\phi_{b,\max} = 135^\circ$ , see [Jos18].

For delay-line based phase shifters, particularly those with limited FoM, e.g., LC-DGS, LC-NaM, the insertion loss and total length are theoretically reduced by 62.5% utilizing

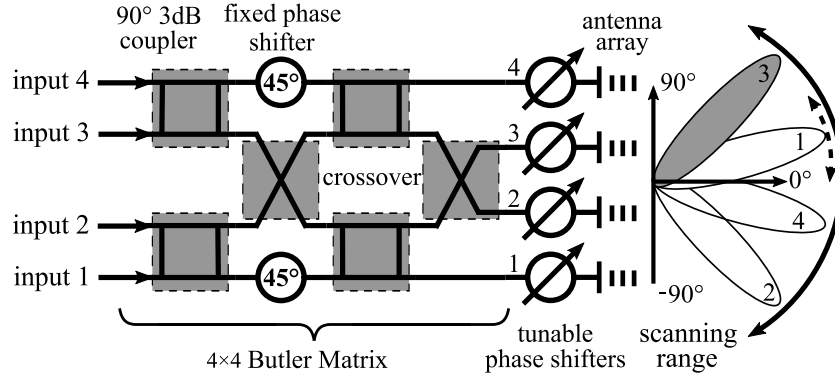


Figure 4.15: Schematic of a continuously steerable phased array fed by a typical  $4 \times 4$  Butler matrix combining phase shifters [Jos18]. The steering range of one input is represented by the dashed arrow. The solid arrow shows the combined steering range of the phased array. The serial numbers of ports and phase shifters, as well as the coordinate system describing the radiation directions are also defined.

135° phase shifters instead of 360° ones. They can be meandered easily within the limited area of  $\lambda_0/2 \times \lambda_0/2$  in an array environment. This is promising in phased arrays of high compactness and high dynamic range. Besides, beam switching combined with a beam scanning range around allows a more efficient targeting and locating of objectives. Such idea has been reported in [CLS10] where a stripline Butler matrix integrated with semiconductor varactor based reflection type phase shifters is reported. However, the structure is complicated and its application in mmW range is questionable. In [Ren+20], a MSL Butler matrix integrated with varactor loaded tunable delay line phase shifters is presented. Nevertheless, the Butler matrix is narrow-band and not applicable at high frequencies either.

In this chapter, a mixed beam-switching and beam-steering IMSL antenna array based on a relatively wideband via-less Butler matrix is proposed, working from 24 GHz to 32 GHz. It consists of 135° LC-DGS phase shifters based on GT7-29001 LC layer of 20  $\mu\text{m}$ , and planar Yagi-Uda antennas. To achieve wideband, double block branch-line quadrature coupler utilizing DGS is applied. A novel wideband via-less crossover is designed to take the advantage of broadside coupling and radial stubs as virtual ground. Biasing of the LC-DGSs is similar as in section 4.1 by using DC blocks and high resistive Cr lines. The demonstrator is measured in terms of S-parameters as well as far field patterns. Finally, a comparison with the previous corporate feed phased array demonstrates the advantage and prospect of the method.

#### 4.2.1 Wideband Branch-Line 3-dB Quadrature Coupler

Compared with coupled line couplers, branch-line couplers requires no critical dimensions, so that it suits MSL circuits very well, especially in mmW range. A conventional

#### 4.2 Butler Matrix Fed Phased Antenna Array for Beam-Switching and Beam-Steering

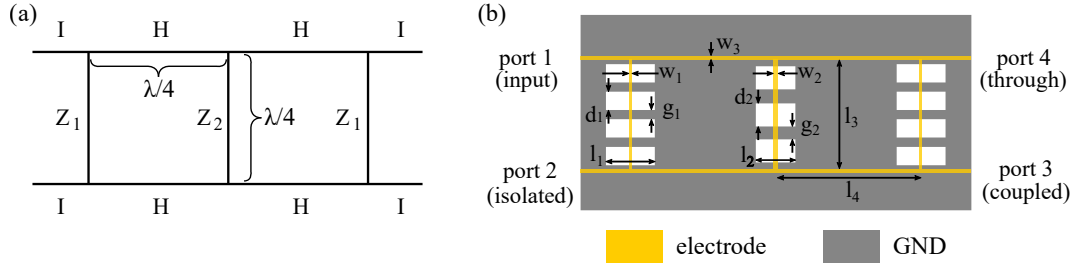


Figure 4.16: (a) Schematic of a double-block branch-line coupler. The letters represent impedance of the branches. The parameters for 3 dB quadrature condition are given as:  $Z_1 = 1/(\sqrt{2} - 1)$ ,  $H^2 = Z_2/\sqrt{2}$ , where H and Z are line impedance normalized to input impedance I. (b) Layer view, design parameters and port definition of the proposed DGS-based double-block coupler:  $w_1 = 25 \mu\text{m}$ ,  $w_2 = 45 \mu\text{m}$ ,  $w_3 = 40 \mu\text{m}$ ,  $d_1 = 188 \mu\text{m}$ ,  $d_2 = 235 \mu\text{m}$ ,  $g_1 = 94 \mu\text{m}$ ,  $g_2 = 140 \mu\text{m}$ ,  $l_1 = 500 \mu\text{m}$ ,  $l_2 = 400 \mu\text{m}$ ,  $l_3 = 1125 \mu\text{m}$  and  $l_4 = 1522 \mu\text{m}$ .

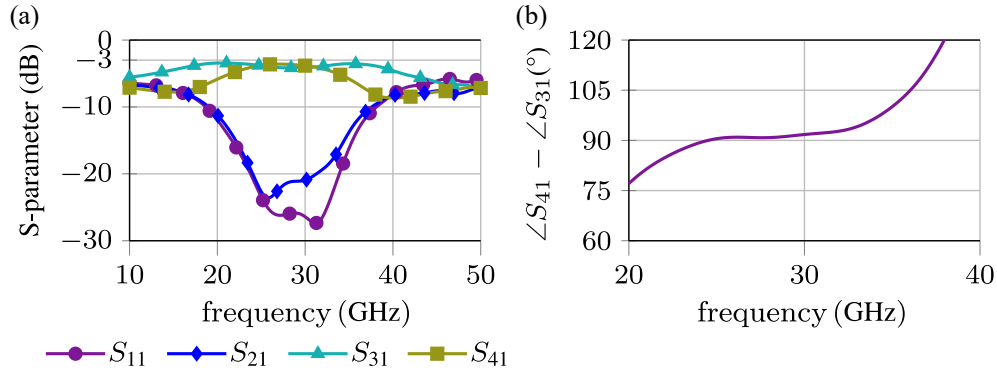


Figure 4.17: Simulation results of the proposed double-block branch-line coupler utilizing DGS: (a) Amplitudes on each port fed from port 1. (b) Phase difference between through and coupled port.

single-block branch-line coupler typically has a bandwidth of  $< 20\%$ . Butler matrix based on the coupler performs less bandwidth. It is worth mentioning, the bandwidth of the coupler not only refers to  $|S_{11}| < -10 \text{ dB}$ , but also the phase and amplitude balance of the two outputs. To match the Yagi-Uda antenna with about  $26\%$  bandwidth, coupler of wider bandwidth is desired to be integrated in the Butler matrix, e.g., double-block branch-line coupler. Schematics and design parameters for double-block branch-line couplers in 3 dB quadrature condition are given in Fig. 4.16 (a).  $Z_1 = 121 \Omega$ , H and  $Z_2$  are chosen to be  $50 \Omega$  and  $71 \Omega$ , respectively, to fulfill the 3 dB condition. Whereas, according to the experience of LC-LMSL design in section 3.3, IMSLs of high  $Z_C$ , i.e.,  $Z_2 = 71 \Omega$  and  $Z_1 = 121 \Omega$  are impractical due to fabrication tolerance and consequential high insertion loss. Therefore, DGSs are applied to achieve high  $Z_C$  while maintaining reasonable widths of the branches, as in LC-DGS. The optimized dimensions of the branches and DGSs are given in Fig. 4.16 (b).

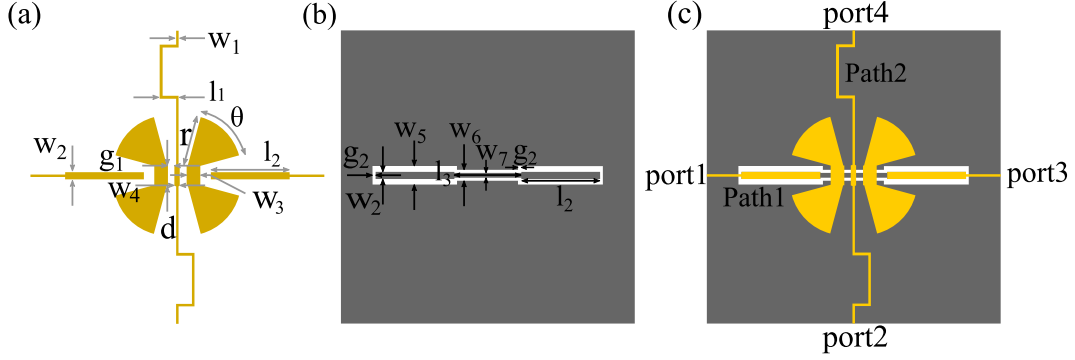


Figure 4.18: Layout of (a) electrode layer, (b) ground plane and (c) alignment of both layers. Dimensions are given as:  $w_1 = 40 \mu\text{m}$ ,  $w_2 = 100 \mu\text{m}$ ,  $w_3 = 200 \mu\text{m}$ ,  $w_4 = 80 \mu\text{m}$ ,  $w_5 = 268 \mu\text{m}$ ,  $w_6 = 160 \mu\text{m}$ ,  $w_7 = 70 \mu\text{m}$ ,  $l_1 = 280 \mu\text{m}$ ,  $l_2 = 1170 \mu\text{m}$ ,  $l_3 = 1000 \mu\text{m}$ ,  $d = 300 \mu\text{m}$ ,  $g_1 = 100 \mu\text{m}$ ,  $g_2 = 45 \mu\text{m}$ ,  $r = 800 \mu\text{m}$ ,  $\theta = 60^\circ$ . LC is filled between the two layers.

Simulation results are given in Fig. 4.17. A relatively wide bandwidth of 40 % from 22 GHz to 33 GHz with return loss  $|S_{11}| \geq 15 \text{ dB}$  and isolation  $|S_{21}| \geq 15 \text{ dB}$  are achieved, where the amplitude deviation between through port  $|S_{41}|$  and coupled port  $|S_{31}|$  is  $\leq 1 \text{ dB}$ . Within the band, a phase difference between port 3 and 4 remains about  $90^\circ$  within  $\pm 10^\circ$  deviation.

#### 4.2.2 Wideband Via-less Crossover

Crossovers are widely used in monolithic microwave circuits, especially in multi-channel systems, since they provide high flexibility to circuit layout by permitting two paths to cross each other on the same layer with decent isolation.

MSL crossovers can be classified in two categories, type (i) fully planar with one patterned metallized layer based on interference without utilizing through substrate vias, and type (ii) with through substrate vias and two patterned metallized layers. Modified rings [WAH13] and cascaded quadrature couplers [YLY11] belong to type (i). They have symmetric one layer design, which results in a small phase and amplitude imbalance. Type (i) crossovers have been widely used in reported MSL Butler matrices due to easy design, easy fabrication, and their intrinsic low imbalance nature: in [Liu+11; TCC08; Liu+05], crossovers are straightforwardly realized by cascading two 3 dB quadrature branch-line couplers; in [Ren+16; Ren+20; TYW14], crossovers use ring or double-ring configurations. However, they are interference-based, and thus, have relatively narrow bandwidth normally less than 20 % and occupy large area related to the guided wavelength  $\lambda_g$ .

Some methods are applied to type (i) crossovers to increase their bandwidth, even though they remain space consuming components. In [WAH13], a crossover achieves a 40 % bandwidth by combining a ring resonator and a circular patch with nearly half  $(\lambda_g^2)/2$  in area. In [YLY11], by cascading 4 branch-line couplers, the crossover has a bandwidth of 33 % but it is longer than  $\lambda_g$ .

#### 4.2 Butler Matrix Fed Phased Antenna Array for Beam-Switching and Beam-Steering

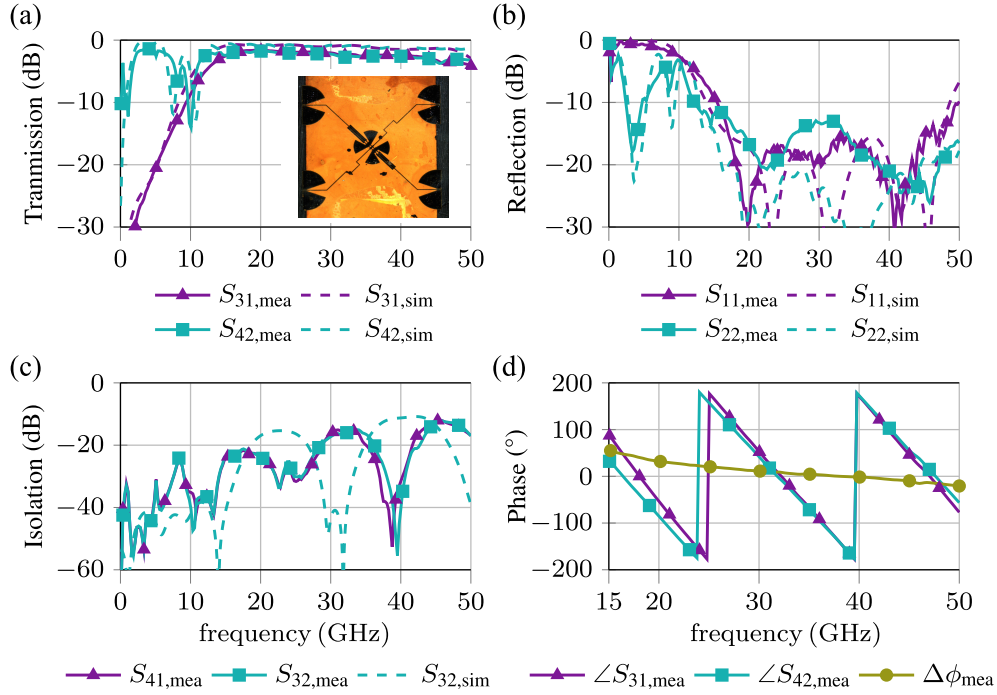


Figure 4.19: Comparison of measured and simulated: (a) transmission coefficient, (b) reflection coefficient, (c) isolation and (d) phase and phase imbalance ( $\Delta\phi_{\text{mea}} = \angle S_{31,\text{mea}} - \angle S_{41,\text{mea}}$ ) of the proposed crossover. Demonstrator is shown in (a).

Meanwhile, two metallized layers with through substrate vias are frequently used in crossover designs [EBM14; Liu+12; TFM18]. Since it is not possible to realize the crossover using only MSL lines, which would require at least three layers (two electrode layers and one common ground plane), several approaches to cross one signal strip under the other one have been proposed. In [EBM14], a MSL to slot-line transition was used, whereas a MSL to CPW transition were used in [Liu+12] and [TFM18]. They convert one path MSL mode to a certain planar mode, while the other path keeps being MSL. In this way, the broadside interference at the intersection region of the two paths is prevented. Therefore, this kind of crossover is not based on interference, and generally wideband. Due to the different design of the two paths, phase and insertion loss on both paths can be different, which is seldom concerned in reported literatures. Only in [EBM14], author adjusts the slot line length to compensate the phase deviation. However, phase imbalance still exists at high frequencies.

Different from the aforementioned type (ii) crossovers, where through substrate vias are used to route signals to different metal layers to avoid collision, the one suitable for LC based IMSL requires being fully planar without real vias, since there is no way to drill holes in LC or forming a decent conductive pillar in LCD manufacturing process.

Broadside coupling and  $\lambda/4$ -radial stubs used as virtual ground have been frequently applied in DC block and CPW-to-IMSL transition in previous chapters. They are utilized

as substitution to TSVs in the proposed two layer type (ii) crossover. The structure of the IMSL crossover filled with LC mimics that of [Liu+12], as shown in Fig. 4.18. The meandered delay line on path 2 is to compensate phase deviation of the two paths. The final demonstrator is shown in Fig. 4.19 (a).

Since the two paths are physically isolated, i.e., not interference based, the 4-port crossover can be measured as 2-port. The 4 ports with CPW-to-IMSL transitions for on-wafer measurements are designed to align parallel such that transmission and isolation can be easily measured without rotating the probes by  $90^\circ$ . Measurement results are shown in Fig. 4.19 with excellent agreement with simulation. Embedded transmissions including CPW-to-IMSL transitions are better than  $-2.0$  dB up to 30 GHz. Deviation of the insertion loss on the two paths is below 0.1 dB from 15 GHz to 45 GHz. Simulation indicates that the de-embedded insertion loss is around 1.6 dB. The return loss of both paths are better than 10 dB in this band, as shown in Fig. 4.19 (b).

The isolation measurement between the two paths should be performed with all four ports loaded, but it is not possible in our lab. Fig. 4.19 (c) shows the 2-port measured isolation as approximation. Isolation better than 10 dB is maintained from 15 GHz to 45 GHz.

The phase of both paths and their deviation are shown in Fig. 4.19 (d). The phase deviation is between  $-25^\circ$  to  $50^\circ$  from 15 GHz to 50 GHz, between  $-10^\circ$  to  $10^\circ$  from 30 GHz to 44 GHz, and equals to  $0^\circ$  at 38 GHz. The design is optimized in CST with wideband equivalent transmission phase of the two paths. The slopes deviate slightly and leads to imbalanced phase in measurement. This is mainly caused by the inaccurate LC layer thickness  $h_{LC}$  due to fabrication tolerances, which changes the electrical properties. This has been verified in simulation by sweeping  $h_{LC}$ , where  $h_{LC} = 22 \mu\text{m}$  suits the measurement best. The spacers' heights are decreased by  $2 \mu\text{m}$  accordingly in the final Butler matrix fabrication to minimize the phase error.

#### 4.2.3 Planar $1 \times 4$ Mixed Beam-Switching and Beam-Steering Antenna Array

Based on the proposed double-block branch-line coupler, the via-less crossover, Yagi-Uda antenna, as well as the tunable phase shifter module from section 4.1, including LC-DGS phase shifter with DC block and Cr bias line, the Butler matrix-based phased array sketched in Fig. 4.15 is constituted, as shown in Fig. 4.20. In Fig. 4.20 (a), the same coaxial-CPW-IMSL transition as in Fig. 4.6 is used at all 4 input ports. Details of the demonstrator refers to (d). (d)-A shows the circuit layout of the Butler matrix part, where the green dots represent the port positions defined for the Butler matrix in simulation. The simulation results of the Butler matrix are shown in Fig. 4.21. (d)-B shows the phase shifter module, and (d)-C shows the antenna.

The Butler matrix shows a simulated bandwidth of 29 % from 24 GHz to 32 GHz, where the return loss is  $|S_{22}| \geq 15$  dB and the isolation to the other input port is larger than 15 dB. This bandwidth matches well with that of the Yagi-Uda antenna. Within the band, the transmission amplitudes on the four output ports are from  $-9$  dB to  $-13$  dB with 4 dB deviation. This deviation is less than 2 dB from 25 GHz to 30 GHz. The progressive phase steps among the output ports are centered at  $-45^\circ$  and  $-225^\circ$ , when fed from port 1 and 2 respectively, with  $\pm 10^\circ$  deviation, see Fig. 4.21 (b). Due to symmetry, they are  $45^\circ$  and

## 4.2 Butler Matrix Fed Phased Antenna Array for Beam-Switching and Beam-Steering

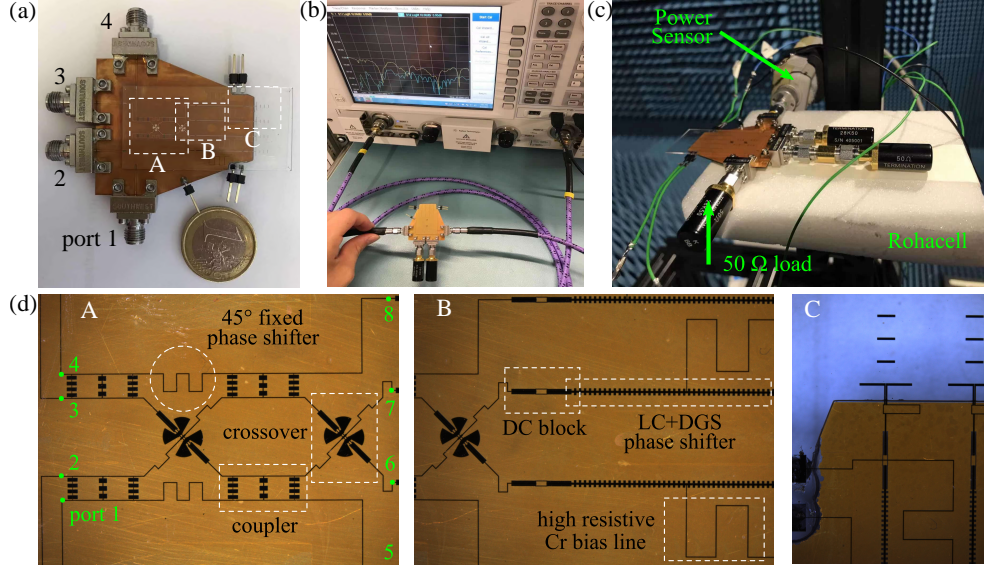


Figure 4.20: (a) Macroscopic view of the Butler matrix-based phased array demonstrator. (b) Measurement setup of its S-parameters. (c) Measurement setup of its far field patterns. (d) Zoomed in view of (a), A: Butler matrix which contains couplers and crossovers, B: interface between Butler matrix and LC-DGS phase shifters, C: antennas, Cr bias line and DC blocks.

225° when fed from port 4 and 3, respectively. The radiating element spacing  $d = 4.5$  mm is chosen, which is slightly smaller than that of the corporate fed phased array. It equals to  $0.48\lambda$  at the maximum possible operation frequency of 32 GHz to prevent grating lobes.

Fig. 4.20 (b) shows the setup of the S-parameter measurement, where two of the four ports are terminated by  $50\ \Omega$  loads, such that a 4-port calibration and measurement are avoided and simplified to 2-port measurements. This is feasible because the four input ports are isolated from each other, such that the reflections on the terminated ports are insignificant and barely influence

the other ports. Besides, the coaxial cables perform rather strong shear force and tension to the circuit, such that two cables instead of four are much easier to handle. The 2-port measurement results of the phased array demonstrator are shown in Fig. 4.22. The isolation between either two of the four ports is better than 20 dB from 24 GHz to 35 GHz. Return loss better than 15 dB from 26 GHz to 30 GHz matches the resonance of the Yagi-Uda antenna, indicating a decent impedance matching over the whole demonstrator.

Fig. 4.20 (c) shows the far field measurement setup for the demonstrator in anechoic chamber. The received power by the array is measured from one port, with the other three ports terminated with matched loads. Different from the measurements of single Yagi-Uda antenna and the corporate fed phased array, the demonstrator is held by a Rohacell platform due to the heavy weight of the screwed connectors, the matched loads, as well as the demonstrator itself. The Rohacell platform with  $\epsilon_r \approx 1$  barely influences the radiation. The cables are used to apply tunable DC bias to the integrated phase shifters from an Agilent

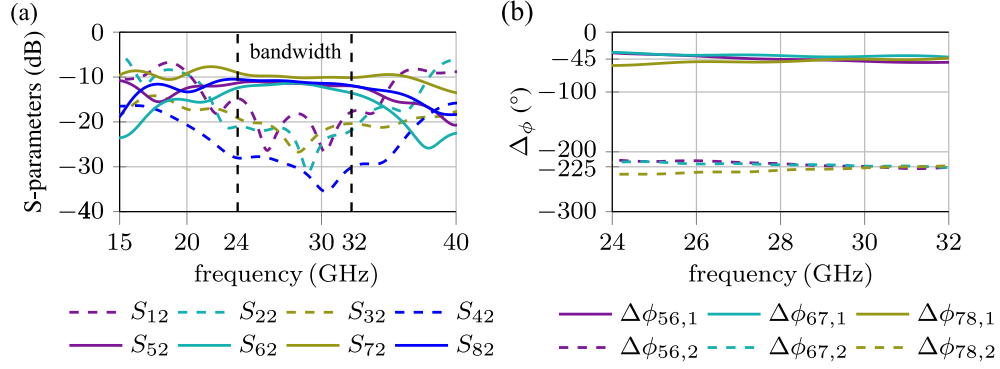


Figure 4.21: Simulated S-parameters of the proposed  $4 \times 4$  Butler matrix only: (a) received power on the 8 ports when fed from port 2; (b) The progressive phase steps between two adjacent ports, where  $\Delta\phi_{ij,k} = \angle S_{ik} - \angle S_{jk}$ .

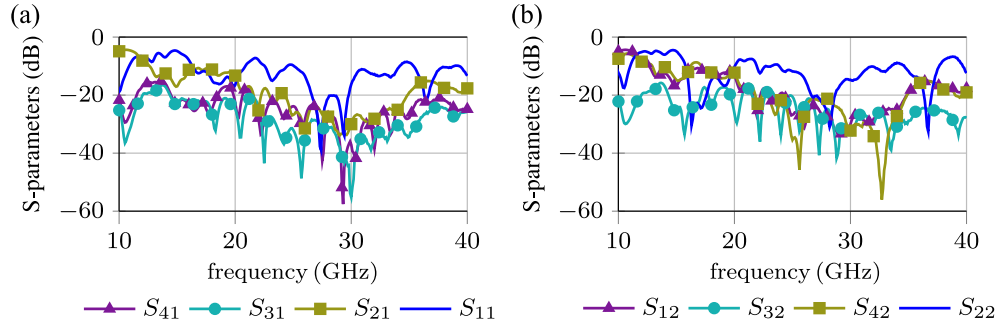


Figure 4.22: Measured S-parameters of the demonstrator when fed from (a) port 1 and (b) port 2.

N6705B 4 channel DC voltage supply.

The array without biasing the phase shifters is characterized in its E-plane from 26 GHz to 30 GHz to demonstrate the switchable beam of the Butler matrix only. Considering the asymmetric via-less crossover, the far field patterns are measured fed from all four ports, as shown in Fig. 4.23.

The beams are switched by the Butler matrix towards approximately  $\pm 15^\circ$  and  $\pm 45^\circ$  when feeding the array from port 1, 4, 2 and 3, respectively, with high symmetry. They are in good agreement with the simulated patterns at 28 GHz in dashed line, except that the measured pattern at  $+45^\circ$  shows slightly narrower beam due to the unexpected spurious lobes at around  $+70^\circ$ . This can be explained by the fabrication tolerance which causes phase error, especially on the crossovers, that deteriorates the directivity at  $+45^\circ$ . Slight beam squint is observable within the bandwidth, the higher the frequency, the less steering of the beam. This is because the Butler matrix keeps almost constant progressive phase step as shown in Fig. 4.21 (b) from 26 GHz to 30 GHz, while the element spacing  $d$  with respect to  $\lambda$  varies. The sidelobe levels (SLL) at 30 GHz fed from port 2 and 3 are as high as  $-4$  dB due to the degraded matching property at 30 GHz, compare Fig. 4.22 (b).



#### 4.2 Butler Matrix Fed Phased Antenna Array for Beam-Switching and Beam-Steering

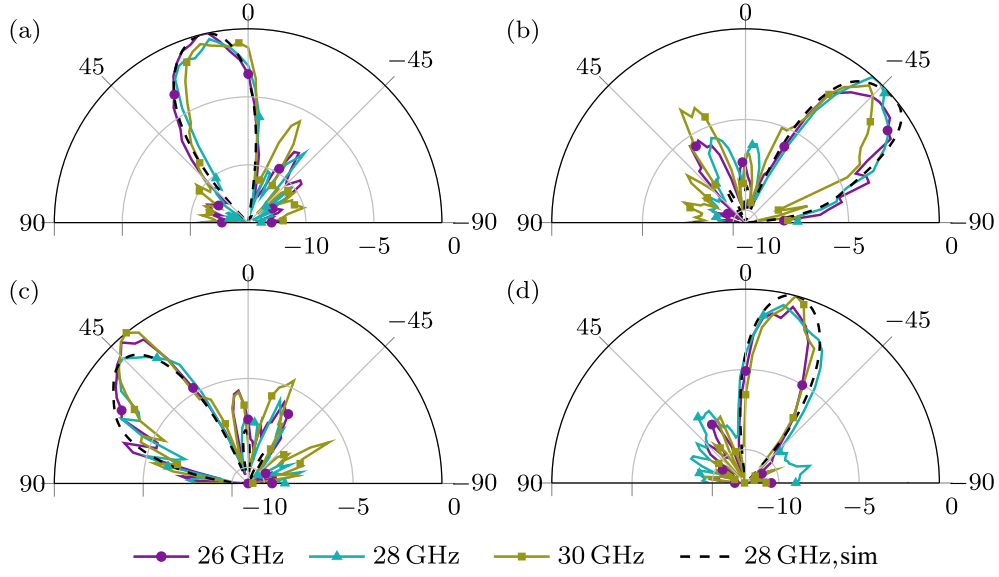


Figure 4.23: Normalized measured switchable far field co-polarization patterns in E-plane of the proposed phased array at 26, 28 and 30 GHz fed from (a) port 1, (b) port 2, (c) port 3 and (d) port 4, respectively, without biasing the phase shifters.

Table 4.2: Bias voltage settings of the phase shifters for beam-steering.

phase shifter	1	2	3	4
bias i(V)	0.0	1.6	2.1	5.0
bias ii(V)	5.0	2.0	1.4	0.0
bias iii(V)	1.9	1.5	1.2	0.0
bias iv(V)	0.0	1.3	1.6	1.9

To characterize the beam-steering capability, an additional measurement on an independently fabricated phase shifter is performed. The phase shift versus bias voltage ( $\Delta\phi_b - V$ ) curve is similar to that in Fig. 4.5.  $\Delta\phi_b = 138^\circ$  is measured at 26 GHz under 5 V with 3.5 dB insertion loss. This fulfills the requirement of  $\Delta\phi_{b,\max} > 135^\circ$  from 26 GHz to 30 GHz. To better demonstrate the beam-steering, the phase shifters are biased to reach the maximum progressive phase step of  $\pm 45^\circ$ , i.e.,  $\Delta\phi_b = 0^\circ, 45(-45)^\circ, 90(-90)^\circ$  and  $135(-135)^\circ$  for the four phase shifters, respectively. In this way, distinguishable intermediate beams among the four switched beam directions in Fig. 4.23 are achieved. In addition, manual tuning effort is largely saved since phase shifters 1 and 4 are kept to be at 0(5) and 5(0) V, only phase shifters 2 and 3 require tuning. Phase shifters' numbers refer to Fig. 4.15. The optimal voltage values found for maximum beam steering in positive and negative directions are named as 'bias i' and 'bias ii', respectively, shown in Table 4.2.

However, 'bias i' doesn't properly steer the beams of port 3 further positively. Instead,

#### 4 LC-based Planar Mixed Beam-Steering and Beam-Switching Networks at Ka-Band

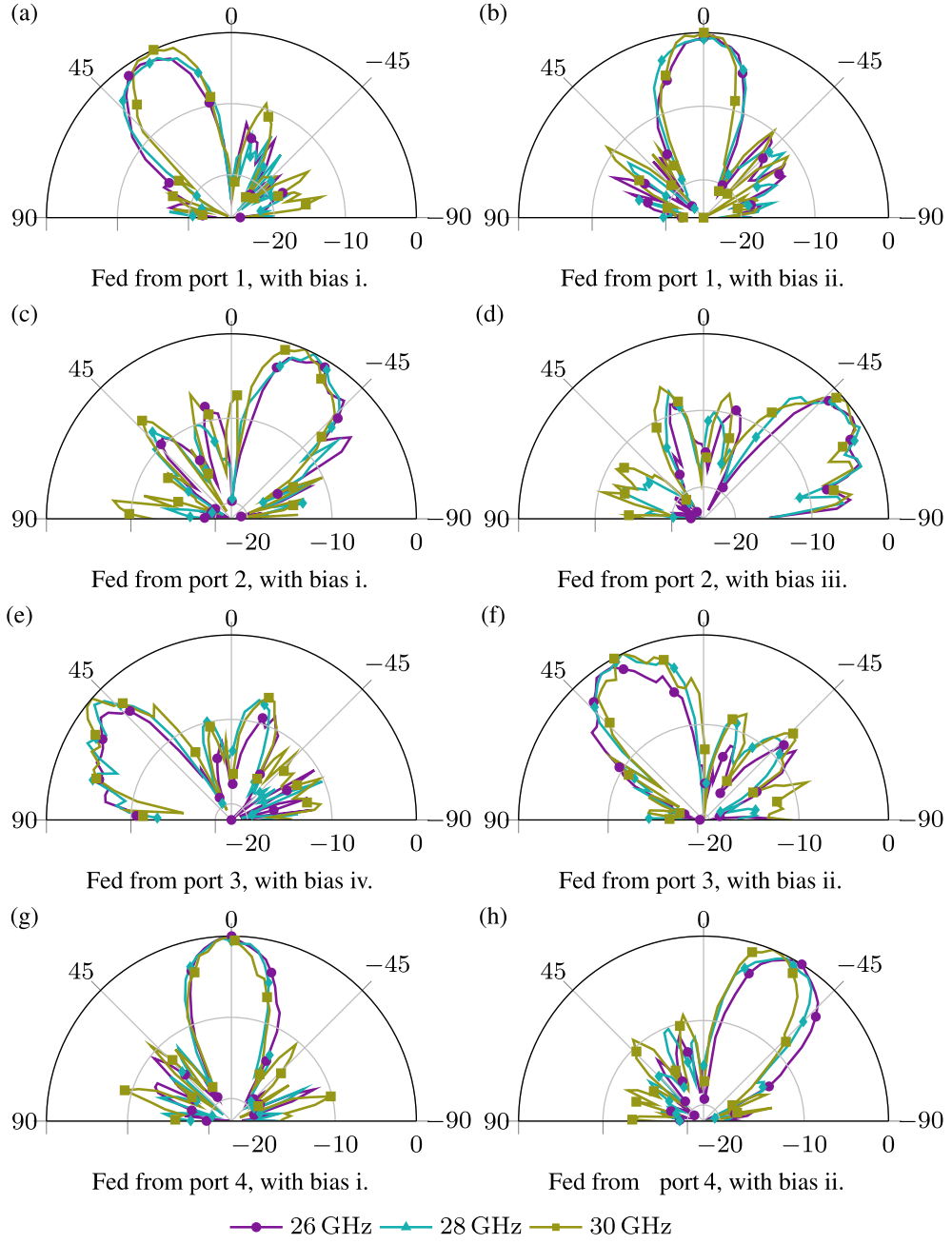


Figure 4.24: Manually-tuned far-field patterns of the phased array with Butler matrix. Patterns are measured for different input ports, frequencies, and bias voltages.

the patterns are significantly deteriorate due to the nearly  $180^\circ$  progressive phase step among the radiating elements. Similarly, ‘bias ii’ doesn’t properly steer the beams of port 2. Therefore, ‘bias iii’ and ‘bias iv’ with less bias are applied when fed from port 2 and port 3, respectively, and the array reaches the maximum possible manual steering angle with

#### 4.2 Butler Matrix Fed Phased Antenna Array for Beam-Switching and Beam-Steering

Table 4.3: Summary of far field performance of the demonstrator.

	f (GHz)	bias i(iv)					bias ii(iii)					no bias				
		$\Delta\phi$ (°)	HPBW (°)	Orientation (°)	SLL (dB)	Gain (dBi)	$\Delta\phi$ (°)	HPBW (°)	Orientation (°)	SLL (dB)	Gain (dBi)	$\Delta\phi$ (°)	HPBW (°)	Orientation (°)	SLL (dB)	Gain (dBi)
Port 1	26		27	30	-12	4.1		24	0	-11	5.1		27	15	-8	4.9
	28	90	27	30	-12	4.0	0	27	0	-11	5.0	45	27	15	-8	4.7
	30		24	27	-9	5.1		24	0	-9	4.7		27	12	-5	4.5
Port 2	26		33	-33	-8	4.8		24	-60	-6	4.1		30	-48	-6	4.0
	28	-90	33	-33	-8	4.7	-150	27	-60	-6	4.0	-135	30	-45	-6	4.9
	30		36	-30	-7	4.9		21	-57	-6	4.4		24	-45	-4	4.3
Port 3	26		27	60	-6	3.4		24	33	-7	4.3		27	45	-7	4.1
	28	150	27	57	-6	4.8	90	33	30	-7	5.0	135	27	45	-6	3.3
	30		24	54	-6	5.0		33	27	-6	5.2		24	45	-5	4.4
Port 4	26		27	0	-11	5.4		30	-33	-12	5.5		27	-15	-8	5.2
	28	0	27	0	-13	5.6	-90	30	-33	-10	5.2	-45	30	-15	-6	5.1
	30		24	3	-8	5.2		24	-27	-9	5.5		24	-15	-8	5.4

\* Patterns are measured from  $-90^\circ$  to  $90^\circ$  in step of  $3^\circ$ .

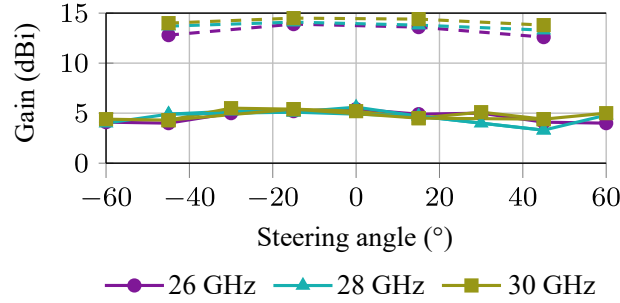


Figure 4.25: Estimated gain in solid line and simulated directivity in dashed line.

reasonable patterns. ‘bias iii’ and ‘bias iv’ are optimized similarly as ‘bias i’ and ‘bias ii’, also given in Table 4.2. The steered patterns measured fed from four ports combining the four bias cases at 26, 28 and 30 GHz are exhibited in Fig. 4.24.

The beam can be steered to around  $0^\circ$ ,  $\pm 30^\circ$  and  $\pm 55^\circ$  continuously. Beam squint is still observed under the same bias voltage, that patterns at 30 GHz are generally slightly less steered than at 26 and 28 GHz. Meanwhile, SLLs at 26, 28 GHz are improved to be  $< -10$  dB at  $0^\circ$  and  $\pm 30^\circ$ ,  $< -6$  dB at  $\pm 55^\circ$ . While the corporate fed array in Section 4.1 has severely degraded patterns at  $\pm 50^\circ$ , they remain practicable in this work, mainly due to the smaller antenna spacing that prevents grating lobes at large scanning angle.

The gain of the array is estimated by comparing it with the single Yagi-Uda antenna in section 4.1 with known de-embedded gain of 9.0 dBi. Therefore, gain of the proposed array using the same coaxial-CPW-IMSL transition is also de-embedded. The different gain values at 26, 28 and 30 GHz with multiple beam directions are summarized in Table 4.3 and plotted in Fig. 4.25. The maximum gain achieved is 5.6 dBi when fed from port 4 with ‘bias i’ at 28 GHz, while the minimum appears when fed from port 3 without bias at 28 GHz with 3.3 dBi. The lower gain of the array than the single Yagi-Uda antenna is due to the loss of the Butler matrix, DC blocks, and phase shifters. Since the far field patterns

match well with the simulation in Fig. 4.23, the directivities of the array are read from simulation. The intermediate bias states of phase shifter 2 and 3 lack of precise  $\epsilon_{r,LC}$  and  $\tan\delta_{LC}$  values for simulation purpose. Therefore, the directivities are only given in the four switched directions.

At 28 GHz and  $15^\circ$  steering, where the simulated radiation pattern fits the measurement best, the gain and directivity are 4.7 dBi and 13.8 dBi, respectively. Hence, the total insertion loss of the array excluding SMA connectors is 9.1 dB, which leads to an overall efficiency of 12 %. Besides the 3.5 dB insertion loss introduced by the phase shifters and DC blocks, the insertion loss of the Butler matrix only is 5.6 dB. Taking all material loss into consideration, the simulated average insertion loss of the Butler matrix is 4.0 dB, which is 1.6 dB less than the measured one. The deviation could be caused by misalignment between two metal layers, surface roughness of printed gold and inaccurate electrical properties of used materials.

Both phased array proposed in this chapter, i.e., with corporate feed and Butler matrix feed are compared with the state-of-the-art planar tunable phased arrays realized in other technologies, as shown in Table. 4.4. The first column only indicates the phase shifter technologies, while the other circuitry of the array system are realized on standard RF mediums such as PCB, LTCC, semiconductor wafer, LCD panel, etc. The advantages and disadvantages of each phase shifter technology have been introduced in chapter 3. As the key component to realize tunability, the phase shifter has decisive influence on the performance and characteristic of the phased arrays, such as frequency range, bias voltage, steering speed.

Except for the phase shifters, the medium based on which the rest of the array circuitry is realized also determines the overall performance. For example, varactor diodes are usually used as reflection loads in hybrid-couplers and are soldered onto PCB engraved with array circuitry [CLS10]. This is easy to be realized, but it works only at low frequencies with bulky volume. CMOS phase shifters and array circuitry are highly integrated on semiconductor wafers. The cost for design and fabrication are high, especially large precious wafer area is occupied by  $\lambda_g$ -related passive circuits, and they cannot handle high power. The ferrite phase shifter in [GS15] is integrated in the array using low temperature co-fired ceramic (LTCC) technology with complex multi-layer design and fabrication, but low gain. Besides, the maximum substrate size of an individual LTCC component is limited such that its application in large scale phased array is questionable. LTCC also has the drawbacks of limited accuracy and density of the circuitry. As for LC technology in this work, the circuitry of LC based planar phased arrays utilize LC as substrate without using its tunability to integrate with the LC phase shifters. As a result, the circuitry introduces high insertion loss, especially when LC layer is designed to be of only several  $\mu\text{m}$  thick for fast beam steering purpose. This explains the relatively low gain of the two proposed LC phased arrays even with high FoM LC phase shifters.

Compared to other reported LC phased arrays, the relatively low gain of the proposed two is partially due to the full  $360^\circ$  phase tunability, such that wider beam scanning range is achieved. More importantly, the reported ones listed in the table use much thicker LC layers ( $> 100\mu\text{m}$ ) than this work to lower their insertion loss at the expense of extremely long response time, although not mentioned in the literature.

#### 4.2 Butler Matrix Fed Phased Antenna Array for Beam-Switching and Beam-Steering

Table 4.4: Comparison of the two proposed phased arrays with the state-of-the-art planar tunable phased arrays in multiple technologies.

Technology	Frequency (GHz)	Element Number	Scanning Range (°)	Phase Shifter Range (°)	Return Loss (dB)	Maximum Gain (dBi)	Bias (V)	Reference
Varactor diode	1.6-2.8	1 × 8	1D, -54 to +54	> 120	10	11.0	5	[CLS10]
Varactor diode	5.8	1 × 4	1D, -51 to +52	90/180	11	8.0	19	[Ren+20]
Varactor diode	5.5	1 × 4	1D, -45 to +45	290	10	11.0	20	[Ji+19]
CMOS	2.4	1 × 4	1D, -27 to +22	197	10	8.4	15	[APE09]
Ferrites	13	1 × 2	1D, 0 to +30	83	10	1.0	/	[GS15]
MEMS	15	1 × 4	1D, 0 to +24	90	10	/	16	[Top+08]
BST	12	4 × 4	2D, -25 to +25	350	10	8.1	180	[Nik+17]
BST	10	3 × 4	1D, -50 to +50	342	13	/	150	[Saz+11b]
LC	17.5	2 × 2	2D, -25 to +25	300	15	5.9	15	[Kar+12b]
LC	35	1 × 4	1D, -22 to +23	270	15	6.7	25	[Li+22]
LC	12.5	1 × 4	1D, -14 to +17	146	14	3.0	20	[Ma+18]
LC	27-30	1 × 4	1D, -40 to +40	360	30	4.5	5	section 4.1
LC	26-30	1 × 4	1D, -55 to +55	135	15	5.6	5	section 4.2

In fact, as written in Section 3.6, most of the reported planar LC phase shifters are not suitable to be integrated into array environment due to either limited RF performance or their incompatibility to LCD manufacturing. Thus, the few reported LC based phased arrays all utilize the simplest conventional LC-IMSL phase shifters with homogeneous thick LC layer as easy proof-of-concept. On one hand, the proposed two are the first phased arrays based on thin LC layers, simultaneously aiming at fast response and decent gain. On the other hand, using LC-DGS topology enables the first high-performance modified IMSL LC phase shifter that is proven to be suitable in agile planar LC phased array.

By comparing the two proposed LC phased arrays, the implementation of a more complex Butler matrix instead of a corporate network increases the gain by 1.1 dB. This means, although the Butler matrix has higher insertion loss than a corporate network, the insertion loss saved by shorter LC phase shifters is more. The result demonstrates that, by combining a proper switched-beam network with smaller continuous phase shifters, it is possible to increase the array gain by saving insertion loss, while realizing a wide combined beam scanning range. A similar idea has been applied in phase shifters as mentioned in section 3.5. In semiconductor technology, a 180° continuous RTPS is combined with 1-bit 0/π STPS to realize 360° phase shift with high FoM [Han+14].

As mentioned, an integrated fixed beam-steering circuitry based on thin LC layer shows a high insertion loss. If the non-tunable circuitry part is realized on a separate thick substrate with small dissipation factor, the current insertion loss of 5.6 dB can be decreased significantly and the array gain increases accordingly. This is industrial feasible as ALCAN Systems GmbH proposed their antenna for Ka-band satellite communication shown in Fig. 4.26, where feeding network module and LC-phase shifter module are built up in different stacks [Hin20]. All parts are designed independently and in a modular fashion. Although technical details are not published, the idea of combining individual LC phase shifters of high FoM and beam-forming network of low insertion loss to achieve high gain phased array with fast response is realistic.

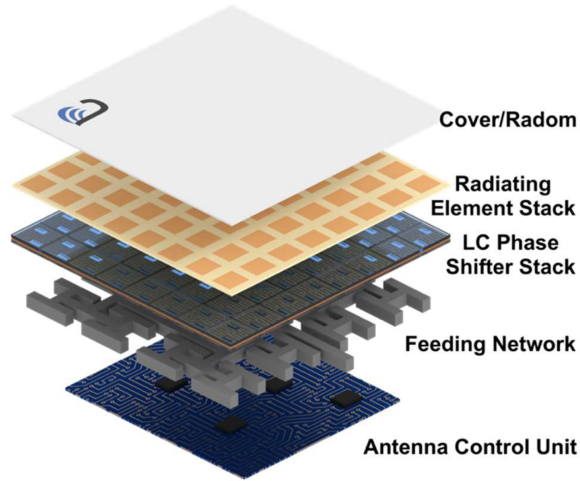


Figure 4.26: LC based phased array layout for a basic module. Courtesy of ALCAN Systems GmbH.

It is worth mentioning, for full  $360^\circ$  phase shift, less insertion loss cannot be achieved by increasing the order of Butler matrix even with low-loss substrates. A MSL  $8 \times 8$  Butler matrix is much more complex than a  $4 \times 4$  Butler matrix and the insertion loss significantly increases, while the insertion loss of the shorter delay line phase shifter decreases only slightly.

Considering the beam scanning speed, it is positively correlated to  $\tau_{\text{off}}$  of LC-DGS phase shifter. However, for steering in a certain angle range, not all phase shifters have to change their phases completely, i.e., by  $360^\circ$  within  $\tau_{\text{on}}$  or  $\tau_{\text{off}}$ , depending on the current and aimed beam position of the phase shifters. This means that the overall steering speed is governed by the distribution of the phase change rate, rather than a minimum or maximum value. As a result, beam-steering duration is always less than the switch-off time  $\tau_{\text{off}}$  (maximum, worst case) of the LC phase shifter. Empirically speaking, beam-steering duration from  $-50^\circ$  to  $50^\circ$  for the corporate feed phased array is less than  $1/3$  of the  $\tau_{\text{off}}$  of the full  $360^\circ$  LC phase shifters [JGW20]. Therefore, less than  $0.7$  s beam-steering duration is estimated for the LC-DGS based corporate feed phased array in this work. Beam-steering duration of the Butler matrix feed array is expected to be even lower due to the pre-defined phase shifts at the outputs. To the author's best knowledge, the two proposed phased arrays are the first reported beam-steering and the first mixed beam-switching and steering phased array, respectively, with theoretically  $< 1$  s scanning duration in Ka-band realized in both MSL topology and LC technology.

Moreover, lower power consumption and much lower cost of LC-based phase shifter than semiconductor phase shifter as mentioned in chapter 3 make LC technology a promising candidate in future mmW phased arrays of particularly civilian applications.

### 4.3 Single-Pole Double-Throw

A single-pole  $n$ -throw (SPnT) is required to switch among the multiple input ports of a multi-port device. For example, a SP4T is desired to switch among the four input ports of the phased array with Butler matrix in section 4.2. As the starting point, the SPnT in its simplest form, i.e., single-pole double-throw (SPDT) will be discussed in this section, utilizing LC technology.

RF switching requires selectivity among different paths, while ensuring high isolation to other unselected paths. In the past, the spotlight of RF switching mainly focused on semiconductor and MEMS technologies that switch between discrete ON- and OFF-state. Certain paths are switched-off when shorted to ground, triggered by a bias current or voltage. By these technologies, compact circuits and low-loss propagation can be realized with high isolation. There are no intermediate states between switched-on and -off. Interference-based LC SPDT introduces such novel property, i.e., a continuously adjustable power splitting ratio, thanks to the integrated continuous tunable LC phase shifters [Jos18; Jos+18a]. This feature is promising in applications requiring high flexibility. The schematic principle of an interference-based LC SPDT is shown in Fig. 4.27 [Jos18; Jos+18a].

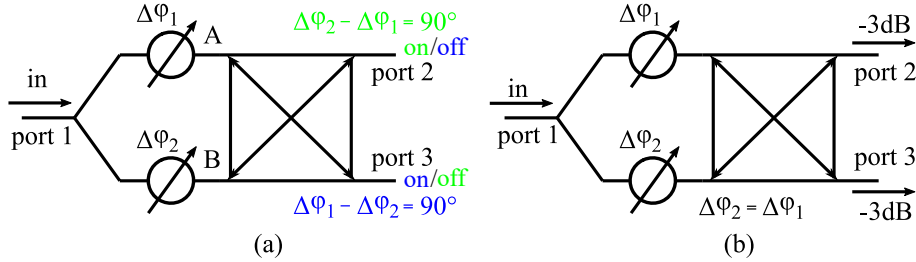


Figure 4.27: Schematic of the interference-based LC SPDT. (a) When the differential phase shift between the two phase shifters equals to  $90^\circ$ , one port is switched on and the other off. (b) When both phase shifters are equally biased, SPDT behaves as a 3 dB power divider.

When working as a SPDT, as in Fig. 4.27 (a), equally divided power goes through two differentially biased LC phase shifters and enters into the 3 dB quadrature coupler with  $90^\circ$  phase difference, such that the power is recombined at either of the two output ports by constructive interference, and cancelled at the other port due to destructive interference. When both phase shifters are identically biased, the SPDT acts as an equal power divider, as Fig. 4.27 (b). Any power splitting ratio between the two output ports is achievable by continuously adjusting the phase difference between  $0^\circ$  and  $90^\circ$ . This feature is useful in beam-forming networks which generate multiple beams simultaneously. In fact, such LC SPDT is already a reconfigurable beam forming network. For example, in [Kar+12a], when the two output signals are fed to a patch antenna in a perpendicular manner, the patch antenna is continuously tunable between linear and circular polarizations. Moreover, the LC SPDT can be used in high power calibration applications as described in Section 3.6 due to the high linearity of LC material where fast response is not required.

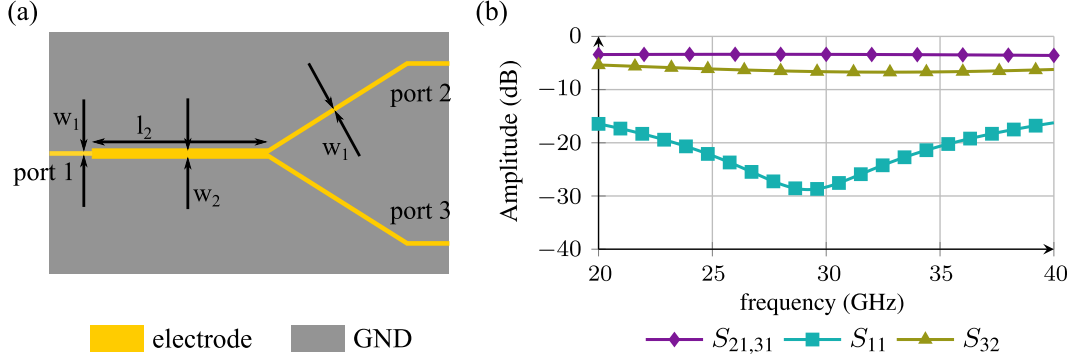


Figure 4.28: (a) Layer view of the IMSL-based power divider with dimensions given as:  $w_1 = 40 \mu\text{m}$ ,  $w_2 = 80 \mu\text{m}$ ,  $l_2 = 1420 \mu\text{m}$ . (b) Simulated S-parameter of the non-Wilkinson power divider.

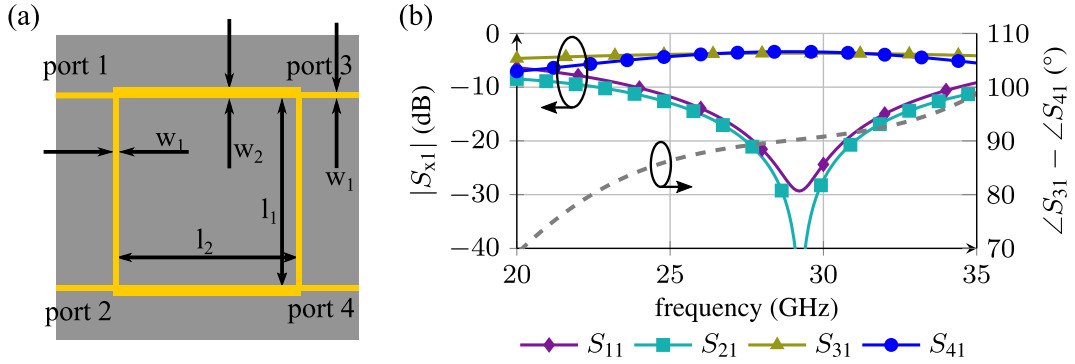


Figure 4.29: (a) Layer view of the IMSL-based branch-line coupler with dimensions given as:  $l_1 = 1500 \mu\text{m}$ ,  $l_2 = 1420 \mu\text{m}$ ,  $w_1 = 40 \mu\text{m}$  with  $Z_C = 50 \Omega$  and  $w_2 = 80 \mu\text{m}$   $Z_C = 35.35 \Omega$ . (b) Simulated S-parameter and phase of the coupler.

The LC SPDT aims at the similar frequency range from 26 GHz to 30 GHz as the Butler matrix feed phased array. It consists of three parts, an equal power divider, phase shifters, and a 3 dB quadrature coupler. The phase shifters are two with LC-DGS topology, with Cr bias lines and DC blocks as in the previous tunable phased arrays. To minimize the insertion loss, the LC-DGS phase shifters are re-designed to be able to provide  $\Delta\phi_{b,\text{max}} > 90^\circ$  at the lower limit frequency at 26 GHz with a shortened line length of 8 mm; DC blocks on both sides of the LC-DGS are DC block C from Fig. 4.2 with only 500  $\mu\text{m}$  gap and 0.5 dB insertion loss each.

Wilkinson power dividers which are commonly used for equal power division in MSL topology, are not suitable to be used in this case, since the circuitry is based on thin LC layer of 20  $\mu\text{m}$  or less, such that the lumped resistor cannot be integrated. The layer view with design parameters of the power divider is shown in Fig. 4.28. The input port 1 is 50  $\Omega$  followed by a  $\lambda/4$ -transformer of 35.35  $\Omega$  to match with the two 50  $\Omega$  output ports in parallel. The power divider has a simulated bandwidth from 20 GHz to 40 GHz with



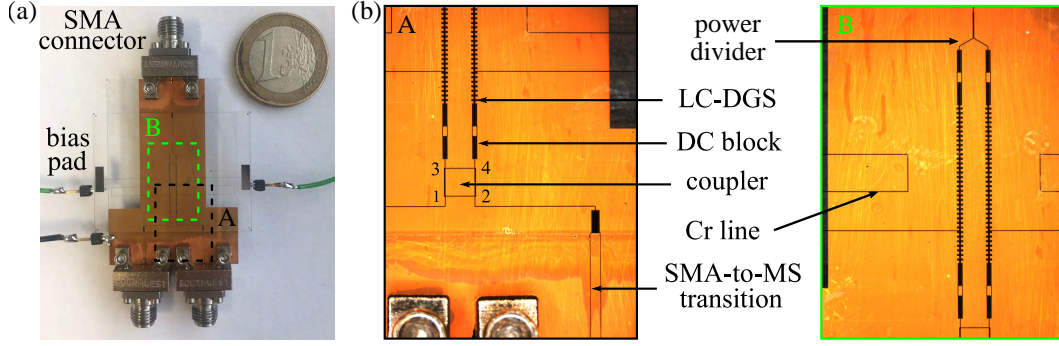


Figure 4.30: Photograph of the SPDT demonstrator in (a) macroscopic view, and (b) microscopic view.

$< 0.6$  dB insertion loss, as shown in Fig. 4.28. The deteriorated isolation  $S_{32}$  is due to lacking of the resistor. Different from the wideband branch-line coupler in section 4.2, the normal single-block branch-line coupler without using DGS is utilized for low insertion loss consideration. The design parameters are shown in Fig. 4.29 (a).

The simulated RF performance of the coupler is given in Fig. 4.29 (b). The transmissions to the through and coupled ports are  $S_{31}$  and  $S_{41}$ , respectively. They are higher than  $-4$  dB from 25 GHz to 33 GHz, with  $< 1$  dB imbalance in amplitude and  $> 13$  dB return loss. The phase difference between  $S_{31}$  and  $S_{41}$  is  $90^\circ$  with  $\pm 5^\circ$  deviation.

The SMA-to-IMSL transition is the same as in previous phased array demonstrators. The final SPDT demonstrator, combining all components, is shown in Fig. 4.30. The dimension of the SPDT excluding bias and transitions is  $18.5 \text{ mm} \times 1.6 \text{ mm} \times 1.42 \text{ mm}$ . When measured using PNA-X, port 3 is loaded with  $50 \Omega$  termination to simplify the 3-port measurement to 2-port, as in section 4.2. Only phase shifter A is biased to switch to port 2. The S-parameters measured from 20 GHz to 35 GHz are given in Fig. 4.31. The DC bias voltage is increased from 0 V to 10 V in steps of 1 V. The maximum transmission  $S_{21}$  appears at 5 V, and decreases with increased voltage afterwards. This indicates the phase shift  $\Delta\varphi_1 = -90^\circ$  under 5 V bias. The raw measured  $|S_{21}|$  (in dashed lines) contains the insertion loss of twice SMA-to-IMSL transition which can be de-embedded by using the back to back connected transitions as in Fig. 4.10. Instead of traditional TRL calibration, the method in [Man+06] gives an easier way to perform de-embedding based only on a ‘thru’ standard. The de-embedded  $|S_{21}|$  is shown in Fig. 4.31 (a) in solid lines.

$S_{11}$  in Fig. 4.31 (b) shows the bandwidth of the SPDT from 26 GHz to 30 GHz with return loss  $> 15$  dB. The bandwidth is limited by the power divider and coupler of relatively narrow band. In this band, SPDT has an de-embedded insertion loss of 3.4 dB to 4.5 dB when switched on. It is also noticed that the transmission  $S_{21}$  has a 2.5 dB to 3.0 dB increment when biased from 0 V to 5 V, as the result of changing from an equal power divider to switch-on state.

Then, the output is changed to SPDT port 3, while maintaining bias on phase shifter A to measure  $S_{31}$ , as shown in Fig. 4.31 (c).  $S_{31}$  equals to  $S_{21}$  when phase shifter A is not biased.  $S_{31}$  decreases to less than  $-28$  dB by  $V_B = 5$  V, when port 2 is switched on and port

#### 4 LC-based Planar Mixed Beam-Steering and Beam-Switching Networks at Ka-Band

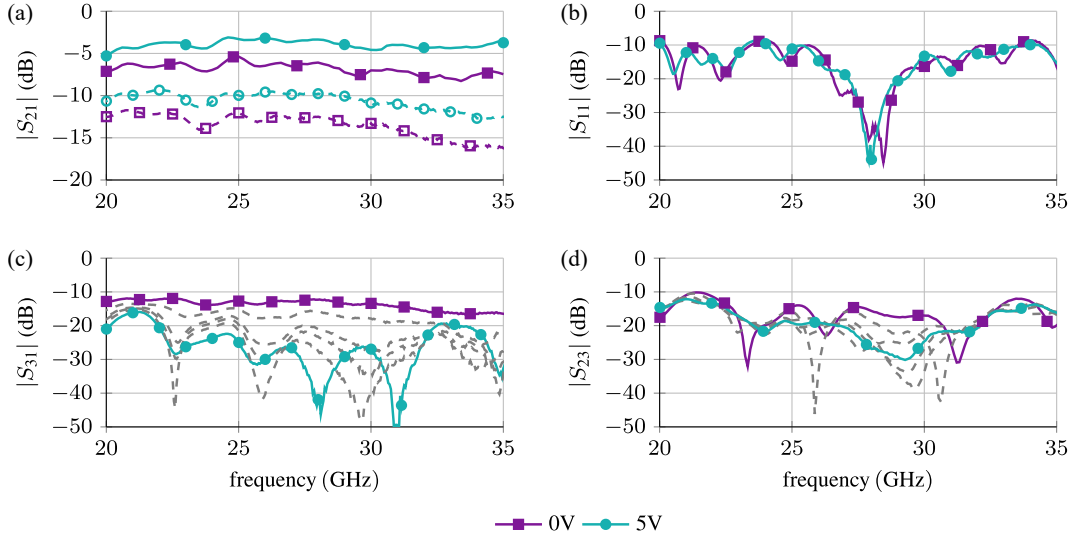


Figure 4.31: Measurement results of SPDT demonstrator: (a) Raw (dashed) and de-embedded (solid) transmission coefficient of switched-on path. (b) Reflection coefficient of switched-on path. (c) Isolation of switched off port, dashed lines represent intermediate states. (d) Isolation between the two output ports.

3 is switched off. The extremely low leakage from the input port to the switched-off port indicates that the demonstrator works well as an SPDT.

The isolation between the two output ports 2 and 3 is measured with port 1 loaded, see Fig. 4.31 (d). Although the isolation between port 2, 3 of the non-Wilkinson power divider is inferior from Fig. 4.28 (b), isolation of SPDT is decent. Under all bias cases,  $|S_{23}| < -15$  dB is measured. Taking the transitions' insertion loss into consideration, good isolation of  $> 10$  dB is still valid for all bias cases even though the resistor is omitted.

The response time of the SPDT when changing from switched-on state to power divider state by releasing the 5 V bias is measured in terms of both, amplitude and phase of  $S_{21}$ , using CW-Time mode of PNA-X, as shown in Fig. 4.32. The SPDT takes around 1.5 s to

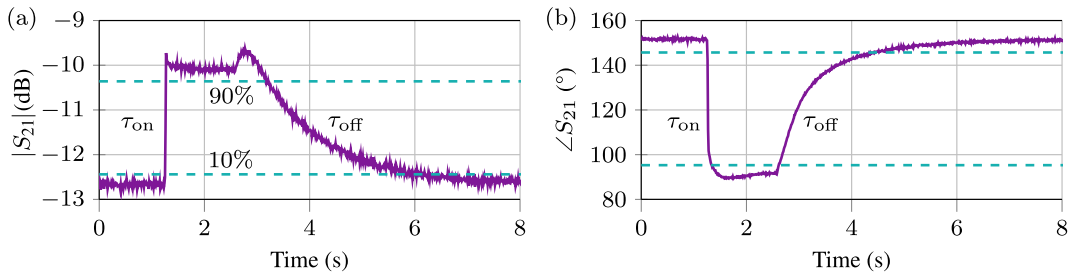


Figure 4.32: Response time measurements of the SPDT in terms of (a) amplitude and (b) phase of  $S_{21}$  at 30 GHz.

Table 4.5: Performance summary of state of the art Ka-band SPDTs.

Technology	f(GHz)	IL(dB)	Isolation(dB)	Size (mm)	$\tau_{\text{on/off}}$ (s)	Reference
MEMS	30	0.9	40	3.8×1.1	< 0.1	[Che+09]
MEMS	30	0.8	35	2.3×1.6	< 0.1	[Zah+15]
PIN diode	27	3.4	27	2.6×1.0	< 0.1	[YY13]
CMOS	35	2.2	30	0.25×0.25	< 0.1	[MR07]
CMOS	35	3.0	33	0.16×0.18	< 0.1	[LLX14]
LC-LTCC	30	9.4	26.5	70×25	> 30	[Jos+18a]
LC-LCD	30	4.5	28	18.5×1.6	1.5	this work

recover the initial power divider state in terms of phase. It is faster than the  $\tau_{\text{off}} = 1.98$  s of the integrated LC-DGS phase shifters as explained in section 4.2.

A brief summary of state-of-the-art SPDTs using multiple technologies is shown in Table. 4.5. It is easy for all the listed SPDTs to reach high isolation between the switched-on and -off ports. As insertion loss is the most important parameter of SPDTs, it is obvious that both LC based SPDTs including the one proposed in this section are not competitive with state-of-the-art SPDTs in the Ka-band. This is because the interference-based SPDT is based on an analog true delay line LC phase shifter with a certain length, which is rather lossy compared to conventional MEMS, PIN diode, or CMOS approaches with digital phase shifts in this frequency range. This is the expense of the continuously adjustable power splitting ratio.

However, the proposed one shows overall much improved performance compared to the previous one in [Jos+18a]. The LTCC technology used in [Jos+18a] limits both the LC layer thickness and minimum possible electrode width to be both  $> 100 \mu\text{m}$  due to limitation of manufacturing technique, which leads to bulky volume and extremely long response time of the device. After the lamination and sintering process, gold electrodes detachment and LTCC layers delamination appear, which influence the RF fields. These defects can only be detected by ultrasound imaging. Therefore, although with thick LC, FoM of LC phase shifter in combination with LTCC is rather poor which leads to high insertion loss. Besides, the proposed LC SPDT realized by LCD manufacturing is more cost-effective than LTCC.

The idea of interference-based LC SPDT has also been applied in W-band in waveguide [Jos+17] and dielectric waveguide [Jos+16] configurations, where higher FoM of the LC phase shifter and less insertion loss of the SPDT are achieved. However, the non-planar waveguide structures as well as the usage of external electric or magnetic LC bias system make the whole device extremely bulky. Besides, the LC of the phase shifters in waveguide configuration has  $\lambda$ -related thickness, which leads to long response time. As a result, both waveguide configurations are not applicable in lower frequencies such as Ka-band, the  $\lambda$ -related cross-section of the waveguide requires huge amount of LC to be filled in. In contrast, MSL LC SPDT has the potential to provide high RF performance with compact size and fast response in W-band. A possible approach is to integrate non-tunable circuits, i.e., power divider and coupler with tunable LC-NaM phase shifters on NaM. LC-NaM

has theoretically increasing FoM towards higher frequencies without cut off up to at least W-band. Low loss and high-Q slow-wave MSL can also be realized on NaM in W-band. Whereas, LC-DGS phase shifter is preferably to be used in low mmW range to enhance performance due to its low-pass nature, as discussed in chapter 3.

### 4.4 Summary

In this chapter, the novel high-performance LC-based IMSL phase shifter, introduced in chapter 3, i.e. LC-DGS phase shifter filled with  $20\mu\text{m}$  GT7-29001, is integrated into three electronically steerable networks: (1.) corporate-fed phased array for beam-steering, (2.) Butler matrix-fed phased array for mixed beam-switching and beam-steering, and (3.) interference-based SPDT with continuously adjustable power splitting ratio. Both phased arrays are  $1 \times 4$  end-fire radiating configurations and achieve wide 1D continuous beam scanning range in their E-plane with decent gain. The SPDT has continuous tunable power splitting ratio at the expense of relatively high insertion loss. This is a useful feature comparing to other state-of-the-art SPDTs with only on/off-states. It also shows much improved performance than the previously reported LC SPDT based on LTCC in terms of insertion loss, response time, volume, fabrication effort, etc. Therefore, the feasibility and promising prospect of applying LC-DGS phase shifter in practical reconfigurable microwave systems is firstly validated among numerous reported LC phase shifters with higher performance than conventional LC-IMSL phase shifter. Although both phased arrays are only steerable in their E-plane, the concept can be scaled in H-plane by stacking of such 1D arrays to realize 2D beam steering. The SPDT can also be directly applied to a polarization-reconfigurable patch antenna as a beam-forming network, such that linear, circular, or any intermediate elliptical polarization can be easily achieved by adjusting the power splitting ratio.

Compared with other technologies, phased arrays based on LC beam-forming networks have the advantages inherited from the delay line based LC phase shifters, such as continuous tunability, wide operational frequency range, low insertion loss, decent gain, passive with high linearity, and low power consumption. They have advantages such as large-scale fabrication with low cost, thanks to the well-established LCD manufacturing line.

As the main drawback of the LC technology, long response time of beam-steering has been significantly improved to be less than 1 s by LC-DGS phase shifters with  $20\mu\text{m}$  thick LC layer. Hence, it is believed that the module stacking technique from ALCAN, combining LC-DGS phase shifters with less than  $4\mu\text{m}$  LC thickness can achieve high gain LC phased arrays with ms level response time. Based on this performance, the tunable LC devices are sufficient not only for most portable applications, such as inter-satellite links from a geostationary relay satellite to a low-earth orbit satellite [Teb+16], but also for on-the-move applications, such as tracking signals from a satellite by a moving car, ship, or airplane [JGW20], and even for modern agile mobile communications with low latency.

Further development of LC-based phase shifters as well as phased arrays are going into the following directions:

1. New generation microwave LCs are aiming for higher physical and chemical stability in harsh environments, e.g.  $-30^{\circ}\text{C}$ , higher anisotropy in relative permittivity up to 1.2, and a larger ratio of rotational viscosity  $\gamma_{\text{rot}}$  over the elastic constant  $K_{11}$  for faster switch off time  $\tau_{\text{off}}$ .
2. Since LC-DGS design with LC layer thickness of  $h_{\text{LC}} = 4.6\mu\text{m}$  already achieved  $\tau_{\text{off}} = 51\text{ ms}$ , LC-DGS topology with precise  $h_{\text{LC}} \leq 2\mu\text{m}$  should achieve  $\tau_{\text{off}} < 10\text{ ms}$  while maintaining or even increasing the FoM and compactness.
3. Inspired by the low-pass-based LC-DGS topology, band-pass artificial structures are promising to be applied in LC phase shifters with narrower passband, targeting directly the band of interest with even higher slow-wave effect.
4. New types of substrates with special electrical properties are promising in combination with LC, for example, NaM with easy and high-quality through substrate via approach. NaM represents a promising interposer in passive mmW devices, as to be discussed in the next chapter. The combination of these advanced materials with LC should find wide use in miniaturized high-performance reconfigurable mmW systems.
5. Advancing assembly technology of the whole electronically steerable array system, including the antenna control unit, the feeding network, the phase shifter panel, and the radiator stack. Integration of thick, low-loss dielectric material in LCD manufacturing as the substrate for non-tunable circuitry is desired.



## 5 Nanowire Membrane (NaM) Interposer Technology at W-band

At lower frequencies, components of an RF system can be connected through cables or printed transmission lines. As the operating frequency increases to mmW range, the components of mmW systems are expected to be close to each other to reduce the signal degradation and space consumption, e.g., fabricating all components on the same substrate as in chapter 4, where feeding network, phase shifters and radiating elements are integrated into one LCD panel. However, different components take advantage of different substrates, such that the feeding network based on LC introduces unnecessarily high insertion loss. Therefore, an interposer technology is required that facilitates the integration of components of different technologies. A good interposer must be able to interconnect components manufactured in different substrates, and redistribute the signals. This can only be achieved by building through substrate vias (TSV) with low loss for vertical integration and ground connection, thus, creating high-quality transmission lines for horizontal integration [Lé+22]. The metallic nanowire filled membrane technology (NaM) fulfills these requirements.

NaM has been introduced in Section 3.5, where its anisotropic permittivity is utilized combining MSL to achieve low loss, and high compactness by generating significant slow-wave effect. In this chapter, instead of using the NaM with large area of homogeneously filled nanowires as an anisotropic material, nanowires are selectively grown into the Anodic Aluminum Oxide (AAO) membrane in specific areas connecting electrodes on both sides of AAO membrane serving as through substrate via. The selectivity growth of nanowires is realized by using standard photo lithography procedure as in Appendix A.1, where the uncovered area by photoresist of AAO membrane is filled with nanowires by electrodeposition. A precise modelling up to 110 GHz of such through substrate via is reported in [Pin+18]. The NaM technology offers a great flexibility in the via design, i.e., no 'drilling' effort,  $\mu\text{m}$  level cross-section, simultaneous fabrication of large quantity, dense distribution, etc., which cannot be obtained with other through substrate via technologies. The through substrate vias show a mean insertion loss of 0.23 dB with  $\pm 0.14$  dB variation up to 110 GHz for different through substrate via dimensions, which clearly advances the state-of-the-art through substrate via technologies such as on Si, Si(HR), liquid crystal polymer (LCP), and glass. These features make the NaM an excellent candidate for the development of low-cost and high-performance interposers for mmW systems. Therefore, in this chapter, a conventional  $4 \times 4$  Butler Matrix (BM) as in chapter 4 is realized on NaM, aiming as a proof-of-concept at 100 GHz.

As in chapter 4, each individual component constituting the Butler matrix is discussed, especially the crossover as key component. Due to the small size and high operating

frequency, coaxial cable measurement and termination with  $50\Omega$  matched loads are infeasible. Instead, the demonstrator is designed with CPW contact pads for on-wafer measurement purpose. A loading method for multi-port on-wafer measurement by using 2-port VNA is developed to ensure a proper design of the Butler matrix. The Butler matrix feed antenna array is finally characterized in terms of S-parameter and far field radiation patterns.

### 5.1 Compact DC to 110 GHz Crossover

The proposed crossover takes the advantage of easy through substrate via realization on AAO, which is a typical crossover of Type (ii) as defined in section 4.2. Two different crossovers are designed (Type 1 and Type 2) as illustrated in Fig. 5.1. In both designs, path A crosses under path B, using back-to-back connected MSL to CPW transitions. Type 1 utilizes MSL-CPW-MSL transition for path A, such that the signal on path A (P1-P2) is routed to the ground plane through vias, while path B (P3-P4) remains as a MSL with a slotted ground plane. In Type 2, both paths utilize MSL-CPW-MSL transitions to improve isolation in the overlapping area between each other. The design of Type 2 originates from the one proposed in [Liu+12], while it is realized at much higher frequency based on an entirely different substrate technology, i.e., NaM.

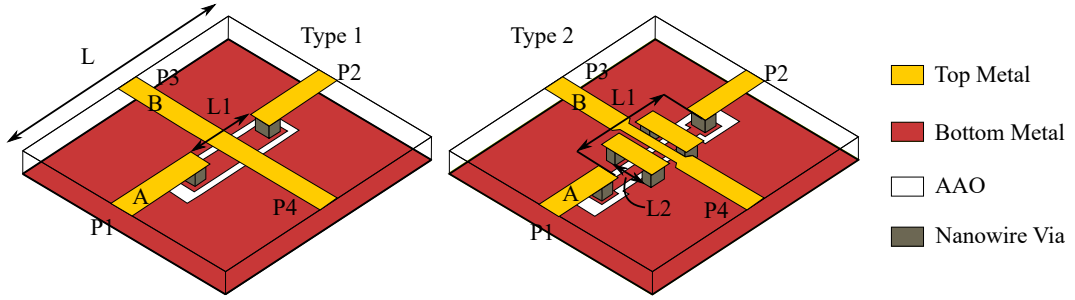


Figure 5.1: 3D schematic view of the two NaM-based crossovers. Nanowire through substrate vias are represented by solid copper blocks.

Different from section 3.5, where the homogeneously nanowire-filled NaM is regarded as an anisotropic material, the nanowire through substrate vias are modelled simply as solid copper blocks due to the dense distribution of the nanowires inside the AAO membrane. The AAO is a normal homogeneous material with  $\epsilon_r = 6.7$  and  $\tan\delta = 0.015$  at 100 GHz. The dimensions of both crossovers in Fig. 5.1 are shown in Table 5.1. The cross-section of the via is expected to be as large as possible to have high conductivity, while it has to be at least  $10\mu\text{m}$  narrower than the top and bottom metal from all sides as misalignment buffer. The  $50\Omega$  MSL on AAO has a width of  $67\mu\text{m}$ , and the vias are  $40\mu\text{m} \times 40\mu\text{m}$ . Both paths are designed to have the same physical length  $L$ . All transmission lines are designed to be  $50\Omega$ .

The fabricated demonstrators are shown in Fig. 5.2. The CPW contact pads utilize through substrate vias to connect to the ground instead of the via-less radial stubs as in



Table 5.1: Dimensions of both proposed crossovers.

dimension ( $\mu\text{m}$ )	Type 1	Type 2
L	1000	1200
$L_1$	170	330
$L_2$	/	95
MSL width	67	67
CPW width A	70	32
CPW gap A	15	21
CPW width B	/	32
CPW gap B	/	15
CPW ground B	/	67

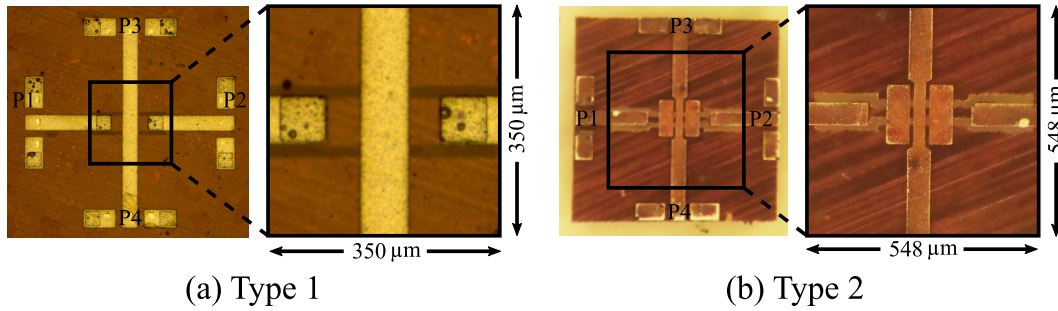


Figure 5.2: Photograph of fabricated crossovers. Bright structure is MSL (top layer), dark area is ground (bottom layer).

#### LC based IMSL.

The equivalent circuits of both designs are given in Fig. 5.3 to help understand the working principle. The through substrate vias are simply represented by an inductor  $L_{\text{vias}}$ , whereas its precise model is given in [Pin+18]. The defective ground in path B of Type 1 is represented by an inductor  $L_{\text{DG}}$ , due to the increase in the return current path that circumvents the slot.  $C_{\text{cross}}$  represents the electric coupling due to the electrode overlapping between two paths and determines the isolation, which is expected to be smaller by decreasing the overlapped area. The electric coupling of Type 1 is stronger, since MSL mode of path B penetrates into AAO membrane and interferes with CPW mode of path A. The coupling of Type 2 is weaker, because both paths have planar CPW mode in the overlapping area but on the opposite sides. For Type 2, the impedance of the CPW of path A is increased to approximately  $63 \Omega$  to compensate for a parasitic capacitance  $C_g$  between the CPW ground of path B and the CPW signal conductor in path A.

Measurements are carried out in two frequency ranges, from 0 GHz to 70 GHz where Keysight's N5227B VNA is used for a precise 4-port on-wafer measurements, and from 70 GHz to 110 GHz where 2-port measurements are realized with OML's frequency extenders. LRRM calibration and MPI's Titan T67 and T110 probes with  $100 \mu\text{m}$  pitch

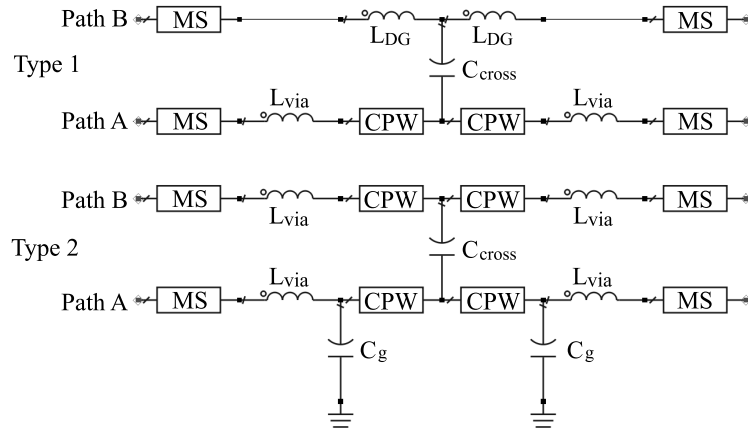


Figure 5.3: Equivalent circuits of both crossovers based on NaM.

are used, respectively. Although both crossovers are 4-port devices, their two paths are physically isolated, i.e., the isolation is not based on interference, such that 2-port measurement can be used to measure the insertion loss and return loss from 70 GHz to 110 GHz. However, isolation measurements are only accurate if the unmeasured ports are loaded with  $50\ \Omega$ . For this reason, isolation measurements are only presented up to 70 GHz. All the results presented here are not de-embedded, i.e., devices are calibrated at probe tips by the LRRM calibration.

Fig. 5.4 (a) shows the measured and simulated insertion loss and return loss for the Type 1 crossover. A good agreement is obtained between measurement and simulation results. Measured insertion loss with 1.2 dB maximum at 110 GHz is obtained for path A, while the maximum insertion loss for path B is 0.9 dB at 110 GHz. In path B, the return loss is better than 18 dB, however, for path A, it degrades to  $< 15$  dB above 42 GHz. This behavior is a result of the path A's CPW in the ground plane of the path B's MSL, which leads to defected ground. The defected ground is represented by the equivalent series inductance  $L_{DG}$  in the model in Fig. 5.3. This is not a problem up to 42 GHz, but as the frequency increases,  $L_{DG}$  degrades the performance significantly. This is verified by 3D-EM simulation using CST that the ground current of MSL in Path B circumvents the slot created by the CPW of Path A, see Fig. 5.5.

To prevent this behavior, crossover Type 2 uses also MSL-CPW-MSL transition on Path B. As can be seen in Fig. 5.4 (b), the high-frequency performance is improved above 42 GHz. The return current does not have to circumvent the defective ground, refer to Fig. 5.5, and the return loss is better than 17 dB for both paths. The insertion loss is equal to 1.3 dB in Path A and 1.5 dB in Path B at 110 GHz, which leads to an insertion loss imbalance of 0.2 dB.

The simulated and measured isolation of both crossovers is presented in Fig. 5.6 (a). In Type 1 crossover, the electric field of the MSL in Path B couples strongly with the CPW in Path A, which degrades the isolation and leads to a measured isolation of 19 dB at 70 GHz and simulated one of 16 dB at 110 GHz, respectively. The Type 2 crossover shows a

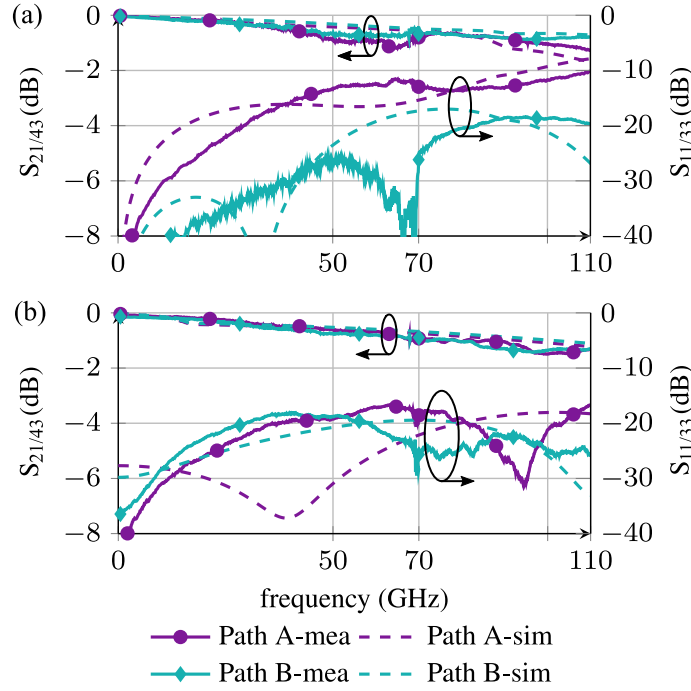


Figure 5.4: Simulated and measured insertion loss and return loss for the both crossovers.

much-improved isolation, better than 33 dB up to 70 GHz. Simulation predicts an isolation better than 35 dB up to 110 GHz. Since the simulated isolation matches with measurement up to 70 GHz, the simulated isolation from 70 GHz to 110 GHz is rather convinced.

Fig. 5.6 (b) shows the phase imbalance of both crossovers, i.e., phase difference between path A and B, which is desired to be  $0^\circ$ . Due to the defective ground, which influences the phase velocity  $v_\phi$  of path B, the Type 1 crossover exhibits a high phase imbalance of  $24^\circ$  at 110 GHz. Besides, the Type 2 crossover exhibits a maximum phase imbalance lower than  $4^\circ$  up to 110 GHz. Thus, Type 1 crossover shows a satisfying performance only up to 42 GHz. Above 42 GHz, the isolation and return loss continuously decrease, and phase imbalances increase to a great extent. While for the Type 2 crossover, except for the naturally increased insertion loss along with the increasing frequency, return loss, phase imbalance, and isolation remain excellent. Although Type 2 crossover is only measured up to 110 GHz, simulation shows it can work properly up to at least 200 GHz, since there is theoretically no cut-off mechanism of Type 2.

## 5.2 Multi-port On-wafer Measurement Method

Multi-port devices are widely used in mmW applications aiming at multi-signal processing scenarios, such as couplers, crossovers, Butler matrices, etc. In section 5.1, the on-wafer measurements of 4-port crossovers are performed only up to 70 GHz due to the difficulties as follows:

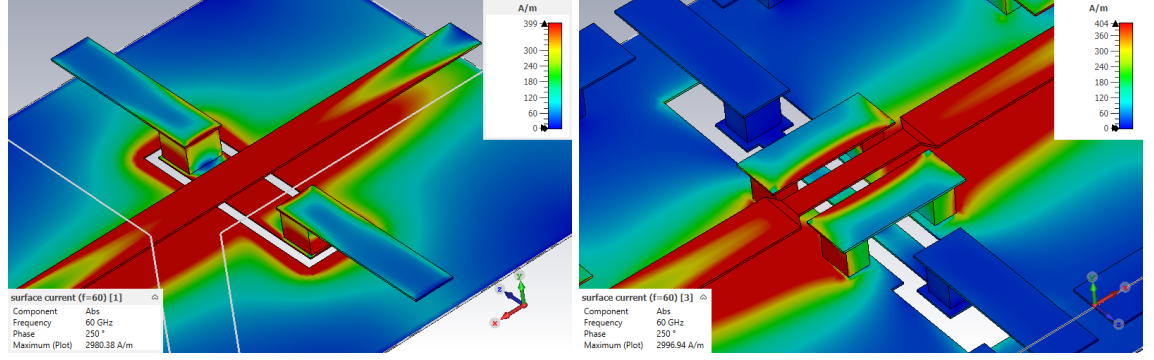


Figure 5.5: Simulated surface current on the ground plane of Path B of both crossovers.

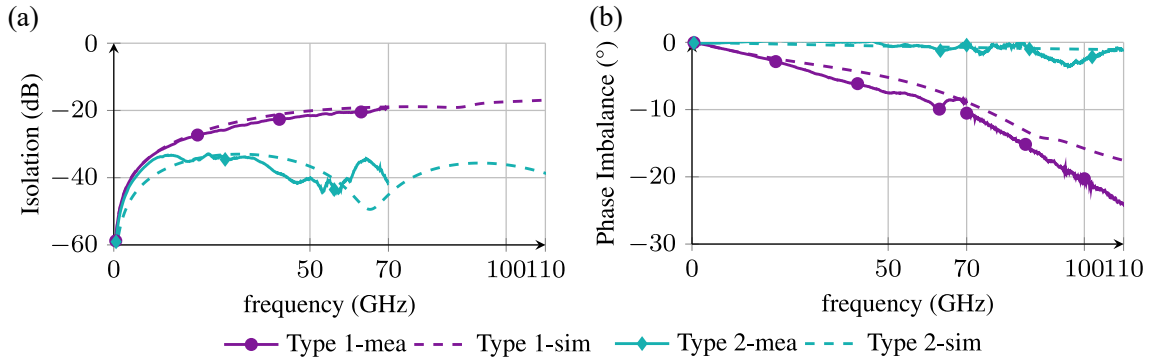


Figure 5.6: Simulated and measured isolation and phase imbalance of both crossovers.

1. Although multi-port on-wafer test sets, including VNA, probe station, probes, impedance standard substrates (ISS), frequency extender, etc., are commercially available, accurate multi-port characterization is still costly and difficult, especially at high frequencies.
2. The design of the multi-port contact pads should correspond to the dimensions of the probes, which complicates the layout.
3. Contact pads and their accesses to the DuT introduce non-negligible parasitics that need to be de-embedded afterwards. Multi-port de-embedding is difficult in terms of both, algorithm and calibration kits design.

Since 2-port VNA with  $50\Omega$  are generally used, only two of the multi-ports can be ideally terminated with internal  $50\Omega$  loads of the VNA. The remaining ports must be terminated with external  $50\Omega$  loads to accurately substitute the corresponding part of the N-port S-parameter by the 2-port measurements. Such idea has been frequently applied in chapter 4, where  $50\Omega$  matched loads are used to terminate the unused ports of Butler matrix and SPDT.

For on-wafer measurements, the external terminations have to be fully integrated. Lumped resistor [LdM09] and thin film resistor [WDR02] have been used as matched

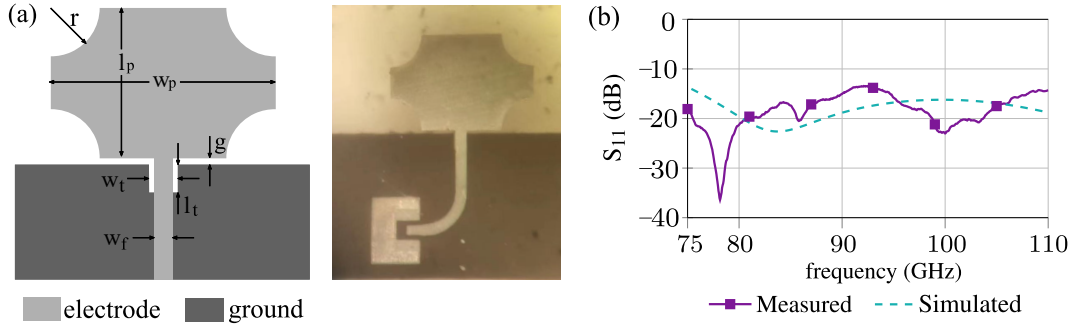


Figure 5.7: (a) Design of the broadband patch antenna load. Dimensions given as  $w_p = 0.9$  mm,  $l_p = 0.6$  mm,  $r = 0.2$  mm,  $g = 0.02$  mm,  $w_t = w_f = 0.067$  mm and  $l_t = 0.1$  mm. (b) Measured and simulated  $S_{11}$  of the broadband antenna.

load. However, they require high fabrication effort, they are highly sensitive to fabrication tolerance, and their applicability at higher frequency band is not proven. For W-band applications in this work, a broad band patch antenna is utilized as a substitution to the  $50\Omega$  loads, since it dissipates the power by radiating with low reflection. Compared with integrated resistors, the antenna can be fabricated together with DuT, which saves effort. No soldering or critical process are required, which makes the method tough against fabrication tolerance.

To realize the method, for the first design, a circular slotted patch with truncated ground plane reported in [SGk19] is utilized as broadband load. The design based on AAO membrane is shown in Fig. 5.7, together with its measured and simulated S-parameters. The cut circular slots of the patch and the distance between the patch and the truncated ground plane tune the capacitive coupling between them. The additional rectangular slot at the upper edge of the ground plane tunes the inductive part of the antenna that neutralizes the capacitive coupling between the ground and the patch, such that impedance matching is achieved in a wide frequency band. According to simulation, the depth, and width of the  $S_{11}$  are inversely related, which means the higher the return loss, the less the mismatch caused by the load, and the smaller the bandwidth. The bandwidth of the load should cover the interested frequency range, and the optimized design parameters are given in Fig. 5.7 (a). The measured and simulated  $S_{11}$  are shown in Fig. 5.7 (b). Although slight difference in terms of resonance frequency exists, the fabricated patch antenna shows a desired broadband matching with  $S_{11} \leq -15$  dB from 75 GHz to 110 GHz. Only at 92 GHz the  $S_{11}$  degrades slightly to  $-13.5$  dB. Therefore, the antenna is regarded as a decent matching load with low reflection.

The patch antenna is then applied to the measurements of a 4-port branch-line coupler designed to be centered at 100 GHz, which is to be integrated into the final Butler matrix. Due to symmetry,  $C_2^4/2 = 3$  loaded couplers are fabricated on the AAO membrane, as shown in Fig. 5.8. The measured S-parameters for the three samples are shown in Fig. 5.9 labelled as ‘2 port-Meal’. As comparison, the 4-port simulated S-parameters of the coupler are plotted as ‘4 port-Sim’.

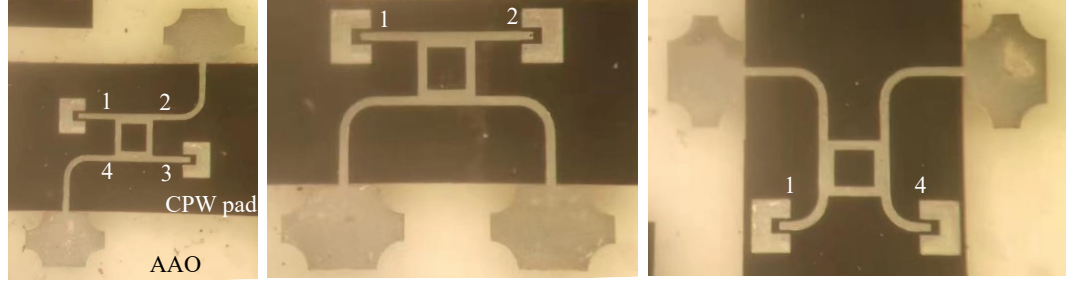


Figure 5.8: Loaded branch-line couplers. From left to right, coupling, thru and isolation are measured, respectively.

Since more complicated crossovers based on AAO membrane have been successfully modelled in simulation, the simulated results of the simpler branch-line coupler are considered to be trustable. Obviously, the 2-port measurement results of the loaded couplers differ significantly from simulation. Measured  $S_{21}$  shows increased insertion loss from 80 GHz to 90 GHz.  $S_{41}$  shows only 10 dB isolation, and  $\Delta\phi_{2,3}$  deviates from  $90^\circ$  at 100 GHz quickly. It is concluded that the loading method is non-optimal, such that relative high reflection occurs due to the loads. A post-processing method in [TS82] is performed to the 2-port measured S-parameters, aiming for de-embedding of the non-matched loads, and thus, reconstructing the 4-port results. A brief explanation of the algorithm is as follows:

1. Based on the 1-port S-parameter of the antenna load in Fig. 5.7, its impedance  $Z$  matrix  $Z_1$  ( $1 \times 1$ ) is extracted.
2. The  $C_2^N$  sets of 2-port S-parameters normalized to  $50 \Omega$  are renormalized to  $Z_1$ . This step obtains the 2-port S-parameters of the loaded couplers with all 4-port re-matched to  $Z_1$ .
3. Combine the  $C_2^N$  sets of  $Z_1$ -matched S-parameters into 4-port S-parameters, and renormalize back to  $50 \Omega$ .

The regenerated 4-port S-parameters almost overlap with the ‘2 port-Mea1’ data with no improvement, thus, it is not shown for simplicity. This indicates the limitation of the post processing algorithms that they might have special requirements of the loads but are not clarified in the literature.

Further researches concentrate on improving the loading manner to obtain good raw measured data. It is noticed from simulation that reflection occurs due to the rounded corner of the antenna feed line and mismatch between the feed line and the antenna. In the second design, meandered long MSLs with  $90^\circ$  corner as well as a new patch load are applied, as shown in Fig. 5.10, measuring  $S_{31}$  for example. The new patch load has similar performance as the previous one, but without truncated ground for easy mask alignment. The long meandered MSL which is estimated to provide 5 dB insertion loss is for power dissipation purpose, such that power dissipates on the feed line before reaching the antenna. Even

## 5.2 Multi-port On-wafer Measurement Method

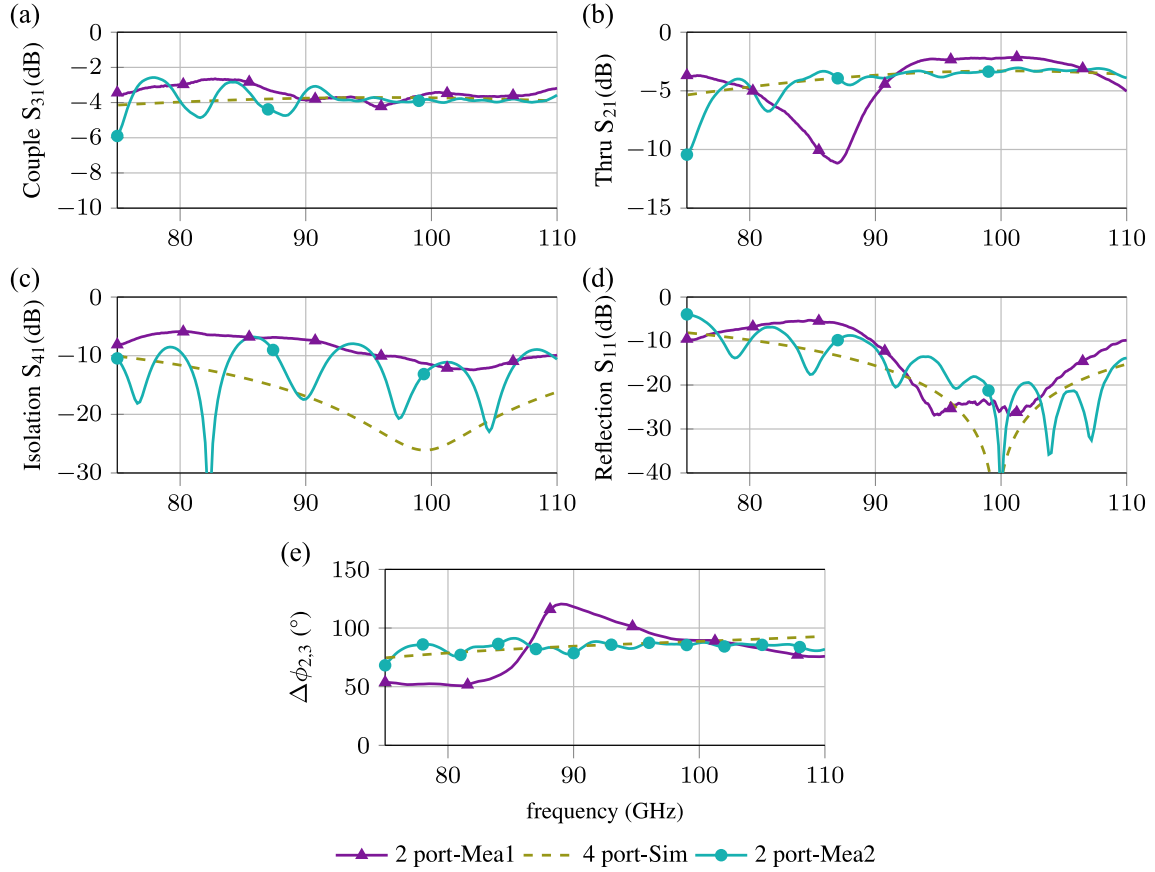


Figure 5.9: S-parameters of the coupler (a)  $S_{31}$ , (b)  $S_{21}$ , (c)  $S_{41}$  and (d)  $S_{11}$ . (e) Differential phase shift  $\Delta\phi_{2,3}$  between  $S_{21}$  and  $S_{31}$ .

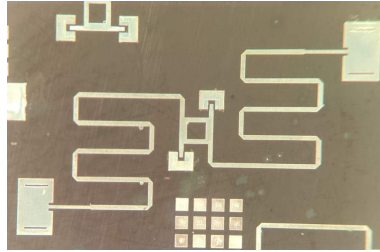


Figure 5.10: Loaded branch-line couplers of which ‘coupled’ transmission  $S_{31}$  is measured loaded with the new broadband patch antenna without a truncated ground.

though reflection happens at the antenna, the reflected power is dissipated once again on the feed line and barely impacts the matching condition.

The 2-port measurement results of the second design are shown in Fig. 5.9 labelled as ‘2 port-Mea2’ with significant improvement over the first one. The important parameters including both transmission coefficients  $S_{21}$ ,  $S_{31}$  and their phase difference  $\Delta\phi_{2,3}$  match



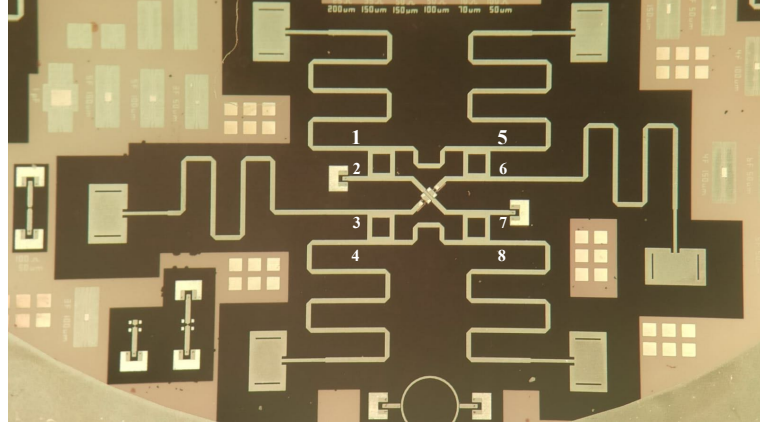


Figure 5.11: Loaded semi-Butler matrix demonstrator for characterizing phases at output ports when fed from port 2.  $S_{7,2}$  is measured in this example. All the samples measuring  $S_{5-8,2}$  are fabricated on the same wafer, others are not shown for simplicity.

with simulation very well in a wide bandwidth from 90 GHz to 110 GHz.  $S_{4,1}$  and  $S_{1,1}$  are also improved within the band. Both the branch-line coupler design and the new loading method are validated. Although the method occupies extra wafer area for fabrication of each loading cases, it is not a big issue for symmetric DuTs which work at high frequencies and without large number of ports as in this work.

### 5.3 Proof-of-Concept: Beam-Switching Broadside Antenna Array with Butler Matrix

Based on the crossover and coupler design, as well as the multi-port on-wafer measurement method at W-band, a Butler matrix based on NaM technology following the same schematic as in Fig. 4.15 can be designed. To realize a beam-switching array with Butler matrix, the output phase of the Butler matrix is of great importance.

The Butler matrix is first fabricated without radiating elements for phase characterization purpose as shown in Fig. 5.11, where six of the eight ports are loaded, and  $S_{7,2}$  is measured for example. Considering the limited space of AAO wafer, the second crossover of the Butler matrix, which is used only to switch the phases at output port 6 and 7 is omitted for phase characterization purpose, and refers to as semi-Butler matrix. For simplicity, output phases of the semi-Butler matrix fed from input port 2 only is measured as given in Fig. 5.12. Actually, when  $\angle S_{5-8,2}$  fulfill their phase relationship at the output ports,  $\angle S_{5-8,1}$  is also fulfilled. This is because, the  $90^\circ$  differential phase between ‘thru’ and ‘coupled’ ports of the coupler is rather precise and the phase balance of the crossover is high.

The transmission to output ports 5-8 is within  $-7$  dB to  $-11$  dB from 95 GHz to 105 GHz. Considering the 6 dB power splitting loss, the semi-Butler matrix brings about  $-1$  dB to  $-5$  dB loss to each channel. The reflections are  $< -17$  dB in this band, representing good



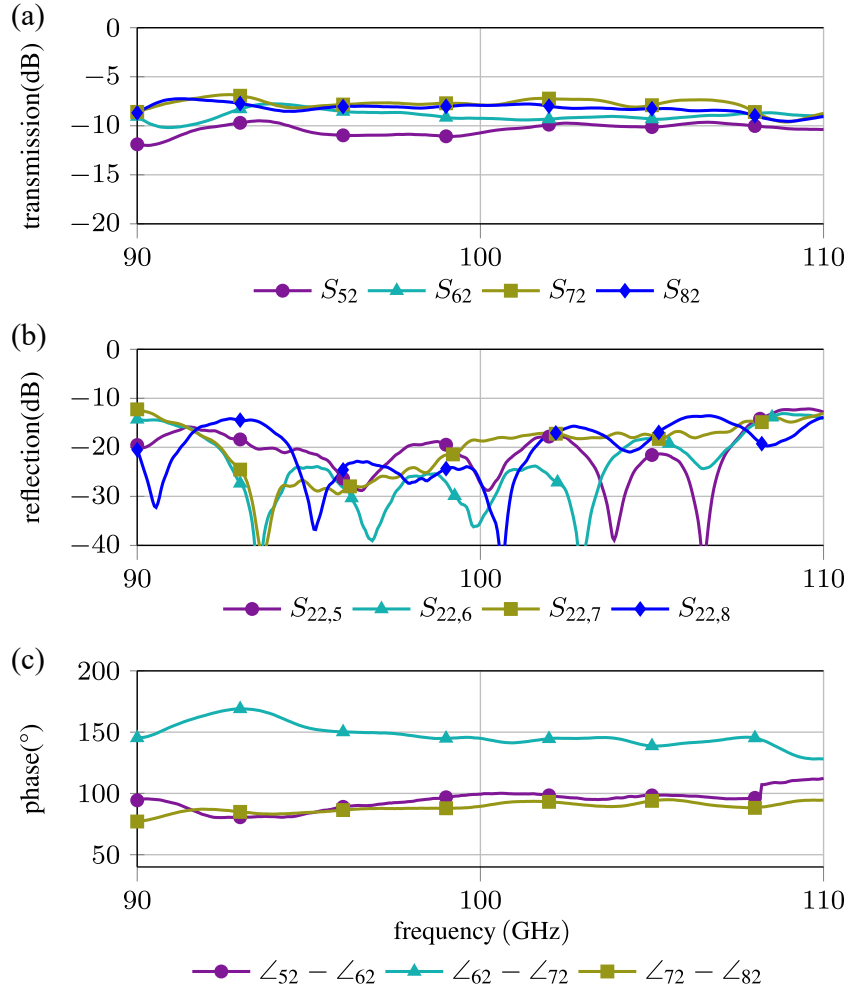


Figure 5.12: Measured S-parameters of the semi-Butler matrix: (a) transmission to the output ports, (b) reflection at different output ports, where  $S_{22,x}$  represent the reflection  $S_{22}$  when port  $x$  is output, and (c) progressive phase shifts at the output ports fed from port 2.

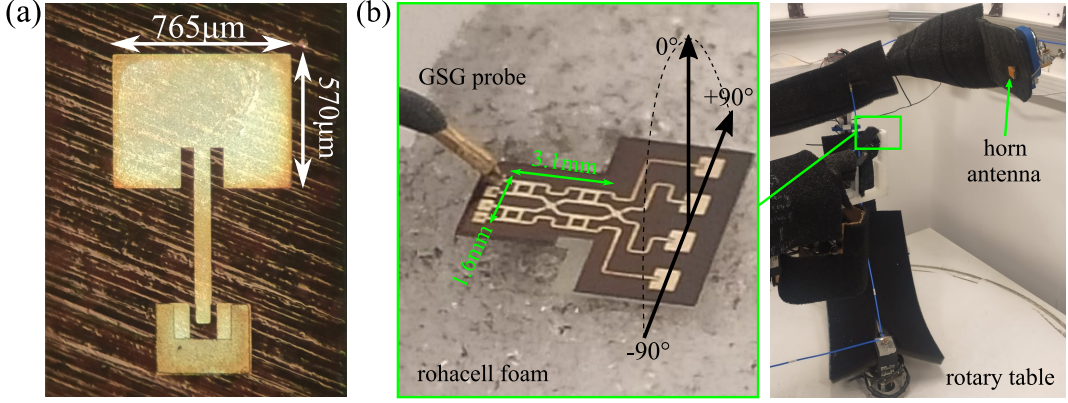


Figure 5.13: (a) Single patch antenna designed for radiating at 100 GHz. (b) Beam-switching antenna array with full Butler matrix, its dimensions, far field coordinate, and far field measurement setups.

matching. In the same frequency range,  $\angle S_{52} - \angle S_{62}$  and  $\angle S_{72} - \angle S_{82}$  are close to the theoretical value,  $90^\circ$  with  $-6^\circ$  to  $10^\circ$  deviation.  $\angle S_{62} - \angle S_{72}$  is close to the theoretical  $135^\circ$  with  $3^\circ$  to  $15^\circ$  deviation. The phase deviations are mainly caused by an inaccurate  $\epsilon_r$  and thickness  $h$  of the AAO used in simulation as well as the misalignment between electrode and ground.

With these acceptable S-parameters measured with the semi-Butler matrices, the design and fabrication of the full beam-switching antenna array with Butler matrix are optimized regarding the phase deviations for the second batch. The single patch antenna designed for radiating at 100 GHz and the final array are shown in Fig. 5.13.

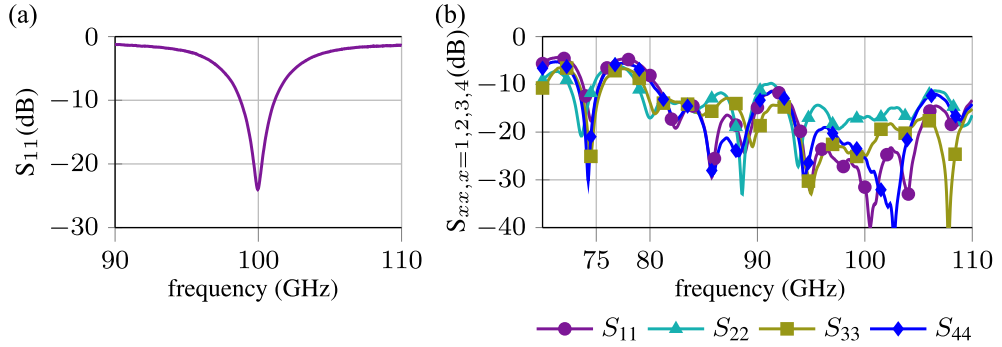


Figure 5.14: Measured S-parameters of the demonstrators in Fig. 5.13, (a) single patch antenna, (b) array with Butler matrix.

The S-parameter and far field measurement setup of the array is presented in Fig. 5.13 (b). In this system, the reference horn antenna is rotated around the fixed antenna under test (AuT) using two stepper motors. The reference horn antenna of W-band and the AuT are connected to the Keysight's N5227B VNA through OML's frequency extenders. The AuT is supported by ROHACELL 51 IG foam with  $\epsilon_r = 1.05$  and  $\tan\delta = 0.0135$  at 26.5 GHz,

### 5.3 Proof-of-Concept: Beam-Switching Broadside Antenna Array with Butler Matrix

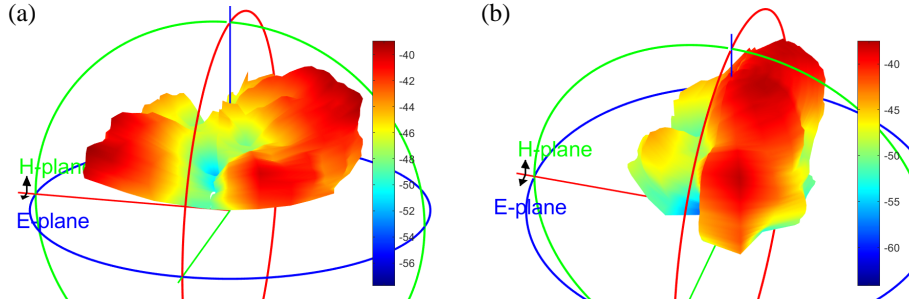


Figure 5.15: 3-D far field patterns of the beam switchable array with Butler matrix excited by (a) port 3 and (b) port 1.

which introduces the minimum influence to the measurement. A digital mobile microscope is used to place the GGB custom probe. To prevent vibration and mechanical damage to the probes, the AuT support is mechanically isolated from the rest of the building. The arms of the rotary system are covered with EMI absorber. Using this system, S-parameters of single patch and the array are measured and shown in Fig. 5.14. The patch resonates at 100 GHz with  $|S_{11}| < -10$  dB matching well with simulation. The array expectedly works from 90 GHz to 100 GHz with reflection  $< -10$  dB at all four input ports. The unexcited ports of the Butler matrix are isolated from the excited port and require no loads during measurement [TCC08]. Therefore, only the excitation port is connected with the probe for both, S-parameter and far field measurements.

The system can measure 3D radiation patterns of the AuT excited by different ports as plotted in Fig. 5.15 at 100 GHz.

The normalized radiation patterns of the array with Butler matrix at 100 GHz in their H-plane are shown in Fig. 5.16 (a). The beam can be switched to  $12^\circ$ ,  $-45^\circ$ ,  $45^\circ$  and  $-12^\circ$  when excited by port 1, 2, 3, 4, respectively, with high symmetry and smooth pattern. The gain of the array with Butler matrix at 100 GHz is measured to be 5.49 dBi, 3.77 dBi, 3.32 dBi and 4.93 dBi, when excited by port 1, 2, 3, 4, respectively, as shown in Fig. 5.16 (b).

A comparison to the state-of-the-art Butler matrix works in planar structure is listed in Table 5.2.

Table 5.2: Comparison of the state-of-the-art Butler matrices in planar structure.

Technology	Frequency (GHz)	phase deviation( $^\circ$ )	amplitude deviation (dB)	return loss (dB)	dimension ( $\lambda \times \lambda$ )	Reference
PCB	6.0	10	0.5	24	$1.4 \times 1.1$	[TYW14]
PCB	2.2	21	2.2	10	$1.3 \times 1.0$	[CLS10]
PCB	5.8	10	3.2	11	$2.8 \times 1.8$	[Ren+20]
PCB	6	<u>15</u>	<u>1.0</u>	<u>10</u>	$2 \times 1.6$	[Liu+11]
PCB	28.0	<u>10</u>	<u>2.5</u>	<u>22</u>	$3.3 \times 5.9$	[Wan+19b]
LCD	28.0	10	2.0	18	$1.57 \times 0.62$	Section 4.2
NaM	100	15	4.0	17	$1.03 \times 0.53$	Section 5.3

Underline represents simulated values

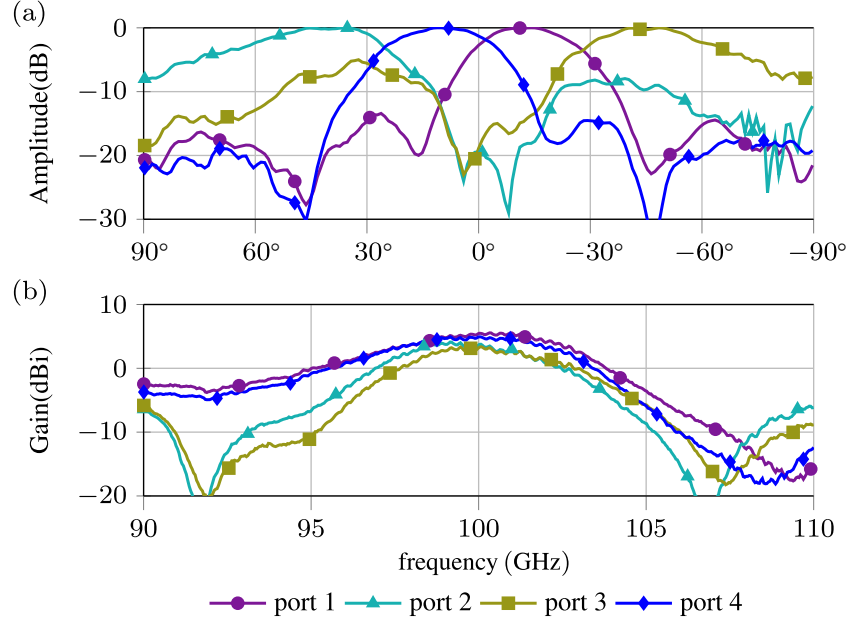


Figure 5.16: (a) Normalized switched far field pattern on each input port at 100 GHz. (b) Measured maximum gain on each input port with respect to frequency.

As the PCB technology is widely used in printed planar RF circuits, large amount of reported Butler matrices are realized on PCB at low frequencies for easy fabrication and characterization. However, regarding the drastically increasing  $\tan\delta$  of common PCB materials, Butler matrices based on PCB are not transferable to W-band. The Butler matrix in LCD configuration proposed in section 4.2 for easy integration with LC phase shifters has high insertion loss due to the unnecessarily thin LC as the substrate for the non-tunable Butler matrix. The proposed array with Butler matrix based on NaM are to the author's best knowledge the first Butler matrix and the first Butler matrix based beam-switching array working at 100 GHz with decent RF performance, mainly due to the low  $\tan\delta$  as well as the flexible through substrate via realization of the AAO membrane.

The dimensions of the full array are  $4.8 \times 5.3$  mm. The Butler matrix part only is  $3.1 \times 1.6$  mm, which equals to  $1.03\lambda_0 \times 0.53\lambda_0$  at 100 GHz. Such good compactness among the state-of-the-art Butler matrix is mainly due to the compact  $\lambda$ -irrelevant design of the crossover, as well as relatively high  $\epsilon_r$  of the AAO membrane.

## 5.4 Summary

In this chapter, a beam-switching phased array with Butler matrix working at 100 GHz is successfully realized on NaM with low fabrication effort, low loss, decent matching, compact size, high symmetry, and high stability, thanks to the special through substrate via process based on NaM. A loading method utilizing broadband patch antenna and dissipative transmission line is first developed. It is the precondition for using the conventional 2-port

VNA in multi-port on-wafer measurements at W-band. The method is validated together with the branch-line coupler at 100 GHz. Then the core component of the Butler matrix, the crossover is realized, taking the advantage of through substrate via processing. It has low loss, low space consumption, low amplitude and phase imbalance, which sets a new benchmark to the state-of-the-art crossovers. Finally, a broadside radiating array with Butler matrix by combining branch-line couplers, crossovers, MSLs and patch antennas are realized for the first time in W-band with switched beams and decent gain.

Besides, NaM is proven to be able to generate slow-wave effect in MSL topology serving as ground plane, combining with other dielectrics, e.g., the LC-NaM phase shifter as discussed in chapter 3 with the state-of-the-art performance. Similarly to that in chapter 4, a simultaneously mixed beam-switching and beam-steering antenna array can be achieved by combining NaM based Butler matrix and LC-NaM phase shifter. It is expected to have very high performance. Therefore, NaM proves to be a promising candidate of interposer technology for mmW components up to at least W-band.



## 6 Conclusion and Outlook

### Conclusion

The ever-increasing demand for high data rates in wireless communication systems requires high frequencies and large absolute bandwidths, which are available at millimeter-waves (mmW) frequencies, that are not well explored yet. However, as frequency increases, the signal suffers from high free-space path loss and is subject to blockage. Therefore, the radio coverage at mmW requests much higher density of base stations compared to wireless communication at lower frequencies, which leads to a higher infrastructure cost and slow deployment. A common solution is to use high gain antenna arrays with beam-steering capability to overcome path loss, such as spatially-steerable power-concentrated pencil beams, and thus, increase the cell coverage radius and angle, and decrease the antenna density consequently. While the high gain pencil beams are achieved by antenna array configurations, the reconfigurability, especially the steerability of the high-gain beams is discussed in detail in this work.

A steerable beam can be achieved by using a mechanically rotary platform. However, this method consumes large space and power, has limited scanning speed and high maintenance cost, and can not provide multiple beams for multi-direction communication. In contrast, electronically steered passive phased arrays (ESPA) overcomes the aforementioned drawbacks, of which the tunable phase shifter is the key component to implement beam-steering.

Microwave liquid crystals (LC) have been applied in realization of ESPA during the past two decades. The orientation of the LC molecules with regarding the guided RF field can be manipulated by using a bias voltage, such that the effective permittivity of the LC-based transmission line varies, resulting in a true delay line with tunable electric length. True delay lines exhibit constant phase slope over frequency, therefore, ESPAs implemented with true delay lines do not show a beam-squinting effect. LC technology is fully electrically tunable. It shows advantage over microelectromechanical systems (MEMS) in terms of life span, continuity, and packaging; over ferroelectric materials such as Barium–Strontium–Titanate (BST) in terms of frequency range and bias voltage. Besides, LC components have high linearity, low power consumption as well as a material-specific low insertion loss, particularly at high frequencies. These make the LC technology suitable for future wideband applications at mmW range.

The main drawback of LC phase shifters is the contradictory relationship between response time and insertion loss, which is closely related to the thickness of the LC layer. While former investigations have proposed methods to realize low-loss LC phase shifters accompanied with long response times, this work deals with innovative structures to achieve better performance in terms of high figure-of-merit and fast response with lower

## 6 Conclusion and Outlook

complexity, i.e., LC phase shifter based on metallic-nanowire-filled-membrane (LC-NaM) and defective ground structure (LC-DGS). Both phase shifter type are with ultra-compact size and advance the state-of-the-art of planar LC phase shifter with peak FoM of  $70^\circ/\text{dB}$  and  $79^\circ/\text{dB}$ , and fast response time of 120 ms and 51 ms, respectively.

The prospect of LC-DGS phase shifter in practical applications is further validated by integrating it into beam-steering networks based on LCD manufacturing, i.e., corporate feed phased array, butler matrix (BM) fed phased array and continuously adjustable single-pole double-throw (SPDT). To convenient the characterization, these demonstrators are designed to work in Ka-band. The  $1 \times 4$  corporate feed phased array with 4 integrated full  $360^\circ$  LC-DGS phase shifters has wide continuous 1D scanning range from  $-40^\circ$  to  $40^\circ$  with a decent maximum gain of 4.5 dBi, and is one of the earliest reported LC-based ESPA with improved response time of less than 0.7 s. Then, a Butler matrix with discrete beam-switching is investigated to substitute the corporate feed network, and LC-DGS phase shifters with only  $135^\circ$  phase shift are implemented to enable continuous beam-steering around the switched beams. It saves around  $2/3$  of loss of the phase shifter compared to the corporate feed array, and results in increased gain.

Different input ports of the Butler matrix need to be selected for beam-switching such that an LC based SPDT is introduced as the premise of SP4T for a Butler matrix with four output ports. This interference based SPDT provides continuously adjustable power-splitting ratio. This allows not only switching among output ports, but also the excitation of more than one output ports at the same time, resulting in multiple beams. As the most straightforward way to realize SP4T is cascading three SPDTs, of which 6 LC phase shifters are required, a possible simplified SP4T schematic proposed in [Jos18] is shown in Fig. 6.1, using only 4 phase shifters with the same  $-90^\circ < \Delta\phi < 90^\circ$  as SPDT thanks to the crossover. The simplified SP4T allows small volume and low loss.

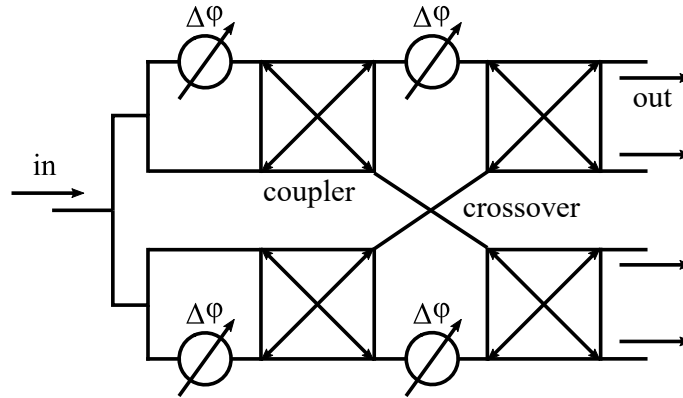


Figure 6.1: Schematic of a possible interference-based SP4T design utilizing LC. Phase shifters provide  $-90^\circ < \Delta\phi < 90^\circ$ .

These planar LC devices utilize inverted microstrip line (IMSL) topology to create a cavity between electrode and ground plane for LC filling. By taking the advantage of the well-established industrial LCD production lines, LC panel devices can be manufactured



cost effectively with around 300 \$/m<sup>2</sup> compared to semiconductor-based phase shifter costs, which are estimated to be around 30000 \$/m<sup>2</sup> when using 30 cm diameter wafers [Dol20].

## Outlook

Beside the tunable devices mentioned already, LC-DGS phase shifters drew attention due to its simplicity in design and fabrication. The LC-DGS design with 4.6  $\mu\text{m}$  thick GT7-29001 LC is chosen for the phase shifters in a 26.5 GHz to 29.5 GHz reconfigurable intelligent surface (RIS) [Neu+23]. RIS can be applied in outdoor communication with blocked line of sight, as well as in critical indoor environment such as factories or hospitals, where stable connection between devices is indispensable. The RIS is a passive reflect array based on 2D extended patch antennas without oscillators or amplifiers. Each individual patch is equipped with an independently tunable reflective LC-DGS phase shifter with far end opened for total reflection of the guided wave, such that the incoming signal is received, manipulated, and re-radiated. Due to the reflective opened end, the incoming signal travels through the LC-DGS phase shifter twice. Therefore, LC-DGS phase shifter of only 180° is required. All the LC-DGS phase shifters of the RIS are biased by an external control unit. The structure of the RIS is similar to that of the IMSL as in Fig. 3.5, except that the patch antenna plated on the other side of the glass of the ground plane, as shown in Fig. 6.2 (a). The IMSL is used as the feed line for the patch, which couples to the patch through a slot on the ground plane. The patch utilizes the top glass as the substrate without influence from the tunable LC. The final single patch antenna demonstrator with LC-DGS phase shifter is shown in Fig. 6.2 (b). The LC-DGS phase shifter is designed to be longer than 180° phase shift to keep a distance between the patch and the K-connector, such that the radiation of the patch is less influenced. The measured radiation patterns of the demonstrator is shown in Fig. 6.3.

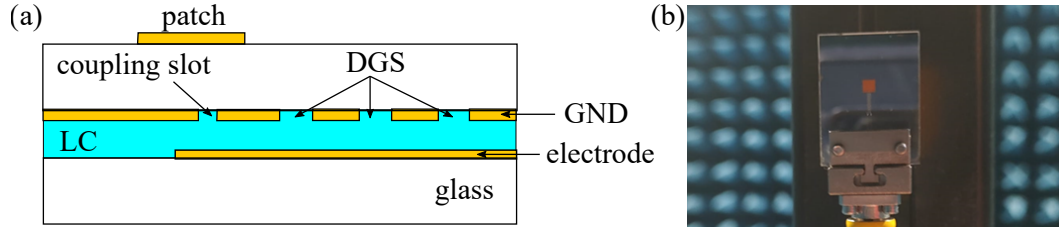


Figure 6.2: (a) Cross section of the patch antenna fed by LC-DGS phase shifter using aperture coupling based on IMSL structure. (b) Fabricated patch antenna demonstrator.

The radiation pattern on E-plane is influenced by the connector such that the radiated power is reflected to the opposite direction. While the pattern on H-plane shows good symmetry, however, with slightly lower HPBW than a normal inset feed patch also due to the influence of the connector.

Based on the single patch design, we are currently working on the first RIS demonstrator with  $3 \times 3$  patch antenna array as proof-of-concept, shown in Fig. 6.4. Each patch antenna is integrated with two open-ended reflective LC-DGS phase shifters for 2-D beam-forming

## 6 Conclusion and Outlook

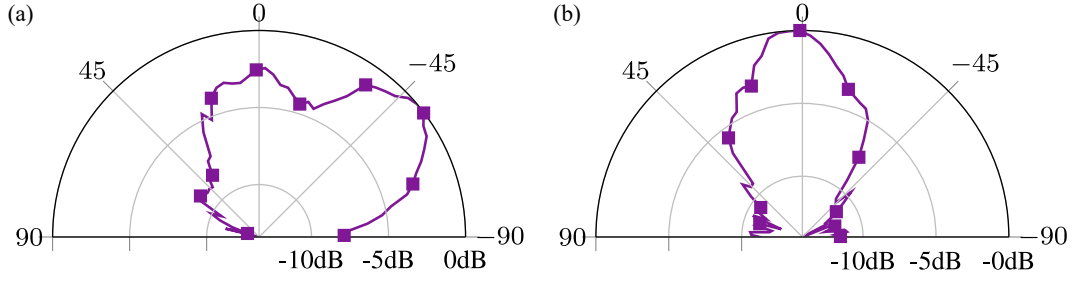


Figure 6.3: Normalized measured far field pattern of the aperture feed patch antenna at 28 GHz on (a) E-plane and (b) H-plane.

purpose. The LC-DGS phase shifters are bent such that an element spacing of only slightly larger than  $0.5\lambda \times 0.5\lambda$  is realized to prevent possible grating lobes. Although the demonstrator is not yet a complete RIS, it is fabricated to verify the layout and to study the single patch performance in the array environment. The measured radiation pattern of the RIS is quite symmetric on H-plane, but deteriorates on E-plane due to the influence of the connector, surface wave and mutual coupling between patches.

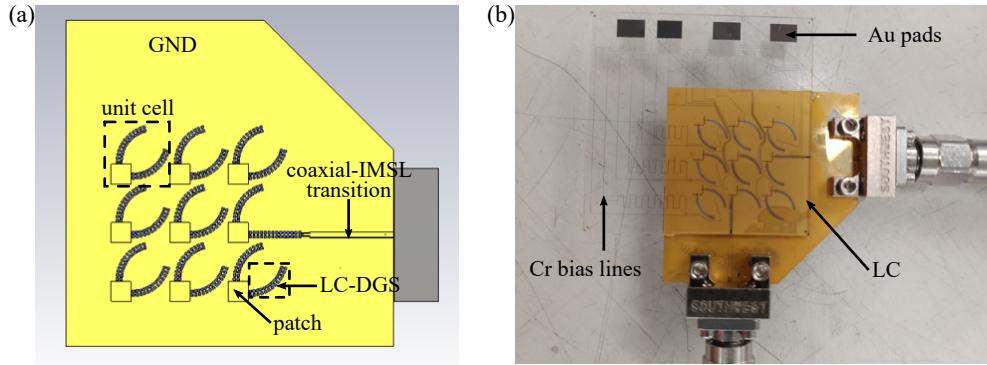


Figure 6.4: (a) Top view on the patches of the simulation model. (b) Bottom view on the LC-DGS phase shifters of the demonstrator. Patches on the back side.

As shown in Fig. 6.5, the excited patch has strong coupling to the neighboring elements and edge effects are observed on ground plane. They are mainly caused by the surface wave in the glass between ground and patch. The strong surface wave traps electromagnetic energy, such that the efficiency and gain of the antenna reduce significantly. The mutual coupling results in the notched radiation pattern and blind scanning angles. Therefore, for the future investigation and development of a RIS, surface waves must be eliminated. This can be realized by using cavities or stacked substrate techniques, however, with the fundamental drawback of increasing the complexity of the MSL antenna and negating the advantages of MSL antennas. Electromagnetic Bandgap Structures (EBG) [KMG15] and DGS [HHR12] are promising candidates that are being used to suppress the surface wave and reduce crosstalk between neighboring antenna elements due to their simple design and light weight.

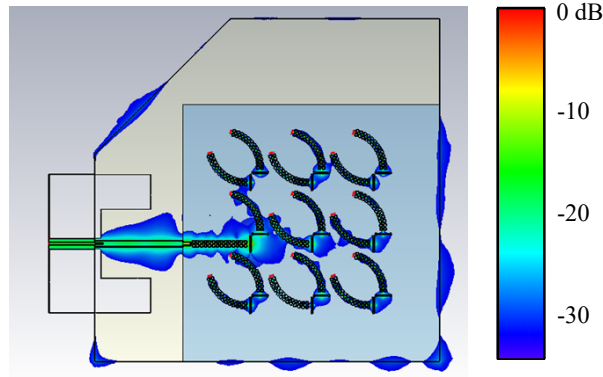


Figure 6.5: Simulated field distribution of the RIS when the middle patch on one edge is excited.

It is worth mentioning, for easy handling and fabrication consideration, the glasses used in the work are all AF32 with a relatively high  $\epsilon_r \approx 5.1$  and high thickness of  $700\mu\text{m}$  for decent stiffness. It leads to decreased tuning efficiency of LC in IMSL, and deteriorates radiation performance of the RIS due to surface wave and crosstalk between patches. New types of materials as substitution to AF32 such as fused silica with lower  $\epsilon_r$ , low  $\tan\delta$  and low thickness are recently under investigation for the RIS realization. Thinner glass not only helps improve the radiation, but also helps in vertical integration of LC phase shifter stack with beam-steering and beam-switching networks realized on different substrates, such as corporate feed network, Butler matrix, etc.. The reason is based on thin glass, through substrate via and via-less coupling are both relatively easy to be realized. Besides, Indium Tin Oxide (ITO) with higher resistance than Cr is considered to be evaporated onto the glass as the seed layer for bias lines with lower RF leakage.

Inspired by the LC-DGS phase shifter, it is noticed that filter structure has rather steep slope of the transmission phase with respect to frequency in its pass-band, i.e., slow-wave effect. LC-DGS design generates high slow-wave effect at the expense of lower cut-off frequency. This limits the applicability of LC-DGS topology in high frequency, as explained in chapter 3. A possible solution is using band-pass filters, as reported in [Kar14], where Split Ring Resonators (SRR) are applied to LC-IMSL phase shifter and achieves band-pass performance. However, due to the high insertion loss and low LC tuning efficiency originated from the design, its overall performance is limited. Nevertheless, it is believed that new IMSL based band-pass topology with LC will improve the performance of MSL LC phase shifter to a certain extent.

LC-NaM phase shifter has theoretically much higher cut-off frequency than the aforementioned loaded-line LC phase shifters. This is because the nanoscale interpore pitch between metallic nanowires is much shorter than the wavelength in the whole mmW range, such that the NaM changes the capacitance and inductance of the IMSL distributedly. While DGS and Split Ring Resonators are lumped elements with cut off mechanism.

As demonstrated in chapter 5, NaM not only provides ultra-wide band slow-wave effect in LC-NaM as an anisotropic material, but also is proven to be an ideal interposer

## 6 Conclusion and Outlook

technology. These features make NaM a promising technology to produce miniaturized planar reconfigurable systems based on LC, especially beyond Ka-band, at least up to W-band.

Besides LC-NaM, the MEMS based on NaM and LC in [Gom+22] achieves discrete phase shift, such that the switched conventional SPnT other than interference-based is realizable on NaM. Compared to the interference-based SPnT, although lacking of continuous tunability, it has much faster response time, much simpler structure and much less insertion loss. Both MEMS-NaM and LC-NaM meet the requirements of most reconfigurable systems. LC combining NaM deserves further attention and should find its application in future reconfigurable wireless communication.

# A Appendix

## A.1 Fabrication Process of LC-Phase Shifter

- **Seed Layer Evaporation**

Chromium (Cr) : Thickness 20 nm, rate<0.5 nm/s

Gold (Au) : Thickness 60 nm, rate<1.0 nm/s

- **Photolithography**

Processing of positive photo resist AZ4533, negative photo resist SU8-3005 and SU8-25 (Table. A.1). OmniCoat is required before SU8 processing to improve SU8 adhesion: spin coat for 30s at 5000rpm followed by 1 minute bake on a 160-200 °C hot plate, then let the sample cool down for around 10 minutes before SU8 processing. AZ4533 of 4 μm thick can be used to grow gold around 2 μm with electroplating.

Table A.1: Photolithography process parameters

Photoresist	AZ4533	SU8-3005	SU8-25
Desired thickness	4 μm	6.6 μm	22 μm
Spin coating	40s @4000rpm	30s @5000rpm	30s @2200rpm
Pre-exposure bake (hot plate)	3.5 min @90°C	1 min @65°C 2 min @95°C	1 min @65°C 3 min @95°C
UV-exposure time (6 mW/cm <sup>2</sup> )	35s	40s	40s
Post exposure bake (hot plate)	/	1 min @65°C 3 min @95°C	5 min @65°C 12 min @95°C
Developer	AZ400K:H <sub>2</sub> O(1:4)	DEK600	DEK600
Developing time	40s @23°C	1 min @23°C	3 min @23°C
Rinse	water	isopropanol +DEK600	isopropanol +DEK600
Hard bake	/	1 hour @150°C	2 hour @150°C

- **Wet Etching and Cr Bias Line**

After photolithography, seed layer is etched to release the structure following Table A.2. DC or low frequency AC (around 1 kHz) bias is applied to IMSL through a highly resistive line which does not influence the RF performance of the IMSL. The bias line

## A Appendix

can be realized by patterning Cr seed layer using photolithography. In practice, it is observed, that Cr lines patterned on the original Cr seed layer are cracked, see Fig. A.1 (a), and they are usually tested to be disconnected using multimeter such that bias voltage cannot be applied. To solve this, Cr layer of 10 nm is evaporated onto the sample and patterned again, after which, smooth and continuous Cr lines of good connectivity are obtained, see Fig. A.1 (b). As measured, the Cr line fabricated in our lab with 20 nm thickness and 50  $\mu\text{m}$  width has a resistivity of 4  $\text{k}\Omega/\text{mm}$  to 5  $\text{k}\Omega/\text{mm}$ .

Table A.2: Wet etching process at 23 °C

Etchant	$\text{NH}_4[\text{Ce}(\text{NO}_3)_6]:\text{HNO}_3:\text{H}_2\text{O}$ 41.15 g:22.5 mL:250 mL	$\text{I}_2:\text{KI}:\text{H}_2\text{O}$ 5 g:20 g:200 mL
Time	10s for 20 nm Cr	8s for 60 nm Au

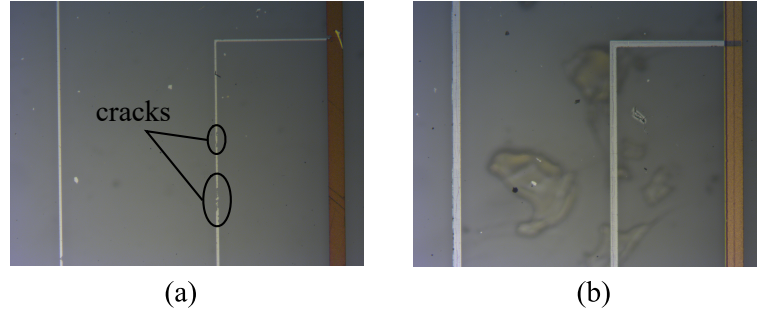


Figure A.1: (a) Cr bias line realized on original Cr seed layer. (b) Thickened Cr bias line.

### • Photoresist removal

While AZ4533 is easily removable by acetone, SU8 is difficult to be removed after exposure and post exposure bake. Wrong processing of SU8 might lead to sample scrapping. However, the thickness of both photoresists are controllable by  $\text{O}_2$  etching.

Table A.3: Photoresist Removal

Photoresist	AZ4533	SU8-3005	SU8-25
Remove	Acetone rinse +Isopropanol rinse	/	/
$\text{O}_2$ etching (flow rate=100sccm @ 190kpa, 200 W)	-0.35 $\mu\text{m}/\text{min}$	-0.35 $\mu\text{m}/\text{min}$	-0.35 $\mu\text{m}/\text{min}$

### • Wafer Dicing

To save fabrication effort, multiple structures are fabricated simultaneously on the same wafer, followed by wafer dicing to separation. Glass substrate evaporated with Cr/Au seed layer can be diced directly with clean edges. However, after electroplating, gold structure cannot be diced, otherwise the gold will peel off from glass along the cutting edge. At least  $25\text{ }\mu\text{m}$  to  $30\text{ }\mu\text{m}$  buffer should be kept between dicing trace and galvanic gold, as shown in Fig. A.2.

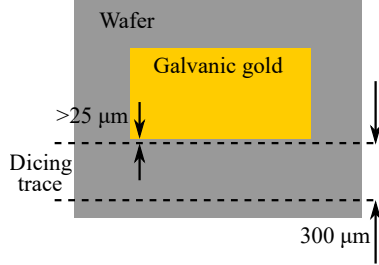


Figure A.2: Wafer dicing using  $300\text{ }\mu\text{m}$  thick blade. Dicing trace should avoid touching the galvanic gold.

#### • Alignment Layer Processing

The material used for alignment layer is a mixture of 1.5 g Nylon6 and 100 g Trichlorethanol. Long time storage can lead to crystallization of the mixture, which can be solved by putting the bottle into  $50\text{--}60\text{ }^{\circ}\text{C}$  hot water bath. The spin coating parameter of the alignment layer is 5000 rpm at 30 s. Then it follows the procedure in Table A.4 to cure the alignment layer. Finally, the surface is gently rubbed using a rotary pillar covered with velvet.

Table A.4: Curing of alignment layer [Kar14].

Hotplate	10 min @ $90^{\circ}\text{C}$
Oven	23- $90^{\circ}\text{C}$ in 30 min
	60 min @ $90^{\circ}\text{C}$
	90- $180^{\circ}\text{C}$ in 30 min
	60 min @ $180^{\circ}\text{C}$

#### • Assemble of Microstrip Line and Ground

Mirostrip line and ground plane can be aligned and glued with the help of a mask aligner. The top glass with microstrip lines is fixed on the transparent holder (glass or hard plastic) from the mask aligner using a drop of water (same method can be used to align mask to wafer), while the bottom glass with ground plane lies on the chuck, as shown in Fig. A.3. Apply UV-curable glue around SU8 spacers, move the chuck

## A Appendix

and align the microstrip lines with ground plane, lift the chuck to press the top and bottom glass hardly. Make sure the glue doesn't spread to microstrip lines. Finally, expose for more than 1 min to cure the glue. For UV-glue curing purpose, the top substrate with microstrip lines must be transparent.

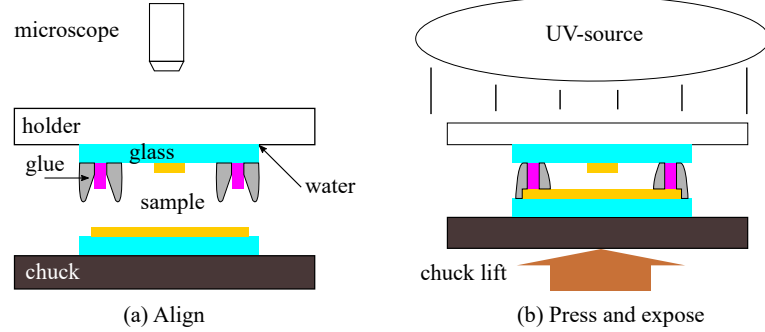


Figure A.3: Final assembly of IMSL. (a) Alignment of microstrip and ground plane. (b) Press and expose.

### • LC Filling

LC filling into IMSL utilizes the capillarity force. The cavity usually has several mm to cm width and length, but  $\mu\text{m}$  height, such that LC is able to spread over the cavity automatically. Vacuum environment is not needed. Although time consuming, LC should be filled from only one point on the edge of the cavity in case air bubble is formed, see Fig. A.4.

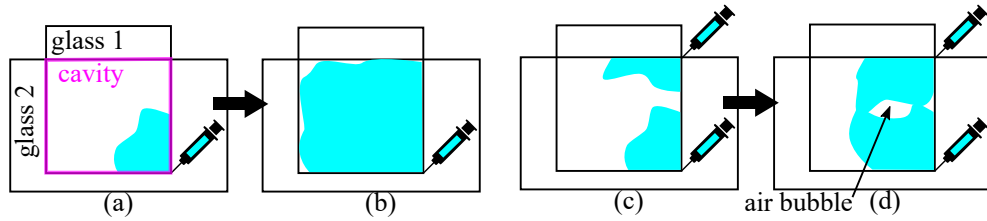


Figure A.4: (a)(b) Properly fill the cavity from one point. (c)(d) Filling from multiple points might lead to air bubbles inside LC.

## A.2 Thru-Reflect-Line Calibration: Mathematics and Practical Considerations

Thru-reflect-line (TRL) calibration is often used for de-embedding S-parameter data, especially on-wafer MMIC data. TRL works well, especially in mmW frequencies and down to a couple of GHz, where the  $\lambda$ -related 'line' standard is with a reasonable length for



fabrication in printed circuits. Although it is possible to de-embed three-port or higher-order data, in this work and more general cases, TRL method is used in its simplest format for de-embedding two-port data. The mathematical principle and practical usage consideration of TRL are discussed in this section.

### Mathematics of TRL

As the name implies, there are three standards that are measured: the ‘thru’, the ‘reflect’ and the ‘line’. ‘Thru’ is the back-to-back connected transitions that are to be de-embedded; the ‘reflect’ is usually a short or open circuit; the ‘line’ is similar as ‘thru’ but with inserted extra length between the transitions that is related to the de-embedding frequency range. The principle of TRL is from [EH79].

For a two-port device, the wave amplitudes  $b_1$ ,  $b_2$  at terminal 1 and 2 are related to the incident waves  $a_1$ ,  $a_2$  by the scattering S-parameter equations

$$\begin{aligned} b_1 &= S_{11}a_1 + S_{12}a_2, \\ b_2 &= S_{21}a_1 + S_{22}a_2, \end{aligned} \quad (\text{A.1})$$

they can be rewritten as

$$w_2 S_{11} + w_1 S_{22} - \Delta = w_1 w_2 \quad (\text{A.2})$$

where

$$w_1 = b_1/a_1, \quad w_2 = b_2/a_2, \quad \Delta = S_{11}S_{22} - S_{12}S_{21} \quad (\text{A.3})$$

Given the S-parameters for the three fictitious two-ports which result from the ‘thru’, ‘reflect’ and ‘line’ kits, the final task is to determine the S-parameters of the individual error boxes  $A$  and  $B$ , as shown in Fig. A.5. From Eq. A.1,  $a_1$  and  $b_1$  can be rewritten as function of  $a_2$  and  $b_2$  as

$$\begin{pmatrix} b_1 \\ a_1 \end{pmatrix} = \frac{1}{S_{21}} \begin{pmatrix} -\Delta & S_{11} \\ -S_{22} & 1 \end{pmatrix} \begin{pmatrix} a_2 \\ b_2 \end{pmatrix} = R \begin{pmatrix} a_2 \\ b_2 \end{pmatrix} \quad (\text{A.4})$$

where the matrix  $R$  is known as the Cascading matrix. Let the cascading matrices of the two error box  $A$ ,  $B$  be denoted by  $R_a$ ,  $R_b$ , respectively, and  $R_t$  represents the ‘thru’ which is cascaded by  $A$  and  $B$ ;  $R_d$  represents the ‘line’ with  $R_l$  representing the inserted length

$$\begin{aligned} R_t &= R_a R_b, \\ R_d &= R_a R_l R_b \end{aligned} \quad (\text{A.5})$$

from Eq. A.5,

$$R_b = R_a^{-1} R_t, \quad (\text{A.6})$$

so that  $R_b$  may be obtained from  $R_a$  and  $R_t$ . Next  $R_b$  from Eq. A.5 can be eliminated by Eq. A.6, which yields

$$T R_a = R_a R_l, \quad \text{where} \quad T = R_d R_t^{-1} \quad (\text{A.7})$$

## A Appendix

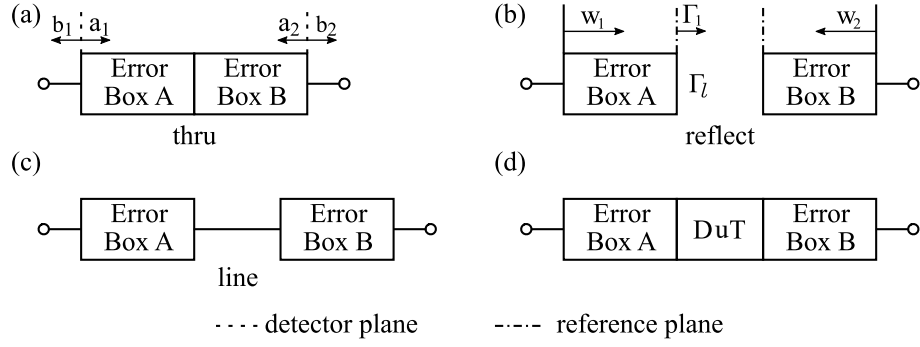


Figure A.5: The fictitious two-ports, from which the parameters of ‘error box’ A and B are ultimately obtained, are formed from ‘thru’, ‘reflect’, and ‘line’ standards.

and which can be found from the parameters of the ‘thru’ and ‘line’.

Let  $\gamma$  and  $l$  represent the propagation constant and length of the inserted delay line, respectively. Assuming the line is nonreflective,

$$R_l = \begin{pmatrix} e^{-\gamma l} & 0 \\ 0 & e^{\gamma l} \end{pmatrix} \quad (\text{A.8})$$

Let the elements of  $R_a$  and  $T$  be represented by  $r_{ij}$  and  $t_{ij}$ , respectively, the extension of Eq. A.7 gives

$$t_{11}r_{11} + t_{12}r_{21} = r_{11}e^{-\gamma l}, \quad (\text{A.9})$$

$$t_{21}r_{11} + t_{22}r_{21} = r_{21}e^{-\gamma l}, \quad (\text{A.10})$$

$$t_{11}r_{12} + t_{12}r_{22} = r_{12}e^{\gamma l} \quad (\text{A.11})$$

$$t_{21}r_{12} + t_{22}r_{22} = r_{22}e^{\gamma l} \quad (\text{A.12})$$

From Eq. A.9 and Eq. A.10, Eq. A.11 and Eq. A.12, Eq. A.13 and Eq. A.14 can be derived, respectively,

$$t_{21}(r_{11}/r_{21})^2 + (t_{22} - t_{11})(r_{11}/r_{21}) - t_{12} = 0 \quad (\text{A.13})$$

$$t_{21}(r_{12}/r_{22})^2 + (t_{22} - t_{11})(r_{12}/r_{22}) - t_{12} = 0. \quad (\text{A.14})$$

The ratio  $(r_{11}/r_{21})$  and  $(r_{12}/r_{22})$  are thus both given by a solution of the same quadratic equation, where the coefficients are parameters of the  $T$ -matrix which are already calculated. Taking the ratio of Eq. A.12 to Eq. A.10,

$$e^{2\gamma l} = \frac{t_{21}(r_{12}/r_{22}) + t_{22}}{t_{12}(r_{21}/r_{11}) + t_{11}} \quad (\text{A.15})$$

thus,  $e^{2\gamma l}$  is also determined by equations from A.9 to A.10. Define

$$\begin{aligned} a &= r_{11}/r_{22}, \\ b &= r_{12}/r_{22}, \\ c &= r_{21}/r_{22} \end{aligned} \quad (\text{A.16})$$

then  $b$  and  $a/c$  have already been calculated by Eq. A.13 and A.14. The reflection coefficient  $w_1$  at the fictitious detector plane for error box A is the S-parameter of the ‘reflect’ standard measured from port 1,

$$w_1 = S_{r,11} \quad (\text{A.17})$$

and  $w_1$  is related to the reflection coefficient of the load  $\Gamma_l$  by

$$w_1 = \frac{a\Gamma_l + b}{c\Gamma_l + 1} \quad (\text{A.18})$$

Rearrange Eq. A.18

$$a = \frac{w_1 - b}{\Gamma_l(1 - w_1 c/a)} \quad (\text{A.19})$$

thus,  $a$  is related to  $\Gamma_l$  and both are yet unknown.

Back to Eq. A.5, it can be written as

$$r_{22}\rho_{22} \begin{pmatrix} a & b \\ c & 1 \end{pmatrix} \cdot \begin{pmatrix} \alpha & \beta \\ \gamma & 1 \end{pmatrix} = g \begin{pmatrix} d & e \\ f & 1 \end{pmatrix} \quad (\text{A.20})$$

where  $\alpha, \beta, \gamma, \rho_{22}$  and  $d, e, f, g$  correspond, respectively to  $a, b, c, r_{22}$  in  $R_b$  and  $R_t$ . Premultiplying Eq. A.20 by  $R_a^{-1}$  and expanding, one can get

$$\gamma = \frac{f - dc/a}{1 - ec/a} \quad (\text{A.21})$$

$$\beta/\alpha = \frac{e - b}{d - bf} \quad (\text{A.22})$$

and

$$a\alpha = \frac{d - bf}{1 - ec/a} \quad (\text{A.23})$$

$d, e, f, g$  can be easily calculated from ratios among the elements of  $R_t$  since  $R_t$  is fully known. Together with the known  $b$  and  $c/a, \gamma, \beta/\alpha$ , and  $a\alpha$  can be obtained from Eq. A.21 to A.23.

For the error box B with reversed direction to A, similar to Eq. A.19

$$\alpha = \frac{w_2 + \gamma}{\Gamma_l(1 + w_2\beta/\alpha)} \quad (\text{A.24})$$

where

$$w_2 = S_{r,22} \quad (\text{A.25})$$

Eliminating  $\Gamma_l$  between Eq. A.19 and A.24,

$$a/\alpha = \frac{(w_1 - b)(1 + w_2\beta/\alpha)}{(w_2 + \gamma)(1 - w_1 c/a)} \quad (\text{A.26})$$

so that by combining Eq. A.23 and Eq. A.26

$$a = \pm \sqrt{\frac{(w_1 - b)(1 + w_2\beta/\alpha)(d - bf)}{(w_2 + \gamma)(1 - w_2 c/a)(1 - ec/a)}} \quad (\text{A.27})$$

## A Appendix

and

$$\alpha = \frac{(d - bf)}{a(1 - ec/a)} \quad (\text{A.28})$$

when the sign of Eq. A.27 is chosen, the requirement that  $\Gamma_l$  be known is eliminated.

$$R_a^{-1} = \frac{1}{r_{22}} \begin{pmatrix} a & b \\ c & 1 \end{pmatrix}^{-1} = \frac{1}{r_{22}(a - bc)} \begin{pmatrix} 1 & -b \\ -c & a \end{pmatrix} \quad (\text{A.29})$$

and similarly,

$$R_b^{-1} = \frac{1}{\rho_{22}(\alpha - \gamma\beta)} \begin{pmatrix} 1 & -\beta \\ -\gamma & \alpha \end{pmatrix} \quad (\text{A.30})$$

From Eq. A.20

$$r_{22}\rho_{22} = \frac{gd}{a\alpha + b\gamma} \quad (\text{A.31})$$

thus,

$$R_{DuT} = R_a^{-1} R_M R_b^{-1} = \frac{1}{r_{22}\rho_{22}(a - bc)(\alpha - \gamma\beta)} \begin{pmatrix} 1 & -b \\ -c & a \end{pmatrix} R_m \begin{pmatrix} 1 & -\beta \\ -\gamma & \alpha \end{pmatrix} \quad (\text{A.32})$$

can be easily calculated where  $R_m$  and  $R_{DuT}$  are the raw and de-embedded cascading matrix.

The two problems left are

1. Eq. A.13 and Eq. A.14 have two roots. Which is  $b$  and which is  $a/c$  should be determined.
2. how to choose the sign of Eq. A.27.

The answers given in [EH79] are

1.  $|b| < |a/c|$
2. The sign of Eq. A.27 is determined by the type of ‘reflect’. When ‘open’ is used as in this work, from Eq. A.19, the reflection coefficient  $\Gamma_1$  at the left reference plane is given by

$$\Gamma_1 = \frac{w_1 - b}{-cw_1 + a}, \quad (\text{A.33})$$

when  $|\angle\Gamma_1| < \pi/2$ , ‘+’ is chosen. When  $|\angle\Gamma_1| > \pi/2$ , ‘-’ is chosen,

respectively.

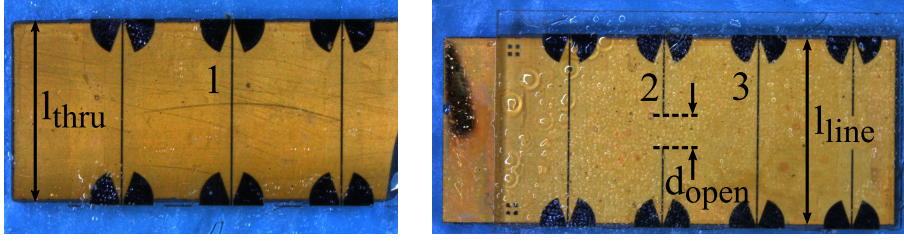


Figure A.6: TRL calibration kits: 1. ‘thru’, 2. ‘open’ and 3. ‘line’ standards. The dimensions are given as:  $l_{\text{thru}} = 4000 \mu\text{m}$ ,  $l_{\text{line}} = 4860 \mu\text{m}$  and  $d_{\text{open}} = l_{\text{line}} - l_{\text{thru}} = 860 \mu\text{m}$ .

### Practical TRL Considerations

The TRL reference plane could be a coaxial interface, or a RF probe interface, or even a waveguide interface. In chapter 3, for the first time, TRL is applied to de-embed microstrip line with via-less transition and tunable fluid dielectrics (LC). To ease the de-embedding, some points are considered during the design and fabrication of the TRL kits and the phase shifters [HT01; Ye+17]:

1. Although theoretically the mismatch between the characteristic impedance  $Z_C$  of DuT and VNA has no impact, since  $\Gamma_l$  is hypothesised to be unknown. However, the lowest reflection coefficient is desired in practice. Therefore, all devices are designed to match  $50 \Omega$ . This can be seen already from the decent matching of raw measurement data in Fig. 3.9, 3.14, 3.18, and 4.3.
2. All devices are processed together on the same glass wafer to minimize the impedance variations caused by fabrication tolerance, which is the premise of a precise TRL de-embedding.
3. The differential electrical length between ‘thru’ and ‘line’ within the interested frequency range must be in the range of  $20^\circ$  to  $160^\circ$ . Otherwise, a multi-line TRL is required. A differential physical length of  $860 \mu\text{m}$  is calculated to fulfill such requirement from 10 GHz to 80 GHz.

The TRL calibration kits used in Fig. 3.9, 3.14, 3.18, and 4.3 are shown in Fig. A.6. They are based on the same  $20 \mu\text{m}$  thick GT3 LC, and the same CPW-to-IMSL transitions as the LC-IMSL, LC-LMSL and LC-DGS phase shifters in chapter 3. These kits can also be biased to de-embed the LC phase shifters under the same bias case.



## B Acronyms

<b>PCB</b>	Printed Circuit Board
<b>MI</b>	Mobile Internet
<b>UHD</b>	Ultra-High Density
<b>mmW</b>	Millimeter-Waves
<b>FSPL</b>	Free-Sspace Path Loss
<b>ESPA</b>	Electronically Steered Passive Phased Array
<b>CMOS</b>	Complementary-Metal-Oxide-Semiconductor
<b>RF</b>	Radio Frequency
<b>MEMS</b>	MicroElectroMechanical Systems
<b>BST</b>	Barium Strontium Titanate
<b>LC</b>	Liquid Crystal
<b>LCD</b>	Liquid Crystal Display
$\bar{n}$	Averaged director of LC molecules
$D$	Antenna Directivity
$\vec{a}$	Director of a LC molecule
$f(\theta, \phi)$	Distribution function
$\vec{P}$	Polarization
$\vec{D}$	Electric displacement
$\chi_e$	Electric susceptibility tensor
$\Delta\epsilon$	Dielectric anisotropy
$W_{\text{elec}}$	Electric energy density

## B Acronyms

$\varepsilon_0$	Permittivity of free space
$\vec{M}$	Magnetisation
$\chi_m$	Magnetic susceptibility tensor
$\vec{B}$	Magnetic induction
$\mu_0$	Permeability in vacuum
$W_{\text{mag}}$	Magnetic energy density
$V_B$	Bias voltage
$V_{\text{TH}}$	Threshold voltage
$\varepsilon_r$	Relative dielectric constant
$\varepsilon_{r,\perp}$	$\varepsilon_r$ of parallelly aligned LC
$\varepsilon_{r,\parallel}$	$\varepsilon_r$ of perpendicularly aligned LC
<b>FoM</b>	Figure-of-Merit
$\tau_{\text{on}}$	Switch-on response time
$\tau_{\text{off}}$	Switch-off response time
$\gamma_r$	Rotational viscosity
$K_{ii}$	Elastic constant
$\tau_{\text{LC}}$	Material's tunability
$\eta_{\text{LC}}$	Material's FoM
<b>TDS</b>	Time Domain Spectroscopy
<b><math>\tan\delta</math></b>	Dissipation factor
<b>CPM</b>	Cavity Perturbation Method
<b>MuT</b>	Material under Test
<b>TL</b>	Transmission Line
<b>SW</b>	Slow-Wave
<b>MSL</b>	Microstrip Line
<b>IMSL</b>	Inverted Microstrip Line
<b>DGS</b>	Defective Ground Structure



<b>NaM</b>	Metallic-Nanowire-Filled-Membrane
<b>BM</b>	Butler Matrix
<b>SPDT</b>	Single-Pole Double-Throw
<b>IL</b>	Insertion Loss
<b>TSV</b>	Through Substrate Via
<b>RIS</b>	Reconfigurable Intelligent Surface
$v_\phi$	Phase velocity
$Z_C$	Characteristic impedance
$Z_L$	Load impedance
$\gamma$	Propagation constant
$\lambda$	Wavelength
<b>TEM</b>	Transverse Electromagnetic
<b>QTEM</b>	Quasi-TEM
<b>EMI</b>	Electromagnetic Interference
<b>LC-IMSL</b>	LC-based IMSL
<b>CPW</b>	Co-Planar Waveguide
<b>GSG</b>	Ground-Signal-Ground
$\eta_D$	Device tuning efficiency
$\tau_{D,eff}$	Effective device tunability
<b>SMA</b>	SubMiniature version A
<b>DuT</b>	Device under Test
<b>f</b>	Frequency
<b>LRRM</b>	Line-Reflect-Reflect-Match
<b>TRL</b>	Thru-Reflect-Line
<b>LMSL</b>	Stub-Loaded IMSL
<b>LC-LMSL</b>	LC-based LMSL
<b>LC-DGS</b>	LC-based IMSL with DGS

## *B Acronyms*

<b>SNR</b>	Signal to Noise Ratio
<b>K</b>	Slow-wave factor
$\Delta\phi_{\max}$	Maximum phase shift
<b>VNA</b>	Vector Network Analyzer
$f_{\text{cutoff}}$	Cut off frequency
$f_{\text{Bragg}}$	Bragg frequency
$\vec{E}_{\text{f}}$	Fringing electric field
$ S_{\text{xx}} $	Amplitude of $S_{\text{xx}}$
$\angle S_{\text{xx}}$	Phase of $S_{\text{xx}}$
$\angle S_{\text{xx, unwrap}}$	Unwrapped phase of $S_{\text{xx}}$
<b>AAO</b>	Anodic Aluminum Oxide
<b>LC-NaM</b>	LC-based IMSL phase shifter with NaM
$\sigma$	Conductivity
<b>STPS</b>	Switch Type Phase Shifter
<b>RTPS</b>	Reflection Type Phase Shifter
<b>MOSFET</b>	Metal-Oxide-Semiconductor Field-Effect Transistor
<b>LC-VCPW</b>	LC-based Varactor loaded CPW phase shifter
<b>LC-VMS</b>	LC-based Varactor loaded MicroStrip phase shifter
<b>IP3</b>	The Third-order Intercept Point
<b>IMD3</b>	The Third-order Intermodulation
<b>OIP3</b>	Output IP3
<b>IIP3</b>	Input IP3
<b>P<sub>1dB</sub></b>	1 dB compression point
<b>PA</b>	Power Amplifier
<b>G</b>	Gain
<b>ITO</b>	Indium Tin Oxide
<b>CPS</b>	CoPlanar Stripline

<b>CPOL</b>	Co-POLarization
<b>XPOL</b>	Cross-POLarization
<b>LTCC</b>	Low Temperature Co-fired Ceramics
$\lambda_g$	Guided wavelength
<b>SLL</b>	Side Lobe Level
<b>SPnT</b>	Single-Pole n-Throw
<b>SP4T</b>	Single-Pole four-Throw
<b>LCP</b>	Liquid Crystal Polymer
<b>ISS</b>	Impedance Standard Substrate
<b>AuT</b>	Antenna under Test
<b>HPBW</b>	Half Power Beam Width
<b>EBG</b>	Electromagnetic BandGap Structure



# Bibliography

- [AG22] Schott AG. *AF32 eco material properties*. 2022. URL: <https://www.pgo-online.com/intl/af32.html> (visited on 06/12/2022).
- [Ahn+01] D. Ahn, J. -. Park, C. -. Kim, J. Kim, Y. Qian, and T. Itoh. “A design of the low-pass filter using the novel microstrip defected ground structure”. In: *IEEE Transactions on Microwave Theory and Techniques* 49.1 (2001), pp. 86–93.
- [Al+08] Mahmoud Al Ahmad, Ludovic Salvagnac, Dominique Michau, Mario Maglione, and Robert Plana. “Investigations of Indium Tin Oxide—Barium Strontium Titanate—Indium Tin Oxide Heterostructure for Tunability”. In: *IEEE Microwave and Wireless Components Letters* 18.6 (2008), pp. 398–400. DOI: 10.1109/LMWC.2008.922631.
- [ALC] Public Link ALCAN Systems. *Multi-Beam ESA Demonstration*. <https://www.youtube.com/watch?v=ArLNgMnYVMY&feature=youtu.be>. Accessed on 5 June 2020.
- [APE09] Mohamed A. Y. Abdalla, Khoman Phang, and George V. Eleftheriades. “A Planar Electronically Steerable Patch Array Using Tunable PRI/NRI Phase Shifters”. In: *IEEE Transactions on Microwave Theory and Techniques* 57.3 (2009), pp. 531–541. DOI: 10.1109/TMTT.2008.2012312.
- [BM10] S. Bulja and D. Mirshekar-Syahkal. “Meander line millimetre-wave liquid crystal based phase shifter”. In: *Electronics Letters* 46.11 (2010), pp. 769–771.
- [Bul+10a] S. Bulja, D. Mirshekar-Syahkal, M. Yazdanpanahi, R. James, S. E. Day, and F. A. Fernández. “60 GHz Reflection Type Phase Shifter based on liquid crystal”. In: *2010 IEEE Radio and Wireless Symposium (RWS)*. 2010, pp. 697–699. DOI: 10.1109/RWS.2010.5434253.
- [Bul+10b] Senad Bulja, Dariush Mirshekar-Syahkal, Richard James, Sally E. Day, and F. Aníbal Fernández. “Measurement of Dielectric Properties of Nematic Liquid Crystals at Millimeter Wavelength”. In: *IEEE Transactions on Microwave Theory and Techniques* 58.12 (2010), pp. 3493–3501. DOI: 10.1109/TMTT.2010.2054332.
- [But61] J. Butler. “Beam-forming matrix simplifies design of electronically scanned antennas”. In: *Electronic Design* 9 (1961), pp. 170–173.

## Bibliography

- [Che+09] Shi Cheng, Pekka Rantakari, Robert Malmqvist, Carl Samuelsson, Tauno Vaha-Heikkilä, Anders Rydberg, and Jussi Varis. “Switched Beam Antenna Based on RF MEMS SPDT Switch on Quartz Substrate”. In: *IEEE Antennas and Wireless Propagation Letters* 8 (2009), pp. 383–386. DOI: 10.1109/LAWP.2009.2018712.
- [Chu+00] Chul-Soo Kim, Jun-Seok Park, Dal Ahn, and Jae-Bong Lim. “A novel 1-D periodic defected ground structure for planar circuits”. In: *IEEE Microwave and Guided Wave Letters* 10.4 (2000), pp. 131–133.
- [CLS10] Chia-Chan Chang, Ruey-Hsuan Lee, and Ting-Yen Shih. “Design of a Beam Switching/Steering Butler Matrix for Phased Array System”. In: *IEEE Transactions on Antennas and Propagation* 58.2 (2010), pp. 367–374. DOI: 10.1109/TAP.2009.2037693.
- [Cun11] J. H. Cunningham. “Design, construction and test of an artificial transmission line [J]”. In: *Transactions of the American institute of electrical engineers* (1911), 1: 245–256.
- [Dau+22] Kassen Dautov, Mohammad S. Hashmi, N. Nasimuddin, Muhammad Akmal Chaudhary, and Galymzhan Nauryzbayev. “Quantifying the Impact of Slow Wave Factor on Closed-Loop Defect-Based WPT Systems”. In: *IEEE Transactions on Instrumentation and Measurement* 71 (2022), pp. 1–10. DOI: 10.1109/TIM.2022.3181938.
- [DD07] Daniel J. Dickrell and Michael T. Dugger. “Silicone Oil Contamination and Electrical Contact Resistance Degradation of Low-Force Gold Contacts”. In: *Journal of Microelectromechanical Systems* 16.1 (2007), pp. 24–28. DOI: 10.1109/JMEMS.2006.885984.
- [Deo+13] Prafulla Deo, Dariush Mirshekar-Syahkal, Lawrence Seddon, Sally E. Day, and F. Aníbal Fernández. “60 GHz liquid crystal phased array using reflection-type phase shifter”. In: *2013 7th European Conference on Antennas and Propagation (EuCAP)*. 2013, pp. 927–929.
- [dJ95] P. G. deGennes and J. Prost. *The Physics of Liquid Crystals*. Clarendon Press, 1995.
- [Dol+93] D. Dolfi, M. Labeyrie, P. Joffre, and J. P. Huignard. “Liquid crystal microwave phase shifter”. In: *Electronics Letters* 29.10 (May 1993), pp. 926–928. DOI: 10.1049/el:19930618.
- [Dol20] André Doll. *5G and Beyond: The Power Consumption Challenge*. 2020. URL: <https://www.alcansystems.com/5g-and-beyond-the-power-consumption-challenge/>.
- [EBM14] Soon Young Eom, Ariunzaya Batgerel, and Laxmikant Minz. “Compact Broadband Microstrip Crossover With Isolation Improvement and Phase Compensation”. In: *IEEE Microwave and Wireless Components Letters* 24.7 (2014), pp. 481–483. DOI: 10.1109/LMWC.2014.2303163.

- [EH79] G.F. Engen and C.A. Hoer. “Thru-Reflect-Line: An Improved Technique for Calibrating the Dual Six-Port Automatic Network Analyzer”. In: *IEEE Transactions on Microwave Theory and Techniques* 27.12 (1979), pp. 987–993. DOI: 10.1109/TMTT.1979.1129778.
- [Fer+22] P. Ferrari, R. Jakoby, O. Karabey, G. Rehder, and H. Maune. *Reconfigurable Circuits and Technologies for Smart Millimeter-Wave Systems*. Cambridge University Press, 2022.
- [Fra+13] Anne-Laure Franc, Onur Hamza Karabey, Gustavo Rehder, Emmanuel Pistono, Rolf Jakoby, and Philippe Ferrari. “Compact and Broadband Millimeter-Wave Electrically Tunable Phase Shifter Combining Slow-Wave Effect With Liquid Crystal Technology”. In: *IEEE Transactions on Microwave Theory and Techniques* 61.11 (2013), pp. 3905–3915. DOI: 10.1109/TMTT.2013.2282288.
- [Fri+11] C. Fritzsche, S. Strunck, S. Bildik, and R. Jakoby. “Investigation of Beam Scanning Speed for Liquid Crystal based Tunable Antennas”. In: *ESA Antenna Workshop on Challenges for Space Antenna Systems*. Mar. 2011. DOI: 10.1109/IRMMW-THz.2019.8873696.
- [Fri+12] Carsten Fritzsche, Flavio Giacomozzi, Onur Hamza Karabey, Saygin Bildik, Sabrina Colpo, and Rolf Jakoby. “Advanced characterization of a W-band phase shifter based on liquid crystals and MEMS technology”. In: *International Journal of Microwave and Wireless Technologies* 4.3 (2012), pp. 379–386. DOI: 10.1017/S1759078712000311.
- [Fri15] Carsten Fritzsche. “Flüssigkristallbasierte Elektronisch Steuerbare Gruppenantennen Technologie, Konzepte und Komponenten”. PhD thesis. Technische Universität Darmstadt, 2015.
- [GJZ16] Chao Gai, Yong-Chang Jiao, and Yu-Long Zhao. “Compact Dual-Band Branch-Line Coupler With Dual Transmission Lines”. In: *IEEE Microwave and Wireless Components Letters* 26.5 (2016), pp. 325–327. DOI: 10.1109/LMWC.2016.2549099.
- [Goe+08] F. Goelden, A. Gaebler, S. Mueller, A. Lapanik, Wolfgang Haase, and Rolf Jakoby. “Liquid-crystal varactors with fast switching times for microwave applications”. In: *Electronics Letters* 44 (Feb. 2008), pp. 480–481. DOI: 10.1049/el:20080161.
- [Goe+09] F. Goelden, A. Gaebler, M. Goebel, A. Manabe, S. Mueller, and R. Jakoby. “c”. In: *Electronics Letters* 45.13 (2009), pp. 686–687.
- [Goe10] Felix Goelden. “Liquid Crystal Based Microwave Components with Fast Response Times: Material, Technology, Power Handling Capability”. PhD thesis. Technische Universität Darmstadt, 2010.

## Bibliography

- [GS15] Farhan A. Ghaffar and Atif Shamim. “A Partially Magnetized Ferrite LTCC-Based SIW Phase Shifter for Phased Array Applications”. In: *IEEE Transactions on Magnetics* 51.6 (2015), pp. 1–8. DOI: 10.1109/TMAG.2015.2404303.
- [Han+14] Ke-Wu Han, Hengrong Cui, Xiao-Wei Sun, and Jian Zhang. “The design of a 60 GHz low loss hybrid phase shifter with 360 degree phase shift”. In: *2014 14th International Symposium on Communications and Information Technologies (ISCIT)*. 2014, pp. 551–554. DOI: 10.1109/ISCIT.2014.7011975.
- [HCY12] Jian-Quan Huang, Qing-Xin Chu, and Hong-Ze Yu. “A Mixed-Lattice Slow-Wave Transmission Line”. In: *IEEE Microwave and Wireless Components Letters* 22.1 (2012), pp. 13–15. DOI: 10.1109/LMWC.2011.2177648.
- [HHR12] Y. Hajilou, H. R. Hassani, and B. Rahmati. “Mutual coupling reduction between microstrip patch antennas”. In: *2012 6th European Conference on Antennas and Propagation (EuCAP)*. 2012, pp. 1–4. DOI: 10.1109/EuCAP.2012.6205886.
- [Hin05] J. Hinojosa. “Broad band electromagnetic characterization method of nematic liquid crystals using a coplanar waveguide”. In: *IEEE International Conference on Dielectric Liquids, 2005. ICDL 2005*. 2005, pp. 449–452. DOI: 10.1109/ICDL.2005.1490122.
- [Hin20] Pat Hindle. *Comprehensive Survey of Commercial mmWave Phased Array Companies*. 2020. URL: <https://www.microwavejournal.com/articles/33357-comprehensive-survey-of-commercial-mmwave-phased-array-companies>.
- [HT01] Hang-Ting Lue and Tseung-Yuen Tseng. “Application of on-wafer TRL calibration on the measurement of microwave properties of Ba/sub 0.5/Sr/sub 0.5/TiO/sub 3/ films”. In: *IEEE Transactions on Ultrasonics, Ferroelectrics, and Frequency Control* 48.6 (2001), pp. 1640–1647.
- [Hu+14] W. Hu, O. H. Karabey, A. Gäbler, A. E. Prasetyadi, M. Jost, and R. Jakoby. “Liquid crystal varactor loaded variable phase shifter for integrated, compact, and fast beamsteering antenna systems”. In: *9th European Microwave Integrated Circuit Conference*. Oct. 2014, pp. 660–663. DOI: 10.1109/EuMIC.2014.6997943.
- [Isk+16] Zyad Iskandar, Jose Lugo-Alvarez, Alfredo Bautista, Emmanuel Pistono, Florence Podevin, Vincent Puyal, Alexandre Siligaris, and Philippe Ferrari. “A 30–50 GHz reflection-type phase shifter based on slow-wave coupled lines in BiCMOS 55 nm technology”. In: *46th European Microwave Conference (EuMC)*. 2016, pp. 1413–1416. DOI: 10.1109/EuMC.2016.7824618.



- [ITU15] International Telecommunication Union (ITU). “MT Vision—Framework and Overall Objectives of the Future Development of IMT for 2020 and beyond”. In: vol. Recommendation ITU-R M.2083-0. 2015.
- [ITU16] International Telecommunication Union (ITU). “Attenuation by atmospheric gases”. In: vol. Recommendation ITU-R P.676-11. 2016.
- [JGW20] Rolf Jakoby, Alexander Gaebler, and Christian Weickhmann. “Microwave Liquid Crystal Enabling Technology for Electronically Steerable Antennas in SATCOM and 5G Millimeter-Wave Systems”. In: *Crystals* 10.6 (2020). DOI: 10.3390/cryst10060514.
- [Ji+19] Yuan Ji, Lei Ge, Jianpeng Wang, Quangang Chen, Wen Wu, and Yujian Li. “Reconfigurable Phased-Array Antenna Using Continuously Tunable Substrate Integrated Waveguide Phase Shifter”. In: *IEEE Transactions on Antennas and Propagation* 67.11 (2019), pp. 6894–6908. DOI: 10.1109/TAP.2019.2927813.
- [Jos+16] M. Jost, R. Reese, C. Weickhmann, C. Schuster, O. H. Karabey, H. Maune, and R. Jakoby. “Tunable dielectric delay line phase shifter based on liquid crystal technology for a SPDT in a radiometer calibration scheme at 100 GHz”. In: *IEEE MTT-S International Microwave Symposium (IMS)*. 2016, pp. 1–4. DOI: 10.1109/MWSYM.2016.7540007.
- [Jos+17] M. Jost, R. Reese, M. Nickel, S. Schmidt, H. Maune, and R. Jakoby. “Interference based W-band single-pole double-throw with tunable liquid crystal based waveguide phase shifters”. In: *IEEE MTT-S International Microwave Symposium (IMS)*. 2017, pp. 184–187. DOI: 10.1109/MWSYM.2017.8059003.
- [Jos+18a] M. Jost, A. Heunisch, A. E. Prasetiadi, B. Schulz, R. Reese, M. Nickel, E. Polat, M. Quibeldey, H. Maune, T. Rabe, R. Follmann, and R. Jakoby. “Liquid Crystal Based SPDT with Adjustable Power Splitting Ratio in LTCC Technology”. In: *48th European Microwave Conference (EuMC)*. 2018, pp. 612–615. DOI: 10.23919/EuMC.2018.8541524.
- [Jos+18b] Matthias Jost, Jay S. K. Gautam, Leonardo G. Gomes, Roland Reese, Ersin Polat, Matthias Nickel, Julio M. Pinheiro, Ariana L. C. Serrano, Holger Maune, Gustavo P. Rehder, Philippe Ferrari, and Rolf Jakoby. “Miniaturized Liquid Crystal Slow Wave Phase Shifter Based on Nanowire Filled Membranes”. In: *IEEE Microwave and Wireless Components Letters* 28.8 (2018), pp. 681–683. DOI: 10.1109/LMWC.2018.2845938.
- [Jos18] Matthias Jost. “Liquid Crystal Mixed Beam-Switching and Beam-Steering Network in Hybrid Metallic and Dielectric Waveguide Technology”. PhD thesis. Technische Universität Darmstadt, 2018.
- [Kan+02] N. Kaneda, W. R. Deal, Yongxi Qian, R. Waterhouse, and T. Itoh. “A broadband planar quasi-Yagi antenna”. In: *IEEE Transactions on Antennas and Propagation* 50.8 (2002), pp. 1158–1160.

## Bibliography

- [Kar+12a] Onur Hamza Karabey, Sara Bausch, Saygin Bildik, Sebastian Strunck, Alexander Gaebler, and Rolf Jakoby. “Design and application of a liquid crystal varactor based tunable coupled line for polarization agile antennas”. In: *2012 42nd European Microwave Conference*. 2012, pp. 739–742. DOI: 10.23919/EuMC.2012.6459335.
- [Kar+12b] Onur Hamza Karabey, Alexander Gaebler, Sebastian Strunck, and Rolf Jakoby. “A 2-D Electronically Steered Phased-Array Antenna With  $2 \times 2$  Elements in LC Display Technology”. In: *IEEE Transactions on Microwave Theory and Techniques* 60.5 (2012), pp. 1297–1306. DOI: 10.1109/TMTT.2012.2187919.
- [Kar14] Onur Hamza Karabey. “Electronic beam steering and polarization agile planar antennas in liquid crystal technology”. PhD thesis. Technische Universität Darmstadt, 2014.
- [KFN02] T. Kuki, H. Fujikake, and T. Nomoto. “Microwave variable delay line using dual-frequency switching-mode liquid crystal”. In: *IEEE Transactions on Microwave Theory and Techniques* 50.11 (2002), pp. 2604–2609.
- [Kim+02] Hong-Teuk Kim, Jae-Hyoung Park, Sanghyo Lee, Seongho Kim, Jung-Mu Kim, Yong-Kweon Kim, and Youngwoo Kwon. “V-band 2-b and 4-b low-loss and low-voltage distributed MEMS digital phase shifter using metal-air-metal capacitors”. In: *IEEE Transactions on Microwave Theory and Techniques* 50.12 (2002), pp. 2918–2923. DOI: 10.1109/TMTT.2002.805285.
- [KMG15] Anand Kumar, Jitendra Mohan, and Hariom Gupta. “Surface wave suppression of microstrip antenna using different EBG designs”. In: *2015 International Conference on Signal Processing and Communication (ICSC)*. 2015, pp. 355–359. DOI: 10.1109/ICSPCom.2015.7150676.
- [KO92] H. Kamitsuna and H. Ogawa. “Novel slow-wave meander lines using multilayer MMIC technologies”. In: *IEEE Microwave and Guided Wave Letters* 2.1 (1992), pp. 8–10. DOI: 10.1109/75.109126.
- [Kom47] R. Kompfner. “The traveling wave tubes as an amplifier at microwaves [J]”. In: *Proceeding of IRE* (1947), 35(2): 124–127.
- [Kuk+02] Takao Kuki, Hideo Fujikake, Toshihiro Nomoto, and Yozo Utsumi. “Design of a microwave variable delay line using liquid crystal, and a study of its insertion loss”. In: *Electronics and Communications in Japan (Part II: Electronics)* 85.2 (2002), pp. 36–42. DOI: <https://doi.org/10.1002/ecjb.1091>. eprint: <https://onlinelibrary.wiley.com/doi/pdf/10.1002/ecjb.1091>. URL: <https://onlinelibrary.wiley.com/doi/abs/10.1002/ecjb.1091>.

- [LdM09] Benito Lopez-Berrocal, JosÉ de-Oliva-Rubio, and Iñigo Molina-Fernandez. “Design and Implementation of DC–20-GHz Lumped Resistor Matched Loads for Planar Microwave Circuits”. In: *IEEE Transactions on Microwave Theory and Techniques* 57.10 (2009), pp. 2439–2443. DOI: 10 . 1109 / TMTT . 2009 . 2029628.
- [Lé+22] J. E. G. Lé, M. Ouvrier-Buffet, L. G. Gomes, R. A. Penchel, A. L. C. Serrano, and G. P. Rehder. “Integrated Antennas on MnM Interposer for the 60 GHz Band”. In: *Journal of Microwaves, Optoelectronics and Electromagnetic Applications [online]* 21.1 (2022), pp. 184–193.
- [Leh89] O. Lehmann. “Über fließende Krystalle”. In: *Zeitschrift für Physikalische Chemie* 4U.1 (1889), pp. 462–472. DOI: doi : 10 . 1515 / zpch - 1889 - 0434.
- [Li+22] Xiao Yu Li, Di Jiang, Juan Liu, and Mei Song Tong. “A Ka-Band Multilayer Beaming-Scanning Antenna Using Liquid Crystals”. In: *IEEE Antennas and Wireless Propagation Letters* 21.1 (2022), pp. 44–48. DOI: 10 . 1109 / LAMP . 2021 . 3116661.
- [Lim+02a] Jong-Sik Lim, Young-Taek Lee, Chul-Soo Kim, Dal Ahn, and Sangwook Nam. “A vertically periodic defected ground structure and its application in reducing the size of microwave circuits”. In: *IEEE Microwave and Wireless Components Letters* 12.12 (2002), pp. 479–481. DOI: 10 . 1109 / LMWC . 2002 . 805941.
- [Lim+02b] Jong-Sik Lim, Jun-Seok Park, Young-Taek Lee, Dal Ahn, and Sangwook Nam. “Application of defected ground structure in reducing the size of amplifiers”. In: *IEEE Microwave and Wireless Components Letters* 12.7 (2002), pp. 261–263. DOI: 10 . 1109 / LMWC . 2002 . 801139.
- [Liu+05] An-Shyi Liu, C.-K.C. Tzuang, Ruey-Beei Wu, and Hsien-Shun Wu. “Ka-band 32-GHz planar integrated switched-beam smart antenna”. In: *IEEE MTT-S International Microwave Symposium Digest, 2005*. 2005, pp. 565–568. DOI: 10 . 1109 / MWSYM . 2005 . 1516661.
- [Liu+11] C. Liu, S. Xiao, Y. Guo, M. Tang, Y. Bai, and B. Wang. “Circularly Polarized Beam-Steering Antenna Array With Butler Matrix Network”. In: *IEEE Antennas and Wireless Propagation Letters* 10 (2011), pp. 1278–1281.
- [Liu+12] Wendong Liu, Zhijun Zhang, Zhenghe Feng, and Magdy F. Iskander. “A Compact Wideband Microstrip Crossover”. In: *IEEE Microwave and Wireless Components Letters* 22.5 (2012), pp. 254–256. DOI: 10 . 1109 / LMWC . 2012 . 2190270.
- [LLX14] Chao Liu, Qiang Li, and Yong-Zhong Xiong. “A compact Ka-band SPDT switch with high isolation”. In: *2014 International Symposium on Integrated Circuits (ISIC)*. 2014, pp. 304–307. DOI: 10 . 1109 / ISICIR . 2014 . 7029563.

## Bibliography

- [LM04] Lei Zhu and W. Menzel. “Broad-band microstrip-to-CPW transition via frequency-dependent electromagnetic coupling”. In: *IEEE Transactions on Microwave Theory and Techniques* 52.5 (2004), pp. 1517–1522.
- [LML93] K. C. Lim, J. D. Margerum, and A. M. Lackner. “Liquid crystal millimeter wave electronic phase shifter”. In: *Applied Physics Letters* 62.10 (1993), pp. 1065–1067. DOI: 10.1063/1.108796. eprint: <https://doi.org/10.1063/1.108796>. URL: <https://doi.org/10.1063/1.108796>.
- [LW16] Yu-Hsuan Lin and Huei Wang. “A low phase and gain error passive phase shifter in 90 nm CMOS for 60 GHz phase array system application”. In: *2016 IEEE MTT-S International Microwave Symposium (IMS)*. 2016, pp. 1–4. DOI: 10.1109/MWSYM.2016.7540372.
- [Ma+18] Shuang Ma, Shao-Qing Zhang, Lei-Qiang Ma, Fan-Yi Meng, Daniel Erni, Lei Zhu, Jia-Hui Fu, and Qun Wu. “Compact planar array antenna with electrically beam steering from backfire to endfire based on liquid crystal”. In: *IET Microwaves, Antennas & Propagation* 12.7 (2018), pp. 1140–1146.
- [Man+06] A. M. Mangan, S. P. Voinigescu, Ming-Ta Yang, and M. Tazlauanu. “De-embedding transmission line measurements for accurate modeling of IC designs”. In: *IEEE Transactions on Electron Devices* 53.2 (Feb. 2006), pp. 235–241. DOI: 10.1109/TED.2005.861726.
- [Mau+18] Holger Maune, Matthias Jost, Roland Reese, Ersin Polat, Matthias Nickel, and Rolf Jakoby. “Microwave Liquid Crystal Technology”. In: *Crystals* 8.9 (2018). DOI: 10.3390/cryst8090355.
- [MR07] Byung-Wook Min and Gabriel M. Rebeiz. “Ka-Band Low-Loss and High-Isolation 0.13  $\mu$ m CMOS SPST/SPDT Switches Using High Substrate Resistance”. In: *2007 IEEE Radio Frequency Integrated Circuits (RFIC) Symposium*. 2007, pp. 569–572. DOI: 10.1109/RFIC.2007.380948.
- [Mue+04] S. Mueller, P. Scheele, C. Weil, M. Wittek, C. Hock, and R. Jakoby. “Tunable passive phase shifter for microwave applications using highly anisotropic liquid crystals”. In: *IEEE MTT-S International Microwave Symposium Digest (IEEE Cat. No.04CH37535)*. Vol. 2. June 2004, 1153–1156 Vol.2. DOI: 10.1109/MWSYM.2004.1339190.
- [Mue+05] S. Mueller, A. Penirschke, C. Damm, P. Scheele, M. Wittek, C. Weil, and R. Jakoby. “Broad-band microwave characterization of liquid crystals using a temperature-controlled coaxial transmission line”. In: *IEEE Transactions on Microwave Theory and Techniques* 53.6 (2005), pp. 1937–1945. DOI: 10.1109/TMTT.2005.848842.

- [Nik+16] Mohammad Nikfalazar, Christian Kohler, Alex Wiens, Arshad Mehmood, Mojtaba Sohrabi, Holger Maune, Joachim R. Binder, and Rolf Jakoby. “Beam Steering Phased Array Antenna With Fully Printed Phase Shifters Based on Low-Temperature Sintered BST-Composite Thick Films”. In: *IEEE Microwave and Wireless Components Letters* 26.1 (2016), pp. 70–72. DOI: 10.1109/LMWC.2015.2505633.
- [Pan+22] Mohammad Ali Panahi, Lap Yeung, Maziar Hedayati, and Yuanxun Ethan Wang. “Sub-6 GHz High FOM Liquid Crystal Phase Shifter for Phased Array Antenna”. In: *IEEE Journal of Microwaves* 2.2 (2022), pp. 316–325. DOI: 10.1109/JMW.2022.3152208.
- [Pen+09] Zhen Peng, Cristiano Palego, James C. M. Hwang, David I. Forehand, Charles L. Goldsmith, Cody Moody, Andrew Malczewski, Brandon W. Pillans, Richard Daigler, and John Papapolymerou. “Impact of Humidity on Dielectric Charging in RF MEMS Capacitive Switches”. In: *IEEE Microwave and Wireless Components Letters* 19.5 (2009), pp. 299–301. DOI: 10.1109/LMWC.2009.2017595.
- [Pol+19a] E. Polat, R. Reese, H. Tesmer, S. Schmidt, M. Spaeth, M. Nickel, C. Schuster, R. Jakoby, and H. Maune. “Characterization of Liquid Crystals Using a Temperature-Controlled 60 GHz Resonator”. In: *2019 IEEE MTT-S International Microwave Workshop Series on Advanced Materials and Processes for RF and THz Applications (IMWS-AMP)*. 2019, pp. 19–21. DOI: 10.1109/IMWS-AMP.2019.8880077.
- [Pol+19b] Ersin Polat, Roland Reese, Matthias Jost, Matthias Nickel, Christian Schuster, Rolf Jakoby, and Holger Maune. “Liquid Crystal Phase Shifter Based on Nonradiative Dielectric Waveguide Topology at W-Band”. In: *2019 IEEE MTT-S International Microwave Symposium (IMS)*. 2019, pp. 184–187. DOI: 10.1109/MWSYM.2019.8700759.
- [Reg+09] James A Rego, Jamie AA Harvey, Andrew L MacKinnon, and Elysse Gatdula. “Asymmetric synthesis of a highly soluble ‘trimeric’ analogue of the chiral nematic liquid crystal twist agent Merck S1011”. In: *Liquid Crystals* 37.1 (2009), pp. 37–43.
- [Ren+16] H. Ren, B. Arigong, M. Zhou, J. Ding, and H. Zhang. “A Novel Design of  $4 \times 4$  Butler Matrix With Relatively Flexible Phase Differences”. In: *IEEE Antennas and Wireless Propagation Letters* 15 (2016), pp. 1277–1280.
- [Ren+20] Han Ren, Peizhao Li, Yixin Gu, and Bayaner Arigong. “Phase Shifter-Relaxed and Control-Relaxed Continuous Steering Multiple Beamforming  $4 \times 4$  Butler Matrix Phased Array”. In: *IEEE Transactions on Circuits and Systems I: Regular Papers* 67.12 (2020), pp. 5031–5039. DOI: 10.1109/TCSI.2020.3009215.

## Bibliography

- [Saz+11a] M. Sazegar, Y. Zheng, H. Maune, C. Damm, X. Zhou, J. Binder, and R. Jakoby. “Low-Cost Phased-Array Antenna Using Compact Tunable Phase Shifters Based on Ferroelectric Ceramics”. In: *IEEE Transactions on Microwave Theory and Techniques* 59.5 (May 2011), pp. 1265–1273. DOI: 10.1109/TMTT.2010.2103092.
- [Saz+11b] M. Sazegar, Y. Zheng, H. Maune, C. Damm, X. Zhou, J. Binder, and R. Jakoby. “Low-Cost Phased-Array Antenna Using Compact Tunable Phase Shifters Based on Ferroelectric Ceramics”. In: *IEEE Transactions on Microwave Theory and Techniques* 59.5 (May 2011), pp. 1265–1273. DOI: 10.1109/TMTT.2010.2103092.
- [Ser+14a] Ariana L. C. Serrano, Anne-Laure Franc, D. P. Assis, Florence Podevin, Gustavo P. Rehder, Nicolas Corrao, and Philippe Ferrari. “Modeling and Characterization of Slow-Wave Microstrip Lines on Metallic-Nanowire-Filled-Membrane Substrate”. In: *IEEE Transactions on Microwave Theory and Techniques* 62.12 (2014), pp. 3249–3254. DOI: 10.1109/TMTT.2014.2366108.
- [Ser+14b] Ariana L. C. Serrano, Anne-Laure Franc, Danilo P. Assis, Florence Podevin, Gustavo P. Rehder, Nicolas Corrao, and Philippe Ferrari. “Slow-wave microstrip line on nanowire-based alumina membrane”. In: *2014 IEEE MTT-S International Microwave Symposium (IMS2014)*. 2014, pp. 1–4. DOI: 10.1109/MWSYM.2014.6848552.
- [SGk19] S. Sivagnanam, E. Gnanamanoharan, and P. kailasapathi. “Multislot Rectangular Patch antenna with Defected Ground Structure for UWB Wireless Applications”. In: *2019 IEEE International Conference on System, Computation, Automation and Networking (ICSCAN)*. 2019, pp. 1–5.
- [She+10] Sharif Iqbal Mitu Sheikh, A. A. P. Gibson, M. Basorrah, G. Alhulwah, K. Alanizi, M. Alfarsi, and J. Zafar. “Analog/Digital Ferrite Phase Shifter for Phased Array Antennas”. In: *IEEE Antennas and Wireless Propagation Letters* 9 (2010), pp. 319–321. DOI: 10.1109/LAWP.2010.2048190.
- [Ste04] I. W. Stewart. *The Static and Dynamic Continuum Theory of Liquid Crystals: A Mathematical Introduction*. Taylor Francis, 2004.
- [TCC08] Chao-Hsiung Tseng, Chih-Jung Chen, and Tah-Hsiung Chu. “A Low-Cost 60-GHz Switched-Beam Patch Antenna Array With Butler Matrix Network”. In: *IEEE Antennas and Wireless Propagation Letters* 7 (2008), pp. 432–435. DOI: 10.1109/LAWP.2008.2001849.
- [Teb+16] M. Tebbe, A. Hoehn, N. Nathrath, and C. Weickhmann. “Simulation of an electronically steerable horn antenna array with liquid crystal phase shifters”. In: *2016 IEEE Aerospace Conference*. 2016, pp. 1–15. DOI: 10.1109/AERO.2016.7500660.

- [TFM18] Ali Tajik, Mohammad Fakharzadeh, and Khashayar Mehrany. “DC to 40-GHz Compact Single-Layer Crossover”. In: *IEEE Microwave and Wireless Components Letters* 28.8 (2018), pp. 642–644. DOI: 10.1109/LMWC.2018.2843134.
- [TN09] Ming-Da Tsai and Arun Natarajan. “60GHz passive and active RF-path phase shifters in silicon”. In: *2009 IEEE Radio Frequency Integrated Circuits Symposium*. 2009, pp. 223–226. DOI: 10.1109/RFIC.2009.5135527.
- [Top+08] Kagan Topalli, Özlem Aydin Civi, Simsek Demir, Sencer Koc, and Tayfun Akin. “A Monolithic Phased Array Using 3-bit Distributed RF MEMS Phase Shifters”. In: *IEEE Transactions on Microwave Theory and Techniques* 56.2 (2008), pp. 270–277. DOI: 10.1109/TMTT.2007.914377.
- [TS82] J.C. Tippet and R.A. Speciale. “A Rigorous Technique for Measuring the Scattering Matrix of a Multiport Device with a 2-Port Network Analyzer”. In: *IEEE Transactions on Microwave Theory and Techniques* 30.5 (1982), pp. 661–666. DOI: 10.1109/TMTT.1982.1131118.
- [TSF19] A. Tajik, A. Shafiei Alavijeh, and M. Fakharzadeh. “Asymmetrical 4×4 Butler Matrix and its Application for Single Layer 8 × 8 Butler Matrix”. In: *IEEE Transactions on Antennas and Propagation* 67.8 (2019), pp. 5372–5379.
- [TT12] Elze T and Tanner TG. “Temporal Properties of Liquid Crystal Displays: Implications for Vision Science Experiments”. In: *PLoS ONE* 7.9 (2012).
- [TVL08] George Tudosie, Ruediger Vahldieck, and Albert Lu. “A novel modularized folded highly compact LTCC Butler matrix”. In: *2008 IEEE MTT-S International Microwave Symposium Digest*. 2008, pp. 691–694. DOI: 10.1109/MWSYM.2008.4632926.
- [TYW14] Ge Tian, Jin-Ping Yang, and Wen Wu. “A Novel Compact Butler Matrix Without Phase Shifter”. In: *IEEE Microwave and Wireless Components Letters* 24.5 (2014), pp. 306–308. DOI: 10.1109/LMWC.2014.2306898.
- [WAH13] Yifan Wang, Amin M. Abbosh, and Bassem Henin. “Broadband Microwave Crossover Using Combination of Ring Resonator and Circular Microstrip Patch”. In: *IEEE Transactions on Components, Packaging and Manufacturing Technology* 3.10 (2013), pp. 1771–1777. DOI: 10.1109/TCPMT.2013.2262110.
- [Wan+19b] Xiaozhou Wang, Xiao Fang, Martin Laabs, and Dirk Plettemeier. “Compact 2-D Multibeam Array Antenna Fed by Planar Cascaded Butler Matrix for Millimeter-Wave Communication”. In: *IEEE Antennas and Wireless Propagation Letters* 18.10 (2019), pp. 2056–2060. DOI: 10.1109/LAWP.2019.2937254.
- [WDR02] Z. Wang, J. Deen, and A. Rahal. “Accurate Modelling of Thin-Film Resistor up to 40 GHz”. In: *32nd European Solid-State Device Research Conference*. 2002, pp. 307–310. DOI: 10.1109/ESSDERC.2002.194930.

## Bibliography

- [Wei+03] C. Weil, S. Muller, Patrick Scheele, P. Best, G. Lussem, and Rolf Jakoby. “Highly-anisotropic liquid-crystal mixtures for tunable microwave devices”. In: *Electronics Letters* 39 (Dec. 2003), pp. 1732–1734. DOI: 10.1049/el:20031150.
- [Wei+13] Christian Weickhmann, Rolf Jakoby, Evan Constable, and R. A. Lewis. “Time-domain spectroscopy of novel nematic liquid crystals in the terahertz range”. In: *2013 38th International Conference on Infrared, Millimeter, and Terahertz Waves (IRMMW-THz)*. 2013, pp. 1–2. DOI: 10.1109/IRMMW-THz.2013.6665423.
- [WLJ02] C. Weil, G. Luessem, and R. Jakoby. “Tunable inverted-microstrip phase shifter device using nematic liquid crystals”. In: *2002 IEEE MTT-S International Microwave Symposium Digest (Cat. No.02CH37278)*. Vol. 1. 2002, 367–371 vol.1. DOI: 10.1109/MWSYM.2002.1011632.
- [XZS17] W. Xiang, K. Zheng, and X. Shen. *5G Mobile Communications*. Springer International Publisher: Cham, Switzerland, 2017. ISBN: 9783319342061.
- [Yaz+10] Mani Yazdanpanahi, Senad Bulja, Dariush Mirshekar-Syahkal, Richard James, Sally E. Day, and F. Aníbal Fernandez. “Measurement of Dielectric Constants of Nematic Liquid Crystals at mm-Wave Frequencies Using Patch Resonator”. In: *IEEE Transactions on Instrumentation and Measurement* 59.12 (2010), pp. 3079–3085. DOI: 10.1109/TIM.2010.2062910.
- [Ye+17] L. Ye, C. Li, X. Sun, S. Jin, B. Chen, X. Ye, and J. Fan. “Thru-Reflect-Line Calibration Technique: Error Analysis for Characteristic Impedance Variations in the Line Standards”. In: *IEEE Transactions on Electromagnetic Compatibility* 59.3 (2017), pp. 779–788.
- [YLY11] Jijun Yao, Cedric Lee, and Swee Ping Yeo. “Microstrip Branch-Line Couplers for Crossover Application”. In: *IEEE Transactions on Microwave Theory and Techniques* 59.1 (2011), pp. 87–92. DOI: 10.1109/TMTT.2010.2090695.
- [YW06] D. K. Yang and S. T. Wu. *fundamentals of Liquid Crystal Devices*. WILEY, 2006.
- [YY13] Jung Gil Yang and Kyoungsoon Yang. “High-Linearity K-Band Absorptive-Type MMIC Switch Using GaN PIN-Diodes”. In: *IEEE Microwave and Wireless Components Letters* 23.1 (2013), pp. 37–39. DOI: 10.1109/LMWC.2012.2234732.
- [ZFB19] Dimitrios C. Zografopoulos, Antonio Ferraro, and Romeo Beccherelli. “Liquid-Crystal High-Frequency Microwave Technology: Materials and Characterization”. In: *Advanced Materials Technologies* 4.2 (2019), p. 1800447. DOI: <https://doi.org/10.1002/admt.201800447>. eprint: <https://onlinelibrary.wiley.com/doi/pdf/10.1002/admt.201800447>.



- [Zha+17] Yizhe Zhao, Cheng Huang, An-Yong Qing, and Xiangang Luo. “A Frequency and Pattern Reconfigurable Antenna Array Based on Liquid Crystal Technology”. In: *IEEE Photonics Journal* 9.3 (2017), pp. 1–7. DOI: 10.1109/JPHOT.2017.2700042.
- [ZSW93] W. Zheng, C. E. Smith, and L. Wang. “Response calibration for automated network analyzer systems”. In: *1993 (25th) Southeastern Symposium on System Theory*. 1993, pp. 29–33. DOI: 10.1109/SSST.1993.522736.



# Publications

## Journal as first Author

- [Wan+21b] Dongwei Wang, Ersin Polat, Henning Tesmer, and Rolf Jakoby. “Wideband evaluation of two types of slow-wave microstrip lines”. In: *Electronics Letters* (2021). DOI: <https://doi.org/10.1049/ell2.12389>.
- [Wan+21c] Dongwei Wang, Ersin Polat, Henning Tesmer, Rolf Jakoby, and Holger Maune. “A Compact and Fast  $1 \times 4$  Continuously Steerable Endfire Phased-Array Antenna Based on Liquid Crystal”. In: *IEEE Antennas and Wireless Propagation Letters* 20.10 (2021), pp. 1859–1862. DOI: 10.1109/LAWP.2021.3096035.
- [Wan+22c] Dongwei Wang, Ersin Polat, Christian Schuster, Henning Tesmer, Gustavo P. Rehder, Ariana L. C. Serrano, Leonardo G. Gomes, Philippe Ferrari, Holger Maune, and Rolf Jakoby. “Fast and Miniaturized Phase Shifter With Excellent Figure of Merit Based on Liquid Crystal and Nanowire-Filled Membrane Technologies”. In: *IEEE Journal of Microwaves* 2.1 (2022), pp. 174–184. DOI: 10.1109/JMW.2021.3131648.
- [Wan+22d] Dongwei Wang, Ersin Polat, Henning Tesmer, Rolf Jakoby, and Holger Maune. “Highly Miniaturized Continuously Tunable Phase Shifter Based on Liquid Crystal and Defected Ground Structures”. In: *IEEE Microwave and Wireless Components Letters* (2022), pp. 1–4. DOI: 10.1109/LMWC.2022.3142410.
- [Wan+22e] Dongwei Wang, Ersin Polat, Henning Tesmer, Holger Maune, and Rolf Jakoby. “Switched and Steered Beam End-Fire Antenna Array Fed by Wideband Via-Less Butler Matrix and Tunable Phase Shifters Based on Liquid Crystal Technology”. In: *IEEE Transactions on Antennas and Propagation* (2022), pp. 1–1. DOI: 10.1109/TAP.2022.3142334.
- [Wan+22f] Dongwei Wang, Bruno M. Verona, Ariana L. C. Serrano, Philippe Ferrari, Rolf Jakoby, Holger Maune, and Gustavo P. Rehder. “Compact DC to 110 GHz Crossover Based on Metallic-Nanowire-Filled Membrane”. In: *IEEE Microwave and Wireless Components Letters* 32.1 (2022), pp. 45–48. DOI: 10.1109/LMWC.2021.3115585.
- [Wan+23] Dongwei Wang, João E. G. L. é, Gustavo Palomino Marcelo, Gustavo Marcati A. Alves, Ariana L. C. Serrano, Rolf Jakoby, and Gustavo P. Rehder. “A 100 GHz Switched Beam Patch Antenna Array With  $4 \times 4$  Butler Matrix

Based on Metallic-Nanowire-Filled Membrane (to be submitted)". In: *IEEE Microwave and Wireless Components Letters* (2023).

## Conference as first Author

- [Neu+23] Robin Neuder, Dongwei Wang(co-first author), Rolf Jakoby, and Alejandro Jiménez-Sáez. "Compact Liquid Crystal-based Defective Ground Structure Phase Shifter for Reconfigurable Intelligent Surfaces (accepted)". In: *2023 17th European Conference on Antennas and Propagation (EuCAP)*. 2023.
- [Wan+19a] Dongwei Wang, Matthias Jost, Matthias Nickel, Roland Reese, Gustavo P. Rehder, Philippe Ferrari, Ariana L.C. Serrano, Leonardo G. Gomes, Rolf Jakoby, and Holger Maune. "A Compact Butler Matrix Design Based on Metallic Nanowire Filled Membrane Technology and Tunable Phase Shifter at 160 GHz". In: *2019 44th International Conference on Infrared, Millimeter, and Terahertz Waves (IRMMW-THz)*. 2019, pp. 1–2. DOI: 10.1109/IRMMW-THz.2019.8873696.
- [Wan+20] Dongwei Wang, Matthias Nickel, Dominic Walk, Alejandro Jiménez, Ersin Polat, Roland Reese, Gustavo P. Rehder, Ariana L. C. Serrano, Leonardo G. Gomes, Philippe Ferrari, Rolf Jakoby, and Holger Maune. "Slow Wave Inverted Microstrip Line Based on Metallic Nanowire Filled Alumina Membrane". In: *2020 German Microwave Conference (GeMiC)*. 2020, pp. 160–163.
- [Wan+21a] Dongwei Wang, Matthias Nickel, Peter Schumacher, Ersin Polat, Henning Tesmer, Rolf Jakoby, and Holger Maune. "A Planar Quasi Yagi-Uda Antenna Designed For Liquid Crystal Based End-Fire Phased Arrays". In: *2021 IEEE Radio and Wireless Symposium (RWS)*. 2021, pp. 164–167. DOI: 10.1109/RWS50353.2021.9360363.
- [Wan+22a] Dongwei Wang, Rolf Jakoby, Holger Maune, Philippe Ferrari, Ariana L. C. Serrano, and Gustavo P. Rehder. "A Broad Band Patch Antenna Used as Auxiliary Load for Measuring Multi-port Device with 2-port VNA at W-band". In: *2022 14th German Microwave Conference (GeMiC)*. 2022, pp. 156–159.
- [Wan+22b] Dongwei Wang, Ersin Polar, Henning Tesmer, and Rolf Jakoby. "Compact Interference Based Microstrip Single-Pole Double-Throw Utilizing Liquid Crystal Phase Shifter". In: *2022 IEEE/MTT-S International Microwave Symposium - IMS 2022*. 2022, pp. 363–366. DOI: 10.1109/IMS37962.2022.9865271.

## Journal as Co-Author

- [Kam+22] Fynn Kamrath, Ersin Polat, Stipo Matic, Christian Schuster, Daniel Miek, Henning Tesmer, Patrick Boe, Dongwei Wang, Rolf Jakoby, Holger Maune, and Michael Höft. “Bandwidth and Center Frequency Reconfigurable Waveguide Filter Based on Liquid Crystal Technology”. In: *IEEE Journal of Microwaves* 2.1 (2022), pp. 134–144. DOI: 10.1109/JMW.2021.3115244.
- [Nic+20] Matthias Nickel, Alejandro Jiménez-Sáez, Prannoy Agrawal, Ahmed Gadallah, Andrea Malignaggi, Christian Schuster, Roland Reese, Henning Tesmer, Ersin Polat, Dongwei Wang, Peter Schumacher, Rolf Jakoby, Dietmar Kissinger, and Holger Maune. “Ridge Gap Waveguide Based Liquid Crystal Phase Shifter”. In: *IEEE Access* 8 (2020), pp. 77833–77842. DOI: 10.1109/ACCESS.2020.2989547.
- [Pol+20] Ersin Polat, Henning Tesmer, Roland Reese, Matthias Nickel, Dongwei Wang, Peter Schumacher, Rolf Jakoby, and Holger Maune. “Reconfigurable Millimeter-Wave Components Based on Liquid Crystal Technology for Smart Applications”. In: *Crystals* 10.5 (2020). DOI: 10.3390/cryst10050346.
- [Pol+22] Ersin Polat, Fynn Kamrath, Stipo Matic, Henning Tesmer, Alejandro Jiménez-Sáez, Dongwei Wang, Holger Maune, Michael Höft, and Rolf Jakoby. “Novel Hybrid Electric/Magnetic Bias Concept for Tunable Liquid Crystal Based Filter”. In: *IEEE Journal of Microwaves* 2.3 (2022), pp. 490–495. DOI: 10.1109/JMW.2022.3180227.
- [Tes+21] Henning Tesmer, Rani Razzouk, Ersin Polat, Dongwei Wang, Rolf Jakoby, and Holger Maune. “Temperature Characterization of Liquid Crystal Dielectric Image Line Phase Shifter for Millimeter-Wave Applications”. In: *Crystals* 11.1 (2021). DOI: 10.3390/cryst11010063.
- [Tes+22b] Henning Tesmer, Rani Razzouk, Ersin Polat, Dongwei Wang, and Rolf Jakoby. “Reconfigurable Liquid Crystal Dielectric Image Line Leaky Wave Antenna at W-Band”. In: *IEEE Journal of Microwaves* 2.3 (2022), pp. 480–489. DOI: 10.1109/JMW.2022.3175625.

## Conference as Co-Author

- [Gom+22] Leonardo Gomes, Dongwei Wang, Gustavo Palomino, João Lé, Rolf Jakoby, Holger Maune, Philippe Ferrari, Ariana L.C. Serrano, and Gustavo P. Rehder. “Slow-Wave MEMS phase shifter with Liquid Crystal for Reconfigurable 5G”. In: *2022 IEEE/MTT-S International Microwave Symposium - IMS 2022*. 2022, pp. 983–986. DOI: 10.1109/IMS37962.2022.9865403.

- [Tes+22a] Henning Tesmer, Ersin Polat, Dongwei Wang, and Rolf Jakoby. “Fully-Integrated Dielectric Image Line Phased Array with Liquid Crystal Phase Shifters at W-Band”. In: *2022 52nd European Microwave Conference (EuMC)*. 2022, pp. 171–174. DOI: 10 . 23919 / EuMC54642 . 2022 . 9924380.
- [Tes+22c] Henning Tesmer, Daniel Stumpf, Ersin Polat, Dongwei Wang, and Rolf Jakoby. “Dielectric Image Line Rod Antenna Array With Integrated Power Divider at W-Band”. In: *2022 16th European Conference on Antennas and Propagation (EuCAP)*. 2022, pp. 1–5. DOI: 10 . 23919 / EuCAP53622 . 2022 . 9769431.

## Supervised Student Theses

- **Lukas Kunkel:** *Design of a Fast Tunable Reflection Type Phase Shifter for Ka Band Utilizing Liquid Crystal*, Master Thesis, January 2020
- **Fahd Tayanne:** *Planar Transitions of Dielectric Image Lines to Metallic Transmission Lines*, Master Thesis, November 2021
- **Zeyu Xiang:** *Single Layer Reconfigurable Antenna*, Master Thesis, November 2021
- **Subramaniam Abinaya:** *RF simulation, component fabrication and measurements of LC-NaM structures*, internship, November 2021
- **Ali Abdallah:** *Steerable Microstrip Travelling Wave Array*, Seminar, November 2021





# Curriculum Vitae

## Personal Details

Name	Dongwei Wang
Date of birth	12.09.1991
Place of birth	Taiyuan, Shanxi, P.R.China

## Education

2018 – 2023	Research assistant Institut für Mikrowellentechnik und Photonik, Technische Universität Darmstadt, Germany
2014 – 2018	Information and Communication Karlsruher Institut für Technologie, Germany (Degree: M.Sc)
2010 – 2014	Electrical Engineering and Automation Zhejiang University, P.R.China (Degree: B.Eng)



# Erklärungen laut Promotionsordnung

## **§ 8 Abs. 1 lit. c PromO**

Ich versichere hiermit, dass die elektronische Version meiner Dissertation mit der schriftlichen Version übereinstimmt.

## **§ 8 Abs. 1 lit. d PromO**

Ich versichere hiermit, dass zu einem vorherigen Zeitpunkt noch keine Promotion versucht wurde. In diesem Fall sind nähere Angaben über Zeitpunkt, Hochschule, Dissertationsthema und Ergebnis dieses Versuchs mitzuteilen.

## **§ 9 Abs. 1 PromO**

Ich versichere hiermit, dass die vorliegende Dissertation selbstständig und nur unter Verwendung der angegebenen Quellen verfasst wurde.

## **§ 9 Abs. 2 PromO**

Die Arbeit hat bisher noch nicht zu Prüfungszwecken gedient.

Darmstadt, 19. Mai 2023

---